



universität
wien

DISSERTATION

Titel der Dissertation

Functionalized Gold-Nanoparticles for Bioanalysis

verfasst von

Mag. Helmut Hubert Hinterwirth

angestrebter akademischer Grad

Doktor der Naturwissenschaften (Dr. rer. nat.)

Wien, 2013

Studienkennzahl lt. Studienblatt:

A 091 419

Dissertationsgebiet lt. Studienblatt:

Dr.-Studium der Naturwissenschaften Chemie

Betreut von:

Prof. Dr. Michael Lämmerhofer



universität
wien

DISSERTATION

Title of the dissertation

Functionalized Gold-Nanoparticles for Bioanalysis

Author

Mag. Helmut Hubert Hinterwirth

Aspired academic degree

Doctor rerum naturalium (Dr. rer. nat.)

Vienna, 2013

Study code: A 091 419

Branch of study: Chemistry

Adviser: Prof. Dr. Michael Lämmerhofer

*All that glisters is not gold,
Often have you heard that told:
Many a man his life hath sold,
But my outside to behold:
Gilded tombs do worms infold.
Had you been as wise as bold,
Young in limbs, in judgment old,
Your answer had not been inscroll'd.
Fare you well, your suit is cold.*

Shakespeare

(The Merchant of Venice)

Danksagung

An dieser Stelle möchte ich allen herzlichen danken, die mich im Laufe meines Studiums und im Speziellen während meiner Dissertation tatkräftig unterstützt haben.

Zuallererst möchte ich meinem Mentor Prof. Michael Lämmerhofer danken, der mir eine interessante Themenstellung ermöglichte und bei zahlreichen interessanten Diskussionen stets seine Hilfestellung bot. Effizienz hat seitdem für mich eine andere Bedeutung. Danken möchte ich ihm auch dafür, dass er mir die Möglichkeit gab, an mehreren nationalen und internationalen Kollaborationen, Meetings und Konferenzen teilzunehmen.

Ein weiterer Dank geht an Prof. Wolfgang Lindner, in dessen Arbeitsgruppe ich mich stets wohl fühlte. Danken möchte ich ihm besonders auch für die motivierenden Gespräche und zahlreichen Anregungen.

Eine wertvolle Unterstützung waren stets meine Kollegen, insbesondere Sissy, Steffi, Andrea(s), Georg, Norbert, Jeannie, Michal, Denise, Reini und Roli. In Erinnerung werden mir stets die netten Grillabende und geselligen Feierabende bleiben, aber auch die interessanten fachlichen Gespräche und gegenseitige Motivation. Besonders hervorheben möchte ich weiters noch Peter, der nicht nur alle technischen Probleme und Hürden beseitigte, sondern auch bei den regelmäßigen Balkon-Gesprächen stets ein offenes Ohr hatte.

Gabriel, Johannes, Reini, Babsi und allen meinen Freunden möchte ich danken für die schönen gemeinsamen Unternehmungen. Freundschaften sind mehr wert als jeder Titel.

Ein besonderer Dank geht an meine Mutter, die mir das Studium ermöglichte und mich immer moralisch und auch finanziell unterstützt hat. Worte können es nicht richtig beschreiben, daher einfach: **DANKE!**

Functionalized Gold-Nanoparticles for Bioanalysis

- Abstract -

Gold nanoparticles (GNPs) are widely used in various nanoscale applications due to their unique physical and chemical properties. Furthermore, GNPs prepared by size-controlled synthesis can be modified by straightforward surface functionalization with thiol containing ligands, which form a self-assembled monolayer utilizing the strong dative gold-sulfur bond. Functionalized GNPs offer a broad range of immobilization and bioconjugation chemistries depending on the nanoparticle size and the properties of the ligands used.

The present dissertation focuses on the optimization of the surface chemistry of nanoparticle-biocatalysts and affinity traps. Therefore, the influence of GNP size and type of spacer and linking ligands, respectively, on the bioactivity of immobilized enzymes and antibodies (Abs) as well as the reduction of unspecific binding was thoroughly investigated. We developed a new method to determine the ligand coverage onto GNPs based on the linear relationship of gold/sulfur ratio and GNP size, whereby the simultaneous measurement of gold and sulfur by inductively coupled plasma-mass spectrometry (ICPMS) was carefully validated and the accurate size of GNPs determined by transmission electron microscopy (TEM). The influence of GNP size and ligands with different chain lengths and hydrophilicity/lipophilicity on the bioactivity of immobilized trypsin was studied by tryptic digestion of proteins. The optimized protocol was used for immobilization of Abs onto GNPs and compared to directed attachment *via* protein G binding. The successful immobilization chemistry was utilized for development of functionalized GNP extraction and enrichment of oxidized low-density lipoproteins (oxLDL) as biomarkers for e.g. atherosclerosis. For this purpose, anti-oxLDL-Abs were bound to GNPs and the dissociation constant K_d was determined. The specific extraction of oxLDL and in particular of oxidized phosphatidylcholines (oxPCs) with GNP-Ab bioconjugate was accomplished by sensitive detection with liquid chromatography/mass spectrometry (LC-MS/MS). Furthermore, the determination of K_d for specific oxidized phospholipids out of oxLDL allowed the identification of antibody specificity and affinity of several anti-oxLDL-antibodies.

In summary, the systematic study of bioconjugation chemistry from GNP size-controlled synthesis over surface functionalization and determination of ligand density to the influence on bioactivity of immobilized proteins is investigated in this thesis. Functionalized GNPs are a useful tool in bioanalysis, however, the bioactivity has to be controlled by fine-tuning of nanoparticle size and immobilization chemistry.

Funktionalisierte Gold-Nanopartikel für die Bioanalytik

- Zusammenfassung -

Die Anwendung von Goldnanopartikeln (GNP) ist wegen ihrer einzigartigen physikalischen und chemischen Eigenschaften in verschiedensten wissenschaftlichen Gebieten weitverbreitet. Ein Grund für deren Attraktivität ist die einfache größengesteuerte Synthese. Des Weiteren kann eine einfache und direkte Oberflächenfunktionalisierung mit Thiol-Liganden erfolgen, wobei die starke Gold-Schwefel Bindung ausgenutzt wird, um eine selbst-assemblierende Monoschicht zu formen. Funktionalisierte GNPs bieten ein weites Spektrum an Immobilisierungs- und Biokonjugationschemie, abhängig von Nanopartikelgröße und den verwendeten Liganden.

Die vorliegende Dissertation beschäftigt sich mit dem Einfluss der Goldnanopartikelgröße und der Liganden auf die Bioaktivität von immobilisierten Enzymen bzw. Antikörpern (Ak) sowie mit der Reduzierung von unspezifischen Bindungsphänomenen. Dabei wurde eine neue Methode entwickelt, um die Ligandendichte auf GNP zu bestimmen. Diese beruht auf dem linearen Zusammenhang zwischen dem Gold/Schwefel Verhältnis und der GNP-Größe. Die gleichzeitige Messung von Gold und Schwefel mittels Massenspektrometrie mit induktiv gekoppeltem Plasma als Ionenquelle wurde sorgfältig validiert und die exakte Größe der Nanopartikel mit einem Transmissionselektronenmikroskop (TEM) bestimmt. Der Einfluss der Nanopartikelgröße und Liganden unterschiedlicher Kettenlängen und hydrophiler/lipophiler Eigenschaften auf die Bioaktivität von auf GNP immobilisiertem Trypsin wurde durch tryptischen Verdau von Proteinen optimiert. Die optimisierte Immobilisierungschemie wurde weiters für die Immobilisierung von Antikörpern auf GNP verwendet und mit der direkten Bindung über Protein G verglichen. Die erfolgreiche Biokonjugationschemie konnte durch die spezifische Extraktion und Anreicherung von oxidiertem Lipoprotein niedriger Dichte (oxLDL, oxidiertes low-density lipoprotein, Biomarker für Arteriosklerose) gezeigt und die Dissoziationskonstante K_d bestimmt werden. Die sensitive Detektion von extrahiertem und angereichertem oxLDL und insbesondere von oxidiertem Phosphatidylcholin mittels GNP-Ak Biokonjugat erfolgte mittels

Flüssigchromatographie gekoppelt mit Massenspektrometrie. Des Weiteren erlaubt die Bestimmung von K_d von einzelnen oxidierten Phospholipiden die Analyse der Ak-Spezifität und Affinität für verschiedene anti-oxLDL-Ak.

Insgesamt wurde die Biokonjugationschemie von der größengesteuerten Synthese von GNPs hin zur Oberflächenfunktionalisierung und Bestimmung der Ligandendichte auf die Bioaktivität von immobilisierten Proteinen systematisch untersucht. Funktionalisierte GNPs bieten ein nützliches Werkzeug für bioanalytische Fragestellungen, jedoch ist die Feinregulierung der Nanopartikelgröße und Immobilisierungsschemie ein kritischer Faktor für die Bioaktivität.

Table of Contents

1.	INTRODUCTION	1
1.1.	Preamble	1
1.2.	Nano – Definitions	3
1.2.1.	Nanomaterials	3
1.2.2.	Nanotechnology	4
1.3.	Gold Nanoparticles	4
1.4.	GNP – Biodistribution and Toxicology	7
1.5.	Synthesis of GNPs – Turkevich-Frens Method	8
1.6.	Characterization of GNPs	10
1.6.1.	(Localized Surface) Plasmon Resonance (LSPR)	10
1.6.2.	Zeta Potential Measurements – Colloidal Stability	13
1.6.3.	GNP – Size Determination Methods	14
1.7.	GNPs - Surface Modification and Functionalization	20
1.8.	Bioconjugation Chemistry on GNPs	25
1.9.	GNPs in Bioanalysis	28
2.	CONCLUDING DISCUSSIONS	35

ABBREVIATIONS.....	36
LIST OF FIGURES	37
LIST OF TABLES	39
REFERENCES	40
3. PUBLICATIONS AND CONFERENCE CONTRIBUTIONS	53
3.1. List of Publications	53
3.2. Oral Presentations.....	54
3.3. Poster Presentations	54
4. COOPERATION PARTNERS.....	55
APPENDIX	57
A-1. Comparative Method Evaluation for Gold Nanoparticle Size and Size Distribution Analysis.....	57
A-2. Quantifying Thiol Ligand Density of Self-Assembled Monolayers on Gold Nanoparticles by Inductively Coupled Plasma-Mass Spectrometry.	83
A-2.1 Supplementary Information	93
A-3. Bioconjugation of trypsin onto gold nanoparticles: Effect of surface chemistry on bioactivity.....	101
A-3.1 Supplementary Information	111

A-4. Gold Nanoparticle Conjugated Anti-Oxidized Low-Density Lipoprotein-Antibodies and Liquid Chromatography/Mass Spectrometry as Tools for Targeted Lipidomics.....	119
A-4.1 Supplementary Information.....	147
B-1. Selectivity Issues in Targeted Metabolomics: Separation of Phosphorylated Carbohydrate Isomers by Mixed-Mode Hydrophilic Interaction/Weak Anion Exchange Chromatography.....	161
B-1.1 Supplementary Information	173
CURRICULUM VITAE	190

1. INTRODUCTION

1.1. Preamble

Nanoparticles attract high attention due to their unique physical and chemical properties. Thereby, the growing field of nanomaterial applications ranges from textiles to electronic implementation and medicine. Nanotechnology is referred to herald a new age.

This thesis focuses in particular on the topic of gold nanoparticles (GNPs). The introduction comprises the description of their physicochemical properties, the preparation and characterization, their surface modification and functionalization, the immobilization chemistry of proteins and their application in bioanalysis. An overview of the subtopics of the work and the used mainly applied methods throughout the dissertation is given in (Figure 1).

The introduction makes no claim to be complete but should give a gross outline about and gain an insight into the potential of GNPs. GNPs are useful tools in biosensors and immunoassays, in drug delivery, therapy, and diagnostic sensors, in sample preparation, and so forth. However, their properties depend significantly on the particle size and surface modification. Thus, next to quality control methods also fundamental studies are necessary to optimize each approach.

El-Sayed summarized the significance of GNPs in biomedicine, *that gold nanotechnology-enabled biomedicine is not simply an act of 'gilding the (nanomedicinal) lily', but that a new 'Golden Age' of biomedical nanotechnology is truly upon us.*¹

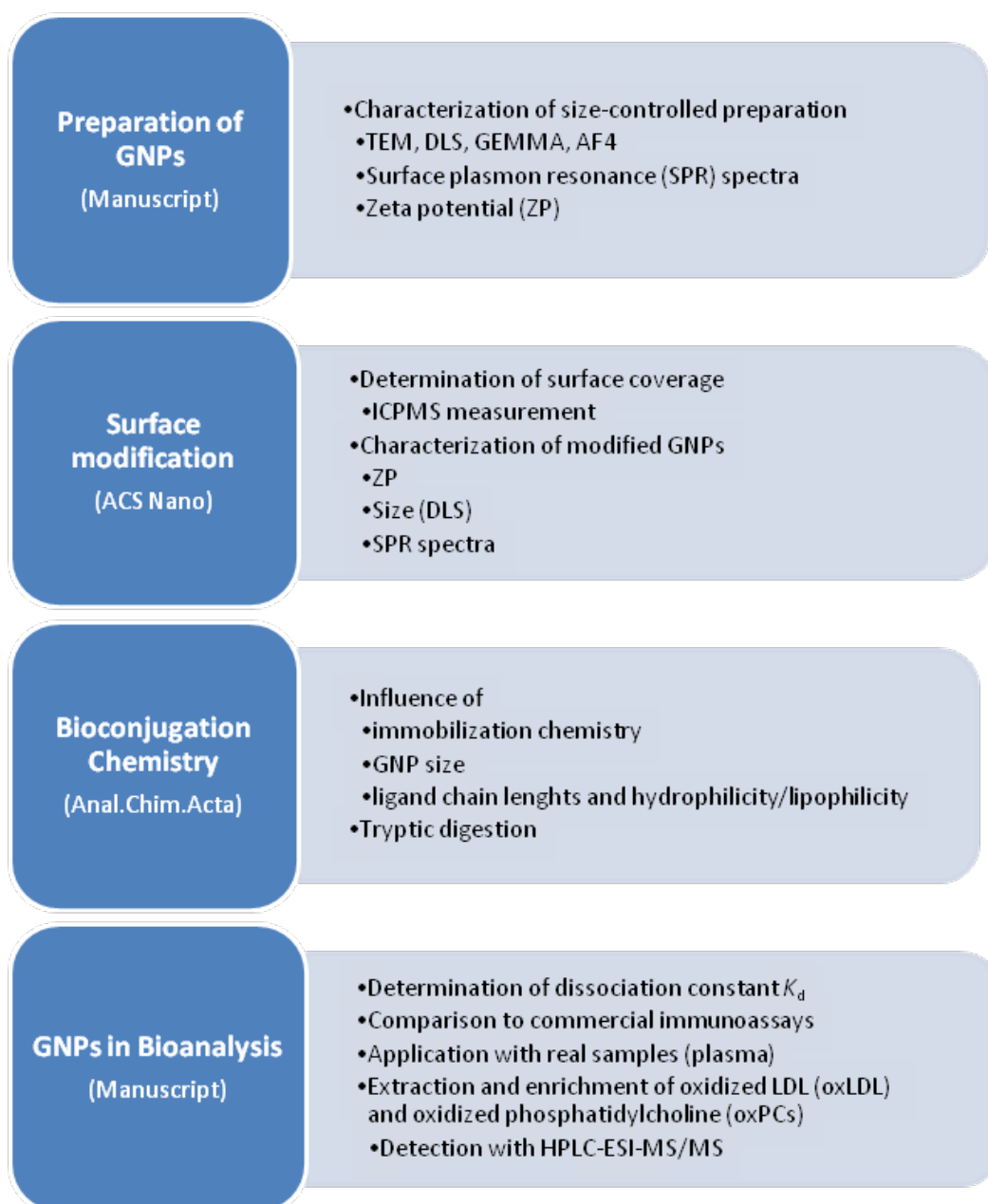


Figure 1: Overview of the subsections of the thesis including size-controlled synthesis of GNPs and their characterization, their surface modification and functionalization, immobilization chemistry of proteins such as trypsin and antibodies and their application in bioanalysis for tryptic digestion and extraction / enrichment of oxidized LDL as biomarkers, respectively. (TEM, transmission electron microscopy; DLS, dynamic light scattering; GEMMA, gas phase electrophoretic molecular mobility analyzer; Af4, asymmetric flow field-flow fractionation; ICPMS, inductively-coupled plasma mass spectrometry)

1.2. Nano – Definitions

Nanomaterials have unique physical and chemical properties different from atomic ones or nanoclusters as well as different from bulk particles with larger diameters. The characteristics of nanoparticles especially depend on their composition, size and size distribution, shape and morphology, their specific surface area and charge as well as their chemical surface modification.

1.2.1. Nanomaterials

In the recommendation of the European Commission from October 2011, particles are defined as nanomaterials if more than 50% of the particles are in the size range of 1 nm to 100 nm as counted by number size distribution. An alternative definition considers materials of which the specific surface area by volume is greater than $60 \text{ m}^2 \text{ cm}^{-3}$. Aggregates and agglomerates of such particles are included as well.²

The relationship between the specific surface area as one criterion for nanomaterials and the diameter of spherical particles is shown in Figure 2. Thereby, the surface area decreases significantly with the inverse of the nanoparticle diameter D and a factor 6,000 from $6,000 \text{ m}^2 \text{ cm}^{-3}$ ($D = 1 \text{ nm}$) to $60 \text{ m}^2 \text{ cm}^{-3}$ ($D = 100 \text{ nm}$).

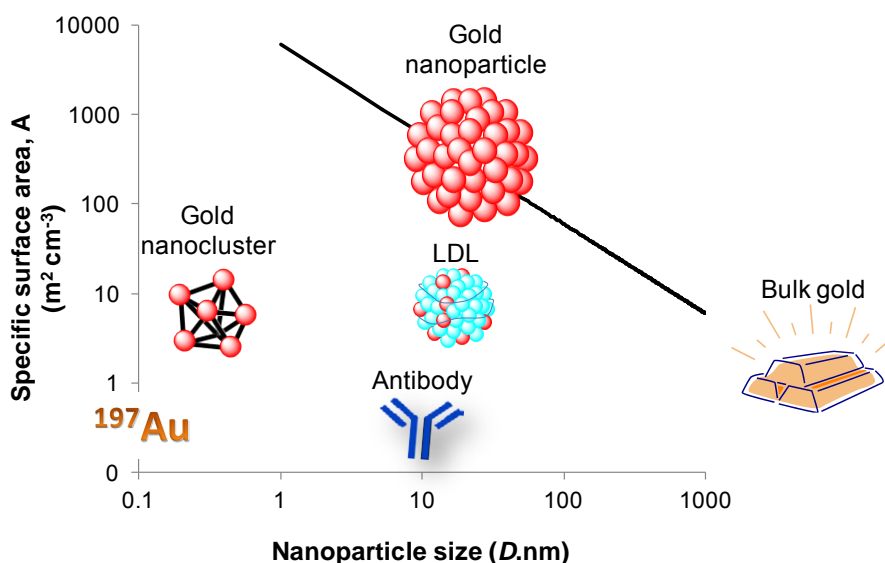


Figure 2: Nanomaterials are defined in the size range of 1 – 100 nm or with a specific surface area greater than $60 \text{ m}^2 \text{ cm}^{-3}$. The relationship calculated for a spherical particle with a diameter D and its surface area A shows a decrease with $A = 6,000 D^{-1}$. Schematically shown are compounds with different sizes in the nanoscale.

1.2.2. Nanotechnology

In the Nanotechnology Research Directions: *Vision for Nanotechnology in the Next Decade* (1999), nanotechnology is defined as:³

Nanotechnology is the ability to control and restructure the matter at the atomic and molecular levels in the range of approximately 1–100 nm, and exploiting the distinct properties and phenomena at that scale as compared to those associated with single atoms or molecules or bulk behavior. The aim is to create materials, devices, and systems with fundamentally new properties and functions by engineering their small structure. This is the ultimate frontier to economically change materials properties, and the most efficient length scale for manufacturing and molecular medicine. The same principles and tools are applicable to different areas of relevance and may help establish a unifying platform for science, engineering, and technology at the nanoscale. The transition from single atoms or molecules behavior to collective behavior of atomic and molecular assemblies is encountered in nature, and nanotechnology exploits this natural threshold.

1.3. Gold Nanoparticles

GNPs are used in various nanoscale applications due to their unique physical and chemical properties. The increasing popularity is caused by their easy and low-cost size-controlled synthesis, the straightforward surface modification and their surface plasmon resonance (SPR). These quality characteristics contributed to the exponential increase of publications dealing with GNPs to more than 6,000 papers and about 200 reviews in 2012 (Figure 3). The growing impact of nanotechnology attracts attention even on the world market where final products incorporating nanotechnology accounted for about \$ 254B in 2009 and will evolve to estimated \$ 3T in 2020 (WTEC panel report, *Nanotechnology Research Directions for Societal Needs in 2020* **2010/09/30**, www.wtec.org/nano2).

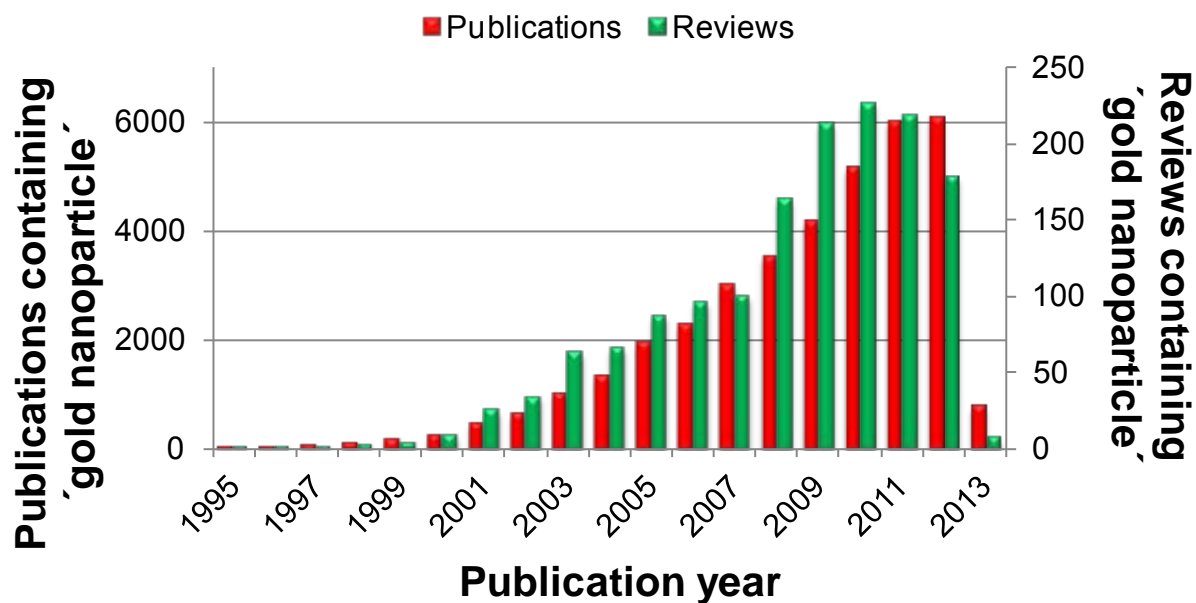


Figure 3: Publications and reviews containing 'Gold nanoparticle' (1995-2013). Data were generated by keyword search in SciFinder® (2013/02/14).

The physical phenomenon of surface plasmon resonance (SPR) was already exploited by ancient and medieval artisans as the first nanotechnologists for the red staining of glass (Figure 4).



Figure 4: The Lycurgus Cup, dating from the 4th century A.D., is made from glass impregnated with gold nanoparticles; seen in (a) transmitted light and (b) reflected light (Paul Mulvaney, MRS Bull. 2001, © Cambridge University Press, Reprinted with permission)⁴

They used gold chloride in molten glass and created therewith red colored gold nanoparticles. Several hundred years later and about 20 years after the invention of the electron microscope, Turkevich undertook the first structural study of citrate capped GNPs in 1951⁵ which was further optimized by Frens for the preparation of monodispersed GNPs (Figure 5).⁶

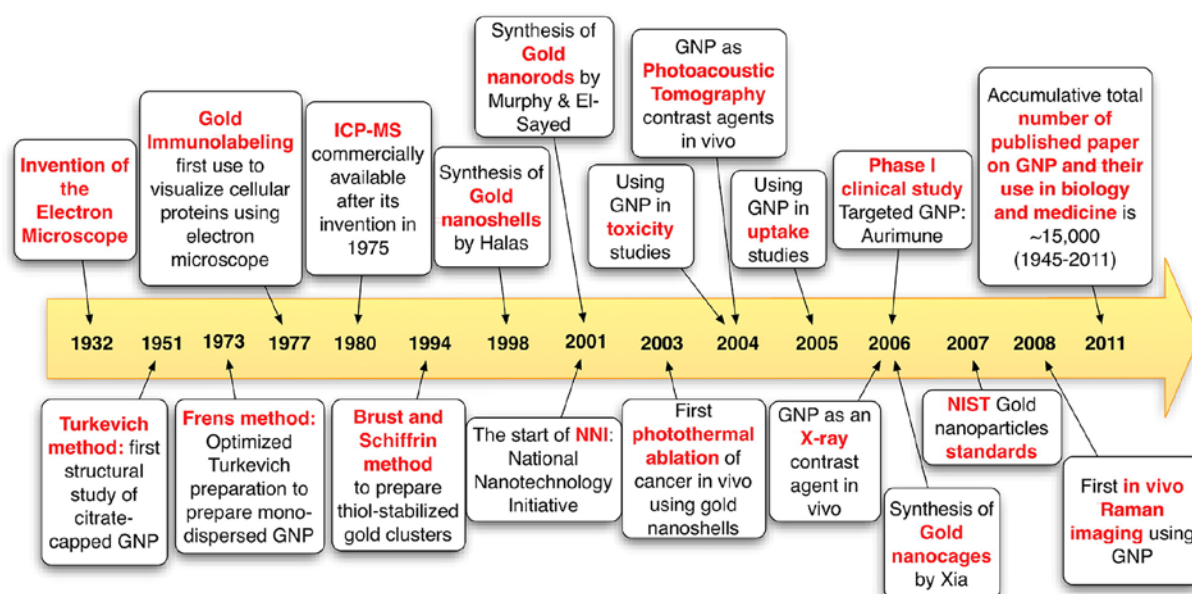


Figure 5: The golden timeline (Alkilany *et al.*, Acc.Chem.Res. 2012, © American Chemical Society, Reprinted with permission)⁷

Different synthesis strategies were developed to prepare thiol-stabilized gold clusters in a one-step synthesis (Brust and Schiffrin)⁸ or to prepare GNPs with different morphology.⁹ The advantage of visualization by immunolabeling contributed to the fast growth in GNP applications which reached a new level with the invention of the inductively-coupled plasma mass spectrometry (ICPMS) for the low and sensitive detection of metals in the 1980s. X-ray crystallography and density functional theory (DFT) studies allowed an insight in the structural composition and theoretical considerations were performed to study ligand density of thiolate-protected gold complexes ($Au_n(SR)_m$) for small gold clusters with about 1 nm diameter in size ($Au_{10} - Au_{144}$).¹⁰⁻¹² Up to now, GNPs are used in a broad range of biomedical^{1, 13-15} and bionanotechnological^{16, 17} applications as well as for chemical, biological, and clinical diagnostic sensing.¹⁸⁻²⁵

The impact of nanotechnology will contribute in the future in screening and detection of new biomarkers in clinical diagnosis. The miniaturization with coinstantaneous high surface-to-volume ratio in combination with bioanalytical tools such as antibody specificity and/or sensitive mass spectrometry detection will improve the search for specific (low-abundant) markers.

For this purpose, the control and measuring of the nanoparticle characteristics such as size and size distributions is necessary for fine-tuning and optimization of its application, but one critical point is still the harmonization of methods as they do not provide comparable results.²

1.4. GNP – Biodistribution and Toxicology

The control of size is not only important for (bio)analytical tools but also of major relevance for dispute environmental and health risks. Jong *et al.* presented a study on particle size-dependent organ distribution of GNPs with 10, 50, 100, and 250 nm in diameter after intravenous administration in rats.²⁶ Thereby, they found small particles with 10 nm distributed in various organs while larger GNPs were only detected in blood, liver, and spleen. As a main key parameter for the bioactivity of GNPs the size is a critical factor. GNPs within the size range of 10 to 100 nm are distributed in all organs of the reticuloendothelial system and small GNPs show the most widespread organ distribution,²⁷ while the blood-brain or blood-retinal barriers are size-dependent with an upper penetration limit of about 15 to 20 nm.²⁸ Furthermore, GNPs with diameters of 1 to 2 nm are potentially toxic as they can bind irreversibly to biopolymers such as to the B-form DNA.²⁹ Although bare GNPs or conjugates are not dangerous *a priori*, GNPs can cause nanospecific toxic effects as they are potential hazards to human health.²⁸

Although the *in vivo* study of toxicity still has to be improved for final concluding remarks, the state of the art can be summarized with the statement of Fadeel and Garcia-Bennett: *Better safe than sorry.*³⁰

1.5. Synthesis of GNPs – Turkevich-Frens Method

The synthesis of GNPs by chemical reduction involves two major parts, a reduction and a stabilization step, whereby the reduction includes a nucleation step followed by successive growth.⁹ The *in situ* synthesis implicates the nucleation and growth steps in the same process; otherwise, it is called 'seed-growth method'.

The first method for GNP preparation was described by Turkevich in 1951 and further optimized by Frens in 1973.^{5, 6} As one of the most established synthetic routes, HAuCl₄ is heated up until boiling and trisodium citrate is added quickly to the solution, whereby the color changes from yellow to brownish and finally to wine-red. Within this method, citrate acts as both reducing and stabilization agent. Thereby, the size of GNPs can be controlled by variation of the citrate/HAuCl₄ ratio (Figure 6, appendix A-2).

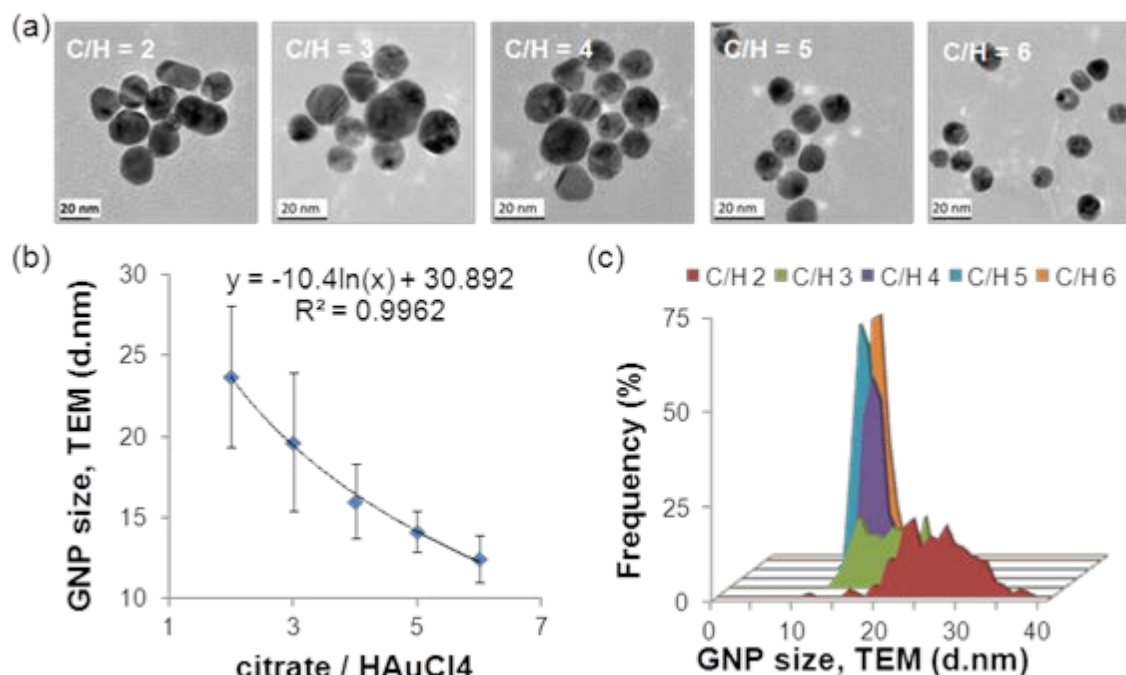
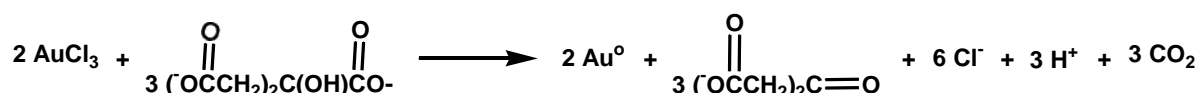


Figure 6: (a) TEM images of GNPs prepared by variation of the citrate/HAuCl₄ (C/H) ratio. (b) The relation can be described in a logarithmic function. (c) TEM histograms of the corresponding GNPs (Hinterwirth *et al.*, ACS Nano 2013, © American Chemical Society, Reprinted with permission).³¹

The reduction of gold chloride with citrate is a multi-step process described by Kumar *et al.*³² The initial process is the oxidation of citrate to dicarboxy acetone followed by the reduction of auric salt to aurous salt and finally a disproportionation to elemental gold. The overall stoichiometry of the reduction reaction is described as follows:



Considering the fact that dicarboxy acetone is lost in side reactions to form acetone, Kumar *et al.* declared a C/H ratio larger than 1.5 for complete conversion of auric chloride to elemental gold.

An insight into the formation of GNPs by the classical citrate method is shown by Polte *et al.* using small-angle X-ray scattering (SAXS) and X-ray absorption near edge structure spectroscopy (XANES).³³ Thereby, they claim a four-step mechanism of GNP formation starting with a fast initial formation of small nuclei, followed by a coalescence of the nuclei into bigger particles and a further slow growth of the particles ending with a subsequent fast reduction (Figure 7).

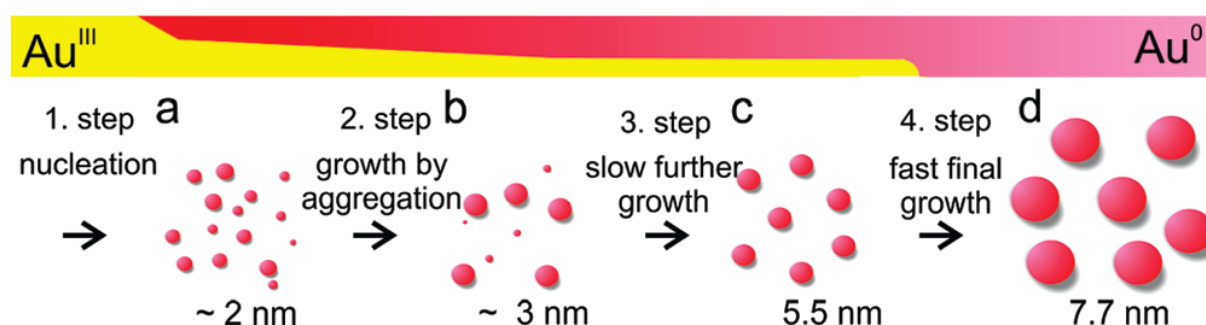


Figure 7: Schematic illustration of the nucleation and growth process in the classical citrate formation method (Polte *et al.*, JACS 2010, © American Chemical Society, Reprinted with permission).³³

The coalescence of small particles is described hereby as a critical step in the formation of monodisperse particles and determines the polydispersity of the GNPs throughout the synthesis reaction. Reaction temperature, concentration and volume of gold and reducing agent, respectively, as well as their ratio and stirring processes are *i.a.* crucial factors and influence significantly the nanoparticle formation process.

1.6. Characterization of GNPs

Up to now, there is no universal detection method for (gold) nanoparticles which cover all key parameters that affect the properties of nanomaterials such as size (including size distribution, surface area, shape, and structure), charge, concentration, agglomeration, and modification. An overview about several common techniques used for GNPs characterization is given in Figure 8. As a separate point, some separation techniques are listed because they are not only applied in sample preparations but also in combination with other detection modes e.g. by coupling with ICP-MS.

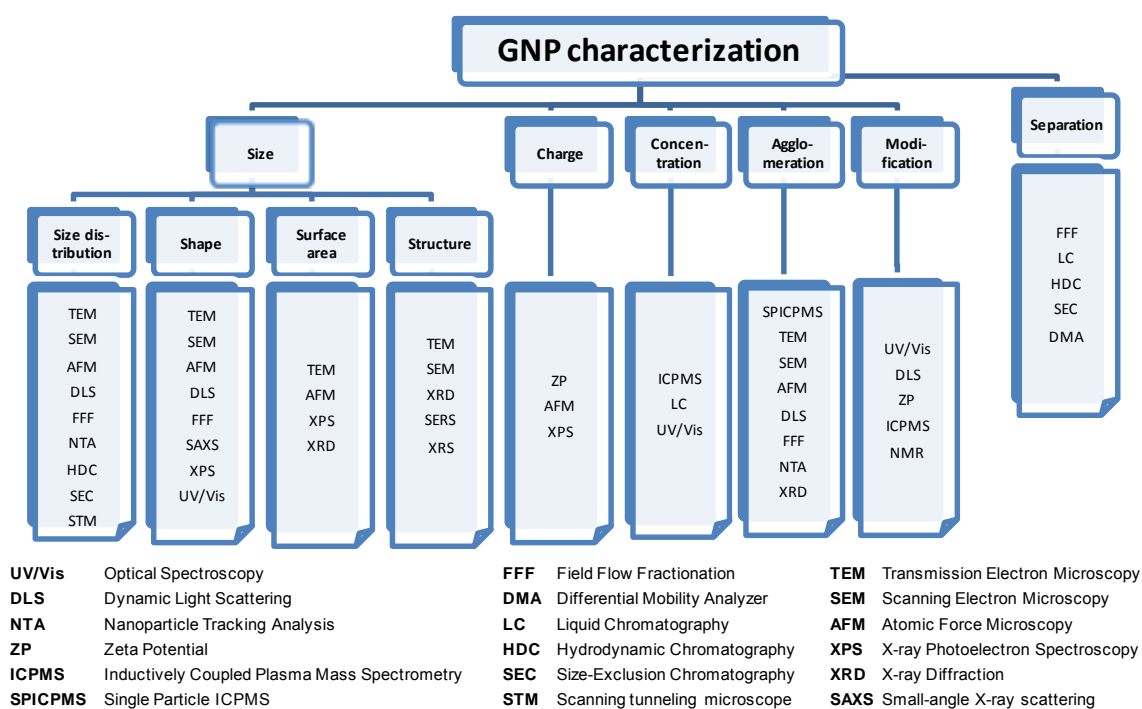


Figure 8: Overview of commonly used methods for the characterization of GNPs (modified from Bandyopadhyay *et.al.*, Appl.Spectr.Rev. 2012).³⁴

1.6.1. (Localized Surface) Plasmon Resonance (LSPR)

In contrast to gold nanoclusters with single-electron transitions with a molecular-like electron system, the optical properties of GNPs are dominated by plasmon excitation and possess a collective nature.^{11, 35} The effect of an optical field on the electron cloud and its resulting surface plasmon resonance (SPR) spectra are schematically shown in Figure 9a, b (appendix A-1).

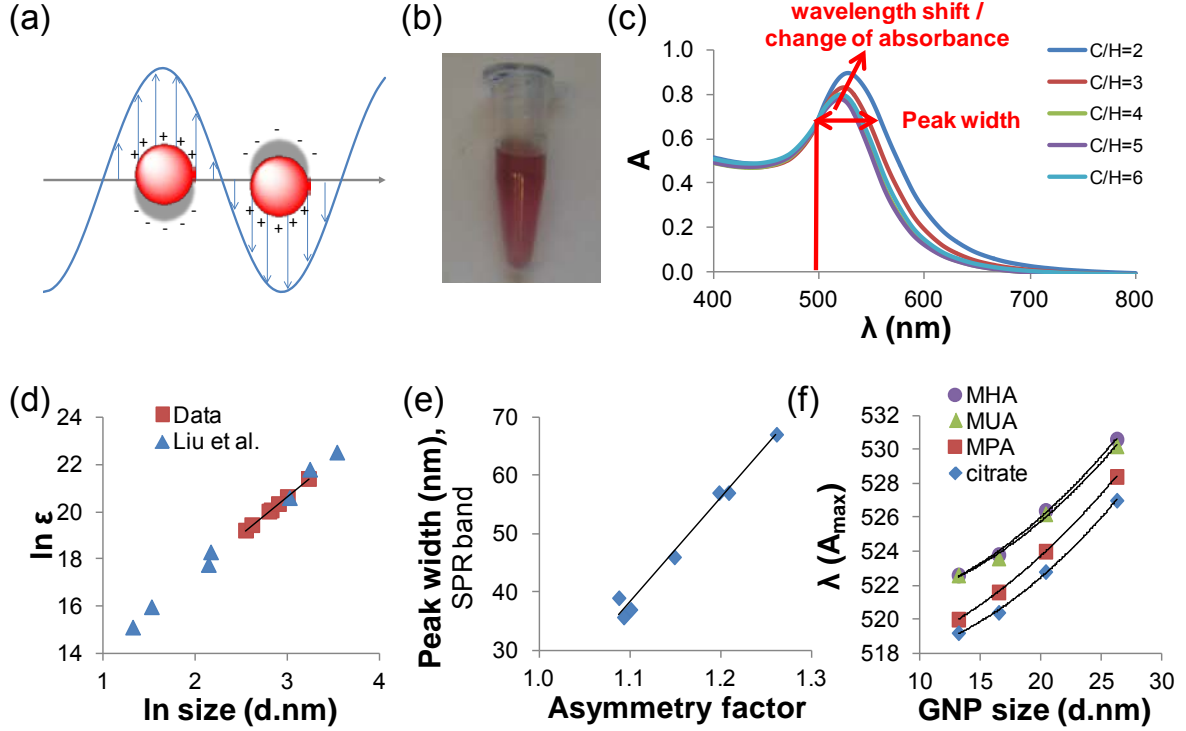


Figure 9: (a) Schematic illustration showing the effect of the optical field on the electron cloud in a spherical metal nanoparticle (adapted from Willets and Van Duyne, *Annu.Rev.Phys.Chem.* 2007)³⁶ (b) Red colored GNP suspension. (c) SPR spectra of GNPs with different sizes have an absorbance maximum at a wavelength of about 530 nm and show an increase of peak width as well as a shift of the wavelength maxima with NP size. (d) The linear relationship of the logarithm of size and the logarithm of the extinction coefficient was described already by Liu *et al.*³⁷ (e) Furthermore, a relationship between the asymmetry factor determined with TEM measurements and the peak width of the SPR band was observed. (f) The shift of the wavelength maximum is not only influenced by the GNP size but also its ligand modification.

The correlation between the logarithms of GNP diameter D and its extinction coefficient ε (Figure 9c) is described by Liu *et al.* (eq.1):³⁸

$$\text{(eq.1)} \quad \ln \varepsilon = 3.32111 \ln D + 10.80505$$

According to the Lambert-Beer law, the concentration of the GNPs can be calculated allowing the determination of GNP size and concentration from the extinction spectrum.³⁹⁻⁴¹ This finding is in agreement with the Mie theory which describes the scattering of electromagnetic radiation by spherical particles. Using the Maxwell's equation, the extinction spectrum can be calculated for metal spheres with a radius R , (where R is much smaller than the wavelength of light λ ; i.e. $R/\lambda < 0.1$) (eq.2).^{36, 42}

$$\text{(eq.2)} \quad E(\lambda) = \frac{24\pi^2 N R^3 \varepsilon_{out}^{3/2}}{\lambda \ln(10)} \left[\frac{\varepsilon_i(\lambda)}{(\varepsilon_r(\lambda) + \chi \varepsilon_{out})^2 + \varepsilon_i(\lambda)^2} \right]$$

where, ε_r and ε_i are the real and imaginary components of the metal dielectric function, respectively, and ε_{out} the dielectric constant of the external environment. For

spherical particles, the value of the factor χ is 2 but depends strongly on the geometry and can take values up to 20 for particles with high aspect ratios.

The asymmetry factor can be determined for GNPs with different sizes by TEM measurements calculating the average of the length and width (*i.e.* by $(l_m + w_m)/2$, where l_m and w_m are the arithmetic mean of the length and width). Thereby, with increase of the diameter, an increase of asymmetry was observed (data not shown). Furthermore, a correlation between the aspect ratios and the peak width of the SPR band is observed (Figure 9d).

Next to the dependency of the extinction spectrum on the particle size and geometry, the LSPR extinction wavelength maximum λ_{\max} changes with the local environment. Since λ_{\max} is correlated to the dielectric constant ε (or refractive index, n ; whereby $\varepsilon = n^2$), the changes on the GNP surface *e.g.* through the adsorption of ligands causes a shift in λ_{\max} (eq.3):³⁶

$$\text{(eq.3)} \quad \Delta\lambda_{\max} = m\Delta n \left[1 - \exp\left(\frac{-2d}{l_d}\right) \right]$$

where m is the refractive-index response of the NP; Δn describes the change in the refractive index induced by the adsorbed compound; d is effective adsorbate layer thickness, and l_d , the characteristic electromagnetic-field-decay length.

GNPs of different sizes were prepared in this work and the surface was saturated with bifunctional thiol-containing ligands (MHA, 16-mercaptohexadecanoic acid; MUA, 11-mercaptopundecanoic acid; MPA, 3-mercaptopropionic acid). In agreement with the calculation in (eq.3), we observed a shift of the wavelength maximum λ_{\max} for citrate stabilized GNPs in dependency of their sizes as well as for ligand modified GNPs (Figure 9e).

In summary, LSPR is a useful tool as fast control mechanism to estimate the GNP size and shape but also its modification with adsorbates.

1.6.2. Zeta Potential Measurements – Colloidal Stability

The stability of particles in suspension is described by the DLVO theory named after the scientists Deryagin, Landau, Verwey, and Overbeek.^{43, 44} By this theory, the colloidal stability is described by the total potential energy function as balance of the potential energy due to the solvent as well as the balance between the Van der Waals attractive forces and the electrostatic repulsive forces. Via the formation of charges on the particle surface, an electrical double layer is formed consisting of an inner Stern layer and an outer boundary layer; the zeta-potential (ZP) represents the potential at the shear surface (Figure 10).

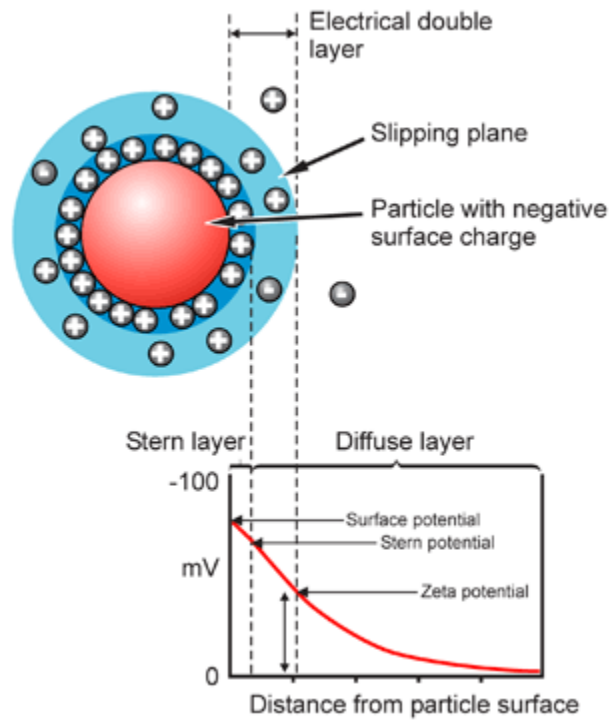


Figure 10: Schematic representation of the zeta potential (www.malvern.com, © Malvern Instruments Ltd.; 2013/02/20)

The determination of the ZP is routinely obtained by electrophoretic light scattering (ELS) measurement, whereby an electric field \vec{E} is applied which induces NP electrophoresis with the electrophoretic velocity \vec{v} (eq.4):⁴⁵

$$\text{(eq.4)} \quad \vec{v} = \mu \vec{E}$$

Using the Smoluchowski equation, the electrophoretic mobility μ can be written as term of the ZP, ζ (eq.5).⁴⁵

$$\text{(eq.5)} \quad \mu = \frac{\varepsilon \varepsilon_0}{\eta} \zeta \quad (\kappa \alpha \gg 1)$$

with ε , dielectric constant of the solvent; ε_0 , vacuum permittivity ($\sim 8.85 \times 10^{-12} \text{ C}^2 \text{ N}^{-1} \text{ m}^{-2}$); η , solvent viscosity; κ , Debye-Hückel parameter; α , radius of the particle.

In conclusion, the measurement of the ZP is a useful tool to estimate the stability of colloids in suspension, whereby particles with ZP lower than -30 mV and higher than +30 mV, respectively, are regarded as stable.

1.6.3. GNP – Size Determination Methods

Measuring size and size distributions in nanomaterials is challenging in many cases and different measurement methods may not provide comparable results. Harmonised measurement methods must be developed with a view to ensuring that the application of the definition leads to consistent results across materials and over time. Until harmonised measurement methods are available, best available alternative methods should be applied. (European Commission, On the Definition of Nanomaterials, 2011).²

Since the size and size distribution of nanomaterials define *i.a.* their properties, the synthesis of monodispersed particles has to be carefully validated. For example, the specific surface area decreases significantly with the inverse of the particle diameter and a factor of 6,000 from $6,000 \text{ m}^2 \text{ cm}^{-3}$ for spheres with 1 nm to $60 \text{ m}^2 \text{ cm}^{-3}$ for spheres with 100 nm (Figure 2).

One attempt for method harmonization is facilitated by the National Institute of Standards and Technology (NIST) which provides gold nanoparticles of different sizes as reference materials (RM).

TEM

So far, all methods for nanoparticle characterization have their pros and cons. Thus, they need to be validated in the most cases by microscopic techniques such as transmission electron microscopy (TEM). TEM measurements provide the accurate size, size distribution, shape, and structure,⁴⁶ however, no information about the charge and concentration of GNPs is obtained.

DLS

Dynamic light scattering (DLS) provides a fast and non-destructive method for size and size distribution as well as for detection of agglomerates.^{47, 48} The successful application of this technique was demonstrated for GNPs in bioanalysis e.g. for biomolecular binding studies and assays, respectively.^{49, 50} DLS measures the Rayleigh scattering from the Brownian motion of the particles. Thereby, the intensity I of the scattered light can be approximately calculated for particles with the diameter D (with D much smaller than the wavelength λ of the laser) (eq.6):

$$\text{(eq.6)} \quad I \propto D^6; I \propto 1/\lambda^4$$

The hydrodynamic diameter D_h can be further calculated by the Stokes-Einstein equation (eq.7):

$$\text{(eq.7)} \quad D_h = \frac{kT}{3\pi\eta D_c}$$

with k , Boltzmann's constant; T , temperature; η , viscosity; D_c , translational diffusion coefficient. Although DLS provides in principal comparable results with TEM measurements, the size and size distribution is always larger (wider) than in TEM because of the solvation shell around the solid particle contrary to TEM. Moreover, temperature and the solvent's viscosity and ionic strength are crucial parameters and have to be controlled and considered in sample preparation.⁴⁷ Furthermore, particles with high aspect ratios are known to produce false negative signals in the low and high size area.⁴⁷

NTA

Another technique which is also based on the Brownian motion of particles in solution and their light scattering is the Nanoparticle Tracking Analysis (NTA). In contrast to DLS, NTA uses high sensitive CCD cameras for capturing the scattered light which additionally allows visualization of the particles in parallel to the analysis of the hydrodynamic diameter.

FFF

Several sub-versions of Field-Flow Fractionation (FFF) such as (Asymmetric) Flow Field-Flow Fractionation (AF4), Sedimentation Field-Flow Fractionation (SdFFF), Thermal Field-Flow Fractionation or Split Flow Thin Cell Fractionation (SPLITT) exist depending on the used forces for particle separation. Figure 11 depicts the principal working scheme of FFF.

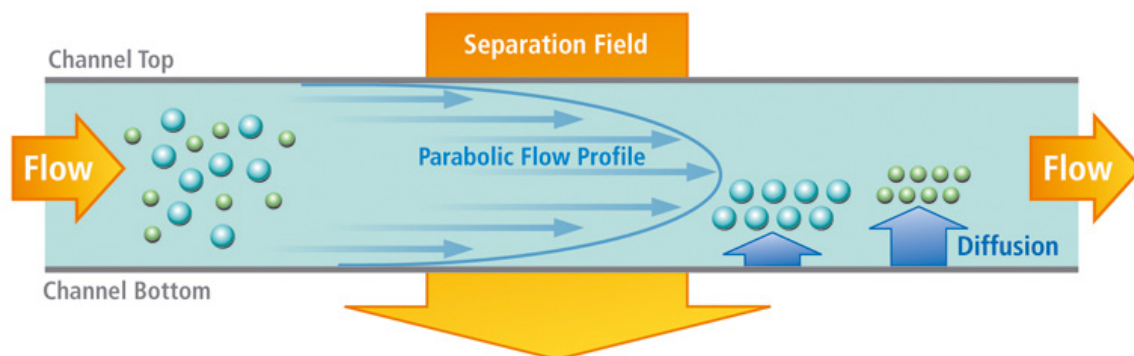


Figure 11: Scheme of FFF principle (www.postnova.com, © Postnova Analytics Inc., 2013/03/01)

The FFF separation is based on the size dependent distribution of particles in a parabolic flow stream separated by an orthogonally applied separation field and a counteracting diffusion force. Thereby, smaller particles in the middle of the flow field migrate faster compared to the bigger ones located in the lower stream line of the flow.

AF4 as the most often applied FFF technique can be coupled e.g. with multi-angle light scattering (MALS)⁵¹⁻⁵⁵ and / or ICPMS.⁵⁴⁻⁵⁷

DMA

Differential mobility analysis (DMA) provides another method for size determination based on ion mobility technique (eq.4). Alternative names for DMA are ion mobility spectrometer (IMS), scanning mobility particle spectrometer (SMPS), gas phase electrophoretic molecular mobility analyzer (GEMMA), and electrical aerosol analyzer (EAA).⁵⁸ The electrophoretic mobility μ is correlated with the electrophoretic mobility diameter D_{em} according to (eq.8):

$$(eq.8) \quad D_{em} = \frac{q_e C_c}{3\pi\eta\mu}$$

with q_e , electrical charge(s); C_c , Cunningham correction factor; η , viscosity of the sheath gas. The classical application employs a condensed particle counter (CPC) for the detection of charged particles. However, the big advantage of DMA is the possibility to couple it with several sample introduction and detection methods (Table 1)⁵⁹ such as liquid chromatography as pre-separation and detection e.g. with highly sensitive ICP-MS.

Table 1: Combination possibilities of DMA with different sample introduction and detection methods (adapted from Kanu *et al.*, JMS 2008).⁵⁹

Sample introduction methods	Ionization sources	Ion mobility spectrometers	Detector
Vapor introduction	Radioactive ionization (RI)	Ambient-pressure ion mobility spectrometry (APIMS)	Condensed particle counter (CPS)
Thermal desorption	Corona discharge ionization (CDI)	Reduced-pressure ion mobility spectrometry	ICP-MS
Gas chromatography	Photoionization (PI)	Aspiration ion mobility spectrometry (AIMS)	Time-of-flight MS
Direct infusion	Electrospray ionization (ESI)	Field-asymmetric ion mobility spectrometry (FAIMS)	Quadrupole MS
Liquid chromatography	Secondary electrospray ionization (SESI)	Differential-mobility spectrometry (DMS)	Ion trap MS
Solid samples	Matrix-assisted laser-desorption ionization (MALDI)	Traveling-wave ion mobility spectrometry (TWIMS)	Fourier transform ion cyclotron MS
Hydrodynamic Chromatography			Magnetic sector MS
			Tandem instruments MS

The combination tool of nano-ESI-IMS-ICPMS proved to be useful for the determination of size and elemental composition of nanoparticles.⁶⁰ A successful prototype of ESI-DMA coupled to ICP-MS for real-time discrimination and elemental analysis of GNPs was recently developed.⁶¹

ICPMS

Inductively-coupled plasma mass spectrometry is a highly sensitive method for trace analysis of metals and has been recently shown to be a robust method for the quantitative analysis of GNPs as well as for the determination of size, size distribution, and elemental characterization.^{17, 26, 31, 60, 62-69} Also the successful hyphenation of separation techniques such as FFF, DMA or liquid chromatography has been demonstrated.

The direct determination of GNPs and quantitation by ICPMS measurement without previous dissolving was shown to be a sensitive and robust technique (Figure 12).⁶⁵

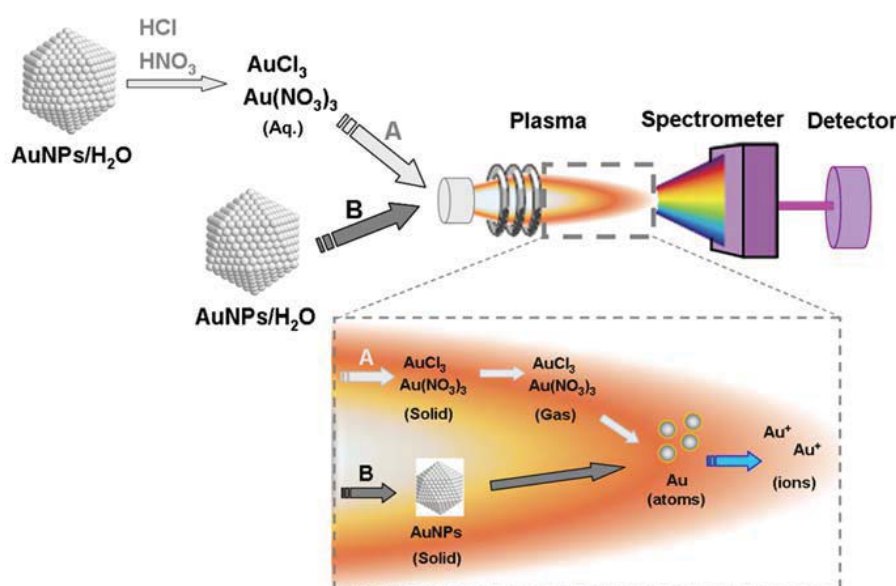


Figure 12: Scheme of GNP analysis by ICP-MS (A) with and (B) without previous gold dissolution (Allabashi *et.al.*, J Nanopart. Res. 2009, © Springer Science and Business Media B.V., Reprinted with permission).⁶⁵

Moreover, the simultaneous measurement of gold and sulfur was demonstrated (Figure 13, appendix A-2.1).³¹ The experiments pinpointed that the presence of high concentrations of gold compared to sulfur does not influence the recovery of spiking experiments when the rejection parameter Rpa value of the dynamic reaction cell (DRC) was additionally optimized to avoid overloading of the secondary electron multiplier detector operated in dual mode.

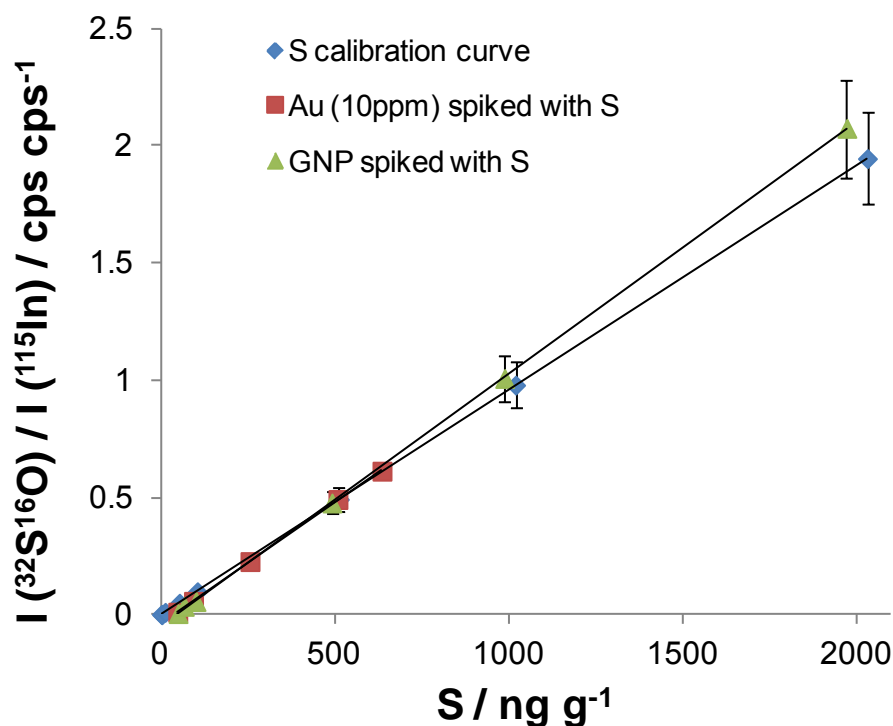


Figure 13: Recovery of sulfur in the presence of gold validated by spiking experiments (Hinterwirth *et al.*, ACS Nano 2013, ©.American Chemical Society; Reprinted with permission).³¹

Other Separation Methods

Other separation methods for GNP characterization include size exclusion chromatography,⁷⁰⁻⁷³ hydrodynamic chromatography,⁷⁴ and capillary electrophoresis.⁷⁵⁻⁷⁷

Comparison of Size Determination Methods

Figure 14 depicts a comparison of different methods for size-determination (appendix A-1). The accurate size of GNPs was determined by TEM measurements. DLS as a fast and non-invasive technique provides comparable results, although the size and size distribution measured as hydrodynamic diameter is always slightly larger. Being a convenient orthogonal method, AF4 shows nearly baseline separation for GNPs with 13 nm and 26 nm, respectively. However, the electrophoretic separation of single-charged particles by GEMMA appeared to have the highest size resolution and the narrowest size distribution.

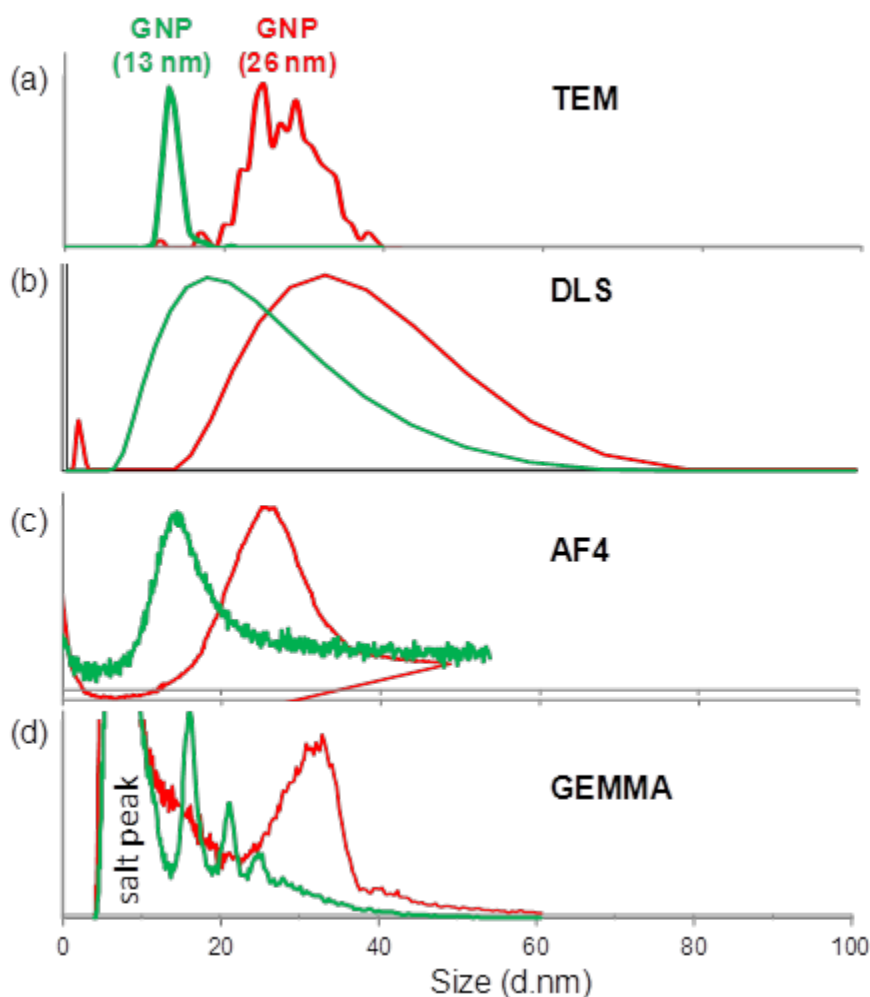


Figure 14: Comparison of different size characterization methods for two distinct GNP batches with 13 nm and 26 nm in diameter as measured with TEM.

1.7. GNPs - Surface Modification and Functionalization

Gold itself is one of the most stable and inert metal. However, one exception represents thiol containing derivatives, in which the bond of sulfur to gold atoms with $40 - 50 \text{ kcal mol}^{-1}$ is close to the strength of gold-gold bond.^{10, 78} This strong dative binding is utilized in many applications for GNP surface modification with bifunctional thiol-containing ligands which form a self-assembled monolayer (SAM) on the outer surface.^{10, 78-82} Such functionalized GNPs offer a broad field for further immobilization chemistry. Other strategies for surface modification and, thus, for alteration of the GNP's properties comprise attachment *via* ionic and hydrophobic interactions, respectively, and coating with polymers and polyelectrolytes (Figure 15).

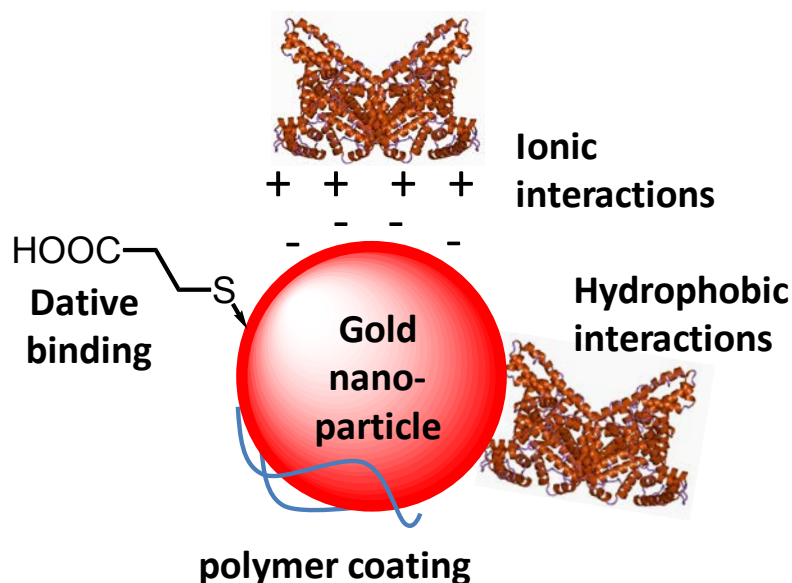


Figure 15: Scheme of different strategies for GNP modification (modified after Greg Hermanson, Bioconjugation Techniques, Elsevier).⁸³

Direct attachment

The attachment of biomolecules *via* ionic and hydrophobic interactions has the advantage of fast immobilization chemistry by simple mixing of GNP and protein solution. However, the effect of pH and pI of the protein⁸⁴ as well as of the nanoparticle size^{85, 86} has to be considered as they influence the quantity of bound amount. The increase of size with additional layers can be determined *e.g.* with DLS^{87, 88} and NTA,⁸⁸ respectively. Another possibility for the measurement of the binding activity of proteins onto GNPs is based on the Mie theory which describes a shift in the LSPR peak with increase of the layer thickness (eq.3).⁸⁵

Lou *et.al.* studied the influence of GNP size under different pH values on the direct binding of different antibody concentrations with regard to stability.⁸⁹ Thereby, they report the highest stability for smaller GNPs (16nm), but a loss of sensitivity for antigen measured by immunochromatographic assay.

One application of this immobilization strategy is the adsorption of protein A/G onto GNPs which can be used in a next step for binding IgG with a high affinity to protein A/G. NTA and DLS provide further application potential to determine the dissociation constant K_d as examined for example of protein A conjugated GNPs towards IgG or of antibody-GNPs conjugates against antigens.^{49, 88}

Polymer coating

Polymers are often used as stabilizer to enhance long-term stability by introduction of steric hindrance and thus, prevent nanoparticle agglomeration as well as by adjustment of the solubility. Further advantages are the functionalization with tunable high-density shell/brush polymers and tailored properties to facilitate compatibility and processability.⁹⁰ Polymer coated GNPs can be prepared by utilizing dative bindings of sulfur to gold (so called grafting techniques) or by physisorption by fabrication of surfactant-stabilized reverse micelles ('templating' technique).⁹⁰

In another example, Masereel *et.al.* prepared layer-by-layer protected GNPs and could control the surface charge using cationic polyallylamine (PAA; positive charge, ZP (GNP/PAA) = +55 mV) and anionic polystyrenesulfonate (PSS, negative charge, ZP (GNP/PAA/PSS) = -39 mV), respectively (Figure 16).⁹¹ Reporting up to 5 alternating layers, they could further tune the size of GNPs. In a last step, they accomplished the successful immobilization of IgG via EDC/NHS coupling by appliance in an ELISA setup.

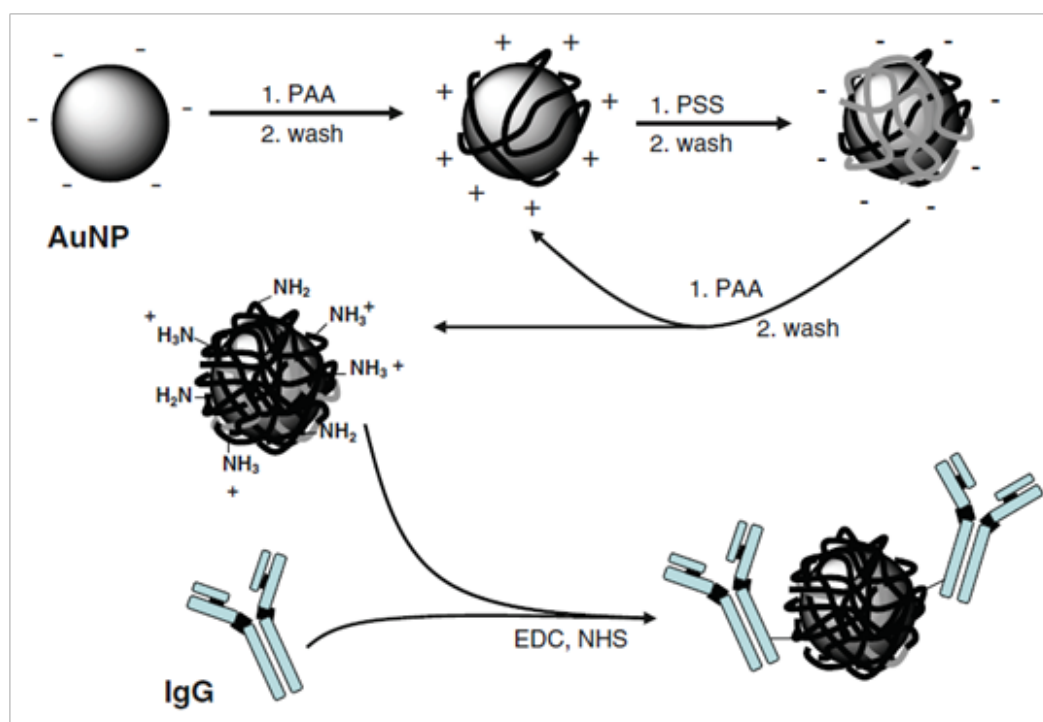


Figure 16: Layer-by-layer coating of GNPs with cationic polyallylamine (PAA) and anionic polystyrenesulfonate (PSS). IgG was finally immobilized via EDC/NHS coupling (Masereel *et al.*, J.Nanopart.Res. 2011, © Springer Science and Business Media B.V.; Reprinted with permission).⁹¹

Dative Binding

In contrast to direct attachment strategy, the strong dative gold-thiol binding has the benefit of high binding stability. Thiolate-protected GNPs can be prepared by simultaneous reduction of auric chloride and HS-ligand according to the Brust-Schiffrin method.⁸

Another approach utilizes SAM formation of thiol-containing molecules with a high surface ligand density.³¹ The coating with protective organic ligands increases the GNP stability and can introduce different functional groups for further immobilization chemistries. In doing so, the properties of GNPs can be controlled and adjusted such as the solubility, chemical reactivity, surface chemistry and supramolecular binding of the nanomaterial.^{92, 93} The knowledge of the structure, composition and ligand density of the protective layer is crucial for many applications but rarely reported in literature. Different techniques were adapted to study ligand packing density onto GNPs such as ICP-OES,⁹⁴ X-Ray⁹⁵ and XPS,⁹⁶ LSPR⁹⁷ and SERS⁹⁸ or using different labeling assays.⁹⁹ Recently, we developed a new method for quantifying thiol ligand density on GNPs.³¹ This method is based on the Au/S ratio measured simultaneously by ICP-MS and its dependency on the GNP size. We found a decrease of the surface coverage was found with increasing ligand chain length from 6.3 molecules nm⁻² for the short mercaptopropionic acid (chain length of 0.68 nm) to 4.3 molecules nm⁻² for the longer mercapto-poly(ethylene glycol) (PEG)₇-carboxylic acid (HS-PEG₇-COOH) ligand (chain length of 3.52 nm) (Figure 17, appendix A-2).

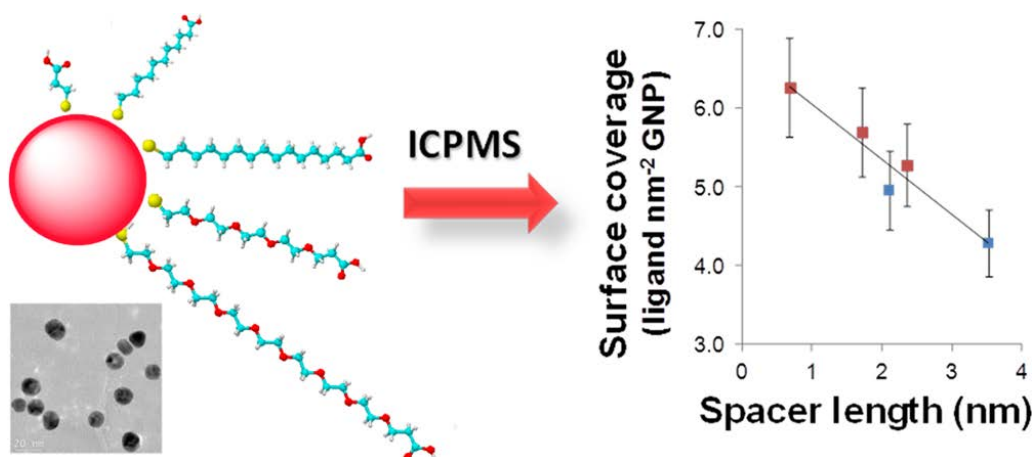


Figure 17: Influence of spacer length on the surface coverage as determined by the simultaneous measurement of Au/S ratio of thiolate-protected GNPs by ICP-MS and its dependency on GNP size (Hinterwirth *et al.* ACS Nano 2013, © American Chemical Society; Reprinted with permission).³¹

Multifunctional GNPs can be prepared by ligand exchange. Therefore, functional ligands can be introduced into the organic layer by replacement reaction which allows subsequent modifications.⁹³

Another approach of ligand design is the coating of GNPs with 3-mercaptopropyltrimethoxysilane followed by a covalent cross-linking of the ligand shell to increase the stability (Figure 18).¹⁰⁰

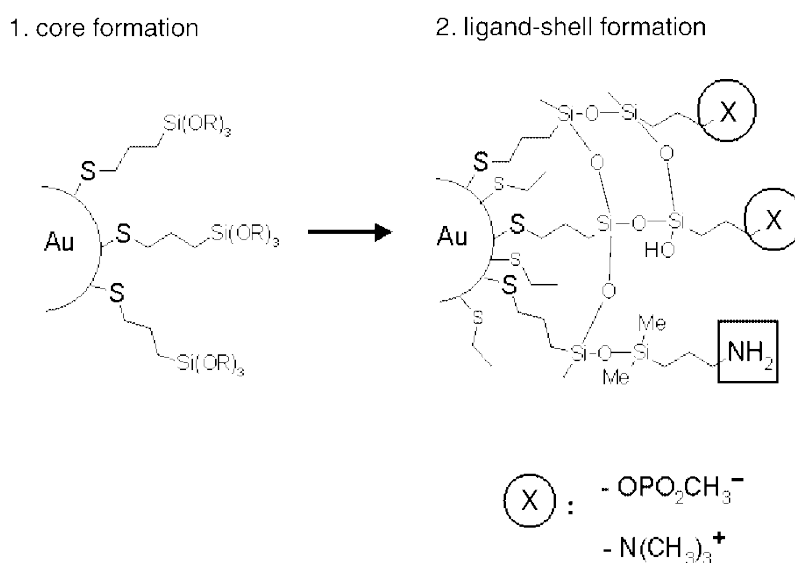


Figure 18: Scheme of GNP coating with trimethoxysilane followed by cross-linking of the ligand shell (Schroedter and Weller, *Angew.Chem.* 2002, © WILEY-VCH Verlag GmbH & Co. KGaA, Weinheim; Reprinted with permission).¹⁰⁰

Analytical methods for the characterization of surface modified GNPs comprise *i.a.* nuclear magnetic resonance (NMR) spectroscopy, surface enhanced Raman spectroscopy (SERS), Fourier-transform infrared (FTIR) spectroscopy, LC-MS, X-ray photoelectron spectroscopy (XPS), combustion elemental analysis, Auger electron spectroscopy (AES) and microscopic techniques (TEM; AFM, *etc.*).^{101, 102}

Functionalized GNPs are used in a various applications and the surface chemistry can be flexibly adjusted for those applications. For example, chromophoric groups can be introduced to create novel physical and optical properties in sensors or photoelectronic materials.¹⁰³ Colorimetric and fluorescent assays based on GNPs were developed for the detection of ions such as Hg^{2+} or Pb^{2+} , and small organic molecules.¹⁰⁴ Furthermore, monolayer protected GNPs are often utilized as vehicles

for delivery of drugs, genetic materials, proteins, and small molecules,¹⁹ whereby the transfection efficiency and the cellular uptake can be increased e.g. with coating of cationic poly(ethyleneimine) (PEI).¹⁰⁵ The opposite effect to minimize interactions and unspecific bindings can be achieved *via* biocompatible polymer protections of the GNPs.¹⁰⁶⁻¹⁰⁸ In summary, SAM protected NPs can be created with favorable properties in dependency of the purpose by introducing new physical and chemical surface characteristics.

1.8. Bioconjugation Chemistry on GNPs

Biomolecules can be attached either directly onto GNPs *via* hydrophobic and ionic interactions or by covalent bond formation *via* functional ligands. Although this strategy is more complex and the immobilization chemistry has to be improved and optimized, it offers wide range of surface properties with tunable particle stability and biocompatibility.

Amine-carboxylate coupling^{86, 91, 109, 110} and 'click' chemistry¹¹¹ are the major strategies for covalent conjugation.¹⁶ The successful 'clicking' of azide nanorods to acetylene-functionalized trypsin (Figure 19) was demonstrated by tryptic digestion of the protein casein.¹¹¹

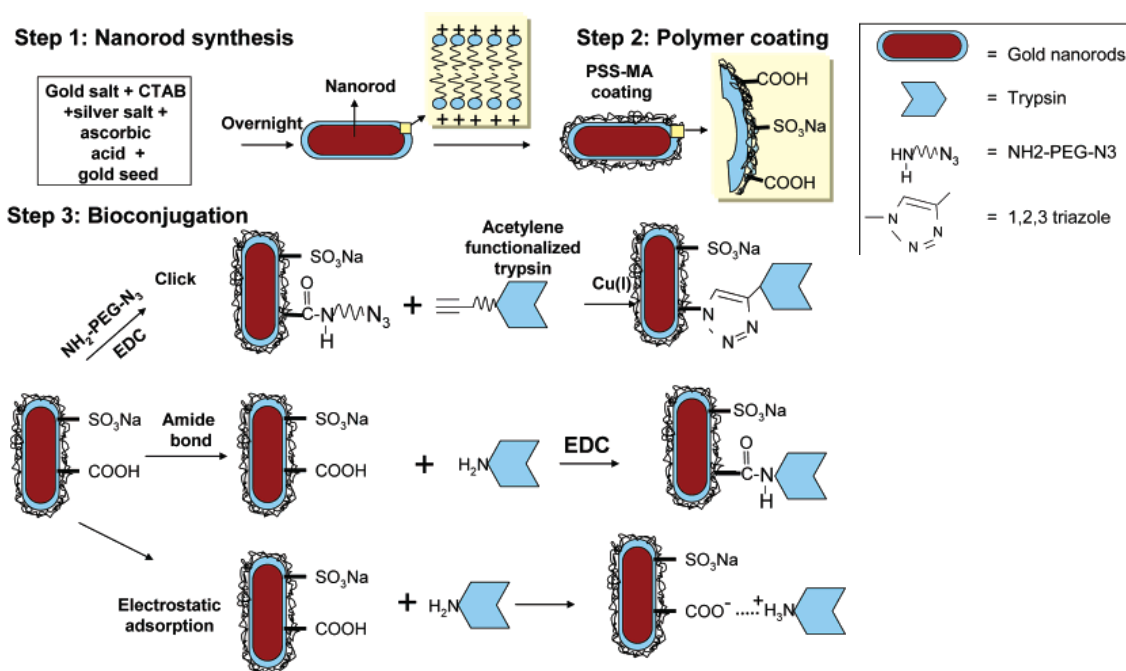


Figure 19: Bioconjugation strategy is shown for 'click' chemistry of azide functionalized gold nanorods to acetylene functionalized trypsin as well as for amine-carboxylate coupling *via* carbodiimide (EDC) linkage (Gole and Murphy, Langmuir 2008, © American Chemical Society, Reprinted with permission).¹¹¹

The immobilization of antibodies on GNPs coated layer-by-layer with polyelectrolytes (Figure 16) was confirmed by enzyme-linked immunosorbent assay (ELISA).⁹¹ Masson *et al.* studied the non-specific binding of serum proteins to Ab immobilized on gold surfaces using different biocompatible polymers by SPR sensors.¹⁰⁷ Using orthopyridyldisulfide-poly(ethylene glycol)-N-hydroxysuccinimide (OPSS-PEG-NHS) instead of carboxymethylated–dextran 500 kDa (CM-dextran) they could reduce the non-specific adsorption of serum proteins up to 73%.

The influence of variation of the chain lengths and hydrophilicity/lipophilicity of ligands for immobilization efficiency of trypsin *via* *N*-(3-dimethylaminopropyl)-*N*-ethylcarbodiimide hydrochloride / *N*-hydroxysuccinimide (EDC/NHS) linkage was examined in this work, whereby an increase of the amount of bound enzyme per GNP accompanied with an increase of enzyme activity was found with increasing spacer chain lengths (Figure 20, appendix A-3).⁸⁶ This effect can be explained by the higher flexibility of the longer linkers. Furthermore, a significant difference on the tryptic digestion was found when the protein was bound *via* hydrophilic PEG ligand compared to the lipophilic alkanoic acid ligand. The change of the spacer property seemed to have more influence than varying the GNP size from 18 nm to 33 nm.

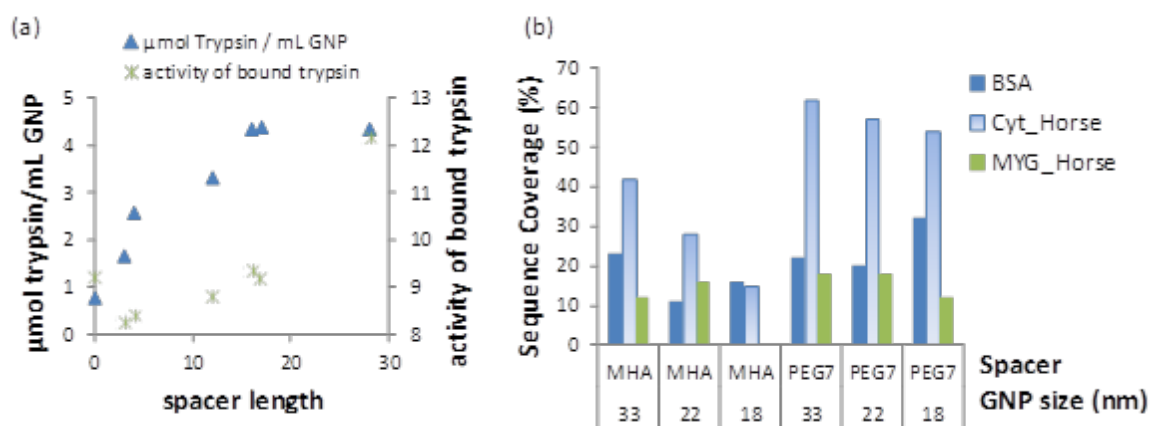


Figure 20: (a) Bioconjugation chemistry of trypsin onto carboxylic acid functionalized GNPs *via* EDC/NHS linkage shows a significant dependency of the enzyme activity and amount of bound protein per GNP on the ligand chain length. (b) Changing the lipophilic mercaptohexadecanoic acid (MHA) linker to the hydrophilic poly(ethylene glycol) (PEG₇) increases the tryptic digestion efficiency for bovine serum albumin (BSA), cytochrome C (CytC) and myoglobin (MYG) as measured by the sequence coverage found by MASCOT database search (Hinterwirth *et.al.* Analytica Chimica Acta 2012, © Elsevier; Reprinted with permission).⁸⁶

In another part of this work, antibodies were immobilized onto GNPs, with the goal to use them for selective capture of biomarkers. The conjugation of Ab *via* HS-PEG₇-COOH ligand on GNPs by EDC/NHS coupling chemistry (GNP-PEG₇-Ab) – similarly to the optimized procedure in the previous work for trypsin immobilization⁸⁶ – was characterized thoroughly during all immobilization steps (Figure 21, appendix A-4). Residual carboxylic acids on the outer particle surface were blocked in a second step by reaction with EDC/NHS and amine-containing Tris by simple buffer change from PBS buffer to Tris/HCl, pH 7.5, to reduce possible ionic interactions and thus, to minimize unspecific bindings.

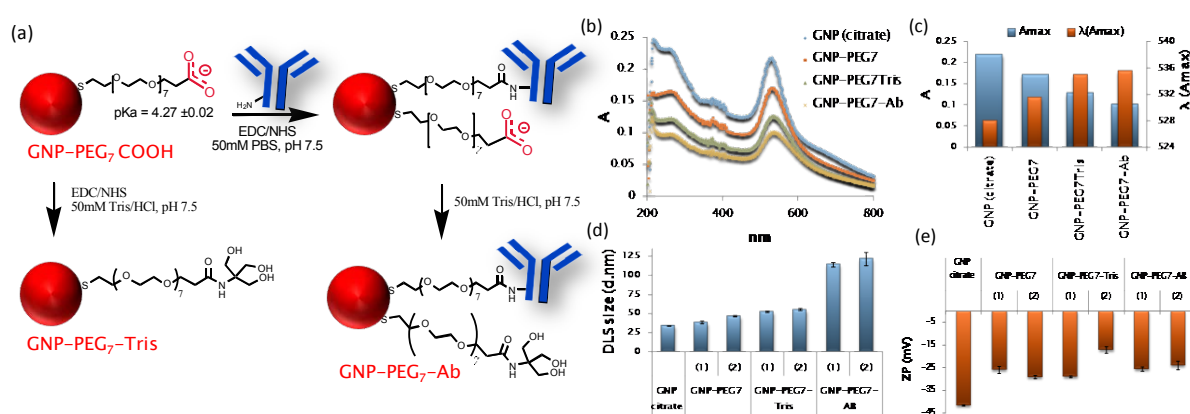


Figure 21: (a) Immobilization of Ab onto carboxy-pegylated GNPs *via* EDC/NHS linkage. The residual carboxylic groups were blocked finally with amine-containing Tris by simple changing of the buffer to suppress ionic interactions and thus, to minimize unspecific bindings. All immobilization steps were characterized by measuring (b, c) the SPR spectra, (d) the hydrodynamic radius by dynamic light scattering (DLS), and (e) the zeta potential (ZP). (c) The decrease of the absorbance maximum as well as the shift to higher wavelength maximum of the extinction spectrum goes along with incremental immobilization layers.

Thereby, the SPR spectra exhibited in all reaction steps a decrease of the absorbance maximum accompanied with a shift to higher wavelengths (Figure 21a, b). This finding is in agreement with the Mie theory which describes the dependency of the extinction spectrum on the particle size but also the correlation of the wavelength maximum with the local environment (chapter 1.6.1). Furthermore, the incremental surface chemistry can be observed and proven by the increase of the size with each step as measured by dynamic light scattering (DLS) (Figure 21d), whereby all bio-conjugates were quite stable with a zeta potential of at least -25 mV (Figure 21e).

Other examples of bioconjugation chemistries make use of the well known biotin-streptavidin affinity principle. Signal enhancement of nano-conjugates can be obtained by utilizing the strong avidin-biotin binding.¹¹²⁻¹¹⁶ Uludag *et al.* used neutravidin modified GNPs for detection of specific DNA sequences of Herpes Simplex virus (HSV) type 1 by signal amplification assay.¹¹³ Fluorescence energy transfer (FRET) was employed to study biotin-avidin interaction between biotinylated (red) GNPs and avidin modified green luminescent nanoparticle.¹¹⁵

In summary, functionalized GNPs offer a variety of immobilization chemistries depending on the functional group such as 'click' chemistry or EDC/NHS linkage. Acting as supporting layer, both polymer coated particles and SAM protected nanomaterials are useful tools for further bioconjugation chemistry of biomolecules such as enzymes or antibodies.

1.9. GNPs in Bioanalysis

GNPs are frequently used in various bioanalytical studies as tools such as immunoassays¹¹⁷ and biosensors,¹¹⁸ diagnostic sensing and therapy,^{20, 21, 119} gene and drug delivery,¹⁹ sample preparation¹²⁰ and separation science.¹²¹

Biosensors and Immunoassays

Immunochromatographic assays (ICA) are fast point of care screening methods for yes / no decisions such as the urine pregnancy test. Novel biofunctionalized GNPs forced the development of innovative nanoparticle-based electrochemical, optical, mass sensitive, colorimetric, and immunodipstick assays.^{20, 117} Recently, the combination of the lateral-flow assay with SERS 'nanotags' allows quantitative information.¹²² The simultaneous multiplexing with ICA on threads (ICAT) was demonstrated by Zhou *et al.* using a flatbed scanner for quantitation (Figure 22).¹²³

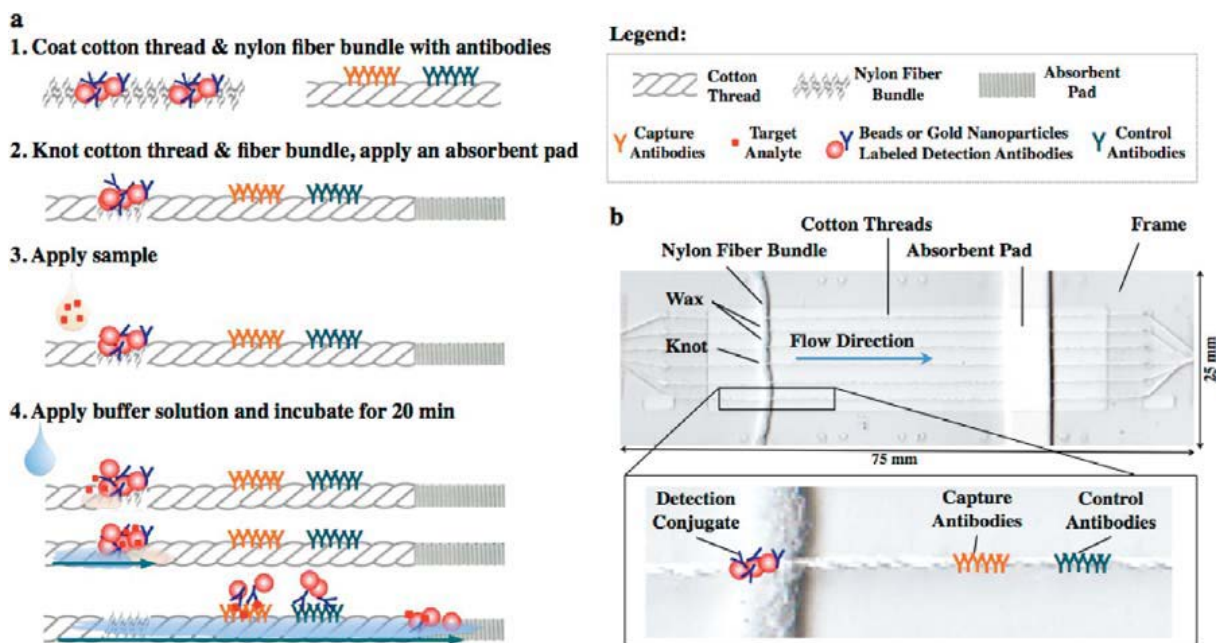


Figure 22: Illustration of the immunochromatographic assay on thread (ICAT) and photograph of one ICAT cartridge. (a) ICAT device assembly and assay protocol. (a1) A nylon fiber bundle is coated with dAb-AuNP, and a section of the cotton thread is coated with cAb and control Ab. (a2) After vacuum drying, the cotton thread and the nylon fiber bundle are knotted and woven on a polymer frame. An absorbent pad is placed at the end of the thread. (a3) The assay starts when sample is applied to the knot and dissolves the dAb-AuNP conjugates. (a4) Immediately after, a buffer solution is applied upstream of the knot and flushes the sample down the length of the thread. (b) Photograph of one ICAT cartridge with six cotton threads in parallel, one nylon fiber bundle knotted across, and an absorbent pad placed at the end. The inset shows a close-up of the knot with a schematic representation of the reagents. (Zhou *et al.*, *Anal.Chem.* 2012, © American Chemical Society, Reprinted with permission).¹²³

GNPs are also widely used for signal amplification in colorimetric immunoassays for either direct visualization or optical readout as for example with SERS.¹²⁴ NPs in electrochemical assays are used as support e.g. as enzyme carrier for amplification of the enzymatic electrochemical signal or for nanostructured modification of the electrotransducer surface.¹¹⁷ The latter setup was applied for adsorption of anti-LDL⁻ antibody on (polyvinyl formal) (PVF)-gold electrode for impedimetric characterization of the electronegative LDL⁻ recognition.¹²⁵ The combination of metallic nanoparticle-labeled immunoassays with ICPMS analysis offers new application fields by using multielement tags for simultaneous analyzing and selective detection of biomolecules (Figure 23).¹⁷

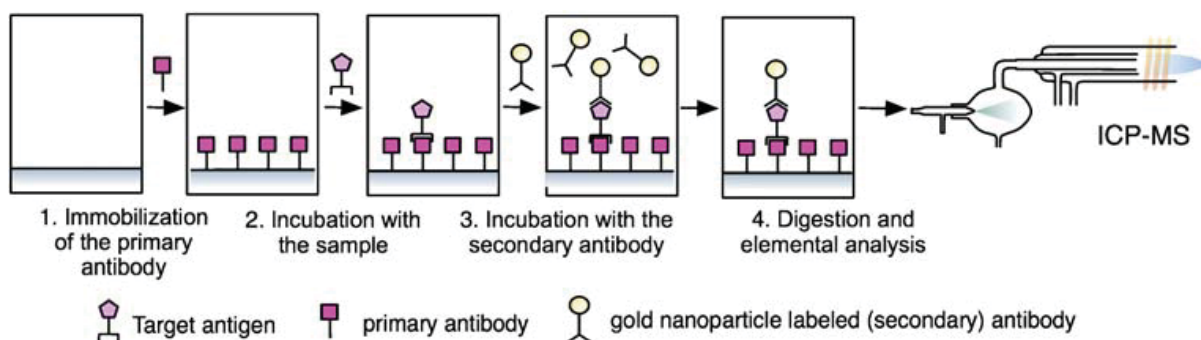


Figure 23: Schematic overview about an ICPMS-linked immunoassay (Scheffer *et al.*, Anal.Bioanal.Chem 2008, © Springer Science and Business Media B.V., Reprinted with permission).¹⁷

Drug Delivery, Therapy, and Diagnostic Sensing

The unique physical and chemical properties of GNPs such as (i) their stability and low-toxicological hazard, (ii) their easy and straightforward surface functionalization, and (iii) their photo-physical properties provide a promising platform for drug delivery.²⁰ Different NP functionalization strategies were employed for covalent and non-covalent drug loading, respectively, as well as to improve the transport to the cell and the final delivery efficiency.¹⁶ The intracellular stability of functionalized GNPs was studied by Zhu *et al.* by parallel measurements with laser desorption/ionization (LDI) for the amount of monolayer on GNPs in cells and inductively coupled plasma (ICP) mass spectrometry for determination of the amount of the gold core.¹²⁶ The difference between both measurements allows the determination of the stability of the functionalized particles in cells. In doing so, they found shorter alkanethiol to be less stable whereas dithiolate groups increased the stability of SAM modified GNPs. Moreover, the influence of surface charge of the gene delivery vector as crucial factor for genetic therapy was demonstrated by Ghosh *et.al.*¹²⁷

Cancer therapy by photothermal treatment was described by Chen *et al.* using pegylated gold nanocages.¹²⁸ The PEG modified GNPs were passively delivered to the tumor cell with relatively high accumulation efficiency. Finally, the tunable optical properties allowed the selective destruction of the tumor by laser irradiation (Figure 24).

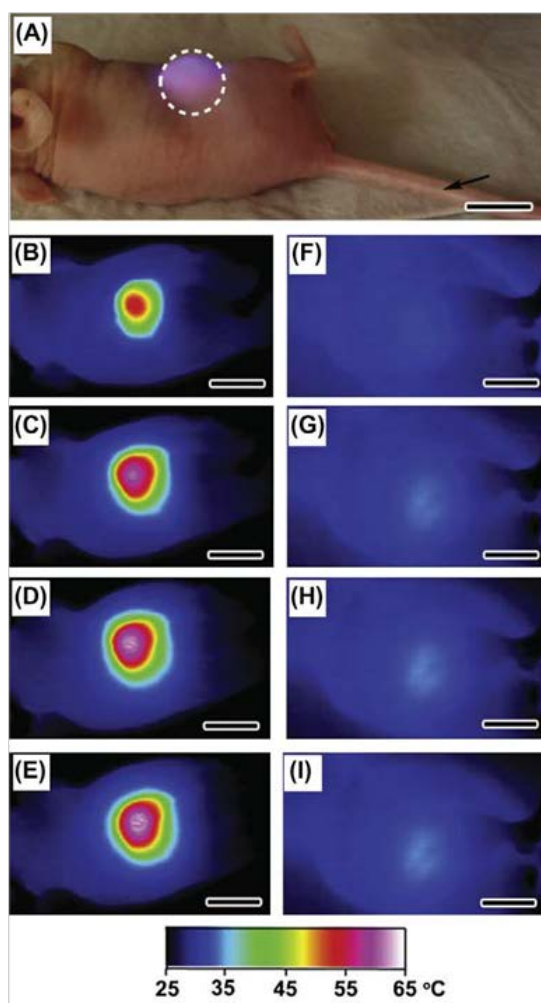


Figure 24: (A) Photograph of a tumor-bearing mouse under the photothermal treatment. 100 μL of pegylated nanocages at a concentration of 9E^{12} particles mL^{-1} or saline was administrated intravenously through the tail vein as indicated by an arrow. After the nanocages had been cleared from the circulation (72 h after injection), the tumor on the right flank was irradiated by the diode laser at 0.7 W/cm^2 with a beam size indicated by the dashed circle. (B–G) Thermographic images of (B–E) nanocage-injected and (F–I) saline-injected tumor-bearing mice at different time points: (B, E) 1 min, (C, F) 3 min, (D, G) 5 min, and (E, I) 10 min. All scale bars are 1 cm (Chen *et.al.*, Small 2010, © WILEY-VCH Verlag GmbH & Co. KGaA, Weinheim; Reprinted with permission).¹²⁸

GNPs in Sample Preparation

The specific binding of the desired analyte to bare GNPs and functionalized GNPs, respectively, is utilized in many applications for extraction and enrichment by the so called nanoextraction.

Wang *et al.* describes a pre-concentration of polycyclic aromatic hydrocarbons (PAHs) from drinking water samples utilizing the strong affinity to citrate stabilized GNPs followed by analysis with HPLC.¹²⁹ Different functional ligands were studied for selective detections of ions including cations (such as Hg^{2+} , Cu^{2+} , Pb^{2+} , As^{3+} , Ca^{2+} , Al^{3+} , *etc.*) and anions (such as NO_2^- , CN^- , PF_6^- , F^- , I^- , oxoanions) and small molecules

(such as cysteine, homocysteine, trinitrotoluene, melamine and cocaine, ATP, glucose, dopamine and so forth).¹⁰⁴ Lerma-Garcia *et al.* functionalized silica coated GNPs additionally with ionic liquids for solid phase extraction of sulfonylurea herbicides (SUHs) from water samples followed by capillary liquid chromatography analysis coupled to diode array detection (CLC–DAD).¹³⁰

Faccenda *et al.* describe the simultaneous isolation and enrichment of free and modified thiol-containing peptides by dative binding to GNPs and subsequent release with dithiothreitol (DTT) and analysis with MALDI-TOF MS.¹³¹ Using this method they were able to identify S-modification sites of protein disulfide isomerase (PDI) and dual specificity phosphatase 12 (DUSP12) as the S-nitrosylation of proteins is regarded to be involved in regulation, subcellular compartmentalization, and degradation of proteins. Tang *et al.* applied boronic acid-modified GNPs for selective enrichment of glycopeptides on-plate for direct MALDI-QIT-TOF-MS analysis.¹³² Since the first use of GNPs as selective matrix for the ionization of biomolecules described by McLean *et al.* in 2005,¹³³ GNPs enjoy increasing popularity as tool for bioanalytical applications with laser desorption ionization mass spectrometry (LDI-MS) because of their ability for extraction and enrichment of analytes but also due to their direct assistance and their tunable efficiency of LDI processes by surface modification.¹⁵

A more complex multiplexed system was developed by Nash *et al.* for the extraction and enrichment of biomarkers such as for malaria.^{134, 135} They immobilized the biotinylated capture antibody to streptavidin decorated GNPs linked *via* a thermally responsive diblock copolymer. Applying a thermal stimulus in conjugation with a magnetic field, they created a coaggregation of the GNP-conjugate together with magnetic NPs functionalized with the same diblock copolymer. Aggregates produce in this manner could be magnetically separated, concentrated by a volume enrichment step, and finally analyzed.¹³⁵

Mackiewicz *et al.* used GNP supports coated with phosphatidylcholine (PC) lipids to mimic low-density lipoprotein (LDL) and studied the interaction with C-reactive protein (CRP).¹³⁶ Thereby, they found a cluster formation in dependence on CRP and

respectively. After several washing steps to remove unspecifically bound entities, bound LDL was released by treating with methanol and brief ultrasonication. GNP-conjugates and proteins such as apolipoproteins precipitate and can be removed by centrifugation as pellet. Establishing MS compatible conditions the methanolic supernatant containing (oxidized) phospholipids can be directly analyzed by HPLC-ESI-MS/MS (Figure 26). The method proved to be suitable for extraction and enrichment of oxPCs by determination of the binding affinity and binding capacity. In addition, the dissociation constant K_d was determined for individual oxPCs by compound-specific single-reaction monitoring (SRM). In doing so, the antibody specificity towards oxidized phospholipids can be determined, and thus, the antigenity of oxPCs appointed. SRM mode allows selective quantitation of known biomarkers, while setting a precursor ion scan of m/z 184.1 for PC detection allows the fast and simultaneous screening of new biomarkers (appendix A-4).

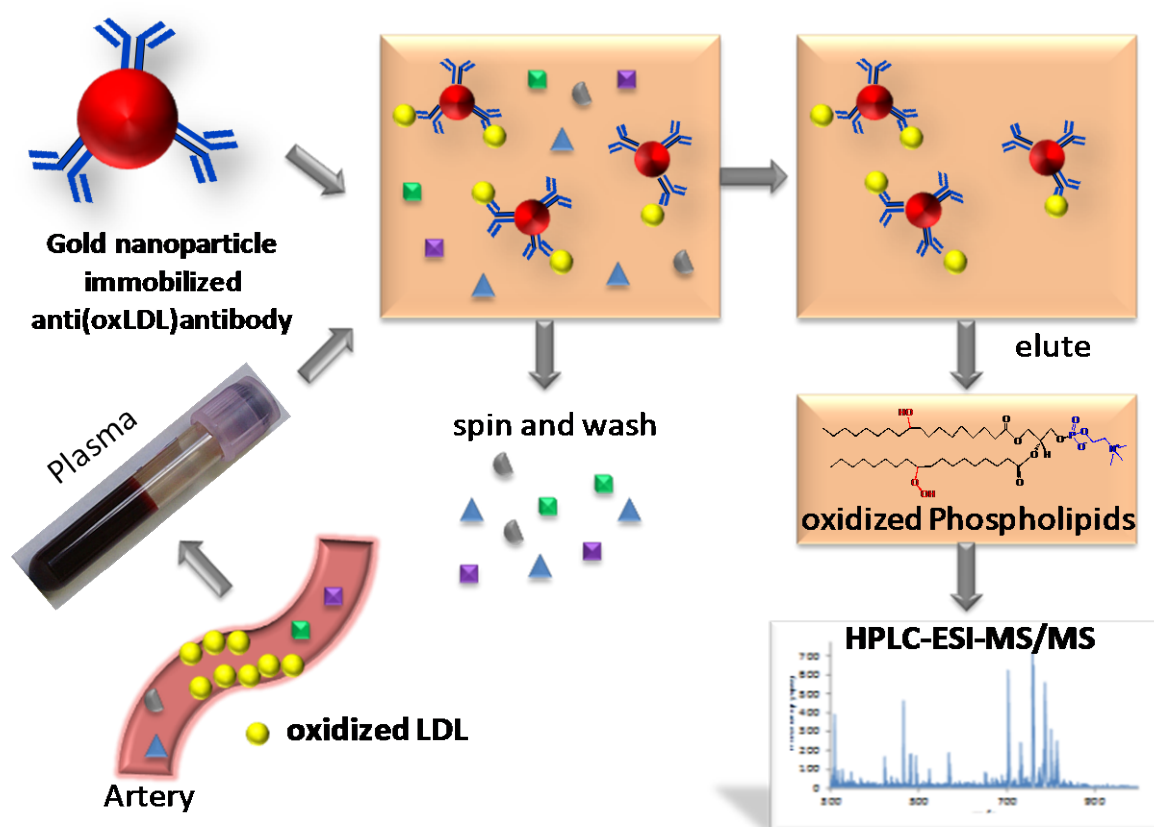


Figure 26: Scheme of nanobased extraction of oxidized phospholipids out of oxidized LDL (oxLDL). anti(oxLDL)-Ab was immobilized onto carboxy-pegylated GNPs and incubated with plasma spiked oxLDL. After several washing steps by simple centrifugation and resuspension, bound oxLDL was released by methanol and brief ultrasonication treatment. GNP-conjugates and proteins (such as apolipoproteins) precipitate in methanolic suspension and are removed by centrifugation as pellet. The supernatant containing (oxidized) phospholipids was finally analyzed by HPLC-ESI-MS/MS.

2. CONCLUDING DISCUSSIONS

The thesis incorporates the systematical study of GNPs from size-controlled synthesis to surface functionalization and optimization of bioconjugation chemistry. The influence of size and ligand chemistry on immobilization of biomolecules was tested in real applications by tryptic digestion of proteins with GNP-enzyme-conjugates as well as by extraction of oxidized LDL with NP bound antibodies.

Different methods were applied for characterization of the functionalized nano-approaches including TEM, SPR spectra, zeta potential, DLS, AF4, GEMMA, ICPMS, and HPLC-ESI-MS (ion trap and triple quadrupole MS, respectively). Methods for size determination were compared as a trial for harmonization.

Furthermore, a new method was developed for experimental determination of ligand density on GNPs by ICPMS measurements. Thereby, a decrease of surface coverage was found with increase of bifunctional thiol-containing ligand chain length which could be explained by steric hindrance and entropic effects. An opposite effect was observed for protein immobilization, whereby the amount as well as the activity of immobilized enzyme increases with spacer chain length which can be asserted with the higher flexibility of the longer ligands.

Finally, we used the optimized bioconjugation chemistry for immobilization of antibodies onto GNPs. The successful approach could be shown by nano-based extraction of oxidized LDL as biomarker *e.g.* for atherosclerosis. Furthermore, the application in real matrix could be demonstrated by saturation experiments with plasma spiking experiments which allowed also the determination of the dissociation constant K_d as well as the maximal binding capacity B_{max} .

The corresponding papers and manuscripts can be found in the appendix.

ABBREVIATIONS

Ab	Antibody
AF4	Asymmetric flow field-flow fractionation
DLS	Dynamic light scattering
EDC	<i>N</i> -(3-dimethylaminopropyl)- <i>N</i> -ethylcarbodiimide hydrochloride
GEMMA	Gas phase electrophoretic molecular mobility analyzer
GNP	Gold nanoparticle
<i>i.a.</i>	inter alia
ICPMS	Inductively-coupled plasma mass spectrometry
K_d	Dissociation constant
LDL	Low-density lipoprotein
NHS	<i>N</i> -hydroxysuccinimide
oxLDL	Oxidized LDL
oxPC	Oxidized PC
PC	Phosphatidylcholine
PEG	Poly(ethylene glycol)
SAM	Self-assembled monolayer
(L)SPR	(Localized) surface plasmon resonance
SRM	Single reaction monitoring
TEM	Transmission electron microscopy
ZP	Zeta potential

LIST OF FIGURES

Ich habe mich bemüht, sämtliche Inhaber der Bildrechte ausfindig zu machen und ihre Zustimmung zur Verwendung der Bilder in dieser Arbeit eingeholt. Sollte dennoch eine Urheberrechtsverletzung bekannt werden, ersuche ich um Meldung bei mir.

I used my best endeavours to seek all claim holders of the pictures and obtain their permission to use their pictures in my thesis. Still, if any copyright infringement should emerge, please inform me.

<i>Figure 1: Overview about the subsections of the thesis including size-controlled synthesis of GNPs and their characterization, their surface modification and functionalization, immobilization chemistry of proteins such as trypsin and antibodies and their application in bioanalysis for tryptic digestion and extraction / enrichment of oxidized LDL as biomarkers, respectively. (TEM, transmission electron microscopy; DLS, dynamic light scattering; GEMMA, gas phase electrophoretic molecular mobility analyzer; Af4, asymmetric flow field-flow fractionation; ICPMS, inductively-coupled plasma mass spectrometry).....</i>	<i>15</i>
<i>Figure 2: Nanomaterials are defined in the size range of 1 – 100 nm or with a specific surface area greater than 60 m² cm⁻³. The relationship calculated for a spherical particle with a diameter D and its surface area A shows a decrease with $A = 6,000 D^{-1}$. Schematically shown are compounds with different sizes in the nanoscale.</i>	<i>16</i>
<i>Figure 3: Publications and reviews containing 'Gold nanoparticle' (1995-2013). Data were generated by keyword search in SciFinder® (2013/02/14).</i>	<i>18</i>
<i>Figure 4: The Lycurgus Cup, dating from the 4th century A.D., is made from glass impregnated with gold nanoparticles; seen in (a) transmitted light and (b) reflected light (Paul Mulvaney, MRS Bull. 2001, © Cambridge University Press, Reprinted with permission)⁴</i>	<i>18</i>
<i>Figure 5: The golden timeline (Alkilany et al., Acc.Chem.Res. 2012, © American Chemical Society, Reprinted with permission)⁷</i>	<i>19</i>
<i>Figure 6: (a) TEM images of GNPs prepared by variation of the citrate/HAuCl₄ (C/H) ratio. (b) The relation can be described in a logarithmic function. (c) TEM histograms of the corresponding GNPs (Hinterwirth et al., ACS Nano 2013, © American Chemical Society, Reprinted with permission).³¹</i>	<i>21</i>
<i>Figure 7: Schematic illustration of the nucleation and growth process in the classical citrate formation method (Polte et al., JACS 2010, © American Chemical Society, Reprinted with permission).³³</i>	<i>22</i>
<i>Figure 8: Overview of commonly used methods for the characterization of GNPs (modified from Bandyopadhyay et.al., Appl.Spectr.Rev. 2012).³⁴</i>	<i>23</i>
<i>Figure 9: (a) Schematic illustration showing the effect of the optical field on the electron cloud in a spherical metal nanoparticle (adapted from Willets and Van Duyne, Annu.Rev.Phys.Chem. 2007)³⁶ (b) Red colored GNP suspension. (c) SPR spectra of GNPs with different sizes have an absorbance maximum at a wavelength of about 530 nm and show an increase of peak width as well a shift of the wavelength maxima with NP size. (d) The linear relationship of the logarithm of size and the logarithm of the extinction coefficient was described already by Liu</i>	

<i>et al.</i> ³⁷ (e) Furthermore, a relationship between the asymmetry factor determined with TEM measurements and the peak width of the SPR band was observed. (f) The shift of the wavelength maximum is not only influenced by the GNP size but also its ligand modification.	24
Figure 10: Schematic representation of the zeta potential (www.malvern.com, © Malvern Instruments Ltd.; 2013/02/20).....	26
Figure 11: Scheme of FFF principle (www.postnova.com, © Postnova Analytics Inc., 2013/03/01)	29
Figure 12: Scheme of GNP analysis by ICP-MS (A) with and (B) without previous gold dissolution (Allabashi <i>et.al.</i> , <i>J Nanopart. Res.</i> 2009, © Springer Science and Business Media B.V., Reprinted with permission). ⁶⁵	31
Figure 13: Recovery of sulfur in the presence of gold validated by spiking experiments (Hinterwirth <i>et.al.</i> , <i>ACS Nano</i> 2013, ©.American Chemical Society; Reprinted with permission). ³¹	32
Figure 14: Comparison of different size characterization methods for two distinct GNP batches with 13 nm and 26 nm in diameter as measured with TEM.....	33
Figure 15: Scheme of different strategies for GNP modification (modified after Greg Hermanson, <i>Bioconjugation Techniques</i> , Elsevier). ⁸³	34
Figure 16: Layer-by-layer coating of GNPs with cationic polyallylamine (PAA) and anionic polystyrenesulfonate (PSS). IgG was finally immobilized via EDC/NHS coupling (Masereel <i>et.al.</i> , <i>J.Nanopart.Res.</i> 2011, © Springer Science and Business Media B.V.; Reprinted with permission). ⁹¹	35
Figure 17: Influence of spacer length on the surface coverage as determined by the simultaneous measurement of Au/S ratio of thiolate-protected GNPs by ICP-MS and its dependency on GNP size (Hinterwirth <i>et.al.</i> <i>ACS Nano</i> 2013, © American Chemical Society; Reprinted with permission). ³¹	36
Figure 18: Scheme of GNP coating with trimethoxysilane followed by cross-linking of the ligand shell (Schroedter and Weller, <i>Angew.Chem.</i> 2002, © WILEY-VCH Verlag GmbH & Co. KGaA, Weinheim; Reprinted with permission). ¹⁰⁰	37
Figure 19: Bioconjugation strategy is shown for 'click' chemistry of azide functionalized gold nanorods to acetylene functionalized trypsin as well as for amine-carboxylate coupling via carbodiimide (EDC) linkage (Gole and Murphy, <i>Langmuir</i> 2008, © American Chemical Society, Reprinted with permission). ¹¹¹	38
Figure 20: (a) Bioconjugation chemistry of trypsin onto carboxylic acid functionalized GNPs via EDC/NHS linkage shows a significant dependency of the enzyme activity and amount of bound protein per GNP on the ligand chain length. (b) Changing the lipophilic mercaptohexadecanoic acid (MHA) linker to the hydrophilic poly(ethylene glycol) (PEG ₇) increases the tryptic digestion efficiency for bovine serum albumin (BSA), cytochrome C (CytC) and myoglobin (MYG) as measured by the sequence coverage found by MASCOT database search (Hinterwirth <i>et.al.</i> <i>Analytica Chimica Acta</i> 2012, © Elsevier; Reprinted with permission). ⁸⁶ ...	39
Figure 21: (a) Immobilization of Ab onto carboxy-pegylated GNPs via EDC/NHS linkage. The residual carboxylic groups were blocked finally with amine-containing Tris by simple changing of the buffer to suppress ionic interactions and thus, to minimize .unspecific bindings. All immobilization steps were characterized by measuring (b, c) the SPR spectra, (d) the hydrodynamic radius by dynamic light scattering (DLS), and (e) the zeta potential (ZP). (c) The decrease of the absorbance maximum as well as the shift to higher wavelength maximum of the extinction spectrum goes along with incremental immobilization layers.	40
Figure 22: Illustration of the immunochromatographic assay on thread (ICAT) and photograph of one ICAT cartridge. (a) ICAT device assembly and assay protocol. (a1) A nylon fiber bundle is coated with dAb-AuNP, and a section of the cotton thread is coated with cAb and control Ab. (a2) After vacuum drying, the cotton thread	

and the nylon fiber bundle are knotted and woven on a polymer frame. An absorbent pad is placed at the end of the thread. (a3) The assay starts when sample is applied to the knot and dissolves the dAb-AuNP conjugates. (a4) Immediately after, a buffer solution is applied upstream of the knot and flushes the sample down the length of the thread. (b) Photograph of one ICAT cartridge with six cotton threads in parallel, one nylon fiber bundle knotted across, and an absorbent pad placed at the end. The inset shows a close-up of the knot with a schematic representation of the reagents. (Zhou et al., Anal.Chem. 2012, © American Chemical Society, Reprinted with permission). ¹²³	42
Figure 23: Schematic overview about an ICPMS-linked immunoassay (Scheffer et al., Anal.Bioanal.Chem 2008, © Springer Science and Business Media B.V., Reprinted with permission). ¹⁷	43
Figure 24: (A) Photograph of a tumor-bearing mouse under the photothermal treatment. 100 µL of pegylated nanocages at a concentration of 9×10^{12} particles mL ⁻¹ or saline was administrated intravenously through the tail vein as indicated by an arrow. After the nanocages had been cleared from the circulation (72 h after injection), the tumor on the right flank was irradiated by the diode laser at 0.7 W/cm ² with a beam size indicated by the dashed circle. (B–G) Thermographic images of (B–E) nanocage-injected and (F–I) saline-injected tumor-bearing mice at different time points: (B, E) 1 min, (C, F) 3 min, (D, G) 5 min, and (E, I) 10 min. All scale bars are 1 cm (Chen et.al., Small 2010, © WILEY-VCH Verlag GmbH & Co. KGaA, Weinheim; Reprinted with permission). ¹²⁸	44
Figure 25: Scheme of biomimetic HDL nanoparticle synthesis which is initiated by addition of Apo A1 to a solution of colloidal AuNPs (5 nm diameter) followed by addition of two phospholipids to the mixture. One of the phospholipids (green) has a disulfide head group that binds with high affinity to the surface of the AuNP. The second phospholipid (blue) is naturally associated with HDLs and forms the outer phospholipid layer (Yang et al., PNAS 2013, © National Academy of Science; Reprinted with permission). ¹⁴⁰	46
Figure 26: Scheme of nanobased extraction of oxidized phospholipids out of oxidized LDL (oxLDL). anti(oxLDL)-Ab was immobilized onto carboxy-pegylated GNPs and incubated with plasma spiked oxLDL. After several washing steps by simple centrifugation and resuspension, bound oxLDL was released by methanol and brief ultrasonication treatment. GNP-conjugates and proteins (such as apolipoproteins) precipitate in methanolic suspension and are removed by centrifugation as pellet. The supernatant containing (oxidized) phospholipids was finally analyzed by HPLC-ESI-MS/MS.	47

LIST OF TABLES

Table 1: Combination possibilities of DMA with different sample introduction and detection methods (adapted from Kanu et.al., JMS 2008). ⁵⁹	30
--	----

REFERENCES

1. Dreaden, E. C.; Alkilany, A. M.; Huang, X.; Murphy, C. J.; El-Sayed, M. A., The Golden Age: Gold Nanoparticles for Biomedicine. *Chem Soc Rev* **2012**, *41*, 2740-79.
2. Commission, E., On the Definition of Nanomaterial (L275). *Official Journal of the European Union* **2011**, *54*, 38-40.
3. Roco, M. C.; Williams, R. S.; Alivisatos, P.; Editors, *Nanotechnology Research Directions: Iwgn Workshop Report; Vision for Nanotechnology R&D in the Next Decade*. Kluwer: **2000**; p 316 pp.
4. Mulvaney, P., Not All That's Gold Does Glitter. *MRS Bull.* **2001**, *26*, 1009-1014.
5. Turkevich, J.; Stevenson, P. C.; Hillier, J., The Nucleation and Growth Processes in the Synthesis of Colloidal Gold. *Discuss. Faraday Soc.* **1951**, *11*, 55-75.
6. Frens, G., Controlled Nucleation for the Regulation of the Particle Size in Monodisperse Gold Suspensions. *Nature Physical Science* **1973**, *241*, 20-22.
7. Alkilany, A. M.; Lohse, S. E.; Murphy, C. J., The Gold Standard: Gold Nanoparticle Libraries to Understand the Nano-Bio Interface. *Acc. Chem. Res.* **2013**, Ahead of Print, DOI: 10.1021/ar300015b.
8. Brust, M.; Fink, J.; Bethell, D.; Schiffrin, D. J.; Kiely, C., Synthesis and Reactions of Functionalized Gold Nanoparticles. *J. Chem. Soc., Chem. Commun.* **1995**, 1655-6.
9. Zhao, P.; Li, N.; Astruc, D., State of the Art in Gold Nanoparticle Synthesis. *Coord. Chem. Rev.* **2013**, *257*, Ahead of Print.
10. Hakkinen, H., The Gold-Sulfur Interface at the Nanoscale. *Nat Chem* **2012**, *4*, 443-55.
11. Jin, R., Quantum Sized, Thiolate-Protected Gold Nanoclusters. *Nanoscale* **2010**, *2*, 343-362.
12. Parker, J. F.; Fields-Zinna, C. A.; Murray, R. W., The Story of a Monodisperse Gold Nanoparticle: Au₂₅18. *Acc. Chem. Res.* **2010**, *43*, 1289-1296.

13. Dykman, L.; Khlebtsov, N., Gold Nanoparticles in Biomedical Applications: Recent Advances and Perspectives. *Chem. Soc. Rev.* **2012**, *41*, 2256-2282.
14. Jiang, X.-M.; Wang, L.-M.; Wang, J.; Chen, C.-Y., Gold Nanomaterials: Preparation, Chemical Modification, Biomedical Applications and Potential Risk Assessment. *Appl. Biochem. Biotechnol.* **2012**, *166*, 1533-1551.
15. Pilolli, R.; Palmisano, F.; Cioffi, N., Gold Nanomaterials as a New Tool for Bioanalytical Applications of Laser Desorption Ionization Mass Spectrometry. *Anal. Bioanal. Chem.* **2012**, *402*, 601-623.
16. Yeh, Y.-C.; Creran, B.; Rotello, V. M., Gold Nanoparticles: Preparation, Properties, and Applications in Bionanotechnology. *Nanoscale* **2012**, *4*, 1871-1880.
17. Scheffer, A.; Engelhard, C.; Sperling, M.; Buscher, W., Icp-MS as a New Tool for the Determination of Gold Nanoparticles in Bioanalytical Applications. *Anal. Bioanal. Chem.* **2008**, *390*, 249-252.
18. Jans, H.; Huo, Q., Gold Nanoparticle-Enabled Biological and Chemical Detection and Analysis. *Chem. Soc. Rev.* **2012**, *41*, 2849-2866.
19. Rana, S.; Bajaj, A.; Mout, R.; Rotello, V. M., Monolayer Coated Gold Nanoparticles for Delivery Applications. *Adv. Drug Delivery Rev.* **2012**, *64*, 200-216.
20. Lu, F.; Doane, T. L.; Zhu, J.-J.; Burda, C., Gold Nanoparticles for Diagnostic Sensing and Therapy. *Inorg. Chim. Acta* **2012**, *393*, 142-153.
21. Larginho, M.; Baptista, P. V., Gold and Silver Nanoparticles for Clinical Diagnostics - from Genomics to Proteomics. *J. Proteomics* **2012**, *75*, 2811-2823.
22. Azzazy, H. M. E.; Mansour, M. M. H.; Samir, T. M.; Franco, R., Gold Nanoparticles in the Clinical Laboratory: Principles of Preparation and Applications. *Clin. Chem. Lab. Med.* **2012**, *50*, 193-209.
23. Bedford, E. E.; Spadavecchia, J.; Pradier, C.-M.; Gu, F. X., Surface Plasmon Resonance Biosensors Incorporating Gold Nanoparticles. *Macromol. Biosci.* **2012**, *12*, 724-739.
24. Saha, K.; Agasti, S. S.; Kim, C.; Li, X.; Rotello, V. M., Gold Nanoparticles in Chemical and Biological Sensing. *Chem. Rev. (Washington, DC, U. S.)* **2012**, *112*, 2739-2779.

25. Tokonami, S.; Yamamoto, Y.; Shiigi, H.; Nagaoka, T., Synthesis and Bioanalytical Applications of Specific-Shaped Metallic Nanostructures: A Review. *Anal. Chim. Acta* **2012**, 716, 76-91.
26. De, J. W. H.; Hagens, W. I.; Krystek, P.; Burger, M. C.; Sips, A. J. A. M.; Geertsma, R. E., Particle Size-Dependent Organ Distribution of Gold Nanoparticles after Intravenous Administration. *Biomaterials* **2008**, 29, 1912-1919.
27. Sonavane, G.; Tomoda, K.; Makino, K., Biodistribution of Colloidal Gold Nanoparticles after Intravenous Administration: Effect of Particle Size. *Colloids Surf., B* **2008**, 66, 274-280.
28. Khlebtsov, N.; Dykman, L., Biodistribution and Toxicity of Engineered Gold Nanoparticles: A Review of in Vitro and in Vivo Studies. *Chem. Soc. Rev.* **2011**, 40, 1647-1671.
29. Liu, Y.; Meyer-Zaika, W.; Franzka, S.; Schmid, G.; Tsoli, M.; Kuhn, H., Gold-Cluster Degradation by the Transition of B-DNA into a-DNA and the Formation of Nanowires. *Angew. Chem., Int. Ed.* **2003**, 42, 2853-2857.
30. Fadeel, B.; Garcia-Bennett, A. E., Better Safe Than Sorry: Understanding the Toxicological Properties of Inorganic Nanoparticles Manufactured for Biomedical Applications. *Adv. Drug Delivery Rev.* **2010**, 62, 362-374.
31. Hinterwirth, H.; Kappel, S.; Waitz, T.; Prohaska, T.; Lindner, W.; Lammerhofer, M., Quantifying Thiol Ligand Density of Self-Assembled Monolayers on Gold Nanoparticles by Inductively Coupled Plasma-Mass Spectrometry. *ACS Nano* **2013**, 7, 1129-1136.
32. Kumar, S.; Gandhi, K. S.; Kumar, R., Modeling of Formation of Gold Nanoparticles by Citrate Method. *Ind. Eng. Chem. Res.* **2007**, 46, 3128-3136.
33. Polte, J.; Ahner, T. T.; Delissen, F.; Sokolov, S.; Emmerling, F.; Thunemann, A. F.; Kraehnert, R., Mechanism of Gold Nanoparticle Formation in the Classical Citrate Synthesis Method Derived from Coupled in Situ Xanes and Saxs Evaluation. *J. Am. Chem. Soc.* **2010**, 132, 1296-1301.
34. Bandyopadhyay, S.; Peralta-Videa, J. R.; Hernandez-Viezcas, J. A.; Montes, M. O.; Keller, A. A.; Gardea-Torresdey, J. L., Microscopic and Spectroscopic Methods Applied to the Measurements of Nanoparticles in the Environment. *Appl. Spectrosc. Rev.* **2012**, 47, 180-206.

35. Hamanaka, Y.; Okada, N.; Fukagawa, K.; Nakamura, A.; Tai, Y.; Murakami, J., Crossover Phenomenon in Third-Order Nonlinear Optical Susceptibilities of Gold Nanoparticles from Plasmons to Discrete Electronic States. *J. Phys. Chem. C* **2012**, *116*, 10760-10765.
36. Willets, K. A.; Van, D. R. P., Localized Surface Plasmon Resonance Spectroscopy and Sensing. *Annu. Rev. Phys. Chem.* **2007**, *58*, 267-297.
37. Liu, X.; Atwater, M.; Wang, J.; Huo, Q., Extinction Coefficient of Gold Nanoparticles with Different Sizes and Different Capping Ligands. *Colloids Surf., B* **2007**, *58*, 3-7.
38. Liu, X.; Atwater, M.; Wang, J.; Huo, Q., Extinction Coefficient of Gold Nanoparticles with Different Sizes and Different Capping Ligands. *Colloids Surf., B* **2007**, *58*, 3-7.
39. Khlebtsov, N. G., Determination of Size and Concentration of Gold Nanoparticles from Extinction Spectra. *Anal. Chem.* **2008**, *80*, 6620-6625.
40. Haiss, W.; Thanh, N. T. K.; Aveyard, J.; Fernig, D. G., Determination of Size and Concentration of Gold Nanoparticles from Uv-Vis Spectra. *Anal. Chem.* **2007**, *79*, 4215-4221.
41. Amendola, V.; Meneghetti, M., Size Evaluation of Gold Nanoparticles by Uv-Vis Spectroscopy. *J. Phys. Chem. C* **2009**, *113*, 4277-4285.
42. Mie, G., Contributions to the Optics of Turbid Media, Especially Colloidal Metal Solutions. *Ann. Phys.* **1908**, *25*, 377-445.
43. Deryagin, B.; Landau, L., Theory of the Stability of Strongly Charged Lyophobic Sols and of the Adhesion of Strongly Charged Particles in Solutions of Electrolytes. *Acta Physicochim. URSS* **1941**, *14*, 633-62.
44. Verwey, E. J. W.; Overbeek, J. T. G., *Theory of the Stability of Lyophobic Colloids*. Elsevier: New York, **1948**; p 216 pp.
45. Doane, T. L.; Chuang, C.-H.; Hill, R. J.; Burda, C., Nanoparticle Z-Potentials. *Acc. Chem. Res.* **2012**, *45*, 317-326.
46. Grabar, K. C.; Brown, K. R.; Keating, C. D.; Stranick, S. J.; Tang, S.-L.; Natan, M. J., Nanoscale Characterization of Gold Colloid Monolayers: A Comparison of Four Techniques. *Anal. Chem.* **1997**, *69*, 471-477.

47. Khlebtsov, B. N.; Khlebtsov, N. G., On the Measurement of Gold Nanoparticle Sizes by the Dynamic Light Scattering Method. *Colloid J.* **2011**, 73, 118-127.
48. Keene, A. M.; Tyner, K. M., Analytical Characterization of Gold Nanoparticle Primary Particles, Aggregates, Agglomerates, and Agglomerated Aggregates. *J. Nanopart. Res.* **2011**, 13, 3465-3481.
49. Driskell, J. D.; Jones, C. A.; Tompkins, S. M.; Tripp, R. A., One-Step Assay for Detecting Influenza Virus Using Dynamic Light Scattering and Gold Nanoparticles. *Analyst* **2011**, 136, 3083-3090.
50. Jans, H.; Liu, X.; Austin, L.; Maes, G.; Huo, Q., Dynamic Light Scattering as a Powerful Tool for Gold Nanoparticle Bioconjugation and Biomolecular Binding Studies. *Anal. Chem.* **2009**, 81, 9425-9432.
51. Reschiglian, P.; Rambaldi, D. C.; Zattoni, A., Flow Field-Flow Fractionation with Multiangle Light Scattering Detection for the Analysis and Characterization of Functional Nanoparticles. *Anal. Bioanal. Chem.* **2011**, 399, 197-203.
52. Cho, T. J.; Hackley, V. A., Fractionation and Characterization of Gold Nanoparticles in Aqueous Solution: Asymmetric-Flow Field Flow Fractionation with Mals, Dls, and Uv-Vis Detection. *Anal. Bioanal. Chem.* **2010**, 398, 2003-2018.
53. Zattoni, A.; Rambaldi, D. C.; Reschiglian, P.; Melucci, M.; Krol, S.; Garcia, A. M. C.; Sanz-Medel, A.; Roessner, D.; Johann, C., Asymmetrical Flow Field-Flow Fractionation with Multi-Angle Light Scattering Detection for the Analysis of Structured Nanoparticles. *J. Chromatogr., A* **2009**, 1216, 9106-9112.
54. Hagendorfer, H.; Kaegi, R.; Traber, J.; Mertens, S. F. L.; Scherrers, R.; Ludwig, C.; Ulrich, A., Application of an Asymmetric Flow Field Flow Fractionation Multi-Detector Approach for Metallic Engineered Nanoparticle Characterization - Prospects and Limitations Demonstrated on Au Nanoparticles. *Anal. Chim. Acta* **2011**, 706, 367-378.
55. Schmidt, B.; Loeschner, K.; Hadrup, N.; Mortensen, A.; Sloth, J. J.; Bender, K. C.; Larsen, E. H., Quantitative Characterization of Gold Nanoparticles by Field-Flow Fractionation Coupled Online with Light Scattering Detection and Inductively Coupled Plasma Mass Spectrometry. *Anal. Chem.* **2011**, 83, 2461-2468.
56. Gray, E. P.; Bruton, T. A.; Higgins, C. P.; Halden, R. U.; Westerhoff, P.; Ranville, J. F., Analysis of Gold Nanoparticle Mixtures: A Comparison of Hydrodynamic Chromatography (Hdc) and Asymmetrical Flow Field-Flow Fractionation (Af4) Coupled to Icp-MS. *J. Anal. At. Spectrom.* **2012**, 27, 1532-1539.

57. Tsai, D.-H.; Cho, T. J.; Del, R. F. W.; Taurozzi, J.; Zachariah, M. R.; Hackley, V. A., Hydrodynamic Fractionation of Finite Size Gold Nanoparticle Clusters. *J. Am. Chem. Soc.* **2011**, *133*, 8884-8887.
58. Guha, S.; Li, M.; Tarlov, M. J.; Zachariah, M. R., Electrospray-Differential Mobility Analysis of Bionanoparticles. *Trends Biotechnol.* **2012**, *30*, 291-300.
59. Kanu, A. B.; Dwivedi, P.; Tam, M.; Matz, L.; Hill, H. H., Jr., Ion Mobility-Mass Spectrometry. *J. Mass Spectrom.* **2008**, *43*, 1-22.
60. Kapellios, E. A.; Pergantis, S. A., Size and Elemental Composition of Nanoparticles Using Ion Mobility Spectrometry with Inductively Coupled Plasma Mass Spectrometry. *J. Anal. At. Spectrom.* **2012**, *27*, 21-24.
61. Elzey, S.; Tsai, D.-H.; Yu, L. L.; Winchester, M. R.; Kelley, M. E.; Hackley, V. A., Real-Time Size Discrimination and Elemental Analysis of Gold Nanoparticles Using Es-Dma Coupled to Icp-Ms. *Anal. Bioanal. Chem.* **2012**, Ahead of Print.
62. Helfrich, A.; Bruechert, W.; Bettmer, J., Size Characterisation of Au Nanoparticles by Icp-Ms Coupling Techniques. *J. Anal. At. Spectrom.* **2006**, *21*, 431-434.
63. Hu, S.; Liu, R.; Zhang, S.; Huang, Z.; Xing, Z.; Zhang, X., A New Strategy for Highly Sensitive Immunoassay Based on Single-Particle Mode Detection by Inductively Coupled Plasma Mass Spectrometry. *J. Am. Soc. Mass Spectrom.* **2009**, *20*, 1096-1103.
64. Gillespie, A.; Jao, D.; Andriola, A.; Duda, T.; Yang, C. F.; Yu, L., Gold Nanoparticle Determination by Inductively Coupled Plasma-Mass Spectrometry, Anodic Stripping Voltammetry, and Flame Atomic Absorption Spectrophotometry. *Anal. Lett.* **2012**, *45*, 1310-1320.
65. Allabashi, R.; Stach, W.; de, I. E.-M. A.; Liste-Calleja, L.; Merkoci, A., Icp-Ms: A Powerful Technique for Quantitative Determination of Gold Nanoparticles without Previous Dissolving. *J. Nanopart. Res.* **2009**, *11*, 2003-2011.
66. Jiang, W.; Hibbert, D. B.; Moran, G.; Akter, R., Measurement of Gold and Sulfur Mass Fractions in L-Cysteine-Modified Gold Nanoparticles by Icp-Drc-Ms after Acid Digestion: Validation and Uncertainty of Results. *J. Anal. At. Spectrom.* **2012**, *27*, 1465-1473.
67. Pace, H. E.; Rogers, N. J.; Jarolimek, C.; Coleman, V. A.; Higgins, C. P.; Ranville, J. F., Determining Transport Efficiency for the Purpose of Counting and

Sizing Nanoparticles Via Single Particle Inductively Coupled Plasma Mass Spectrometry. *Anal. Chem.* **2011**, 83, 9361-9369.

68. Tiede, K.; Boxall, A. B. A.; Tiede, D.; Tear, S. P.; David, H.; Lewis, J., A Robust Size-Characterization Methodology for Studying Nanoparticle Behaviour in Real' Environmental Samples, Using Hydrodynamic Chromatography Coupled to Icp-*Ms. J. Anal. At. Spectrom.* **2009**, 24, 964-972.

69. Degueldre, C.; Favarger, P. Y.; Wold, S., Gold Colloid Analysis by Inductively Coupled Plasma-Mass Spectrometry in a Single Particle Mode. *Anal. Chim. Acta* **2006**, 555, 263-268.

70. Liu, F.-K., Sec Characterization of Au Nanoparticles Prepared through Seed-Assisted Synthesis. *Chromatographia* **2007**, 66, 791-796.

71. Helfrich, A.; Bettmer, J., Analysis of Gold Nanoparticles Using Icp-*Ms*-Based Hyphenated and Complementary Esi-*Ms* Techniques. *Int. J. Mass Spectrom.* **2011**, 307, 92-98.

72. Liu, F.-K., Using Sec for Analyzing the Sizes of Au/Pt Core/Shell Nanoparticles. *Chromatographia* **2010**, 72, 473-480.

73. Liu, F.-K., Monitoring the Synthesis of Au Nanoparticles Using Sec. *Chromatographia* **2008**, 68, 81-87.

74. Pergantis, S. A.; Jones-Lepp, T. L.; Heithmar, E. M., Hydrodynamic Chromatography Online with Single Particle-Inductively Coupled Plasma Mass Spectrometry for Ultratrace Detection of Metal-Containing Nanoparticles. *Anal. Chem.* **2012**, 84, 6454-6462.

75. Schnabel, U.; Fischer, C.-H.; Kenndler, E., Characterization of Colloidal Gold Nanoparticles According to Size by Capillary Zone Electrophoresis. *J. Microcolumn Sep.* **1997**, 9, 529-534.

76. Liu, F.-K.; Tsai, M.-H.; Hsu, Y.-C.; Chu, T.-C., Analytical Separation of Au/Ag Core/Shell Nanoparticles by Capillary Electrophoresis. *J. Chromatogr., A* **2006**, 1133, 340-346.

77. Buecking, W.; Nann, T., Electrophoretic Analysis of Gold Nanoparticles: Size-Dependent Electrophoretic Mobility of Nanoparticles. *IEE Proc.: Nanobiotechnol.* **2006**, 153, 47-53.

78. Pensa, E.; Cortes, E.; Corthey, G.; Carro, P.; Vericat, C.; Fonticelli, M. H.; Benitez, G.; Rubert, A. A.; Salvarezza, R. C., The Chemistry of the Sulfur-Gold Interface: In Search of a Unified Model. *Acc. Chem. Res.* **2012**, *45*, 1183-1192.
79. Jadhav, S. A., Functional Self-Assembled Monolayers (Sams) of Organic Compounds on Gold Nanoparticles. *J. Mater. Chem.* **2012**, *22*, 5894-5899.
80. Pieters, G.; Prins, L. J., Catalytic Self-Assembled Monolayers on Gold Nanoparticles. *New J. Chem.* **2012**, *36*, 1931-1939.
81. Love, J. C.; Estroff, L. A.; Kriebel, J. K.; Nuzzo, R. G.; Whitesides, G. M., Self-Assembled Monolayers of Thiolates on Metals as a Form of Nanotechnology. *Chem. Rev.* **2005**, *105*, 1103-1169.
82. Ulman, A., Formation and Structure of Self-Assembled Monolayers. *Chem. Rev. (Washington, D. C.)* **1996**, *96*, 1533-1554.
83. Hermanson, G., *Bioconjugate Techniques*. 2 ed.; Elsevier: Rockford, Illinois, USA, **2008**.
84. Geoghegan, W. D., The Effect of Three Variables on Adsorption of Rabbit IgG to Colloidal Gold. *J. Histochem. Cytochem.* **1988**, *36*, 401-7.
85. Kaur, K.; Forrest, J. A., Influence of Particle Size on the Binding Activity of Proteins Adsorbed onto Gold Nanoparticles. *Langmuir* **2012**, *28*, 2736-2744.
86. Hinterwirth, H.; Lindner, W.; Laemmerhofer, M., Bioconjugation of Trypsin onto Gold Nanoparticles: Effect of Surface Chemistry on Bioactivity. *Anal. Chim. Acta* **2012**, *733*, 90-97.
87. Liu, H.; Pierre-Pierre, N.; Huo, Q., Dynamic Light Scattering for Gold Nanorod Size Characterization and Study of Nanorod-Protein Interactions. *Gold Bull.* **2012**, *45*, 187-195.
88. James, A. E.; Driskell, J. D., Monitoring Gold Nanoparticle Conjugation and Analysis of Biomolecular Binding with Nanoparticle Tracking Analysis (Nta) and Dynamic Light Scattering (Dls). *Analyst* **2013**, *138*, 1212-1218.
89. Lou, S.; Ye, J.-y.; Li, K.-q.; Wu, A., A Gold Nanoparticle-Based Immunochromatographic Assay: The Influence of Nanoparticulate Size. *Analyst* **2012**, *137*, 1174-1181.

90. Shan, J.; Tenhu, H., Recent Advances in Polymer Protected Gold Nanoparticles: Synthesis, Properties and Applications. *Chem. Commun.* **2007**, 4580-4598.
91. Masereel, B.; Dinguizli, M.; Bouzin, C.; Moniotte, N.; Feron, O.; Gallez, B.; Vander, B. T.; Michiels, C.; Lucas, S., Antibody Immobilization on Gold Nanoparticles Coated Layer-by-Layer with Polyelectrolytes. *J. Nanopart. Res.* **2011**, 13, 1573-1580.
92. Woehrle, G. H.; Brown, L. O.; Hutchison, J. E., Thiol-Functionalized, 1.5-Nm Gold Nanoparticles through Ligand Exchange Reactions: Scope and Mechanism of Ligand Exchange. *J. Am. Chem. Soc.* **2005**, 127, 2172-2183.
93. Caragheorgheopol, A.; Chechik, V., Mechanistic Aspects of Ligand Exchange in Au Nanoparticles. *Phys. Chem. Chem. Phys.* **2008**, 10, 5029-5041.
94. Elzey, S.; Tsai, D.-H.; Rabb, S. A.; Yu, L. L.; Winchester, M. R.; Hackley, V. A., Quantification of Ligand Packing Density on Gold Nanoparticles Using Icp-Oes. *Anal. Bioanal. Chem.* **2012**, 403, 145-149.
95. Ivanov, M. R.; Haes, A. J., Anionic Functionalized Gold Nanoparticle Continuous Full Filling Separations: Importance of Sample Concentration. *Anal. Chem.* **2012**, 84, 1320-1326.
96. Techane, S. D.; Gamble, L. J.; Castner, D. G., Multitechnique Characterization of Self-Assembled Carboxylic Acid-Terminated Alkanethiol Monolayers on Nanoparticle and Flat Gold Surfaces. *J. Phys. Chem. C* **2011**, 115, 9432-9441.
97. Lanterna, A. E.; Coronado, E. A.; Granados, A. M., When Nanoparticle Size and Molecular Geometry Matter: Analyzing the Degree of Surface Functionalization of Gold Nanoparticles with Sulfur Heterocyclic Compounds. *J. Phys. Chem. C* **2012**, 116, 6520-6529.
98. Zhang, D.; Ansar, S. M., Ratiometric Surface Enhanced Raman Quantification of Ligand Adsorption onto a Gold Nanoparticle. *Anal. Chem.* **2010**, 82, 5910-5914.
99. Xia, X.; Yang, M.; Wang, Y.; Zheng, Y.; Li, Q.; Chen, J.; Xia, Y., Quantifying the Coverage Density of Poly(Ethylene Glycol) Chains on the Surface of Gold Nanostructures. *ACS Nano* **2012**, 6, 512-522.
100. Schroedter, A.; Weller, H., Ligand Design and Bioconjugation of Colloidal Gold Nanoparticles. *Angew. Chem., Int. Ed.* **2002**, 41, 3218-3221.

101. Zhang, B.; Yan, B., Analytical Strategies for Characterizing the Surface Chemistry of Nanoparticles. *Anal. Bioanal. Chem.* **2010**, 396, 973-982.
102. Baer, D. R.; Gaspar, D. J.; Nachimuthu, P.; Techane, S. D.; Castner, D. G., Application of Surface Chemical Analysis Tools for Characterization of Nanoparticles. *Anal. Bioanal. Chem.* **2010**, 396, 983-1002.
103. Thomas, K. G.; Kamat, P. V., Chromophore-Functionalized Gold Nanoparticles. *Acc. Chem. Res.* **2003**, 36, 888-898.
104. Liu, D.; Wang, Z.; Jiang, X., Gold Nanoparticles for the Colorimetric and Fluorescent Detection of Ions and Small Organic Molecules. *Nanoscale* **2011**, 3, 1421-1433.
105. Hu, C.; Peng, Q.; Chen, F.; Zhong, Z.; Zhuo, R., Low Molecular Weight Polyethylenimine Conjugated Gold Nanoparticles as Efficient Gene Vectors. *Bioconjugate Chem.* **2010**, 21, 836-843.
106. Chen, H.; Yuan, L.; Song, W.; Wu, Z.; Li, D., Biocompatible Polymer Materials: Role of Protein-Surface Interactions. *Prog. Polym. Sci.* **2008**, 33, 1059-1087.
107. Masson, J.-F.; Battaglia, T. M.; Davidson, M. J.; Kim, Y.-C.; Prakash, A. M. C.; Beaudoin, S.; Booksh, K. S., Biocompatible Polymers for Antibody Support on Gold Surfaces. *Talanta* **2005**, 67, 918-925.
108. Masson, J.-F.; Battaglia, T. M.; Cramer, J.; Beaudoin, S.; Sierks, M.; Booksh, K. S., Reduction of Nonspecific Protein Binding on Surface Plasmon Resonance Biosensors. *Anal. Bioanal. Chem.* **2006**, 386, 1951-1959.
109. Di Pasqua, A. J.; Mishler, R. E.; Ship, Y.-L.; Dabrowiak, J. C.; Asefa, T., Preparation of Antibody-Conjugated Gold Nanoparticles. *Mater. Lett.* **2009**, 63, 1876-1879.
110. Pandey, P.; Singh Surinder, P.; Arya Sunil, K.; Gupta, V.; Datta, M.; Singh, S.; Malhotra Bansi, D., Application of Thiolated Gold Nanoparticles for the Enhancement of Glucose Oxidase Activity. *Langmuir* **2007**, 23, 3333-7.
111. Gole, A.; Murphy, C. J., Azide-Derivatized Gold Nanorods: Functional Materials for "Click" Chemistry. *Langmuir* **2008**, 24, 266-272.
112. Kitano, H.; Anraku, Y.; Shinohara, H., Sensing Capabilities of Colloidal Gold Monolayer Modified with a Phenylboronic Acid-Carrying Polymer Brush. *Biomacromolecules* **2006**, 7, 1065-1071.

113. Uludag, Y.; Hammond, R.; Cooper, M. A., A Signal Amplification Assay for Hsv Type 1 Viral DNA Detection Using Nanoparticles and Direct Acoustic Profiling. *J. Nanobiotechnol.* **2010**, *8*, No pp given.
114. Yu, A.; Geng, T.; Fu, Q.; Chen, C.; Cui, Y., Biotin-Avidin Amplified Magnetic Immunoassay for Hepatitis B Surface Antigen Detection Using Goldmag Nanoparticles. *J. Magn. Magn. Mater.* **2007**, *311*, 421-424.
115. Saleh, S. M.; Ali, R.; Hirsch, T.; Wolfbeis, O. S., Detection of Biotin-Avidin Affinity Binding by Exploiting a Self-Referenced System Composed of Upconverting Luminescent Nanoparticles and Gold Nanoparticles. *J. Nanopart. Res.* **2011**, *13*, 4603-4611.
116. Guven, B.; Basaran-Akgul, N.; Temur, E.; Tamer, U.; Boyaci, I. H., Sers-Based Sandwich Immunoassay Using Antibody Coated Magnetic Nanoparticles for Escherichia Coli Enumeration. *Analyst* **2011**, *136*, 740-748.
117. Tang, D.; Cui, Y.; Chen, G., Nanoparticle-Based Immunoassays in the Biomedical Field. *Analyst* **2013**, *138*, 981-990.
118. Jain, P. K.; Huang, X.; El-Sayed, I. H.; El-Sayed, M. A., Noble Metals on the Nanoscale: Optical and Photothermal Properties and Some Applications in Imaging, Sensing, Biology, and Medicine. *Acc. Chem. Res.* **2008**, *41*, 1578-1586.
119. Kim, D.; Jon, S., Gold Nanoparticles in Image-Guided Cancer Therapy. *Inorg. Chim. Acta* **2012**, *393*, 154-164.
120. Lucena, R.; Simonet, B. M.; Cardenas, S.; Valcarcel, M., Potential of Nanoparticles in Sample Preparation. *J. Chromatogr., A* **2010**, *1218*, 620-637.
121. Sykora, D.; Kasicka, V.; Miksik, I.; Rezanka, P.; Zaruba, K.; Matejka, P.; Kral, V., Application of Gold Nanoparticles in Separation Sciences. *J. Sep. Sci.* **2010**, *33*, 372-387.
122. Noble, J.; Attree, S.; Horgan, A.; Knight, A.; Kumarswami, N.; Porter, R.; Worsley, G., Optical Scattering Artifacts Observed in the Development of Multiplexed Surface Enhanced Raman Spectroscopy Nanotag Immunoassays. *Anal. Chem.* **2012**, *84*, 8246-8252.
123. Zhou, G.; Mao, X.; Juncker, D., Immunochromatographic Assay on Thread. *Anal. Chem.* **2012**, *84*, 7736-7743.

124. Cao, X.; Ye, Y.; Liu, S., Gold Nanoparticle-Based Signal Amplification for Biosensing. *Anal. Biochem.* **2011**, *417*, 1-16.
125. Oliveira, M. D. L.; Abdalla, D. S. P.; Guilherme, D. F.; Faulin, T. E. S.; Andrade, C. A. S., Impedimetric Immunosensor for Electronegative Low Density Lipoprotein (Ldl-) Based on Monoclonal Antibody Adsorbed on (Polyvinyl Formal)-Gold Nanoparticles Matrix. *Sens. Actuators, B* **2011**, *B155*, 775-781.
126. Zhu, Z.-J.; Tang, R.; Yeh, Y.-C.; Miranda, O. R.; Rotello, V. M.; Vachet, R. W., Determination of the Intracellular Stability of Gold Nanoparticle Monolayers Using Mass Spectrometry. *Anal. Chem.* **2012**, *84*, 4321-4326.
127. Ghosh, P. S.; Kim, C.-K.; Han, G.; Forbes, N. S.; Rotello, V. M., Efficient Gene Delivery Vectors by Tuning the Surface Charge Density of Amino Acid-Functionalized Gold Nanoparticles. *ACS Nano* **2008**, *2*, 2213-2218.
128. Chen, J.; Glaus, C.; Laforest, R.; Zhang, Q.; Yang, M.; Gidding, M.; Welch, M. J.; Xia, Y., Gold Nanocages as Photothermal Transducers for Cancer Treatment. *Small* **2010**, *6*, 811-817.
129. Wang, H.; Campiglia, A. D., Determination of Polycyclic Aromatic Hydrocarbons in Drinking Water Samples by Solid-Phase Nanoextraction and High-Performance Liquid Chromatography. *Anal Chem* **2008**, *80*, 8202-9.
130. Jesus, L.-G. M.; Simo-Alfonso, E. F.; Zougagh, M.; Rios, A., Use of Gold Nanoparticle-Coated Sorbent Materials for the Selective Preconcentration of Sulfonylurea Herbicides in Water Samples and Determination by Capillary Liquid Chromatography. *Talanta* **2013**, Ahead of Print.
131. Faccenda, A.; Bonham, C. A.; Vacratsis, P. O.; Zhang, X.; Mutus, B., Gold Nanoparticle Enrichment Method for Identifying S-Nitrosylation and S-Glutathionylation Sites in Proteins. *J. Am. Chem. Soc.* **2010**, *132*, 11392-11394.
132. Tang, J.; Liu, Y.; Qi, D.; Yao, G.; Deng, C.; Zhang, X., On-Plate-Selective Enrichment of Glycopeptides Using Boronic Acid-Modified Gold Nanoparticles for Direct Maldi-Qit-Tof Ms Analysis. *Proteomics* **2009**, *9*, 5046-5055.
133. McLean, J. A.; Stumpo, K. A.; Russell, D. H., Size-Selected (2-10 Nm) Gold Nanoparticles for Matrix Assisted Laser Desorption Ionization of Peptides. *J. Am. Chem. Soc.* **2005**, *127*, 5304-5305.

134. Nash, M. A.; Yager, P.; Hoffman, A. S.; Stayton, P. S., Mixed Stimuli-Responsive Magnetic and Gold Nanoparticle System for Rapid Purification, Enrichment, and Detection of Biomarkers. *Bioconjugate Chem.* **2010**, *21*, 2197-2204.
135. Nash, M. A.; Waitumbi, J. N.; Hoffman, A. S.; Yager, P.; Stayton, P. S., Multiplexed Enrichment and Detection of Malarial Biomarkers Using a Stimuli-Responsive Iron Oxide and Gold Nanoparticle Reagent System. *ACS Nano* **2012**, *6*, 6776-6785.
136. Mackiewicz, M. R.; Hodges, H. L.; Reed, S. M., C-Reactive Protein Induced Rearrangement of Phosphatidylcholine on Nanoparticle Mimics of Lipoprotein Particles. *J. Phys. Chem. B* **2010**, *114*, 5556-5562.
137. Thaxton, C. S.; Daniel, W. L.; Giljohann, D. A.; Thomas, A. D.; Mirkin, C. A., Templated Spherical High Density Lipoprotein Nanoparticles. *J. Am. Chem. Soc.* **2009**, *131*, 1384-1385.
138. McMahon, K. M.; Mutharasan, R. K.; Tripathy, S.; Veliceasa, D.; Bobeica, M.; Shumaker, D. K.; Luthi, A. J.; Helfand, B. T.; Ardehali, H.; Mirkin, C. A.; Volpert, O.; Thaxton, C. S., Biomimetic High Density Lipoprotein Nanoparticles for Nucleic Acid Delivery. *Nano Lett.* **2011**, *11*, 1208-1214.
139. Luthi, A. J.; Zhang, H.; Kim, D.; Giljohann, D. A.; Mirkin, C. A.; Thaxton, C. S., Tailoring of Biomimetic High-Density Lipoprotein Nanostructures Changes Cholesterol Binding and Efflux. *ACS Nano* **2012**, *6*, 276-285.
140. Yang, S.; Damiano, M. G.; Zhang, H.; Tripathy, S.; Luthi, A. J.; Rink, J. S.; Ugolkov, A. V.; Singh, A. T. K.; Dave, S. S.; Gordon, L. I.; Thaxton, C. S., Biomimetic, Synthetic Hdl Nanostructures for Lymphoma. *PNAS*, *Early Ed.* **2013**, 1-6.

3. PUBLICATIONS AND CONFERENCE CONTRIBUTIONS

3.1. List of Publications

Hinterwirth H.; Wiedmer S.K.; Moilanen M.; Lehner A.; Allmaier G.; Waitz T.; Lindner W.; Lämmerhofer M.; Comparative Method Evaluation for Gold Nanoparticle Size and Size Distribution Analysis. *unpublished manuscript*

Hinterwirth, H.; Kappel, S.; Waitz, T.; Prohaska, T.; Lindner, W.; Laemmerhofer, M.; Quantifying Thiol Ligand Density of Self-Assembled Monolayers on Gold Nanoparticles by Inductively Coupled Plasma-Mass Spectrometry. *ACS Nano* **2013**, 7, 1129-1136

Hinterwirth, H.; Lindner, W.; Laemmerhofer, M., Bioconjugation of Trypsin onto Gold Nanoparticles: Effect of Surface Chemistry on Bioactivity. *Analytica Chimica Acta* **2012**, 733, 90-97

Hinterwirth H.; Lindner W.; Lämmerhofer M.; Gold Nanoparticle Conjugated Anti-Oxidized Low-Density Lipoprotein-Antibodies and Liquid Chromatography/Mass Spectrometry as Tools for Targeted Lipidomics. *unpublished manuscript*

Hinterwirth, H.; Laemmerhofer, M.; Preinerstorfer, B.; Gargano, A.; Reischl, R.; Bicker, W.; Trapp, O.; Brecker, L.; Lindner, W., Selectivity Issues in Targeted Metabolomics: Separation of Phosphorylated Carbohydrate Isomers by Mixed-Mode Hydrophilic Interaction/Weak Anion Exchange Chromatography. *Journal of Separation Science* **2010**, 33, 3273-3282.

3.2. Oral Presentations

2013/03

MSB 2013, Charlottesville, VA, USA

Gold Nanoparticles as Tool for Extraction and Enrichment of Biomarkers – Influence of Bioconjugation Chemistry

2013/01

Doktorandenseminar (PhD student symposium of separation science), Hohenroda, Germany

Gold Nanoparticles as Tool for Extraction and Enrichment of Biomarkers – From Sample Preparation to Detection with MS

2010/06

6th ASAC JunganalytikerInnen Forum (PhD student symposium), Vienna, Austria;
Isomer Separations of Phosphorylated Carbohydrates on RP/WAX

3.3. Poster Presentations

2013/03

MSB 2013, Charlottesville, VA, USA; *Ligand Density Determination on Gold Nanoparticles by ICPMS: Dependence on Ligand Length*

2012/06

HPLC conference, Anaheim, US; *Bioconjugation of Trypsin onto GNPs: A New Heterogeneous Nano-Structured Biocatalyst for LC-MS/MS Based Proteomics*

2011/06

HPLC conference, Budapest, Hungary, best Poster Award, 3rd price: *Selectivity Issues in Targeted Metabolomics: Separation of Phosphorylated Carbohydrate Isomers by Mixed-Mode Hydrophilic Interaction / Weak Anion Exchange Chromatography*

2011/03

Anakon, Zurich, Swiss; *Selectivity Issues in Targeted Metabolomics: Separation of Phosphorylated Carbohydrate Isomers by Mixed-Mode Hydrophilic Interaction / Weak Anion Exchange Chromatography*

4. COOPERATION PARTNERS

**Medical University of Vienna, Austria; Technoclone Austria;
University Marseille, France; Kratos, UK**

FFG project: Nano-MALDI

Long title: Nano-Particles Based Surface Chemistry as Novel Tool for Detection of Oxidized Phospholipids and Proteins by MALDI-MS.

University of Natural Resources and Life Sciences (BOKU-UFT), Vienna

Department of Chemistry, Division of Analytical Chemistry-VIRIS Laboratory, Konrad-Lorenz-Straße 24, 3430 Tulln, Austria

The ICPMS measurements for the determination of the Au / S ratio of thiol modified GNPs for ligand density calculations were optimized and carefully validated by Stefanie Kappel and Thomas Prohaska.

University of Vienna

Physics of Nanostructured Materials, Faculty of Physics, Boltzmanngasse 5, 1090 Vienna, Austria

Thomas Waitz performed the TEM measurements for the accurate size characterization of GNP.

University of Technology, Vienna

Institute of Chemical Technologies und Analytics, Getreidemarkt 9/164-AC, 1060 Vienna, Austria

Angela Lehner and Günter Allmaier did the characterization of GNPs by nES-GEMMA.

University of Helsinki, Finland

Department of Chemistry, POB 55, 00014

Susanne K. Wiedmer and Maria Moilanen did the measurements of GNPs with AsFIFFF.

Ruprecht-Karls-Universität

Organisch-Chemisches Institut, Im Neuenheimer Feld 270, 69120 Heidelberg, Germany

Oliver Trapp calculated apparent kinetic rate constants of on-column mutarotations using the DCXplorer software.

APPENDIX

A-1. Comparative Method Evaluation for Gold Nanoparticle Size and Size Distribution Analysis.

Hinterwirth H.; Wiedmer S.K.; Moilanen M.; Lehner A.; Allmaier G.; Waitz T.; Lindner W., Lämmerhofer M.;

unpublished manuscript

Comparative Method Evaluation for Gold Nanoparticle Size and Size Distribution Analysis

*Helmut Hinterwirth*¹, *Susanne K. Wiedmer*², *Maria Moilanen*², *Angela Lehner*³,
*Günter Allmaier*³, *Thomas Waitz*⁴, *Wolfgang Lindner*¹, *Michael Lämmerhofer*^{5, *}

¹ Department of Analytical Chemistry, University of Vienna, Währingerstrasse 38, 1090 Vienna, Austria

² Department of Chemistry, POB 55, 00014 University of Helsinki, Finland

³ Institute of Chemical Technologies und Analytics, Vienna University of Technology, Getreidemarkt 9/164-AC, 1060 Vienna, Austria

⁴ Physics of Nanostructured Materials, Faculty of Physics, University of Vienna, Boltzmanngasse 5, 1090 Vienna, Austria

⁵ Institute of Pharmaceutical Sciences, University of Tübingen, Auf der Morgenstelle 8, 72076 Tübingen, Germany

* Corresponding Author

Prof. Dr. Michael Lämmerhofer

Pharmaceutical Analysis and Bioanalysis

Institute of Pharmaceutical Sciences

University of Tübingen

Auf der Morgenstelle 8

72076 Tübingen, Germany

T +49 7071 29 78793, F +49 7071 29 4565

E-mail: michael.laemmerhofer@uni-tuebingen.de

Author Contributions

The manuscript was written through contributions of all authors. All authors have given approval to the final version of the manuscript.

ABSTRACT

Gold nanoparticles (GNPs) are popular colloidal substrates in various sensor, imaging, and sample preparation applications. The reasons for this popularity are their low costs, ability for their size-controlled synthesis with well defined narrow nanoparticle size distributions as well as their straightforward surface functionalization by self-assembling (of thiol containing) molecules.

GNPs of different diameters in the range between 26.2 nm and 13.5 nm were synthesized. The distinct GNPs were characterized by measuring their ζ -potential (ZP) and surface plasmon resonance (SPR) spectra. Size and size distributions were determined by various methods comprising transmission electron microscopy (TEM), dynamic light scattering (DLS), asymmetrical flow field-flow fractionation (AsFIFFF), and nanoelectrospray gas-phase electrophoretic mobility molecular analysis (nES-GEMMA). Weaknesses and strengths of each method are comparatively assessed and discussed.

KEYWORDS

Gold nanoparticles (GNP), dynamic light scattering (DLS), transmission electron microscopy (TEM), asymmetrical flow field-flow fractionation (AsFIFFF), nanoelectrospray gas-phase electrophoretic mobility molecular analysis (nES-GEMMA), zeta-potential (ζ -potential, ZP)

1. INTRODUCTION

The unique physical and chemical properties of gold nanoparticles (GNPs) contributed to the exponential increase in various nanobased applications rising up to more than 6,000 papers and about 200 reviews dealing with GNPs in 2012 (Scifinder search for the keyword 'gold nanoparticles', 2013/02/14). Nanomaterials as defined in the range of 1 nm to 100 nm significant differs from smaller atoms and nanoclusters as well as from bulk materials. These characteristics strongly depend next to their composition *i.a.* on their size and size distribution, their specific surface area and charge, their shape and morphology. Up to now, different methods exist to determine the size as crucial property of GNPs. However, measuring size and size distribution is still a challenge as not all methods provides comparable results and not all measurement methods are harmonized.¹

A fast and widely used method for GNP characterization is their surface plasmon resonance (SPR) which is exploited in advantage *e.g.* for chemical sensing and detection concepts. Furthermore, information on size² and concentration of GNPs^{3, 4} can be inferred from UV/Vis spectra as the extinction spectra are depend on the particle size, geometry and local environment according to the Mie theory^{5, 6}. For instance, Liu *et al.* reported a linear relationship between the logarithms of extinction coefficients and core diameters of GNPs independent of the capping ligands and the solvents⁷. However, also alteration of the surface *e.g.* by attachment of (bio)molecules and agglomerations or aggregations may lead to indicative changes in the SPR band shape⁵.

One of the most adopted methods for fast and easy size-controlled synthesis is based on the simultaneous reduction and stabilization of HAuCl_4 with trisodium citrate as first described by Frens and Turkevich^{8, 9}. The size of GNPs can be varied by changing the ratio of citrate/ HAuCl_4 , whereby a stoichiometric ratio larger than 1.5

is required for complete conversion of auric chloride to GNPs¹⁰. The straightforward surface functionalization of GNPs with bifunctional (thiol containing) molecules which form a self-assembled monolayer (SAM) further contributes to their great attractiveness. Besides their chemical properties also their size and the size distribution are playing a key role for their functionality and can be monitored by various nanoparticle classification techniques. Common methods for size determination are microscopic techniques (TEM, SEM, AFM, etc.)¹¹, dynamic light scattering (DLS)¹², size-exclusion chromatography (SEC)¹³, differential mobility analysis (DMA; gas phase electrophoretic molecular mobility analyzer, GEMMA)^{14, 15}, and field-flow fractionation (FFF)^{16, 17}. Although all measurements methods provide in principle comparable results the measured values are not always similar such as accurate size from TEM vs. hydrodynamic diameter as obtained by DLS or FFF. Thus, combination of several methods are developed to overcome drawbacks and to increase possible information about the nanoparticle properties. For example, several papers also describe the separation with FFF coupled to DLS and ICPMS, respectively, for detection and quantitative determination of GNPs^{16, 18-20}. In contrast to the hydrodynamic radius (DLS, FFF), DMA allows the size analysis of macromolecules and nanoparticles as correlation with the electrophoretic mobility diameter (EMD), whereby the particles are separated electrophoretically in the gas-phase at ambient pressure^{21, 22, 21-23}.

Another important property of nanoparticles is their surface charge, which can be determined through ζ -potential (ZP) measurements²⁴. The stability of colloidal suspensions of nanoparticles can be assessed by studying possible changes in the ZPs. Nanoparticles with ZPs above +30 mV or below -30 mV are commonly regarded stable.

In this article, we utilize a variety of complementary nanoparticle size classification methods comprising TEM, DLS, asymmetrical flow field flow fractionation (AsFIFFF), and GEMMA with the goal to get detailed insight into modalities, mode diameters, size distributions, and shapes of employed GNPs. In support of above NP sizing methods and for harmonization of those, correlations between various NP properties and SPR band characteristics of measured UV/Vis spectra are presented. Such UV/Vis measurements can be readily utilized as a fast and low-cost analysis tool for GNP quantification, but also for qualification in quality control. Herein, we show a systematic comparison of GNPs from the same synthesis batch by above mentioned techniques.

2. RESULTS AND DISCUSSION

2.1. THEORETICAL CALCULATIONS

The number of GNPs in solution can be calculated from the ratio of the initial Au(III) atoms (e.g. 55 mL of 1.14 mM HAuCl₄ were used for this study) and the number of gold atoms per nanoparticle in dependence on the particle size (eq.1):

$$(eq.1) \quad N_{GNP} = \frac{N_{Au(III)}}{N_{Au/GNP}} = \frac{1.14E-03 mol L^{-1} \times 0.055 L \times N_A}{30.89602 D^3} = 1.2221E18 D^{-3}$$

From eq.1, the molar concentration of nanoparticles c_{GNP} in solution can be further calculated by (eq.2):

$$(eq.2) \quad c_{GNP} = \frac{N_{GNP}}{V N_A} = 3.6898E-05 D^{-3}$$

where N_A is the Avogadro's constant. With the calculated GNP concentration, the extinction coefficient $\epsilon_{\lambda(max)}$ according to the Lambert-Beer law can be determined measuring the absorption spectrum. Finally, unknown concentrations of GNP suspension can be calculated with (eq.3):

$$(eq.3) \quad A_{\lambda(max)} = \epsilon_{\lambda(max)} c_{GNP} d$$

2.2.DETERMINATION OF GNP DIAMETERS, SIZE DISTRIBUTIONS, AND SHAPES

GNPs were prepared by size-controlled synthesis through variation of citrate/HAuCl₄ (C/H) ratio according to Table 1.

Table 1: GNPs were prepared with different sizes by variation of the citrate/HAuCl₄ (C/H) ratio. Theoretical calculations consider the surface area, molecular weight (MW) and concentration of GNPs. The extinction coefficient ϵ was calculated from the absorbance maximum. A comparison of TEM, DLS, DLS after AsFIFFF, and GEMMA is further shown.

C/H	GNP surface [nm ²]	MW (GNP)	c (GNP) mM	A (λ_{max}) (1:5 dilution)	ϵ (λ_{max})	TEM (d.nm)	DLS (d.nm)	DLS, after AsFIFFF separation	GEMMA (d.nm)
C/H=2	2163.7	1.10E+08	2.04E-06	0.897213	4.40E+05	26.2 ±4.4	34.3 ±0.1	21.6 ± 2.2	32.9
C/H=3	1302.6	5.14E+07	4.37E-06	0.830321	1.90E+05	20.4 ±4.3	29.9 ±0.3	25.6 ± 1.77	26.5
C/H=4	853.6	2.73E+07	8.24E-06	0.797786	9.68E+04	16.5 ±2.3	26.4 ±0.9	26.8 ± 1.25	17.1
C/H=5	544.5	1.39E+07	1.62E-05	0.77878	4.82E+04	13.2 ±1.3	21.4 ±0.4	19.5 ± 4.59	16.2
C/H=6	571.4	1.49E+07	1.50E-05	0.80002	5.32E+04	13.5 ±1.4	21.6 ±0.6	20.3 ± 1.92	15.6

The resultant citrate-capped GNPs were characterized by TEM, DLS, AsFIFFF, and GEMMA as well as by ZP and SPR measurements.

All citrate-stabilized GNPs were highly stable with an average ζ -potential of -38.7 ±4.4 mV (electrophoretic mobility of $-3.04 \pm 0.35 \cdot 10^{-8} \text{ m}^2 \text{ V}^{-1} \text{ s}^{-1}$, conductivity of $0.08 \pm 0.16 \text{ mS cm}^{-1}$, the pH of the suspension was approximately neutral). As pointed out above, such highly negative ZPs of the GNPs guarantee a sufficient colloidal stability and are therefore of utmost importance for their solution-based real applications.

Citrate-capped GNPs synthesized by changing the ratio of C/H from 2 to 6 were analyzed by TEM. TEM measures particle diameters in dry state *i.e.* without their solvation shell and the method provides information on the shape and morphology of particles. It becomes evident from Figure 1 that the GNPs have close to perfect spherical shape, in particular those with smaller diameter.

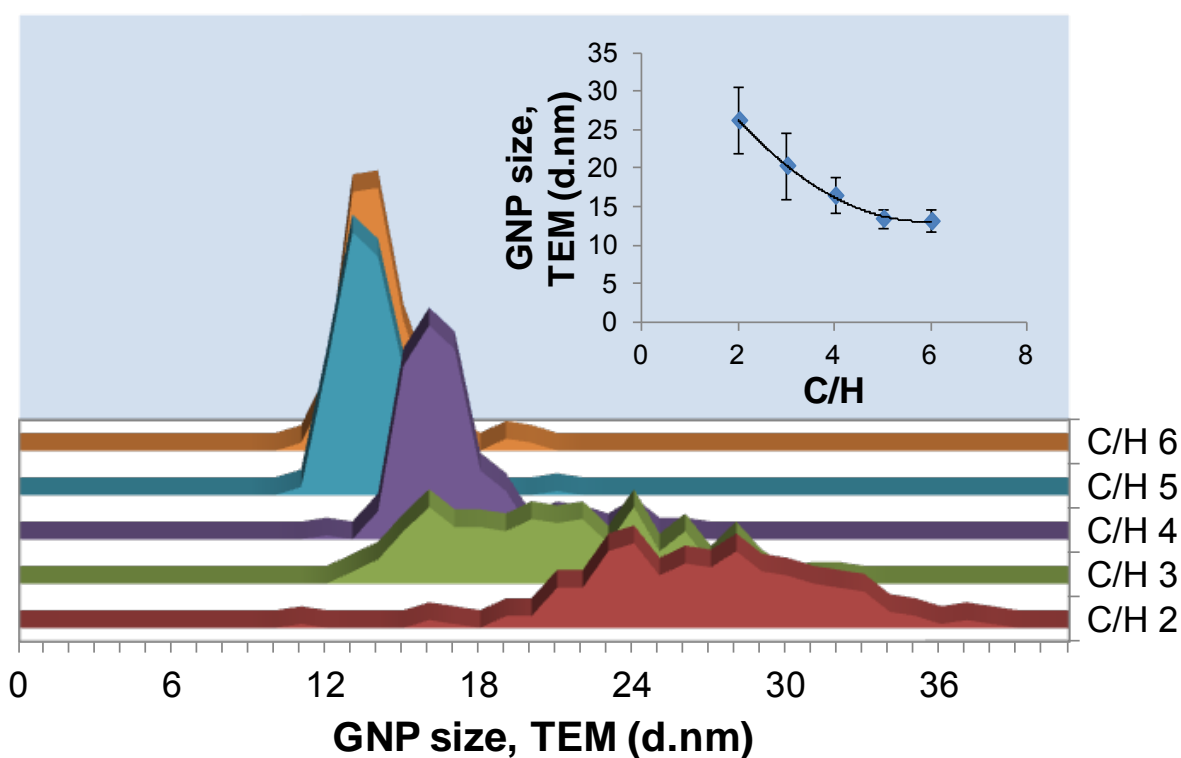


Figure 1: Histograms of GNPs prepared by changing the citrate/HAuCl₄ (C/H) ratio. The insert shows the logarithmic correlation of C/H on the GNP size.

As expected and reported previously C/H ratios in the range of 2 to 6 yield nanoparticles with average sizes between 26.2 ± 4.4 nm and 13.5 ± 1.4 nm (Figure 1). GNPs from these batches were used for all further studies. A logarithmic relationship was found between the C/H ratio and the GNP size (Figure 1, insert), which can be readily utilized in a predictive manner for size-controlled synthesis. Statistical analysis of large numbers of particles in each TEM measurement allows also determination of size distributions. It is evident that larger nanoparticles show wider size distributions and less uniform spherical shape (defined as ratio of length-to-width) changing from 1.21 ± 0.18 to less than 1.09 ± 0.09 within the specified range of NP diameters. Even though TEM measurements allow the determination of size, size distribution, and shape of nanoparticles, information about solution properties such as aggregation and agglomeration or surface charge is lost which is relevant for their suitability in many applications. On contrary, dynamic light scattering (DLS) provides

an orthogonal method for size determinations of GNPs in colloidal suspensions. DLS measures NPs with their solvation shell (*i.e.* the hydrodynamic radius of a particle) (Figure 2a). Thus, the GNP diameters measured by DLS (a method which is suitable for monodisperse distributions but usually fails for multimodal distributions due to insufficient size resolution) are larger than those of TEM.

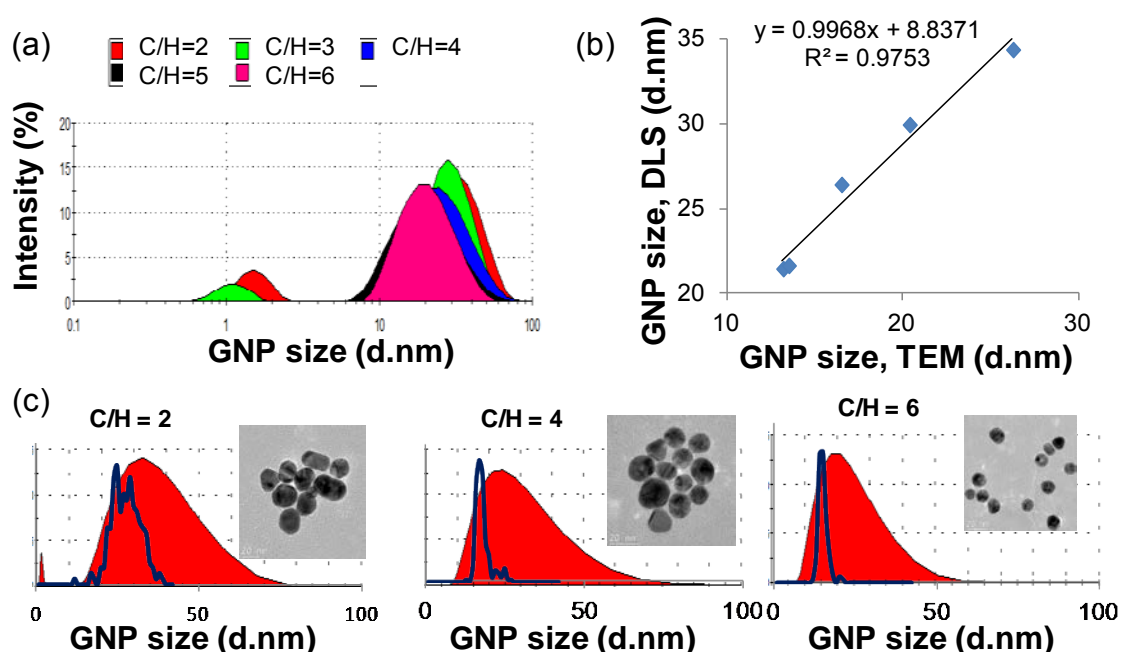


Figure 2: Size distribution by intensity (%) as measured with DLS: (a) Overlay of intensity distributions of GNP suspensions diluted by a factor of 1:5. (b) Correlation of mode diameters as measured by DLS and TEM. (c) Comparison of hydrodynamic diameters and size distributions by DLS (red area) with corresponding dry-state figures of TEM (blue line).

A linear correlation between diameters determined by these two techniques was found for current citrate-capped GNPs (Figure 2b). The DLS signals in the low nanometer range (Figure 2a) for the larger GNPs (C/H = 2 and C/H = 3) are artifacts which could not be found in TEM images. Other authors explained such artifacts by deviation from a spherical shape¹². Average asymmetry factors of 1.21 ± 0.18 and 1.15 ± 0.13 , respectively, were found by TEM for above GNP batches, as mentioned already before, but such a minor asymmetry can hardly explain this apparent bimodal

191 distribution. The asymmetry factor was below 1.10 for the smaller GNPs (C/H = 4, 5
192 and 6). It is also striking that the size distributions are much broader for DLS
193 measurements than TEM and again become narrower for the smaller particle sizes
194 (see Figure 2c). A polydispersity index (PDI) of 0.56 and 0.30 was measured by DLS
195 for the larger particles with C/H = 2 and C/H = 3, respectively, while it was below 0.29
196 for C/H = 4, 5, and 6. The skewed distribution towards larger diameters may be a
197 measurement artifact of DLS. It is well known that DLS is a mass concentration
198 dependent method (*i.e.* particles with large masses like larger particles are
199 overestimated and particles with low masses like smaller particles are
200 underestimated). This problem of DLS is well recognized and partly compensated by
201 transformation to volume and number distributions, respectively (Figure 3). However,
202 the reliability is questionable and the peak at around 1 nm is supposed to be an
203 artifact.

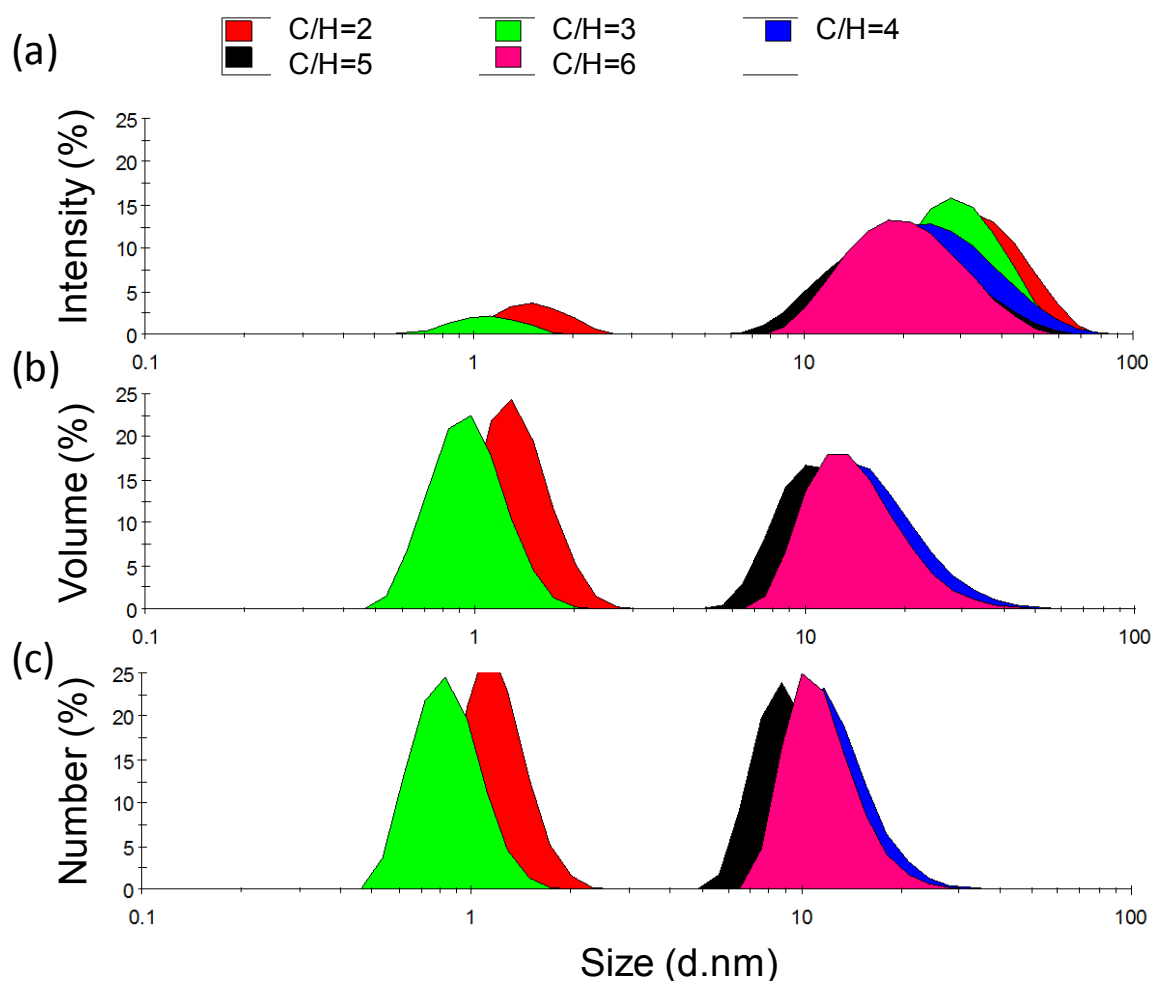


Figure 3: DLS measurements: Size distributions by (a) intensity, (b) volume and (c) number. Larger particles which are less spherical show a false positive peak in the low-nanometer range. Recalculation to size distribution by volume or Number number overestimates this peak which may easily lead to erroneous conclusions without reference method.

Thus, validation by complementary techniques such as AsFIFFF and GEMMA were envisioned for further confirmation.

A convenient orthogonal method for characterization of solvated particles measuring hydrodynamic diameters like DLS is AsFIFFF, which is a hydrodynamic separation method for nanoparticles possible to hyphenate with several detection modes, e.g. UV/Vis, DLS, or ICP-MS^{16, 18-20}. Various parameters such as membrane material, cross-flow rate, and channel thickness were optimized and the finally utilized parameters of the optimized method are specified in the experimental section. GNPs

of different size give differential elution times in AsFIFFF as revealed by Figure 4a, while GNPs with larger diameter elute later in AsFIFFF (Figure 4b).

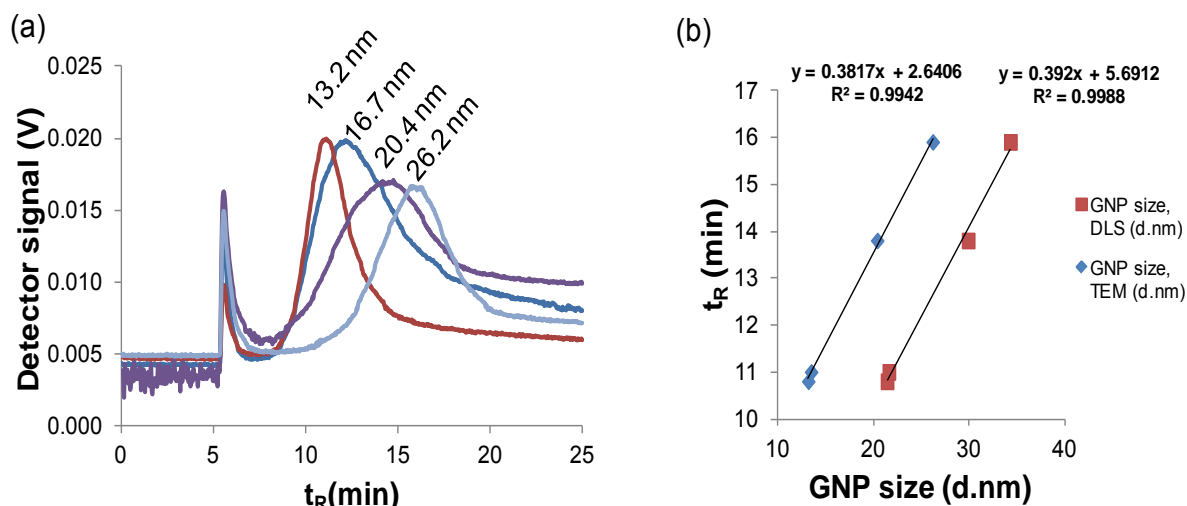


Figure 4: (a) Overlay of AsFIFFF fractograms of citrate-capped GNPs of different sizes. (b) Dependence of elution time t_R (min) on GNP size measured by DLS and TEM, respectively.

If adequate size calibrants are available, AsFIFFF represents a straightforward method for analyzing particle diameters and size distributions in liquid state. On the other hand, AsFIFFF has also preparative capability. It could be used for particle classification of multimodal particle mixtures and purification of modified GNPs. The potential of AsFIFFF in this regard is demonstrated by baseline resolution of GNPs with hydrodynamic diameters of 13.2 nm (C/H ratio 5) and 26.2 nm (C/H ratio 2). To document the resolving power of AsFIFFF, in addition to the injections of individual GNPs, a mixture of citrate capped GNPs (C/H ratio = 2 and C/H ratio = 5) was injected as well. Figure 5a shows the overlay of fractograms of individual samples and the mixture, respectively.

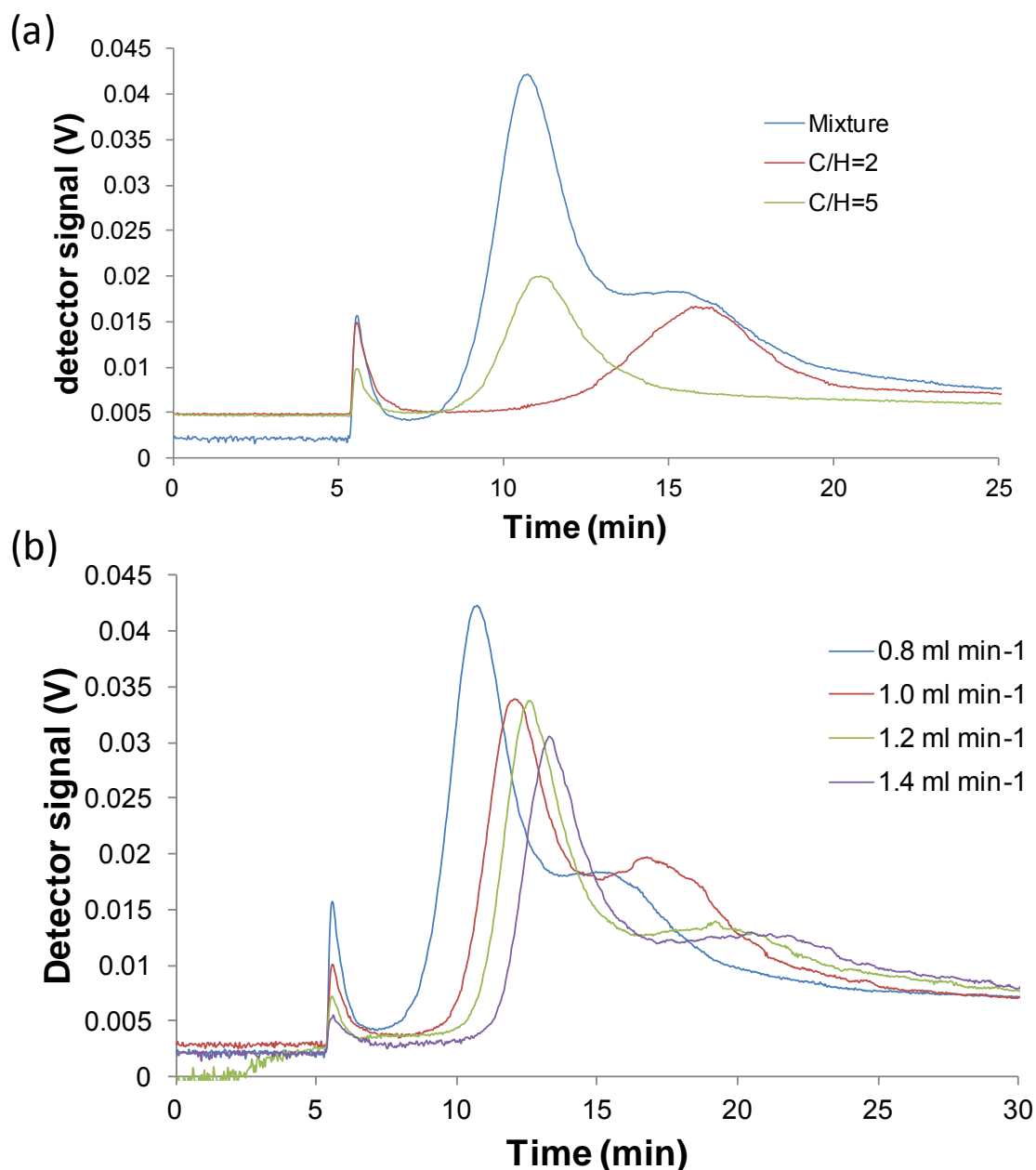


Figure 5: (a) Overlay of fractograms of individual samples of GNP citrate (C/H=2 and C/H=5) and mixture of the two. Detector signal is from UV (520 nm). (b) Overlay of fractograms of the mixture C/H=2 citrate and C/H=5 citrate in different cross flows.

Because the separation of the two samples was not complete, different cross flows were tested. In Figure 5b an overlay of fractograms of the mixture using different cross flows is shown. The separation was not significantly improved at higher cross flows but the useful resolving power for preparative purpose in which a narrow band of individual GNPs can be isolated is certainly indicated. Critical factors in AsFIFFF

are membrane adsorption, excessive peak broadening due to axial diffusion contributions and resultant low size resolution.

Good size resolution and high precision for nanoparticles > 3 nm has been reported for GEMMA^{23, 25}. GEMMA allows electrophoretic separation of singly charged particles in the gas phase at atmospheric pressure and from such experiments the electrophoretic mobility diameter (EMD) of NPs can be calculated. Multiply charged ions are generated using electrospray process by applying a voltage and a particle-free sheath gas flow. Singly charged particles and neutrals are produced from the multiply charged particles by charge reduction with a Polonium-210 source (whereby approximately 99% of ions are converted to neutral particles and these are not used for analysis). The charged particles are then separated with a nano differential mobility analyzer and detected with a condensation particle counter suited for single particle detection. Some restrictions pertain to the application of volatile buffers comparable to electrospray ionization mass spectrometry (ESI MS) and running the spray device in the cone-jet mode contrary to classical ESI MS. Yet, GEMMA has the advantage of measuring dry particles in gas phase at atmospheric pressure without solvent effects, however, particles may be encrusted occasionally with nonvolatile salts²⁵. Thus, results should be slightly closer to TEM measurements as compared to DLS which measures the hydrodynamic radius and has some difficulties in case of multimodal particle size distributions in samples. Moreover, as a particle number concentration (number of NPs per volume) dependent method it is not biased towards a particular particle size and should therefore give more realistic nanoparticle distributions as compared to DLS.

The direct analysis of citrate stabilized GNPs, however, was not successful due to unfavorable effects stemming from excessive nonvolatile sodium citrate in the sample solution. Thus, desalting of samples to a certain extent was required. After simple

spin-filtration of a small sample volume still a dominant peak at EMD < 10 nm was detected, which is related to the concentration-dependent formation of sodium citrate salt particles (Figure 6a). Such phenomena are used sometimes to calibrate DMA systems with sucrose²⁶. Due to the partial removal of stabilizing citrates (which hinder aggregation), however, also di- and trimers of the GNPs can be observed in Figure 6a and also in Figure 7d.

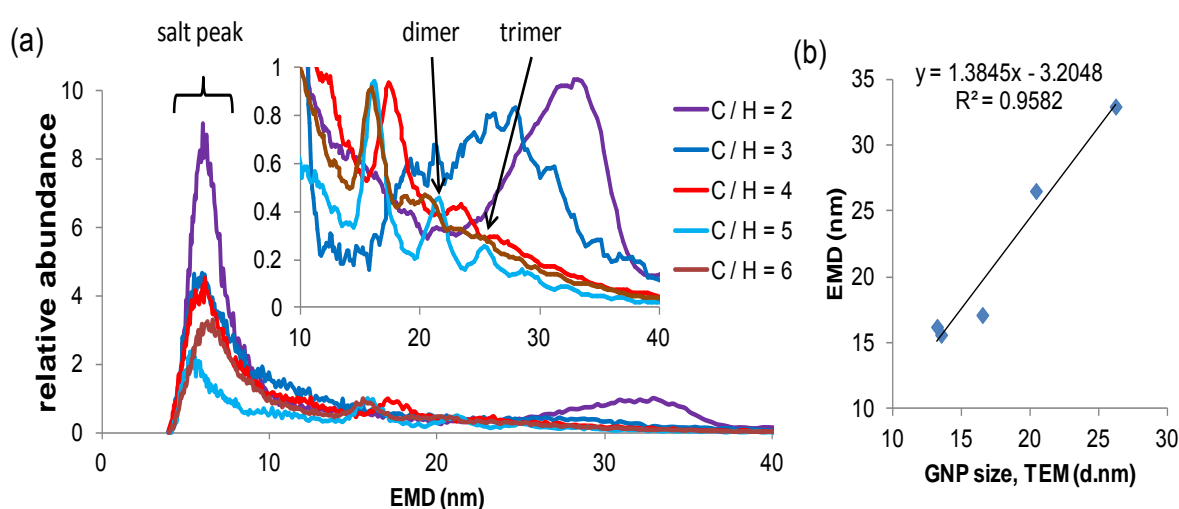


Figure 6: (a) Analysis of GNPs of different sizes by GEMMA (insert shows the zoomed region from 10 to 40 nm; each scaled to the largest peak). The peak in the lower nanometer range (< 10 nm) is a system peak aggregate. Beside the monomer analyte peak there are also di-, tri- and further multimer peaks visible, which can be explained by removal of the stabilizing agent citrate. (b) Correlation of particle diameters as measured by TEM and GEMMA (as EMD in nm).

The peaks at EMD > 10 nm in the GEMMA spectra of Figure 4a (insert) show the particle size distributions of GNPs. The GEMMA spectra show good size resolution for GNPs in the range between 13.2 and 26.2 nm (C/H ratio between 6 and 2). Compared to TEM, GEMMA yielded slightly larger diameters but a good correlation (Figure 6b). As became evident from the discussion above, mode and average NP diameters, size distributions as well as size resolution are to some extent dependent on the utilized NP sizing technique. To document this, Figure 7 shows a direct comparison of the results and performance of the different investigated NP size

classification methods for two distinct GNP sizes, namely mode diameter of 13.2 nm (C/H = 5) and 26 nm (C/H = 2).

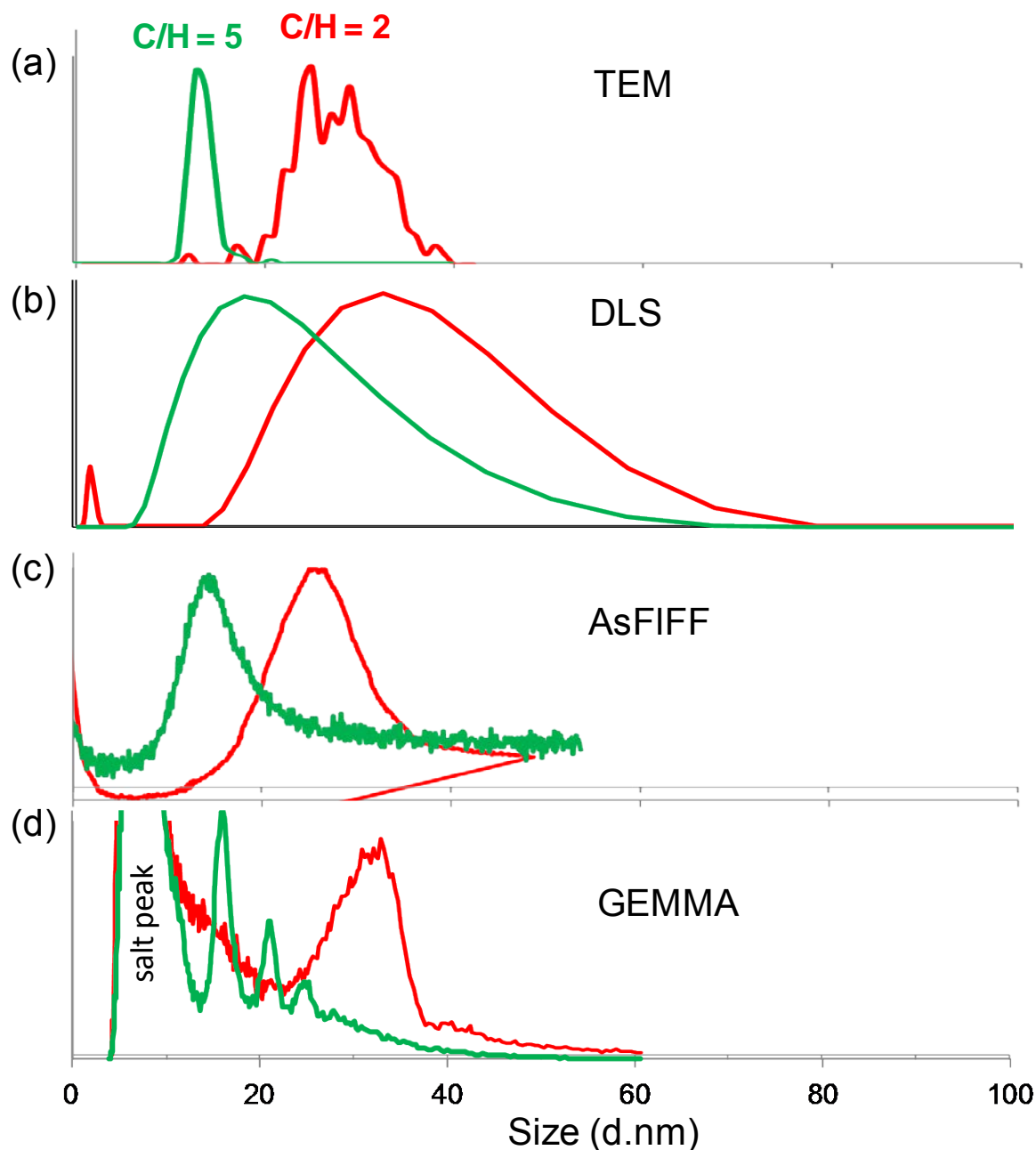


Figure 7: Comparison of different size characterization methods for two distinct GNP batches with 13 nm (C/H = 5) and 26 nm (C/H = 2).

It can be seen that the modal value is largely in agreement for the distinct methods. However, GEMMA and TEM seem to furnish the narrowest particle size distributions

and hence, it can be assumed that they measure the real distributions. Due to the fact that both techniques are particle number concentration techniques, there is no bias towards small or large NPs. In sharp contrast, DLS and AsFIFFF are mass concentration dependent techniques, which means a bias towards large NPs (*i.e.* an overestimation of these NPs). GEMMA allows also the collection of NPs after separation and further investigations by TEM²². AsFIFFF shows good agreement with these two techniques for the larger particles in terms of width of the distribution and polydispersity. Some extra peak broadening effects for the smaller GNPs due to instrumental factors let appear the distribution as obtained by AsFIFFF broader than it actually is. The worst results in terms of distribution width are accomplished by DLS. The particle size distributions are broad for both types of GNPs tested and show a significant asymmetry, which could be due to overestimation of larger particles. It seems that the curves are not fully representing the real distributions but give a good estimate for the mode size of the GNPs in solvated state.

Overall each of these sizing techniques has its advantages and shortcomings, and provides particular feasibilities. Ideally, they are combined for a comprehensive size classification and nanoparticle analysis. Of particular interest could be to perform sizing by a so-called parallel DMA which allows the separation and detection as well as collection of NPs with selected size ranges²⁷ or the on-line combination of AsFIFFF with ICPMS^{18, 19, 28}.

2.3. SPR SPECTROSCOPY AS AN ORTHOGONAL METHOD

Another orthogonal method for NP characterization, but restricted to metallic NPs like gold and silver NPs, is UV/Vis spectroscopy. While the aforementioned instrumental methodologies, *i.e.* DLS, AsFIFFF, and GEMMA are less common, UV/Vis spectroscopy is available in more or less every chemical laboratory. Its utility for GNP characterization is based on the sensitivity of the SPR band to minute molecular

alterations on the surface. On the one hand, it provides quantitative information about GNP concentrations but also qualitative information about size, shape, and surface modifications of nanoparticles.

All of the aforementioned particles as well as their modified counterparts have been systematically characterized during this study by UV/Vis spectroscopy as well. Figure 8a shows spectra of the set of citrate-capped GNPs.

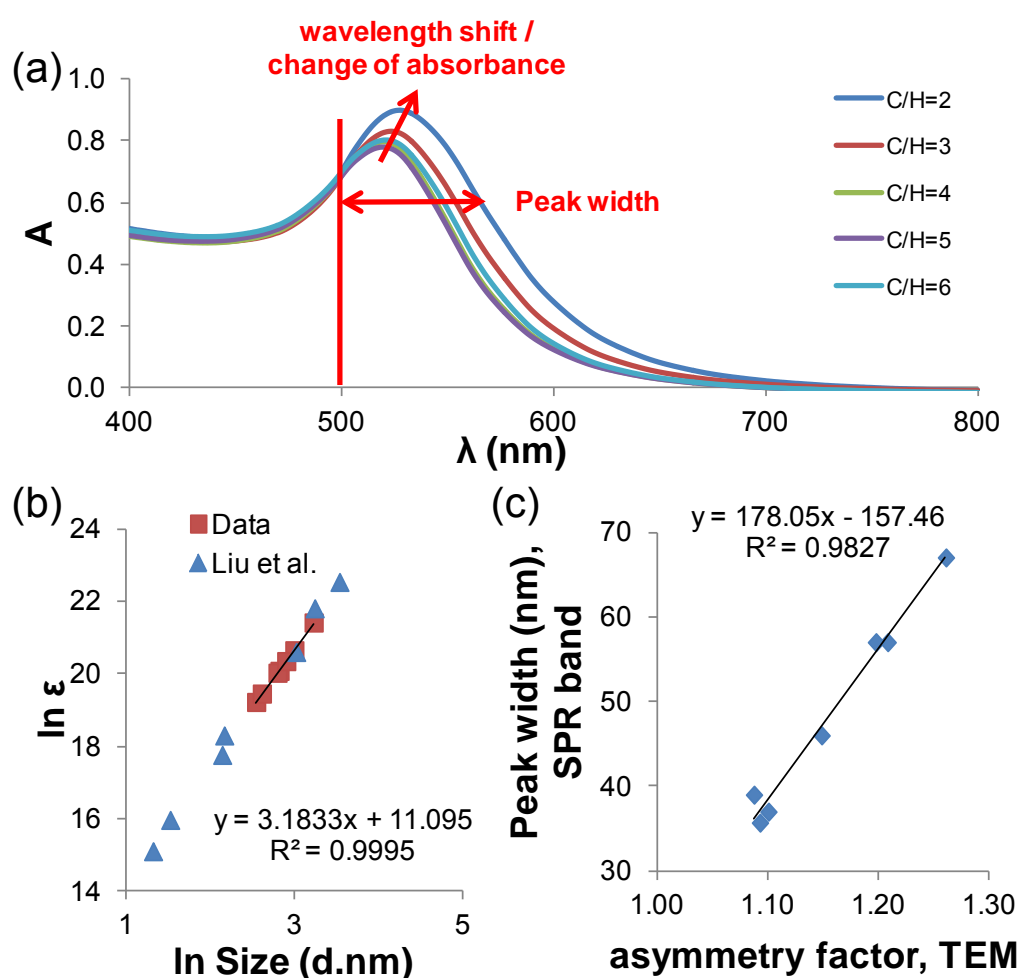


Figure 8: (a) UV/vis spectra of GNPs with well-known sizes (1:5 diluted). (b) Correlation between extinction coefficient ϵ and GNP size (double logarithmic). (c) Dependence of peak width of SPR band on asymmetry factor as measured by TEM (1 = highly spherical). (d) Shift of wavelength maxima in dependence on GNP size and surface modification.

It is evident that the distinct GNPs (which have all been prepared with the same amount of Au(III) in the reaction mixture) differ in absorbance and λ_{\max} . Both,

345 absorbance and λ_{\max} , are affected by NP diameter. As has already been
346 demonstrated recently, ϵ varies with particle diameter whereby a linear relationship of
347 $\ln \epsilon$ and the logarithmic scale of GNP size was found in accordance with literature ⁷
348 (Figure 8b). This may explain the change in absorbance of the distinct GNPs.
349 Interestingly, there is also a clear relation between the (peak) width of the SPR
350 absorbance band and the asymmetry factor of the GNPs as determined by TEM,
351 used herein as indicator for the spherical shape of GNPs. This correlation is useful to
352 predict the quality of the GNPs from UV/Vis spectra (Figure 8c).
353 Table 2 summarizes the advantages and disadvantages of different measurement
354 methods to characterize and analyze distinct unique physical and chemical properties
355 of GNPs.

Table 2: Summary of different measurement methods with regard to their applicability to determine unique physical and chemical properties of GNPs.

	Size	Size distribution	Shape	Surface area	Concentration	Surface charge	Aggregation / agglutination	Separation	Advantages	Disadvantages
TEM	yes	yes	yes	yes	no	no	yes	no	visualization of size and morphology	counting of $n > 200$ particles for statistical analysis
DLS	yes, but always overestimated (hydrodynamic radius)	yes, but always overestimated	false positive peak at low-nanometer area for non-spherical particles	no		no	yes	no	direct measurement of the suspension; control of aggregation / agglutination	size overestimated; false positive peaks possible
AsFIF	separation by size, coupling with DLS possible		no	no		no	yes	yes, coupling with DLS, ICPMS etc. possible		material losses e.g. due to cell membrane adsorption; change of solvent medium during gradient; surfactant often necessary for stabilization of particles
GEMMA	correlated with EMD		no	no		(EMD)	yes	EMD	measures dried single-charged particles without solvent effect	ion-suppression by trisodium citrate and limitation to volatile buffers
UV/vis	wavelength shift of the absorbance maximum with GNP size		peak width correlates with peak symmetry but also with size distribution	no	(logarithm of extinction coefficient linear to logarithm of GNP size)	no	yes (second peak at wavelength of about 650 nm)	no	fast and low-cost control analysis	UV/vis shape influenced by several parameters; LOD for small alterations
ZP	no	no	no	no	no	yes			fast measurement for stability	

CONCLUSIONS

In this paper we present the systematical study of gold nanoparticles (GNPs) from preparation to surface modification. We investigated different techniques for quantitative and qualitative analyses.

A variety of different orthogonal methods for GNP size analyses were used and compared to TEM measurements. TEM images allow the determination of GNP size, size distribution, and shape, while DLS may provide additional information on solution properties such as aggregation. Also AsFIFFF and GEMMA were found to be powerful orthogonal NP size classification techniques, the former complementing DLS in solution phase characterization and the latter TEM as a gas-phase analysis technique but at atmospheric pressure. Overall, larger-sized GNPs showed less uniform spherical shapes and wider size distributions compared to smaller ones. TEM provided the smallest mode diameter followed by GEMMA and DLS. TEM gives also information on shape and asymmetry of NPs. AsFIFFF is of interest due to its preparative scale applicability and capability to be hyphenated to different detection methods. Overall, GEMMA appears to have the highest size resolution and thus provided the narrowest size distributions while they were broadest with DLS which is moreover biased towards larger particles.

Finally, we established useful correlations between characteristic parameters of the UV/Vis spectra and ligand densities as well as GNP sizes. Thus, measurement of SPR band shifts provides a powerful, fast, and cheap analysis tool for GNP characterization as the size of GNPs can be estimated from the wavelength at the absorbance maximum. Subsequently, quantitative analysis is possible for GNPs with known sizes by their extinction coefficient but also qualitative information can be derived from the shape and the peak width of the SPR band.

3. METHODS

3.1. CHEMICALS

Gold(III) chloride trihydrate (auric chloride, $\text{HAuCl}_4 \cdot 3 \text{H}_2\text{O}$) and trisodium citrate, were all obtained from Sigma-Aldrich (Vienna, Austria).

INSTRUMENTS and METHODS

TEM: TEM measurements of GNPs were performed as described in previous work²⁹. In brief, GNP were deposited on amorphous carbon spanning Cu grids and the aqueous solution evaporated obtaining a high number density of $> 100 \text{ GPNs } \mu\text{m}^{-2}$.

TEM images were acquired with a PHILIPS CM200 (acceleration voltage 200 kV, equipped with a CompuStage goniometer, a CCD Camera System (Gatan Orius SC600, and a carbon free vacuum system) with a point resolution of 0.26 nm of the microscope. Standard calibration line and cross grating replicas with 1200 and 2160 lines / mm for low and intermediate magnifications, respectively, were used for calibration of the magnification at the CCD camera. The high magnifications were calibrated with graphitized carbon and the calibration was further justified by obtaining lattice fringe images of the GNPs that showed a fringe spacing deviating by less than 2% from the spacing of (111) lattice planes. 200 particles were analyzed for statistical evaluation of each sample and their diameter was determined by the average of length and width (*i.e.* by $(l_m + w_m)/2$, where l_m and w_m denote the arithmetic mean of the length and width, respectively).

DLS and ZP: Size and zeta potential (ZP) of gold nanoparticles were determined by Malvern Zetasizer Instruments Nano series (Prager Instruments) using following settings for gold material: refractive index $RI = 0.197$, absorption = 3.090 and for water as dispersant: temperature $T = 25^\circ\text{C}$, viscosity = 0.8872 cP, $RI = 1.330$. The dispersant viscosity was set as the same as sample viscosity with the Mark-Houwink

parameters of $A = 0.428$ and $K = 7.67E-05 \text{ cm}^2 \text{ s}^{-1}$. The measurement duration was adjusted automatically with three numbers of measurements per sample. UV-micro cuvettes (Plastibrand) were used for DLS and folded capillary cells (Malvern) for ZP measurements.

AsFIFFF: For asymmetric flow field-flow fractionation (AsFIFFF) an AF2000 Focus model from Postnova Analytics (Landsberg/Lech, Germany), with online UV/Vis detector operated at wavelength 520 nm and dynamic light scattering detector from Malvern Instruments (Herrenberg, Germany) was used. The channel thickness (spacer thickness) was 350 μm . The semi-permeable membrane was regenerated cellulose membrane with a cut off of 10 kDa (Alfa Laval, Espoo, Finland). The carrier liquid was 0.05 % SDS with 0.02 % NaN_3 added. Samples were injected *via* manual injector valve and a sample loop of 100 μL .

The detector flow was 0.50 mL min^{-1} and the slot outlet flow zero. For focusing, the injection flow was set to 0.20 mL min^{-1} with an injection time of 4.00 min and the cross flow to 0.80 mL min^{-1} with a transition time of 1.00 min. For elution a gradient profile as follows was used: 0 – 20 min: 0.8 mL min^{-1} , 20 – 25 min: $0.8 - 0 \text{ mL min}^{-1}$ and 25 – 35 min: 0 mL min^{-1} (constant).

GEMMA: For desalination carried out with VWR Centrifugal Filters (molecular weight cut off: 10 kDa) 60 μL of GNP solution was put onto the membrane and 340 μL of ammonium acetate (AA) solution, 20 mM, pH 7.0 was added. Centrifugation was done for 3-4 min at 5000 g and eluates were discarded. 400 μL of AA were added on the membrane, centrifugation repeated and eluates discarded again. This was repeated another time. The GNPs remaining on the membrane were dispersed with the liquid remaining on the membrane and were pipetted into a vial. By weight determination the dilution factor was estimated assuming an AA solution density of $1 \text{ mg } \mu\text{L}^{-1}$.

The GEMMA instrument consisted of the nano electrospray unit type 3480, the nano differential mobility analyzer type 3080 and the condensation particle counter type 3025A working with butanol (all parts from TSI, Shoreview, MN, USA). The electrospray unit was operated in positive ion mode; 0.5 L min⁻¹ compressed air generated by a table top compressor (Dürr-Technik, Bietigheim-Bissingen, Germany), 0.1 L min⁻¹ CO₂ (99.995%, Air Liquid, Schwechat, Austria) and a voltage of 2.5 kV were applied. A cone tipped fused silica capillary with an inner diameter of 40 µm was used; a pressure of 4 psi was applied to the sample chamber (approx. 0.3 bar pressure difference across the capillary). The nano differential mobility analyzer was operated with a sheath flow of 15 L min⁻¹ allowing the analysis in a size range of approx. 2 to 61 nm.

UV/Vis: UV/vis spectra were acquired by Specord50 photometer (Analytik Jena, Germany) setting bidistilled water as reference.

pH: The pH values were measured with the pH electrode DG100-SC (Mettler Toledo) using Mettler DL67 titrator.

3.2. SIZE CONTROLLED PREPARATION OF CITRATE STABILIZED GNPs

GNPs with distinct sizes were prepared by variation of the citrate/HAuCl₄ ratio as described previously^{29, 30}. In brief, to boiled 50 mL gold(III) chloride trihydrate solution in bidistilled water (final concentration was 1.14 mM) 5 mL trisodium citrate (concentration varied depending on the final citrate / HAuCl₄ ratio in solution) was added and heated for further 10 min, while the color changes to brown and red. All chemicals were prepared freshly before use.

CONFLICT OF INTERESTS

The authors declare no competing financial interest.

ACKNOWLEDEMENTS

Financial support of the “Nano-MALDI” project by the Austrian BMVIT via the “Austrian Nano-Initiative” and “MNT-ERA.NET” is gratefully acknowledged. M.M., S.K.W., and M.L. are grateful for financial support by the Academy of Finland (project no. 1257175) and German Academic Exchange Service (project no. 54655966).

REFERENCES

1. Commission, E., On the Definition of Nanomaterial (L275). *Official Journal of the European Union* **2011**, *54*, 38-40.
2. Amendola, V.; Meneghetti, M., Size Evaluation of Gold Nanoparticles by Uv-Vis Spectroscopy. *J. Phys. Chem. C* **2009**, *113*, 4277-4285.
3. Haiss, W.; Thanh, N. T. K.; Aveyard, J.; Fernig, D. G., Determination of Size and Concentration of Gold Nanoparticles from Uv-Vis Spectra. *Anal. Chem.* **2007**, *79*, 4215-4221.
4. Khlebtsov, N. G., Determination of Size and Concentration of Gold Nanoparticles from Extinction Spectra. *Anal. Chem.* **2008**, *80*, 6620-6625.
5. Willets, K. A.; Van, D. R. P., Localized Surface Plasmon Resonance Spectroscopy and Sensing. *Annu. Rev. Phys. Chem.* **2007**, *58*, 267-297.
6. Mie, G., Contributions to the Optics of Turbid Media, Especially Colloidal Metal Solutions. *Ann. Phys.* **1908**, *25*, 377-445.
7. Liu, X.; Atwater, M.; Wang, J.; Huo, Q., Extinction Coefficient of Gold Nanoparticles with Different Sizes and Different Capping Ligands. *Colloids Surf., B* **2007**, *58*, 3-7.
8. Turkevich, J.; Stevenson, P. C.; Hillier, J., The Nucleation and Growth Processes in the Synthesis of Colloidal Gold. *Discuss. Faraday Soc.* **1951**, *11*, 55-75.
9. Frens, G., Controlled Nucleation for the Regulation of the Particle Size in Monodisperse Gold Suspensions. *Nature Physical Science* **1973**, *241*, 20-22.
10. Kumar, S.; Gandhi, K. S.; Kumar, R., Modeling of Formation of Gold Nanoparticles by Citrate Method. *Ind. Eng. Chem. Res.* **2007**, *46*, 3128-3136.
11. Bandyopadhyay, S.; Peralta-Videa, J. R.; Hernandez-Viezcas, J. A.; Montes, M. O.; Keller, A. A.; Gardea-Torresdey, J. L., Microscopic and Spectroscopic Methods Applied to the Measurements of Nanoparticles in the Environment. *Appl. Spectrosc. Rev.* **2012**, *47*, 180-206.
12. Khlebtsov, B. N.; Khlebtsov, N. G., On the Measurement of Gold Nanoparticle Sizes by the Dynamic Light Scattering Method. *Colloid J.* **2011**, *73*, 118-127.
13. Liu, F.-K., Sec Characterization of Au Nanoparticles Prepared through Seed-Assisted Synthesis. *Chromatographia* **2007**, *66*, 791-796.
14. Kanu, A. B.; Dwivedi, P.; Tam, M.; Matz, L.; Hill, H. H., Jr., Ion Mobility-Mass Spectrometry. *J. Mass Spectrom.* **2008**, *43*, 1-22.
15. Guha, S.; Li, M.; Tarlov, M. J.; Zachariah, M. R., Electrospray-Differential Mobility Analysis of Bionanoparticles. *Trends Biotechnol.* **2012**, *30*, 291-300.
16. Reschiglian, P.; Rambaldi, D. C.; Zattoni, A., Flow Field-Flow Fractionation with Multiangle Light Scattering Detection for the Analysis and Characterization of Functional Nanoparticles. *Anal. Bioanal. Chem.* **2011**, *399*, 197-203.
17. Zattoni, A.; Rambaldi, D. C.; Reschiglian, P.; Melucci, M.; Krol, S.; Garcia, A. M. C.; Sanz-Medel, A.; Roessner, D.; Johann, C., Asymmetrical Flow Field-Flow Fractionation with

- Multi-Angle Light Scattering Detection for the Analysis of Structured Nanoparticles. *J. Chromatogr., A* **2009**, 1216, 9106-9112.
18. Schmidt, B.; Loeschner, K.; Hadrup, N.; Mortensen, A.; Sloth, J. J.; Bender, K. C.; Larsen, E. H., Quantitative Characterization of Gold Nanoparticles by Field-Flow Fractionation Coupled Online with Light Scattering Detection and Inductively Coupled Plasma Mass Spectrometry. *Anal. Chem.* **2011**, 83, 2461-2468.
 19. Hagendorfer, H.; Kaegi, R.; Traber, J.; Mertens, S. F. L.; Scherrers, R.; Ludwig, C.; Ulrich, A., Application of an Asymmetric Flow Field Flow Fractionation Multi-Detector Approach for Metallic Engineered Nanoparticle Characterization - Prospects and Limitations Demonstrated on Au Nanoparticles. *Anal. Chim. Acta* **2011**, 706, 367-378.
 20. Harada, K.; Ohyama, Y.; Tabushi, T.; Kobayashi, A.; Fukusaki, E., Quantitative Analysis of Anionic Metabolites for Catharanthus Roseus by Capillary Electrophoresis Using Sulfonated Capillary Coupled with Electrospray Ionization-Tandem Mass Spectrometry. *J. Biosci. Bioeng.* **2008**, 105, 249-260.
 21. Koropchak, J. A.; Sadain, S.; Yang, X.; Magnusson, L.-E.; Heybroek, M.; Anisimov, M.; Kaufman, S. L., Nanoparticle Detection Technology for Chemical Analysis. *Anal. Chem.* **1999**, 71, 386A-394A.
 22. Allmaier, G.; Laschober, C.; Szymanski, W. W., Nano Es Gemma and Pdma, New Tools for the Analysis of Nanobioparticles-Protein Complexes, Lipoparticles, and Viruses. *J. Am. Soc. Mass Spectrom.* **2008**, 19, 1062-1068.
 23. Mueller, R.; Laschober, C.; Szymanski, W. W.; Allmaier, G., Determination of Molecular Weight, Particle Size, and Density of High Number Generation Pamam Dendrimers Using Maldi-Tof-Ms and Nes-Gemma. *Macromolecules (Washington, DC, U. S.)* **2007**, 40, 5599-5605.
 24. Doane, T. L.; Chuang, C.-H.; Hill, R. J.; Burda, C., Nanoparticle Z-Potentials. *Acc. Chem. Res.* **2012**, 45, 317-326.
 25. Pease, L. F., III; Tsai, D.-H.; Zangmeister, R. A.; Zachariah, M. R.; Tarlov, M. J., Quantifying the Surface Coverage of Conjugate Molecules on Functionalized Nanoparticles. *J. Phys. Chem. C* **2007**, 111, 17155-17157.
 26. Kaufman, S. L., Electrospray Diagnostics Performed by Using Sucrose and Proteins in the Gas-Phase Electrophoretic Mobility Molecular Analyzer (Gemma). *Anal. Chim. Acta* **2000**, 406, 3-10.
 27. Allmaier, G.; Maisser, A.; Laschober, C.; Messner, P.; Szymanski, W. W., Parallel Differential Mobility Analysis for Electrostatic Characterization and Manipulation of Nanoparticles and Viruses. *TrAC, Trends Anal. Chem.* **2011**, 30, 123-132.
 28. Gray, E. P.; Bruton, T. A.; Higgins, C. P.; Halden, R. U.; Westerhoff, P.; Ranville, J. F., Analysis of Gold Nanoparticle Mixtures: A Comparison of Hydrodynamic Chromatography (Hdc) and Asymmetrical Flow Field-Flow Fractionation (Af4) Coupled to Icp-Ms. *J. Anal. At. Spectrom.* **2012**, 27, 1532-1539.
 29. Hinterwirth, H.; Kappel, S.; Waitz, T.; Prohaska, T.; Lindner, W.; Lammerhofer, M., Quantifying Thiol Ligand Density of Self-Assembled Monolayers on Gold Nanoparticles by Inductively Coupled Plasma-Mass Spectrometry. *ACS Nano* **2013**, 7, 1129-1136.
 30. Hinterwirth, H.; Lindner, W.; Laemmerhofer, M., Bioconjugation of Trypsin onto Gold Nanoparticles: Effect of Surface Chemistry on Bioactivity. *Anal. Chim. Acta* **2012**, 733, 90-97.

A-2. Quantifying Thiol Ligand Density of Self-Assembled Monolayers on Gold Nanoparticles by Inductively Coupled Plasma-Mass Spectrometry.

Hinterwirth, H.; Kappel, S.; Waitz, T.; Prohaska, T.; Lindner, W.; Laemmerhofer, M.

ACS Nano **2013**, 7, 1129-1136

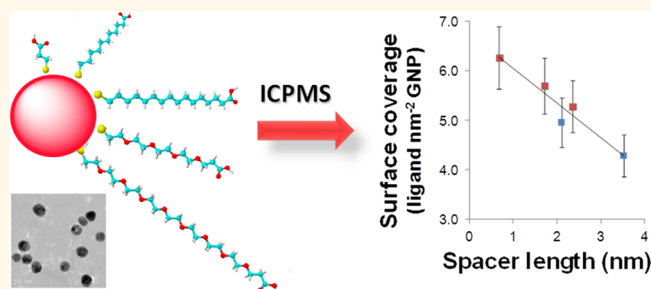
Quantifying Thiol Ligand Density of Self-Assembled Monolayers on Gold Nanoparticles by Inductively Coupled Plasma–Mass Spectrometry

Helmut Hinterwirth,[†] Stefanie Kappel,[‡] Thomas Waitz,[§] Thomas Prohaska,[‡] Wolfgang Lindner,[†] and Michael Lämmerhofer^{1,*}

[†]Department of Analytical Chemistry, University of Vienna, Währingerstrasse 38, 1090 Vienna, Austria, [‡]Department of Chemistry, Division of Analytical Chemistry–VIRIS Laboratory, University of Natural Resources and Life Sciences (BOKU–UFT), Vienna, Konrad-Lorenz-Straße 24, 3430 Tulln, Austria,

[§]Physics of Nanostructured Materials, Faculty of Physics, University of Vienna, Boltzmannngasse 5, 1090 Vienna, Austria, and ¹Institute of Pharmaceutical Sciences, University of Tübingen, Auf der Morgenstelle 8, 72076 Tübingen, Germany

ABSTRACT Gold nanoparticles (GNPs) are often used as colloidal carriers in numerous applications owing to their low-cost and size-controlled preparation as well as their straightforward surface functionalization with thiol containing molecules forming self-assembling monolayers (SAM). The quantification of the ligand density of such modified GNPs is technically challenging, yet of utmost importance for quality control in many applications. In this contribution, a new method for the determination of the surface coverage of GNPs with thiol containing ligands is proposed. It makes



use of the measurement of the gold-to-sulfur (Au/S) ratio by inductively coupled plasma mass spectrometry (ICP–MS) and its dependence on the nanoparticle diameter. The simultaneous ICP–MS measurement of gold and sulfur was carefully validated and found to be a robust method with a relative standard uncertainty of lower than 10%. A major advantage of this method is the independence from sample preparation; for example, sample loss during the washing steps is not affecting the results. To demonstrate the utility of the straightforward method, GNPs of different diameters were synthesized and derivatized on the surface with bifunctional (lipophilic) ω -mercapto-alkanoic acids and (hydrophilic) mercapto-poly(ethylene glycol) (PEG)_n-carboxylic acids, respectively, by self-assembling monolayer (SAM) formation. Thereby, a size-independent but ligand-chain length-dependent ligand density was found. The surface coverage increases from 4.3 to 6.3 molecules nm⁻² with a decrease of ligand chain length from 3.52 to 0.68 nm. Furthermore, no significant difference between the surface coverage of hydrophilic and lipophilic ligands with approximately the same ligand length was found, indicating that sterical hindrance is of more importance than, for example, intermolecular strand interactions of Van der Waals forces as claimed in other studies.

KEYWORDS: inductively coupled plasma mass spectrometry · transmission electron microscopy · surface coverage · self-assembling monolayer

Gold nanoparticles (GNPs) have become popular substrates in nanoscience and nanotechnology for a broad range of biomedical^{1–4} and bionanotechnology^{5,6} applications as well as for chemical, biological, and clinical diagnostic sensing.^{7–14} Besides their unique physical and chemical properties, also their size and size distribution play a key role for their functionality. Therefore, excellent control over properties like size, shape, chemical and colloidal stability, and in particular surface modification of GNPs is crucial in various

applications. Thus, tools for their qualitative and quantitative analysis are of extreme importance, not only for quality control in (mass) production but also for health and environmental risk assessment.^{15–20}

GNPs can be easily prepared by fast and straightforward size-controlled synthesis through the reduction of HAuCl₄. The most frequently utilized method introduced by Frens and Turkevich^{21,22} is based on the reduction and simultaneous stabilization with trisodium citrate. In this approach, the size of the nanoparticles can be finely controlled

* Address correspondence to michael.laemmerhofer@uni-tuebingen.de.

Received for review September 7, 2012 and accepted January 20, 2013.

Published online January 21, 2013
10.1021/nn306024a

© 2013 American Chemical Society

by the ratio of HAuCl_4 /reducing agent. Kumar *et al.* described a model for the formation of GNPs that depends on the correlation of citrate/gold ratio and GNP diameter.²³ In this study it is also reported that a stoichiometric ratio larger than 1.5 is needed for complete conversion of auric chloride.

Besides flexible size adjustment, the great popularity of GNPs originates also from their straightforward surface modification by formation of self-assembling monolayers (SAM) with thiol-containing bifunctional ligands.^{8,24–26} The bonding of functional ligands exploiting the strong dative bond of sulfur to gold atoms ($40\text{--}50\text{ kcal mol}^{-1}$ with a strength close to gold–gold bond^{27,28}) provides chemically stable functional nanoparticles. This flexible surface functionalization makes this approach technologically attractive.²⁹

For many applications, knowledge of the surface coverage of functionalized nanoparticles would be useful, but is seldom reported. Only few papers deal with this issue. X-ray crystallography and density functional theory (DFT) studies have been performed to derive theoretical considerations on the ligand density of thiolate-protected gold complexes ($\text{Au}_n(\text{SR})_m$) for small gold clusters with about 1 nm diameter in size ($\text{Au}_{10}\text{--}\text{Au}_{144}$).^{27,30,31} However, gold nanoclusters have due to their ultrasmall size fundamentally different unique properties compared to the larger crystalline GNPs in which the optical properties are dominated by plasmon excitation and possess a collective nature (as opposed to the single-electron transition in gold nanoclusters).³⁰

The full-coverage phase, by definition, corresponds to the highest possible packing of the molecules; that is, the surface is saturated. Early studies of the structure of alkanethiols on Au(111) with molecular-level resolution reported diffraction peaks representative of a $(\sqrt{3} \times \sqrt{3})\text{R}30^\circ$ structure relative to the underlying Au(111) substrate which corresponds to a molecule–molecule spacing of 5 Å and an area per molecule of 21.6 Å^2 (about $4.6\text{ molecules nm}^{-2}$).³² Up to now, experimental data on ligand densities, in particular of GNPs defined in the range of 10–100 nm are still rare.¹⁵ Elzey *et al.* reported an average size-independent ligand packing density of $7.8 \pm 1.2\text{ nm}^{-2}$ for 5–100 nm gold nanoparticles which were conjugated with 3-mercaptopropionic acid and analyzed by ICP–OES.³³ Packing densities of 4.97 ± 0.01 , 4.58 ± 0.01 , and $2.20 \pm 0.03\text{ ligand molecules nm}^{-2}$ were determined by use of X-ray photoelectron spectroscopy (XPS) for GNPs modified with mercaptoundecanoic acid, mercaptohexanoic acid, and thiocetic acid, respectively.³⁴ Techane *et al.* used XPS for the measurement of the carbon/Au atomic ratio of GNPs with carboxylic acid-terminated alkanethiol monolayers and their characterization dependent of both GNP diameter and alkyl chain length.³⁵ For a given surface the XPS carbon/Au atomic ratio increased with the chain length

owing to the increased number of carbon atoms per molecule. Furthermore, it was shown for a given chain length an increase of the XPS carbon/Au atomic ratio and an increase of the apparent SAM thickness with decrease of GNP size which they explained by the increased curvature of the smaller particles. Lanterna *et al.* determined the degree of surface functionalization based on the shifts of localized surface plasmon resonance spectroscopy (LSPR) as a function of the number of molecules added per nanoparticle.³⁶ They report a surface density of around $3\text{ molecules nm}^{-2}$ (ranging from 2 to $5\text{ molecules nm}^{-2}$) for sulfur heterocyclic compounds and described the coverage as almost size-independent. However, they postulated a greater packing density with an increase of the length of the lateral chain changing from 1.2 ± 0.4 to $3 \pm 1\text{ molecules nm}^{-2}$ for thiones with a ligand length of 1.2 and 2 nm, respectively. They explained this finding by enforced interstrand Van der Waals (VdW) interactions of ligands with longer chain length. Different labeling assays were explored by Xia *et al.* for quantifying the coverage density of $\text{HS-(PEG)}_n\text{-NH}_2$ ligands on the surface of gold nanostructures. By this indirect approach they found a decrease of coverage density with an increase of poly(ethylene glycol) (PEG) chain length. Coverage densities of 2.21, 1.33, and 0.21 per nm^2 with the ninhydrin-based assay and of 1.64, 0.85, and 0.14 per nm^2 with fluorescamine-based assay were determined for $\text{HS-PEG}_{3000}\text{-NH}_2$, $\text{HS-PEG}_{5000}\text{-NH}_2$, and $\text{HS-PEG}_{20000}\text{-NH}_2$, respectively.³⁷ Ratiometric surface-enhanced Raman spectroscopy with an isotope-encoded SERS reference was applied to determine the binding constant and packing density for mercaptobenzimidazole on GNPs *via* measurement of the amount of unbound ligand in the supernatant and fitting of the binding data to the Langmuir isotherm. Saturation capacities of $571 \pm 4.6\text{ pmol cm}^{-2}$ were obtained³⁸ which would be equivalent to about $3.4\text{ ligands per nm}^2$.

In this paper, we describe a new method for the quantification of the surface coverage of self-assembled thiol ligands bound onto GNPs. This approach is based on the linear correlation between the gold-to-sulfur ratio and the size of SAM-coated GNPs, whereby the ligand density can be calculated from its slope. This method is independent of the nanoparticle concentration, and thus, losses of GNPs during sample preparation, for example, due to adsorption on vessel walls or due to washing steps, will not influence the results. On the other hand, the method needs an accurate determination of the nanoparticle diameter which was analyzed by TEM. Gold nanoparticles with ligands differing in chain length and hydrophilicity/lipophilicity (Table 1) were analyzed by inductively coupled plasma mass spectrometry (ICP–MS). ICP–MS measurements for sulfur in the presence of gold were carefully validated by spiking and recovery experiments.

TABLE 1. Overview of Ligands Used for SAM Modification of GNPs and Their Properties

ligand	abbreviation	formula	MW	ligand length (nm) ^a	log <i>P</i> ^b
3-mercaptopropionic acid	MPA	HS-(CH ₂) ₂ -COOH	106.14	0.68	0.43 ± 0.26
11-mercaptoundecanoic acid	MUA	HS-(CH ₂) ₁₀ -COOH	218.36	1.71	3.93 ± 0.24
16-mercaptohexadecanoic acid	MHA	HS-(CH ₂) ₁₅ -COOH	287.49	2.35	6.58 ± 0.24
SH-PEG4-COOH	PEG ₄	HS-(CH ₂ CH ₂ O) ₄ CH ₂ CH ₂ -COOH	282.11	2.10	-0.66 ± 0.54
SH-PEG7-COOH	PEG ₇	HS-CH ₂ CH ₂ (OCH ₂ CH ₂) ₇ OCH ₂ CH ₂ -COOH	458.57	3.52	-2.09 ± 0.72

^a The molecular length was determined for a single molecule in vacuum with the most extended chain configuration. Conformations with minimal energy were obtained using the program package Gaussian 03. ^b The values for log *P* were calculated using ACD/Log *P* DB (ACD/Laboratories, 7.00 Release. Product version 7.07).

The application of ICP-MS for simultaneous measurement of sulfur and gold turned out to be a robust method with relative standard uncertainties lower than 10%.

ICP-MS was demonstrated to be a powerful technique in metal nanoparticle analysis. Along this line, it was recently employed for quantitative analysis of GNPs as well as for size, size distribution, and elemental characterization with and without prior dissolving with aqua regia.^{6,39–48} Also the successful hyphenation of chromatographic and electrophoretic techniques with ICP-MS has been realized for characterization of GNPs.^{49–53} A combination of laser desorption/ionization and ICP-MS has been recently utilized for the determination of GNP monolayer stability.⁵⁴ However, it has not been propagated for surface coverage analysis *via* simultaneous gold to sulfur ratio determination.

RESULTS AND DISCUSSION

Theoretical Calculations. If we assume a set of spherical GNPs saturated with a thiol ligand on the surface, the gold-to-sulfur ratio will depend directly proportionally on the volume-to-surface area ratio. Thus, with increase of diameter *D* the average number of gold atoms per GNP (*N*_{Au/GNP}) will increase with cube⁵⁵

$$N_{\text{Au/GNP}} = \frac{\pi \rho D^3}{6 M_{\text{Au}}} \quad (1)$$

while the number of sulfur atoms per GNP (*N*_{S/GNP}) will increase with square and proportionally with the maximal coverage factor *k*_{max} eq 2.

$$N_{\text{S/GNP}} = k\pi D^2 \quad (2)$$

Hence, by combining eqs 1 and 2 it follows that under the assumption of spherical and monodispersed nanoparticles as well as complete saturation of the surface with a monolayer of thiol ligands, the Au/S ratio should increase linearly with the diameter eq 3

$$\frac{N_{\text{Au/GNP}}}{N_{\text{S/GNP}}} = \frac{\pi \rho D^3}{6 M_{\text{Au}} k\pi D^2} = k_{\text{max}}^{-1} \times 9.83 \times D \quad (3)$$

wherein *D* is the average diameter of GNPs (in nm), ρ is the density for fcc gold (19.3 g cm⁻³) and *M*_{Au} is the atomic weight of gold (196.97 g mol⁻¹) (CAS7440-57-5). Since nanoparticles consist typically as more or less

TABLE 2. Calculation of Ligand Coverage As Obtained from the Slope of Au/S Ratios (Measured by ICP-MS) vs GNP Size. Given are the Coefficients (Slope and Intercept) of the Linear Regression Function with Standard Errors

ligand	slope	intercept	<i>R</i> ²	coverage (S nm ⁻²)
PEG ₇	2.32 ± 0.28	-2.3 ± 5.1	0.9595	4.29 ± 0.45
PEG ₄	2.00 ± 0.12	-0.3 ± 2.1	0.9903	4.96 ± 0.27
MHA	1.88 ± 0.08	-4.8 ± 1.5	0.9947	5.28 ± 0.21
MUA	1.74 ± 0.04	-0.1 ± 0.7	0.9985	5.70 ± 0.13
MPA	1.59 ± 0.17	-1.7 ± 3.1	0.9683	6.26 ± 0.59

narrow distributions rather than strictly monodisperse particles, Au/S ratios represent also narrow distributions but are experimentally measured as ensemble-averages.

Equation 3 allows the straightforward calculation of the maximum ligand density (i.e., the saturation capacity) *k*_{max} from the slope of plots of the Au/S ratio *versus* nanoparticle diameter assuming a constant and NP size-independent *k*_{max}. The validity of this assumption is supported by Supporting Information, Figure S2 which proves a linear dependency and thus a constant slope (statistical parameters see Table 2). If the ligand density would change with nanoparticle diameter, the slope would change with *D* as well, and this would be materialized by a nonlinear relationship. If the surface coverage for a given ligand is known, the amount of bound ligand per nanoparticle can be easily calculated.

This method has the benefit of being nanoparticle-concentration independent and thus, unaffected by loss of GNPs, for example, during sample preparation and washing steps. Gold and sulfur concentrations and their ratio can be determined simultaneously by ICP-MS and are obtained as ensemble-averages of the particle distributions.

Determination of GNP Diameters, Size Distributions, and Shapes. To establish the correlation of eq 3, GNPs of different sizes were synthesized according to the method by Frens and Turkevich.^{21,22} Thus, citrate-capped GNPs were prepared by size-controlled synthesis at variable citrate/HAuCl₄ (C/H) ratio between 2 and 6 and analyzed by TEM (Figure 1a).

As expected and reported previously, C/H ratios in the range of 2–6 yield nanoparticles with average sizes between 26.2 ± 4.4 nm and 13.2 ± 1.4 nm in diameter

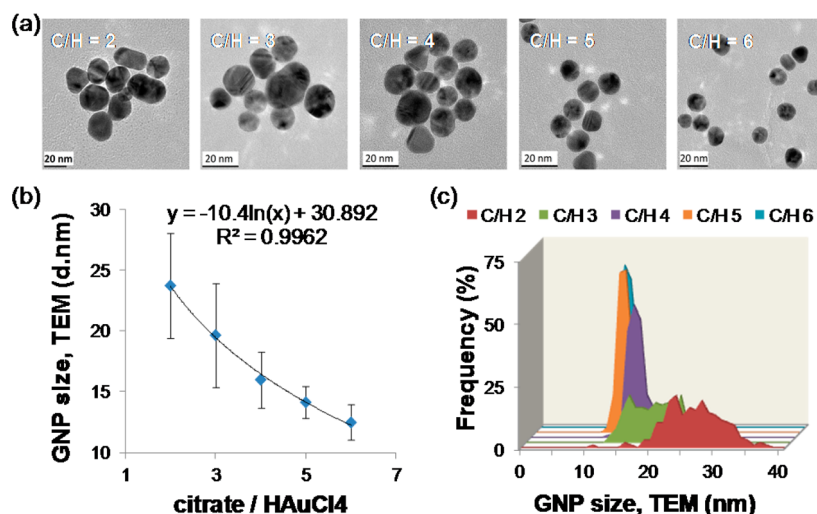


Figure 1. Size and particle size distribution analysis of citrate-capped GNPs by TEM: (a) TEM images of GNPs prepared by different ratios of citrate to HAuCl_4 (C/H) from 2 to 6, (b) dependency of GNP diameter on C/H ratio, and (c) polydispersity of GNPs as revealed by corresponding frequency distributions of particle sizes. The trend in panel b can be described by a logarithmic function.

(Figure 1b). GNPs from these batches were used for all further studies. A logarithmic relationship was found between the C/H ratio and the GNP size (Figure 1b), which can be readily utilized in a predictive manner for size-controlled synthesis. Statistical analysis of sufficiently large numbers of particles (>200) in each TEM measurement gives access to information on representative size distributions and morphology. Like in a previous study,³⁵ it turned out that larger nanoparticles show wider size distributions (Figure 1c) and less uniform spherical shape. Asymmetry factors defined as length-to-width proportion change from 1.21 ± 0.18 for the largest particles to less than 1.09 ± 0.09 for the small GNPs within the specified range of NP diameters.

In a subsequent step, the bifunctional ligands specified in Table 1 were immobilized on the surface of GNPs by formation of SAM coatings. To ensure complete saturation of the GNP surface a large excess of thiol (>10 fold) was used. Finally, the modified GNPs were washed several times to remove excess of unbound ligands.

Determination of Ligand Density. The determination of the ligand coverage *via* the gold-to-sulfur ratio is based on the fact that each ligand on the nanoparticle surface carries a single sulfur atom only while gold atoms constitute the voluminous particle core. Thus, gold increases with cube and sulfur with square of the particle diameter D , providing a simple linear relationship between the Au/S ratio and D .

For ICP–MS measurements of the Au/S ratio, 2% HCl (v/v) was used for dilution of the samples and preparation of standards. The measured signal intensities were normalized to ^{115}In as internal standard and blank corrected. A prior digestion step before introduction to ICP–MS was not necessary.⁴² Quantification was accomplished by external calibration. Furthermore,

spike recovery experiments were carried out to validate the sulfur measurement method and to make sure that the presence of gold will not affect the results. In accordance to the work of Jiang *et al.*⁴⁴ ICP–MS application for simultaneous measurement of gold and sulfur was found herein to be robust with relative standard uncertainties lower than 10% (for more information see Supporting Information).

The ratio of Au/S as determined by ICP–MS was plotted against the GNP size for the distinctly modified nanoparticles. In fact, for each of the particles linear dependencies as described by eq 3 were observed (see Figure S2 of Supporting Information). Thus, the ligand densities of the fully saturated GNP surfaces could be estimated from the slopes and are summarized in Table 2 along with corresponding data of the regression functions.

It can be seen that the denseness and saturation capacity, respectively, strongly depend on the ligand type (Figure 2a). With an increase of the spacer length, the ligand density dropped significantly from 6.3 molecules nm^{-2} for the short ligand MPA (spacer length = 0.68 nm) to 4.3 molecules nm^{-2} for the longer PEG₇ ligand (spacer length = 3.52 nm) (see Table 2).

This means that for short-chain ligand molecules slightly higher coverages can be achieved experimentally for GNPs as compared to small gold nanoclusters with $(\sqrt{3} \times \sqrt{3})\text{R}30^\circ$ structure on Au(111) modified with alkanethiols for which theoretical calculations predicted a maximal upper density limit of ~ 4.6 molecules nm^{-2} .^{26,56} The deviation can be explained by the occupancy of alternative binding sites (edges and corners). This trend of decreasing ligand density for longer-spaced ligands, on the other hand, is largely in agreement with experimentally determined data from Xia *et al.* for long HS-(PEG)_{*n*}-NH₂ chains.³⁷

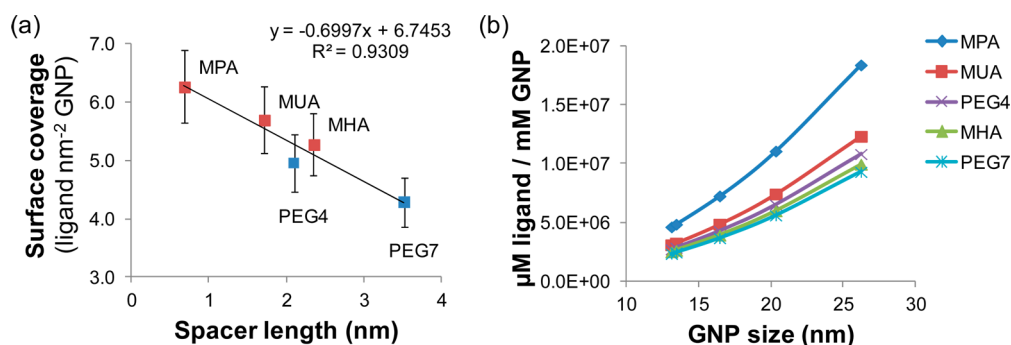


Figure 2. (a) Influence of ligand length on surface coverage (squares, red = mercapto-alkanoic acid, blue = mercapto-(PEG)_n-carboxylic acid). (b) Total number of ligands per GNP as calculated from the results of panel a and particle size for the different types of surface modifications.

However, it stands in contradiction to reports of *Lantern et al.* who measured a slight increase of ligand density with an increase of alkyl chain length of sulfur heterocyclic compounds.³⁶ This increase with ligand chain length was explained by enforced intermolecular VdW interactions between ligand strands. Stronger VdW interactions with increase of ligand chain-length have also been reported by *Techane et al.*³⁵ They studied the crystallinity of the SAMs of mercapto-alkanoic acids on flat gold by monitoring the positions of the CH stretching frequencies with FTIR-ATR analysis and described a well-ordered SAM of MHA also on 14 nm GNP. Our experiments revealed that GNPs modified with long chain ligands such as HS-PEG₇-COOH, HS-PEG₄-COOH, and MHA are more stable compared to the short-chain MPA-modified GNPs which could be due to interstrand VdW interactions in long-spaced analogues. Although interstrand VdW interactions may be a plausible reason for high surface coverages with longer alkyl chain ligands, our finding seems also to be reasonable. It may be postulated that steric hindrance has a significant impact on the maximally achievable saturation capacity. This hypothesis is supported by the fact that no significant difference in surface coverages between the lipophilic MHA and the hydrophilic PEG₄ ligands (log *P* values of 6.58 and −0.66; spacer lengths of 2.35 and 2.10 nm, respectively) was found (ligand density of 5.3 and 5.0 molecules per nm², respectively). Stronger VdW interactions and higher surface coverage would be expected for the former if interstrand VdW interactions were the determinant factor for saturation capacities which, however, is not the case. Explanations are on the one hand the increase of the tilt angle with an increase of alkyl chain-length,⁵⁷ but also gauche defects and entropic contributions will become increasingly important for longer chains;³² both contributing to the decreased coverage with an increase of ligand chain-length.

It is evident that the current ICP–MS methodology may be a valuable tool to quantify ligand densities on GNPs. With the maximal surface coverage in hand, one

TABLE 3. Instrumental Parameters for ICP–QMS (ELAN DRC-e)

RF power/W	1300
nebulizer gas flow/L min ^{−1}	0.94
auxiliary gas flow/L min ^{−1}	0.7
plasma gas flow/L min ^{−1}	15
DRC cell gas	O ₂
DRC cell gas flow rate (S, Au, In)/L min ^{−1}	0.65
<i>R</i> _{pq} value	
S	0.4
Au	0.45
In	0.4
<i>R</i> _{pa} value	
S	0
Au	0.047
In	0
lens voltage (V)	7.5
analogue stage voltage (V)	−2156
pulse stage voltage (V)	1200
detector	Dual
autolens	ON
isotopes monitored	³² S, ¹⁶ O, ³⁴ S, ¹⁵ O, ¹⁹⁷ Au, ¹¹⁵ In
scanning mode	peak hopping
sweeps (reading)	6
readings (replicate)	1
replicates	15
dwell time (ms)	50
integration time (ms)	300

can calculate the average number of ligands attached to the surface of GNPs (Figure 2b) and the actually available ligands per volume of GNP solution (see Supporting Information for a detailed discussion), which is the practically relevant figure in many applications.

CONCLUSIONS

We present a new method for determination of surface coverage of GNPs based on the linear relationship of the gold/sulfur (Au/S) ratio measured by ICP–MS, and the GNP size, measured by TEM. We found that the ligand density linearly dropped with increasing ligand chain length. The surface densities ranged between 6.3 molecules nm^{−2} for the short ligand MPA (spacer length = 0.68 nm) and 4.3 molecules nm^{−2} for the

longer PEG₇ ligand (spacer length = 3.52 nm). Thereby, no significant difference between lipophilic mercaptoalkanoic acid and hydrophilic mercapto-(PEG)₄-carboxylic spacer was observed. It is obvious that the presented

method should be equally useful for other metallic nanoparticles such as silver NPs, more so as the determination and analysis of silver nanoparticles with ICP–MS has already been described.^{58,59}

METHODS

Chemicals. Gold(III) chloride trihydrate (auric chloride, $\text{HAuCl}_4 \times 3\text{H}_2\text{O}$), trisodium citrate, 16-mercaptohexadecanoic acid (MHA), 11-mercaptoundecanoic acid (MUA), 3-mercaptopropionic acid (MPA), and *O*-(2-carboxyethyl)-*O'*-2-mercaptoethylheptaethylene glycol (PEG₇) were all obtained from Sigma-Aldrich (Vienna, Austria). Thiol-dPEG₄-acid (PEG₄) was obtained from Celares (Berlin, Germany). HNO_3 (p.a. grade) and the ICP–MS standards (CertiPUR) indium, gold, and sulfur were obtained from Merck KGaA (Darmstadt, Germany). Both, the purified water and the 65% (w/w) HNO_3 p.a. grade underwent one-step and two-step, respectively, sub-boiling in a distillation apparatus (MLS DuoPur, MLS, Leutkirch im Allgäu, Germany) for ICP–MS measurements.

Instruments and Methods. **TEM.** For the TEM analysis, GNPs were deposited on standard support films of amorphous carbon spanning Cu grids. The grids were immersed in the GNP suspension. When the grids were withdrawn, the solution evaporated leaving a high number density of GNPs (typically >100 GNPs μm^{-2}). The Cu grids were transferred to the microscope using a single tilt holder. TEM images were acquired with a Philips CM200 (acceleration voltage 200 kV, equipped with a CompuStage goniometer, a CCD Camera System (Gatan Orius SC600) and a carbon free vacuum system). The point resolution of the microscope is 0.26 nm; previous investigations clearly demonstrated the resolution of Au_{55} clusters (diameter of 1.4 nm) deposited on amorphous carbon films similar to the present study. The magnification at the CCD camera was calibrated using standard calibration line and cross grating replicas with 1200 and 2160 lines mm^{-1} for low and intermediate magnifications, respectively. High magnifications were calibrated using graphitized carbon. This calibration was directly justified by obtaining lattice fringe images of the GNPs that showed a fringe spacing deviating by less than 2% from the spacing of (111) lattice planes. For statistical evaluation 200 particles were analyzed for each sample. Their diameter was determined by the average of length and width as estimation for a spherical model (i.e., by $(l_m + w_m)/2$, where l_m and w_m denote the arithmetic mean of the length and width, respectively).

Inductively Coupled Plasma–Quadrupole Mass Spectrometry. The analyses were accomplished with inductively coupled plasma–quadrupole mass spectrometry (ICP–QMS, ICP–MS) instrument (ELAN DRC-e, PerkinElmer, Waltham, Massachusetts, USA) operated in dynamic reaction cell (DRC) operation mode using O_2 as DRC cell gas. S is measured as $^{32}\text{S}^{16}\text{O}$ and/or $^{34}\text{S}^{16}\text{O}$, which enables riddance of the oxygen interference present in the standard operation mode measuring at masses 32 and 34. ^{197}Au and ^{115}In were also measured in DRC mode in order to circumvent a switching between modes.

The DRC cell gas flow rate and the R_{pq} values were optimized prior to the analysis by means of ICP standard solutions of Au (i.e., 10 ng g^{-1}) and S (i.e., 100 ng g^{-1}). Indium was used as the internal normalization standard added to all analyzed solutions with a final In concentration of 1 ng g^{-1} . HCl (2% v/v) was recorded as a blank solution prior to analysis of each individual sample in order to monitor memory effects.

Preliminary studies of GNP samples yielded Au concentrations that were up to 60 times higher than the respective S concentrations (i.e., 83–150 ng g^{-1}). Thus, the R_{pa} value was additionally optimized for Au measurements in order to decrease the Au signal and to avoid overloading of the secondary electron multiplier detector operated in dual mode when measuring S and Au simultaneously in the same solution. The Au signal reaching the detector was reduced to approximately 0.1% of the original signal by applying a R_{pa} value of 0.047. It was shown already by Jiang *et al.* in a validated method that the

presence of Au even in high concentrations has a negligible effect on the intensity of $^{32}\text{S}^{16}\text{O}$ under DRC mode.⁴⁴ Operating parameters are given in (Table 3).

All used flasks, test-tubes, and pipet tips were cleaned prior to usage according to a three-step purification procedure: (1) 24 h in a 10% (v/v) HNO_3 bath; (2) 24 h in a 1% (v/v) HNO_3 bath, and (3) rinsing with deionized water. The items were double seal-bagged using polyethylene bags.

Dilutions of samples and standard solutions were performed with 2% (v/v) HCl. HCl (2% v/v) was prepared by diluting 37% (m/m) HCl (p.a. grade, Merck KGaA, Darmstadt, Germany) with reagent grade type I water (18.2 M Ω cm at 25 °C, Purelab Classic, Veolia Water Systems Austria GmbH, Vienna, Austria). Both, the reagent grade type I water and the 37% (m/m) HCl were additionally purified by sub-boiling distillation (Saville Corporation, Eden Prairie, MN, USA, and MLS DuoPur, MLS, Leutkirch im Allgäu, Germany) before use.

The measured signal intensities were normalized to the observed ^{115}In intensity. Blank correction was performed by subtraction of the normalized blank intensity from the normalized signal intensities of the samples and the standard solutions. As 2% (v/v) HCl was recorded as blank solution prior to analysis of each individual sample, each individual sample was blank corrected with its respective blank. The ^{197}Au , $^{32}\text{S}^{16}\text{O}$ and $^{34}\text{S}^{16}\text{O}$ concentrations (in ng g^{-1}), respectively, were computed by using the $y = kx + d$ relationships of the linear regressions resulting from the external calibrations. Afterward, the concentrations of ^{197}Au , $^{32}\text{S}^{16}\text{O}$, and $^{34}\text{S}^{16}\text{O}$ in mol g^{-1} were calculated by using the atomic weight of Au (196.97 g mol^{-1}) and S (32.06 g mol^{-1}), respectively. Finally, the $^{197}\text{Au}/^{32}\text{S}^{16}\text{O}$ ratios were determined by dividing the ^{197}Au and $^{32}\text{S}^{16}\text{O}$ concentrations expressed in mol g^{-1} .

Ligand Length Calculations. The molecular length of each ligand was determined for a single molecule in vacuum with the most extended chain configuration. Conformations with minimal energy were obtained using the program package Gaussian 03; log P values were calculated using ACD/log P DB (ACD/Laboratories, 7.00 Release. Product version 7.07).

Size Controlled Preparation of Citrate-Stabilized GNPs. Gold nanoparticles with different sizes were prepared according to the method described previously.⁶⁰ In brief, 50 mL of gold(III) chloride trihydrate solution in bidistilled water (final concentration 1.14 mM) was heated in a clean Erlenmeyer flask under stirring until boiling. All glassware and stirrer were cleaned before use with aqua regia, acetone, and bidistilled water. Under further heating, 5 mL of trisodium citrate (concentration varied depending on the final citrate/ HAuCl_4 (C/H) ratio in solution; C/H > 2 for complete conversion of HAuCl_4 ²³) was added and afterward the color changed to brown and red. All chemicals were prepared freshly before use.

Self-Assembling of Thiol Containing Ligands. GNPs were derivatized by the self-assembly of bifunctional thiol containing reagents yielding a carboxylic functionalized surface. Therefore, 100 μL of 7 mM mercapto-alkanoic acid and mercapto-(PEG)_{*n*}-carboxylic acid, respectively, were added to 1 mL of GNP solution and stirred overnight at ambient temperature. An overview about the ligands employed is given in Table 1. The modified nanoparticles were washed 4 \times by centrifugation (13400 rpm, 20 min, MiniSpin, Eppendorf) and resuspended in sub-boiled water.

Conflict of Interest: The authors declare no competing financial interest.

Acknowledgment. Financial support of the “Nano-MALDI” project by the Austrian BMVIT via the “Austrian Nano-Initiative” and “MNT-ERA.NET” is gratefully acknowledged. S.K. and T.P.

acknowledge the financial support of the FWF (START FWF267N11). We are grateful to Michal Kohout for DFT calculations.

Supporting Information Available: Additional tables and figures as described in the text. This material is available free of charge via the Internet at <http://pubs.acs.org>.

REFERENCES AND NOTES

- Dykman, L.; Khlebtsov, N. Gold Nanoparticles in Biomedical Applications: Recent Advances and Perspectives. *Chem. Soc. Rev.* **2012**, *41*, 2256–2282.
- Dreaden, E. C.; Alkilany, A. M.; Huang, X.; Murphy, C. J.; El-Sayed, M. A. The Golden Age: Gold Nanoparticles for Biomedicine. *Chem. Soc. Rev.* **2012**, *41*, 2740–79.
- Jiang, X.-M.; Wang, L.-M.; Wang, J.; Chen, C.-Y. Gold Nanomaterials: Preparation, Chemical Modification, Biomedical Applications and Potential Risk Assessment. *Appl. Biochem. Biotechnol.* **2012**, *166*, 1533–1551.
- Pilolli, R.; Palmisano, F.; Cioffi, N. Gold Nanomaterials as a New Tool for Bioanalytical Applications of Laser Desorption Ionization Mass Spectrometry. *Anal. Bioanal. Chem.* **2012**, *402*, 601–623.
- Yeh, Y.-C.; Creran, B.; Rotello, V. M. Gold Nanoparticles: Preparation, Properties, and Applications in Bionanotechnology. *Nanoscale* **2012**, *4*, 1871–1880.
- Scheffer, A.; Engelhard, C.; Sperling, M.; Buscher, W. ICP–MS as a New Tool for the Determination of Gold Nanoparticles in Bioanalytical Applications. *Anal. Bioanal. Chem.* **2008**, *390*, 249–252.
- Jans, H.; Huo, Q. Gold Nanoparticle-Enabled Biological and Chemical Detection and Analysis. *Chem. Soc. Rev.* **2012**, *41*, 2849–2866.
- Rana, S.; Bajaj, A.; Mout, R.; Rotello, V. M. Monolayer-Coated Gold Nanoparticles for Delivery Applications. *Adv. Drug Delivery Rev.* **2012**, *64*, 200–216.
- Lu, F.; Doane, T. L.; Zhu, J.-J.; Burda, C. Gold Nanoparticles for Diagnostic Sensing and Therapy. *Inorg. Chim. Acta* **2012**, *393*, 142–153.
- Larguinho, M.; Baptista, P. V. Gold and Silver Nanoparticles for Clinical Diagnostics—From Genomics to Proteomics. *J. Proteom.* **2012**, *75*, 2811–2823.
- Azzazy, H. M. E.; Mansour, M. M. H.; Samir, T. M.; Franco, R. Gold Nanoparticles in the Clinical Laboratory: Principles of Preparation and Applications. *Clin. Chem. Lab. Med.* **2012**, *50*, 193–209.
- Bedford, E. E.; Spadavecchia, J.; Pradier, C.-M.; Gu, F. X. Surface Plasmon Resonance Biosensors Incorporating Gold Nanoparticles. *Macromol. Biosci.* **2012**, *12*, 724–739.
- Saha, K.; Agasti, S. S.; Kim, C.; Li, X.; Rotello, V. M. Gold Nanoparticles in Chemical and Biological Sensing. *Chem. Rev.* **2012**, *112*, 2739–2779.
- Tokonami, S.; Yamamoto, Y.; Shiigi, H.; Nagaoka, T. Synthesis and Bioanalytical Applications of Specific-Shaped Metallic Nanostructures: A Review. *Anal. Chim. Acta* **2012**, *716*, 76–91.
- European Commission, On the Definition of Nanomaterial (L275). *Off. J. Eur. Union* **2011**, *54*, 38–40.
- Yu, L.; Andriola, A. Quantitative Gold Nanoparticle Analysis Methods: A Review. *Talanta* **2010**, *82*, 869–875.
- Lapresta-Fernandez, A.; Fernandez, A.; Blasco, J. Nanotoxicity Effects of Engineered Silver and Gold Nanoparticles in Aquatic Organisms. *Trend Anal. Chem.* **2012**, *32*, 40–59.
- Johnston, H. J.; Hutchison, G.; Christensen, F. M.; Peters, S.; Hankin, S.; Stone, V. A Review of the *in Vivo* and *in Vitro* Toxicity of Silver and Gold Particulates: Particle Attributes and Biological Mechanisms Responsible for the Observed Toxicity. *Crit. Rev. Toxicol.* **2010**, *40*, 328–346.
- Mueller, R.; Laschober, C.; Szymanski, W. W.; Allmaier, G. Determination of Molecular Weight, Particle Size, and Density of High Number Generation PAMAM Dendrimers Using MALDI-TOF-MS and nES-GEMMA. *Macromolecules* **2007**, *40*, 5599–5605.
- Harkness, K. M.; Cliffliff, D. E.; McLean, J. A. Characterization of Thiolate-Protected Gold Nanoparticles by Mass Spectrometry. *Analyst* **2010**, *135*, 868–874.
- Turkevich, J.; Stevenson, P. C.; Hillier, J. The Nucleation and Growth Processes in the Synthesis of Colloidal Gold. *Faraday Discuss. Chem. Soc.* **1951**, No. 11, 55–75.
- Frens, G. Controlled Nucleation for the Regulation of the Particle Size in Monodisperse Gold Suspensions. *Nat. Phys. Sci.* **1973**, *241*, 20–22.
- Kumar, S.; Gandhi, K. S.; Kumar, R. Modeling of Formation of Gold Nanoparticles by Citrate Method. *Ind. Eng. Chem. Res.* **2007**, *46*, 3128–3136.
- Jadhav, S. A. Functional Self-Assembled Monolayers (SAMs) of Organic Compounds on Gold Nanoparticles. *J. Mater. Chem.* **2012**, *22*, 5894–5899.
- Pieters, G.; Prins, L. J. Catalytic Self-Assembled Monolayers on Gold Nanoparticles. *New J. Chem.* **2012**, *36*, 1931–1939.
- Love, J. C.; Estroff, L. A.; Kriebel, J. K.; Nuzzo, R. G.; Whitesides, G. M. Self-Assembled Monolayers of Thiolates on Metals as a Form of Nanotechnology. *Chem. Rev.* **2005**, *105*, 1103–1169.
- Hakkinen, H. The Gold-Sulfur Interface at the Nanoscale. *Nat. Chem.* **2012**, *4*, 443–55.
- Pensa, E.; Cortes, E.; Corthey, G.; Carro, P.; Vericat, C.; Fonticelli, M. H.; Benitez, G.; Rubert, A. A.; Salvarezza, R. C. The Chemistry of the Sulfur-Gold Interface: In Search of a Unified Model. *Acc. Chem. Res.* **2012**, *45*, 1183–1192.
- Ulman, A. Formation and Structure of Self-Assembled Monolayers. *Chem. Rev.* **1996**, *96*, 1533–1554.
- Jin, R. Quantum Sized, Thiolate-Protected Gold Nanoclusters. *Nanoscale* **2010**, *2*, 343–362.
- Parker, J. F.; Fields-Zinna, C. A.; Murray, R. W. The Story of a Monodisperse Gold Nanoparticle: Au25L18. *Acc. Chem. Res.* **2010**, *43*, 1289–1296.
- Schreiber, F. Structure and Growth of Self-Assembling Monolayers. *Prog. Surf. Sci.* **2000**, *65*, 151–256.
- Elzey, S.; Tsai, D.-H.; Rabb, S. A.; Yu, L. L.; Winchester, M. R.; Hackley, V. A. Quantification of Ligand Packing Density on Gold Nanoparticles Using ICP–OES. *Anal. Bioanal. Chem.* **2012**, *403*, 145–149.
- Ivanov, M. R.; Haes, A. J. Anionic Functionalized Gold Nanoparticle Continuous Full Filling Separations: Importance of Sample Concentration. *Anal. Chem.* **2012**, *84*, 1320–1326.
- Techane, S. D.; Gamble, L. J.; Castner, D. G. Multitechnique Characterization of Self-Assembled Carboxylic Acid-Terminated Alkanethiol Monolayers on Nanoparticle and Flat Gold Surfaces. *J. Phys. Chem. C* **2011**, *115*, 9432–9441.
- Lanterna, A. E.; Coronado, E. A.; Granados, A. M. When Nanoparticle Size and Molecular Geometry Matter: Analyzing the Degree of Surface Functionalization of Gold Nanoparticles with Sulfur Heterocyclic Compounds. *J. Phys. Chem. C* **2012**, *116*, 6520–6529.
- Xia, X.; Yang, M.; Wang, Y.; Zheng, Y.; Li, Q.; Chen, J.; Xia, Y. Quantifying the Coverage Density of Poly(ethylene glycol) Chains on the Surface of Gold Nanostructures. *ACS Nano* **2012**, *6*, 512–522.
- Zhang, D.; Ansar, S. M. Ratiometric Surface-Enhanced Raman Quantification of Ligand Adsorption onto a Gold Nanoparticle. *Anal. Chem.* **2010**, *82*, 5910–5914.
- Helfrich, A.; Bruechert, W.; Bettmer, J. Size Characterisation of Au Nanoparticles by ICP–MS Coupling Techniques. *J. Anal. Atom. Spectrom.* **2006**, *21*, 431–434.
- Hu, S.; Liu, R.; Zhang, S.; Huang, Z.; Xing, Z.; Zhang, X. A New Strategy for Highly Sensitive Immunoassay Based on Single-Particle Mode Detection by Inductively Coupled Plasma Mass Spectrometry. *J. Am. Soc. Mass Spectrom.* **2009**, *20*, 1096–1103.
- Gillespie, A.; Jao, D.; Andriola, A.; Duda, T.; Yang, C. F.; Yu, L. Gold Nanoparticle Determination by Inductively Coupled Plasma–Mass Spectrometry, Anodic Stripping Voltammetry, and Flame Atomic Absorption Spectrophotometry. *Anal. Lett.* **2012**, *45*, 1310–1320.
- Allabashi, R.; Stach, W.; Escosura-Muniz, A.; Liste-Calleja, L.; Merkoci, A. ICP–MS: A Powerful Technique for Quantitative Determination of Gold Nanoparticles without Previous Dissolving. *J. Nanopart. Res.* **2009**, *11*, 2003–2011.

43. De Jong, W. H.; Hagens, W. I.; Krystek, P.; Burger, M. C.; Sips, A. J. A. M.; Geertsma, R. E. Particle Size-Dependent Organ Distribution of Gold Nanoparticles after Intravenous Administration. *Biomaterials* **2008**, *29*, 1912–1919.
44. Jiang, W.; Hibbert, D. B.; Moran, G.; Akter, R. Measurement of Gold and Sulfur Mass Fractions in L-Cysteine-Modified Gold Nanoparticles by ICP–DRC–MS after Acid Digestion: Validation and Uncertainty of Results. *J. Anal. Atom. Spectrom.* **2012**, *27*, 1465–1473.
45. Kapellios, E. A.; Pergantis, S. A. Size and Elemental Composition of Nanoparticles Using Ion Mobility Spectrometry with Inductively Coupled Plasma Mass Spectrometry. *J. Anal. Atom. Spectrom.* **2012**, *27*, 21–24.
46. Pace, H. E.; Rogers, N. J.; Jarolimek, C.; Coleman, V. A.; Higgins, C. P.; Ranville, J. F. Determining Transport Efficiency for the Purpose of Counting and Sizing Nanoparticles via Single Particle Inductively Coupled Plasma Mass Spectrometry. *Anal. Chem.* **2011**, *83*, 9361–9369.
47. Tiede, K.; Boxall, A. B. A.; Tiede, D.; Tear, S. P.; David, H.; Lewis, J. A Robust Size-Characterization Methodology for Studying Nanoparticle Behaviour in Real Environmental Samples, Using Hydrodynamic Chromatography Coupled to ICP–MS. *J. Anal. Atom. Spectrom.* **2009**, *24*, 964–972.
48. Degueldre, C.; Favarger, P. Y.; Wold, S. Gold Colloid Analysis by Inductively Coupled Plasma–Mass Spectrometry in a Single Particle Mode. *Anal. Chim. Acta* **2006**, *555*, 263–268.
49. Hagendorfer, H.; Kaegi, R.; Traber, J.; Mertens, S. F. L.; Scherrers, R.; Ludwig, C.; Ulrich, A. Application of an Asymmetric Flow Field Flow Fractionation Multi-detector Approach for Metallic Engineered Nanoparticle Characterization—Prospects and Limitations Demonstrated on Au Nanoparticles. *Anal. Chim. Acta* **2011**, *706*, 367–378.
50. Helfrich, A.; Bettmer, J. Analysis of Gold Nanoparticles Using ICP–MS-Based Hyphenated and Complementary ESI-MS Techniques. *Int. J. Mass Spectrom.* **2011**, *307*, 92–98.
51. Schmidt, B.; Loeschner, K.; Hadrup, N.; Mortensen, A.; Sloth, J. J.; Bender, K. C.; Larsen, E. H. Quantitative Characterization of Gold Nanoparticles by Field-Flow Fractionation Coupled Online with Light Scattering Detection and Inductively Coupled Plasma Mass Spectrometry. *Anal. Chem.* **2011**, *83*, 2461–2468.
52. Haider, S. R.; Sharp, B. L.; Reid, H. J. On-Line Coupling of Gel Electrophoresis and Inductively Coupled Plasma–Mass Spectrometry. *Trend. Anal. Chem.* **2011**, *30*, 1793–1808.
53. Gray, E. P.; Bruton, T. A.; Higgins, C. P.; Halden, R. U.; Westerhoff, P.; Ranville, J. F. Analysis of Gold Nanoparticle Mixtures: A Comparison of Hydrodynamic Chromatography (HDC) and Asymmetrical Flow Field-Flow Fractionation (AF4) Coupled to ICP–MS. *J. Anal. Atom. Spectrom.* **2012**, *27*, 1532–1539.
54. Zhu, Z.-J.; Tang, R.; Yeh, Y.-C.; Miranda, O. R.; Rotello, V. M.; Vachet, R. W. Determination of the Intracellular Stability of Gold Nanoparticle Monolayers Using Mass Spectrometry. *Anal. Chem.* **2012**, *84*, 4321–4326.
55. Liu, X.; Atwater, M.; Wang, J.; Huo, Q. Extinction Coefficient of Gold Nanoparticles with Different Sizes and Different Capping Ligands. *Colloid Surface, B* **2007**, *58*, 3–7.
56. Hostetler, M. J.; Wingate, J. E.; Zhong, C.-J.; Harris, J. E.; Vachet, R. W.; Clark, M. R.; Londono, J. D.; Green, S. J.; Stokes, J. J.; Wignall, G. D.; *et al.* Alkanethiolate Gold Cluster Molecules with Core Diameters from 1.4 to 5.2 Nanometers: Core and Monolayer Properties as a Function of Core Size. *Langmuir* **1998**, *14*, 17–30.
57. Ramin, L.; Jabbarzadeh, A. Odd-Even Effects on the Structure, Stability, and Phase Transition of Alkanethiol Self-Assembled Monolayers. *Langmuir* **2011**, *27*, 9748–9759.
58. Tuoriniemi, J.; Cornelis, G.; Hasseløev, M. Size Discrimination and Detection Capabilities of Single-Particle ICP–MS for Environmental Analysis of Silver Nanoparticles. *Anal. Chem.* **2012**, *84*, 3965–3972.
59. Franze, B.; Streng, I.; Engelhard, C. Single Particle Inductively Coupled Plasma Mass Spectrometry: Evaluation of Three Different Pneumatic and Piezo-Based Sample Introduction Systems for the Characterization of Silver Nanoparticles. *J. Anal. Atom. Spectrom.* **2012**, *27*, 1074–1083.
60. Hinterwirth, H.; Lindner, W.; Laemmerhofer, M. Bioconjugation of Trypsin onto Gold Nanoparticles: Effect of Surface Chemistry on Bioactivity. *Anal. Chim. Acta* **2012**, *733*, 90–97.

A-2.1 **Supplementary Information**

Hinterwirth, H.; Kappel, S.; Waitz, T.; Prohaska, T.; Lindner, W.; Laemmerhofer, M.

ACS Nano **2013**, 7, 1129-1136

1 **Supporting Information**

2
3 **Quantifying Thiol Ligand Density of Self-assembled Monolayers on Gold**
4 **Nanoparticles by Inductively Coupled Plasma Mass Spectrometry**

5
6 *Helmut Hinterwirth*¹, *Stefanie Kappel*², *Thomas Waitz*³, *Thomas Prohaska*²,
7 *Wolfgang Lindner*¹, *Michael Lämmerhofer*^{4, *}

8
9 ¹ Department of Analytical Chemistry, University of Vienna, Währingerstrasse 38,
10 1090 Vienna, Austria

11 ² University of Natural Resources and Life Sciences (BOKU-UFT), Vienna,
12 Department of Chemistry, Division of Analytical Chemistry-VIRIS Laboratory, Konrad-
13 Lorenz-Straße 24, 3430 Tulln, Austria

14 ³ Physics of Nanostructured Materials, Faculty of Physics, University of Vienna,
15 Boltzmannngasse 5, 1090 Vienna, Austria

16 ⁴ Institute of Pharmaceutical Sciences, University of Tübingen, Auf der Morgenstelle
17 8, 72076 Tübingen, Germany

18
19 *** Corresponding Author**

20 Prof. Dr. Michael Lämmerhofer
21 Pharmaceutical Analysis and Bioanalysis
22 Institute of Pharmaceutical Sciences
23 University of Tübingen
24 Auf der Morgenstelle 8
25 72076 Tübingen, Germany
26 T +49 7071 29 78793, F +49 7071 29 4565
27 E-mail: michael.laemmerhofer@uni-tuebingen.de

1. ICPMS MEASUREMENTS

1.1. DETERMINATION OF MATRIX OF CHOICE FOR ICPMS

MEASUREMENTS

For preliminary investigations and method optimization GNPs of different sizes were diluted 1:10 using H₂O, 2% (v/v) HCl and 2% (v/v) HNO₃, respectively. All solutions were purified before use by sub-boiling distillation. Aim of the preceding study was to investigate the influence of different matrices on the analysis results, evaluated by means of the measurement precision. The precisions of the measured intensities of the analytes of interest are given in Table S1. It can be seen that measurements performed in a 2% (v/v) HCl matrix yielded better precisions for the measured intensities compared to other GNP matrix solutions (*i.e.* H₂O and HNO₃). Thus, 2% (v/v) HCl was the matrix of choice for the subsequent GNP analyses.

Table S1: Precision of measured intensities for GNPs of different sizes coated with 16-mercaptohexadecanoic acid (MHA)

Sample	Matrix	Measured intensity RSD / %			
		³² S ¹⁶ O	³⁴ S ¹⁶ O	¹⁹⁷ Au	¹¹⁵ In
GNP (10 nm)	H ₂ O	2.4	3.2	1.6	7.5
	2 % (v/v) HNO ₃	4	4.2	2.8	2
	2 % (v/v) HCl	2.2	4.2	2	0.8
GNP (25 nm)	H ₂ O	3.9	3.2	4.4	7.1
	2 % (v/v) HNO ₃	10.9	8.7	12.4	7.3
	2 % (v/v) HCl	2.1	3.3	1.9	1
GNP (50 nm)	H ₂ O	6	5.1	3.3	10.2
	2 % (v/v) HNO ₃	4.1	3.5	3.1	1.1
	2 % (v/v) HCl	3.2	5.1	2.2	1.1

In a next step, the influence of prior dissolving of Au in aqua regia compared to dilution with 2% (v/v) HCl as matrix before GNP analysis on the ¹⁹⁷Au / ³²S¹⁶O ratio was examined. Thereby, no significant difference between the two matrices could be

observed with both between 7-10% RSU (k=2) (data not shown). This is also in good accordance with Allabashi et al. (*J.Nanopart.Res.* 2009, 11, 2003-2011), who observed that a preliminary digestion of GNP colloid solutions with aqua regia is not always necessary.

1.2.Uncertainty calculation

Expanded (k=2) total combined standard uncertainties (U_c) were calculated according to ISO/GUM (ISO/IEC Guide 98-3, 2008) and EURACHEM (EURACHEM/CITAC Guide CG 4) guidelines. The single parameters propagated for computing the expanded total combined standard uncertainties of the Au/S measurements are given in Table S2.

Table S2: Propagated parameters for computing the expanded total combined standard uncertainties

Propagated parameter
Slope (k) of linear regression - S
Slope (k) of linear regression - Au
Intercept (d) of linear regression - S
Intercept (d) of linear regression - Au
Intensity (I) of S
Intensity (I) of Au
Intensity (I) of In

65

The model equation used for calculation of U_c is given in eq. S1.

67

$$(eq\ S1) \frac{Au}{S} = \frac{\left(\frac{\left(\frac{I_{Sample(Au)}}{I_{Sample(In)}} - \frac{I_{Blank(Au)}}{I_{Blank(In)}} \right) - d_{Au}}{k_{Au}} \right) \times 10^{-9}}{196.97} \bigg/ \frac{\left(\frac{\left(\frac{I_{Sample(S)}}{I_{Sample(In)}} - \frac{I_{Blank(S)}}{I_{Blank(In)}} \right) - d_{Au}}{k_S} \right) \times 10^{-9}}{32.06}$$

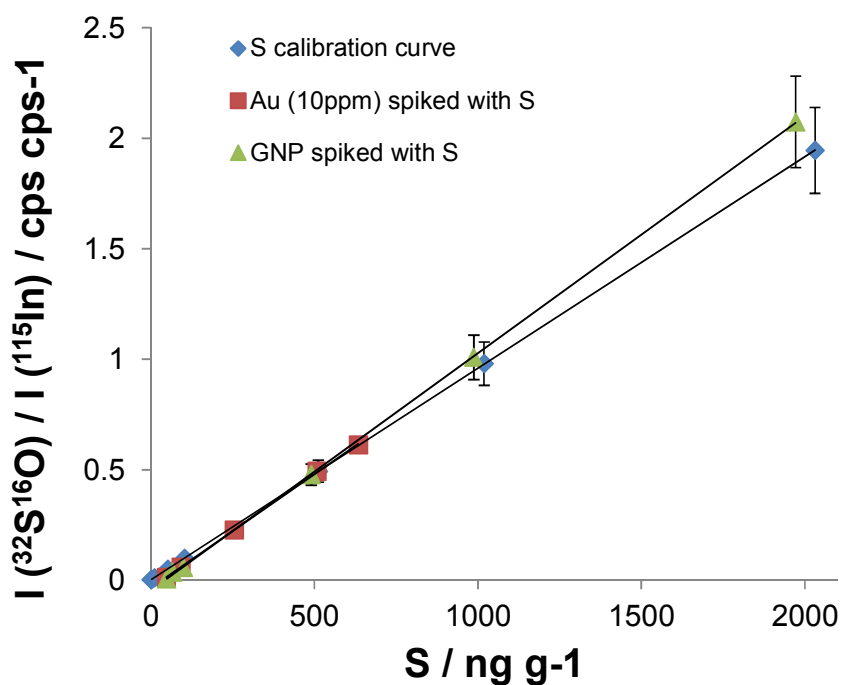
68

69

70 1.3. Spiking recovery experiments

71 Au standards (10 ppm) as well as citrate stabilized GNP solutions were spiked with S
72 standards to evaluate the influence of the presence of Au on sulfur measurements.

73 Within the working range of sulfur measurements no detrimental effect of gold on the
74 recovery measurements of sulfur was found and also in the high concentration area of sulfur
75 concentrations the recovery is still within RSU of 10%.



76

77 **Figure S1:** Validation of recovery of sulfur in presence of gold.

2. DETERMINATION OF LIGAND DENSITY

Figure S2 shows the dependencies of the Au/S ratio on the GNP size for the distinct nanoparticle types, *i.e.* GNPs modified with different ligands. The corresponding linear regression data for each type of particles are given in Table 2 of the main document.

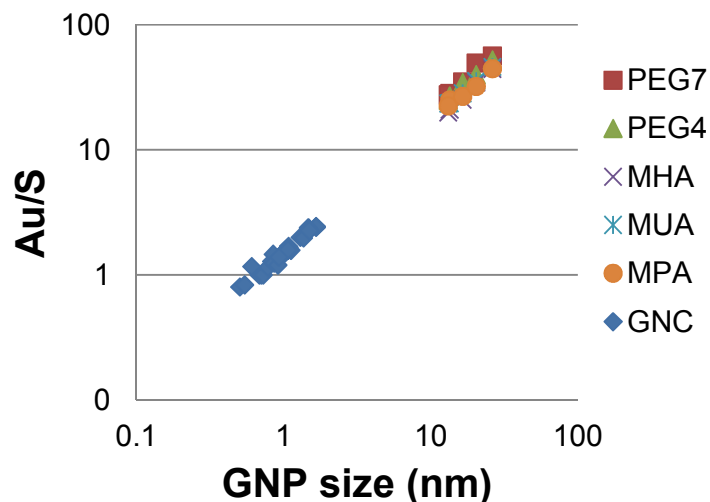


Figure S2: Plot of Au/S ratio as determined by ICPMS measurement vs. GNP size and comparison to data from literature for gold nanoclusters (GNC) measured by X-ray crystallography and density functional theory (DFT) studies.

3. CALCULATIONS OF LIGANDS BOUND PER GNP

Besides surface coverage, also the totally available surface and the concentration of GNPs must be known for the calculation of the totally available ligand concentration bound onto GNPs. Along this line, the concentration of GNPs can be calculated applying the following consideration. The number of nanoparticles N_{GNP} in solution arise from the ratio of the initial Au(III) atoms $N_{Au(III)}$ (*e.g.* for this study 55 mL of 1.14 mM HAuCl₄ final concentration were used) to the number of gold atoms per GNP $N_{Au/GNP}$. At a citrate/HAuCl₄ ratio > 1.5 the conversion of Au(III) to colloidal gold is quantitative and hence it follows (eq.S2)

$$(eq.S2) \quad N_{GNP} = \frac{N_{Au(III)}}{N_{Au/GNP}} = \frac{1.14E-03M \times 0.055L \times N_A}{\frac{\pi \rho D^3}{6 M_{Au}}} = 1.22E18D^{-3}$$

The molar concentration of nanoparticles c_{GNP} in solution can be calculated by

(eq.S3)

$$(eq.S3) \quad c_{GNP} = \frac{N_{GNP}}{VN_A} = 3.69E-05D^{-3}$$

wherein N_A is Avogadro's constant and V the volume of the solution.

In practice, the totally available ligand concentration c_L per colloidal NP suspension c_{GNP} but not the ligand density itself is of practical experimental relevance in many applications of functionalized GNPs (e.g. in adsorption studies). It can be calculated for the different GNP sizes and ligand lengths taking into account the determined surface coverages for individual modified GNPs and the GNP concentrations in solutions. Complete conversion of Au(III) which has been proven for C/H ratios > 1.5 and no loss of thiol ligand after washing is assumed. The results are summarized in Table S3. It can be seen that the molar ligand concentration drops by a factor of about 2 when a PEG₇-spacer is used instead of a -(CH₂)₃-spacer such as in MPA modified GNPs. On the other hand, the ligand concentration is by a factor of 4 decreased when 13 nm particle size is exchanged for 26 nm particle diameter. This clearly emphasizes the overall benefit of smaller nanoparticles in adsorption based applications.

Table S3: Calculated ligand concentrations for GNPs of different sizes prepared by variation of the citrate/HAuCl₄ (C/H) ratio. Values were calculated for initial HAuCl₄ concentration of 1.14 mM and volume of 55 mL.

C / H	GNP Size, (TEM, nm)	MW (GNP)	c, GNP (mM)	Surface / GNP (nm ²)	surface area (m ² ml ⁻¹)	MPA	MUA	MHA	PEG4	PEG7
2	26.2	1.10E+08	2.0E-06	2164	2.66E-03	1.84E+07	1.23E+07	9.95E+06	1.08E+07	9.30E+06
3	20.4	5.14E+07	4.4E-06	1303	3.43E-03	1.11E+07	7.42E+06	5.99E+06	6.51E+06	5.60E+06
4	16.5	2.73E+07	8.2E-06	854	4.23E-03	7.26E+06	4.87E+06	3.93E+06	4.27E+06	3.67E+06
5	13.2	1.39E+07	1.6E-05	544	5.30E-03	4.63E+06	3.10E+06	2.50E+06	2.72E+06	2.34E+06
6	13.5	1.49E+07	1.5E-05	571	5.18E-03	4.86E+06	3.26E+06	2.63E+06	2.86E+06	2.46E+06

4. UV/VIS SPECTRA OF GNPS

Citrate stabilized GNPs were characterized by measuring their surface plasmon resonance (SPR) spectra. The corresponding spectra are shown in Figure S3.

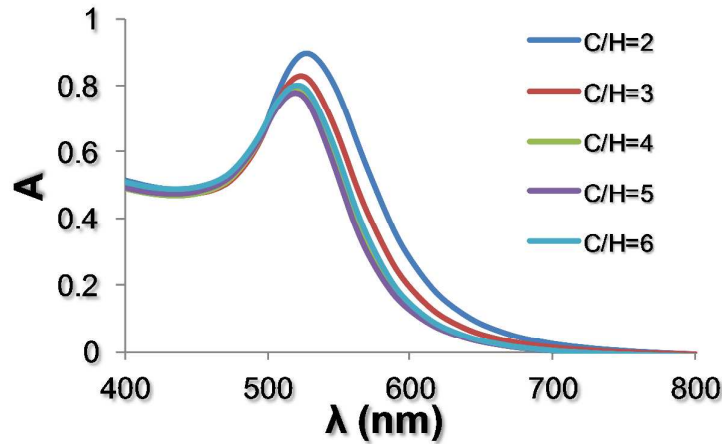


Figure S3: SPR spectra of citrate stabilized GNPs

A-3. Bioconjugation of trypsin onto gold nanoparticles: Effect of surface chemistry on bioactivity.

Hinterwirth, H.; Lindner, W.; Laemmerhofer, M.

Analytica Chimica Acta **2012**, 733, 90-97



Bioconjugation of trypsin onto gold nanoparticles: Effect of surface chemistry on bioactivity

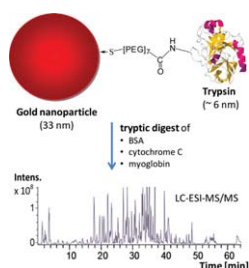
Helmut Hinterwirth, Wolfgang Lindner, Michael Lämmerhofer*

Department of Analytical Chemistry, University of Vienna, Währingerstrasse 38, 1090 Vienna, Austria

HIGHLIGHTS

- Size and spacer affect bioactivity of nanoparticulate trypsin reactor.
- Increase of GNP's size increases activity of bound trypsin.
- Increase of spacer length increases amount and activity of immobilized enzyme by factor 6.
- Decrease of digestion time up to less than 1 h when trypsin immobilized onto GNPs.
- Reduced auto-digestion compared to trypsin in-solution.

GRAPHICAL ABSTRACT



ARTICLE INFO

Article history:

Received 7 February 2012

Received in revised form 19 April 2012

Accepted 24 April 2012

Available online 8 May 2012

Keywords:

Enzyme immobilization
Self-assembling monolayer
Enzyme activity
Protein digestion
Auto-digestion
Mass spectrometry

ABSTRACT

The systematic study of activity, long-time stability and auto-digestion of trypsin immobilized onto gold nanoparticles (GNPs) is described in this paper and compared to trypsin in-solution. Thereby, the influence of GNP's size and immobilization chemistry by various linkers differing in lipophilicity/hydrophilicity and spacer lengths was investigated with regard to the bioactivity of the conjugated enzyme. GNPs with different sizes were prepared by reduction and simultaneous stabilization with trisodium citrate and characterized by UV/vis spectra, dynamic light scattering (DLS), ζ -potential measurements and transmission electron microscopy (TEM). GNPs were derivatized by self-assembling of bifunctional thiol reagents on the nanoparticle (NP) surface via dative thiol-gold bond yielding a carboxylic acid functionalized surface. Trypsin was either attached directly via hydrophobic and ionic interactions onto the citrate stabilized GNPs or immobilized via EDC/NHS bioconjugation onto the carboxylic functionalized GNPs, respectively. The amount of bound trypsin was quantified by measuring the absorbance at 280 nm. The activity of bound enzyme and its Michaelis Menten kinetic parameter K_m and v_{max} were measured by the standard chromogenic substrate N_α -Benzoyl-DL-arginine 4-nitroanilide hydrochloride (BAPNA). Finally, digestion of a standard protein mixture with the trypsin-conjugated NPs followed by analysis with LC-ESI-MS and successful MASCOT search demonstrated the applicability of the new heterogenous nano-structured biocatalyst. It could be shown that the amount of immobilized trypsin and its activity can be increased by a factor of 6 using a long hydrophilic spacer with simultaneous reduced auto-digestion and reduced digestion time. The applicability of the new trypsin bioreactor was proven by digestion of casein and identification of α - as well as κ -casein by subsequent MASCOT search.

© 2012 Elsevier B.V. All rights reserved.

Abbreviations: GNP, gold nanoparticle; GNP-trypsin, GNP immobilized trypsin; DLS, dynamic light scattering; TEM, transmission electron microscopy; SPR, surface plasmon resonance; PEG, polyethylene glycol; MHA, 16-mercaptohexadecanoic acid; EDC, N-(3-dimethylaminopropyl)-N'-ethylcarbodiimide hydrochloride; NHS, N-hydroxysuccinimide; BAPNA, N_α -benzoyl-DL-arginine 4-nitroanilide hydrochloride; ZP, zeta potential.

* Corresponding author at: Pharmaceutical Analysis and Bioanalysis, Institute of Pharmaceutical Sciences, University of Tübingen, Auf der Morgenstelle 8, 72076 Tübingen, Germany. Tel.: +43 1 4277 52323/+49 7071 29 78793; fax: +49 7071 29 4565.

E-mail address: michael.laemmerhofer@uni-tuebingen.de (M. Lämmerhofer).

1. Introduction

Trypsin (E.C.3.4.21.4) is a serine protease commonly used in proteomics for digestion of proteins. However, drawbacks are long digestion times (up to 24 h), auto-digestion sub-products and poor enzyme-to-substrate ratio limiting high-throughput protein identification [1]. To overcome the main problems of in-solution digestion different approaches of enzyme immobilization strategies were developed to increase the enzyme-to-substrate ratio and thus, to reduce the digestion time by higher turn-over rate as well as to reduce the auto-digestion and thus, to increase the long-time stability of the enzyme. On-line and off-line approaches of enzyme reactors to increase the enzyme efficiency comprise co-polymerization in polymer matrices (sol-gel enzyme encapsulation) [2], immobilization onto monoliths [3–5], lab-on-a-chip platforms [6] as well as open tubular enzyme reactors [7] and immobilization onto micro- and nanobeads.

Breakthroughs in nanotechnology enforced the development of nanostructures for enzyme stabilization [8] and regulation of enzyme activity [9]. Thereby, pore size and volume, charge interactions, hydrophobic interactions and multiple attachments, surface chemistry and immobilization strategy are crucial points for engineering enzyme reactors on beads with regard to enzyme longevity and efficiency. Magnetic [10], silica coated magnetic [11], chitosan [12], and gold nanoparticles are the most common nanobeads for enzyme attachment and immobilization. In our study, we focused on the immobilization strategy of trypsin onto gold nanoparticles with regard to the influence of surface chemistry on enzyme stability and activity.

Gold nanoparticles (GNPs) in the range of 1–100 nm are used in a broad application field in chemistry, physics, medicine, pharmacy and biology [13]. They have been utilized for biosensors [14,15], for determination of ions (heavy metal cations and anions) [16] and small molecules [17], for DNA detection and peptide/protein analysis [18], and enrichment [19,20], for enzymatic activity assay [21,22] and cellular analysis [13] as well as in separation sciences [23,24] and in sample preparation [25]. In general, nanotechnology is getting more and more important in natural sciences.

GNPs can be easily prepared with low-cost by reduction of gold(III) chloride. The most common synthesis is established by Turkevich–Frens [26,27] by reduction and simultaneous stabilizing with citrate. Thereby, the size of the particles can be controlled by the molar ratio of gold(III)/reducing agent. Insights in the mechanisms of GNPs formation is given by Ojea-Jimenez et al. [28], Polte et al. [29] and Kumar et al. [30]. The size controlled synthesis generates nanoparticles with spherical-like appearance having unique physical, chemical and optical properties and large surface-to-volume ratio.

Additional advantages of GNPs compared to other nanoparticle materials is the surface plasmon resonance (SPR) band of GNPs at about 520 nm often utilized in chemical sensing and imaging. Furthermore, the size and concentration of GNPs can be determined from UV/vis and extinction spectra [31–34]. However, shifts of SPR maxima and shape changes of SPR curves are not only caused by particle size but also by formation of aggregates and/or adsorption of modifying molecules [24]. Thus, the UV/vis spectra provide a fast and easy control mechanism. Next to photometric assay, the size can be determined by microscopic techniques (TEM, SEM, AFM etc.), dynamic light scattering (DLS) [35], field flow fractionation and size exclusion chromatography [36]. Moreover, the zeta potential (ZP) of the nanoparticles is a measure for the stability of the colloidal GNP solution. The stability of a colloidal solution is described by the DLVO theory in the 1940s named after the scientists Deryagin, Landau, Verwey and Overbeek [37,38]. They suggest that the stability depends on the total potential energy function as a balance of attractive and repulsive forces (i.e. of van der Waals

attraction and electrostatic repulsion) as well as of the potential energy due to solvational effects.

GNPs are also attractive because of their straightforward modification for sake of their functionalization, but also stabilization [39]. Functional groups can be introduced onto GNPs by dative binding and self-assembling of bifunctional ligands with terminal thiol groups and/or by ligand exchange with thiol containing molecules in a second step [40]. Biomolecules like proteins, enzymes and antibodies can either be attached directly to GNPs via ionic and hydrophobic interactions or by immobilization via linkers. The successful direct binding of trypsin onto GNPs is described by IR and Moessbauer spectroscopy measurements [41]. The attachment of trypsin was controlled by shift of absorbance maximum from 528 nm to 540 nm and change in shape of the UV/vis spectra with a slightly enhancement of the activity bound onto GNPs by 12% compared to in-solution [42]. The tryptic digest of GNP attached trypsin and analysis by micellar electrokinetic chromatography describes a change in enzyme specificity which was explained by change in conformation of attached enzyme [43]. The immobilization chemistry of trypsin onto gold nano-rods modified with a copolymer containing sulfonate and maleic acid groups via “click” chemistry, EDC coupling or electrostatic adsorption was compared by Gole and Murphy [44]. Polymer coating of nanoparticles is often used for stabilization and prevent aggregation of GNPs and/or entrapping of enzymes e.g. for on-line proteolysis [45].

Promising advantages of GNP-conjugated biomolecules for specific recognition (enzyme–substrate, antibody–antigen, biotin–avidin etc.) are the increased concentration on the surface (high surface/volume ratio) resulting in higher recognition efficiency, the visualization due to SPR band, the ability of removal and/or extraction from solution by centrifugation and in case of the proteolytic enzyme trypsin the reduced auto-digestion compared to enzyme in-solution digestion.

In this paper, we describe the effect of the bioconjugation chemistry of biomolecules on GNPs, in particular GNP size, surface chemistry and influence of linker and spacer length on their functionality (i.e. bioactivity). Thereby, trypsin was used as standard enzyme to control the amount of bound protein as well as the enzyme activity in dependence of the chemistry. The principle of the bioconjugation chemistry of trypsin onto GNPs used in our study is shown in Fig. 1.

2. Materials and methods

2.1. Materials and instruments

2.1.1. Chemicals

Trypsin (from hog pancreas, E.C.3.4.21.4, foreign activities: chymotrypsin $\leq 0.2\%$, 13,644 U mg⁻¹), cytochrome C (CYC.horse, from horse heart, E.C. 232-700-9, purity 97% based on water content of 5%, MW 12,384 Da), myoglobin (MYG.horse, from horse skeletal muscle, E.C. 309-705-0, 95–100%), casein, N_α-benzoyl-DL-arginine 4-nitroanilide hydrochloride (BAPNA), tris(2-carboxyethyl)phosphine hydrochloride (TCEP), urea, gold(III) chloride trihydrate, trisodium citrate, 16-mercaptohexadecanoic acid (MHA), 11-mercaptoundecanoic acid, 3-mercaptopropionic acid, O-(2-carboxyethyl)-O'-(2-mercaptoethyl)heptaethylene glycol, N-(3-dimethylaminopropyl)-N'-ethylcarbodiimide hydrochloride (EDC), N-hydroxysuccinimide (NHS) and formic acid were all obtained from Sigma–Aldrich (Vienna, Austria). Thiol-dPEG₄TM-acid was obtained from Celares (Berlin, Germany), the bovine serum albumin (BSA, ~99%, E.C. 232-936-2, protease free, essentially γ -globulin free) from SAFC (supplied by Sigma–Aldrich, Vienna, Austria) and ammonia and sodium bicarbonate from Merck KGaA (supplied by VWR, Vienna, Austria).

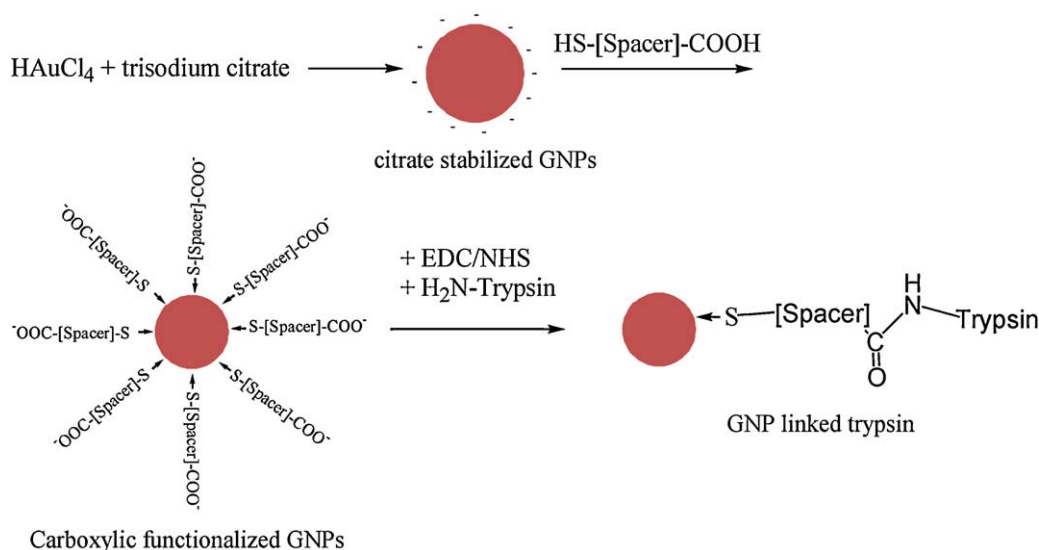


Fig. 1. Size controlled synthesis of citrate stabilized GNPs by variation of the ratio of HAuCl_4 and the reducing agent citrate followed by dative binding and self-assembling of thiol containing bifunctional linker with defined length leading to carboxylic acid functionalized GNPs. Finally, trypsin was immobilized by EDC/NHS as coupling agents linking carboxylic acid and amino groups.

2.1.2. Instruments

HPLC–ESI–MS experiments were performed on an Agilent 1100 series LC/MSD ion-trap (IT) system (Waldbronn, Germany). The HPLC system was equipped with a binary gradient pump, autosampler, vacuum degasser and a temperature-controlled column compartment (Agilent, Waldbronn, Germany). The mobile phase flow rate was 0.4 mL min^{-1} and the column temperature was set to 25°C . The injection volume was $20 \mu\text{L}$.

The size and the zeta potential of the gold nanoparticles were studied with Malvern Zetasizer Instruments Nano series (Prager Instruments). The UV/vis spectra were taken by Specord50 photometer (Analytik Jena). TEM images were acquired with PHILIPS CM200 (Acceleration voltage 200 kV , EDAX Energy-dispersive X-ray microanalysis), equipped with CompuStage goniometer, CCD Camera System (Gatan Orius SC600), cooling holder and heating holder for in situ experiments, straining holder, and carbon free vacuum system.

2.2. Experimental

2.2.1. Preparation of citrate stabilized gold nanoparticles

Gold nanoparticles with different sizes were prepared according to the method of Turkevich and Frens [26,27]. In brief, 20 mL 1.28 mM gold(III) chloride trihydrate in bidistilled water were heated in a clean Erlenmeyer flask under stirring until boiling. All glassware and stirrer were cleaned before use with aqua regia, acetone and bidistilled water. Under further heating, 2.5 mL trisodium citrate (final concentration was between 20.5 mM and 71.8 mM , depending on the desired size of the nanoparticles) were added while the color changes to brown and red. The GNPs were characterized by UV/vis spectra, DLS, ζ -potential and TEM.

2.2.2. Surface chemistry and immobilization of trypsin onto GNPs

For surface functionalization of GNPs with carboxylic acid moieties, $625 \mu\text{L}$ 3.5 mM mercapto-alkanoic acid (spacer length = 4, 12, 17 atoms between thiol and carboxylic acid groups) and $2 \mu\text{L}$ mercapto-(PEG) $_n$ -carboxylic acid ($n = 4, 7$; spacer length = 16, 28), respectively, were added to 5 mL GNP solution and stirred overnight at ambient temperature. An overview about the spacers is given in Table 1. After centrifugation and washing with bidistilled water, the carboxylic acid groups were reacted for 2 h with $625 \mu\text{L}$

12 mM EDC and 60 mM NHS. EDC is an activation reagent for carboxylic acids forming an active ester intermediate. The coupling efficiency with amine nucleophiles can be increased by the formation of an NHS ester intermediate [46]. For removal of the excess of unreacted reagents, the GNPs were centrifuged and washed $3 \times$ with 50 mM ammonium bicarbonate buffer, $\text{pH } 8.5$. Trypsin ($625 \mu\text{L}$ of 1 mg mL^{-1}) was immobilized via its amino groups to the NHS ester intermediate. After stirring overnight, the unbound enzyme was removed by centrifugation and washing with buffer.

2.2.3. Determination of the amount of immobilized trypsin

The concentration of GNP immobilized trypsin was determined after several centrifugation and washing steps by the mass difference of trypsin in the supernatant and the used amount. The concentration in the supernatant was determined by Bradford assay as well as by measuring the absorbance at 280 nm . Quantitation was performed via calibration function and back calculation for the immobilized trypsin by the mass difference of reacted/unreacted enzyme.

2.2.4. Determination of immobilized trypsin activity and of its Michaelis Menten kinetic parameter

The immobilized trypsin activity was measured by the standard chromogenic substrate BApNA (Fig. 2). Trypsin cleaves p-nitroaniline (pNA) which can be measured at an absorbance of

Table 1
Overview of spacers used for immobilization of trypsin and their spacer lengths.

Spacer	Formula	Spacer length ^a
Direct binding via ionic interactions	–	0
Mercaptoacetic acid	HSCH_2COOH	3
3-Mercaptopropionic acid	$\text{HS}(\text{CH}_2)_2\text{COOH}$	4
11-Mercaptoundecanoic acid	$\text{HS}(\text{CH}_2)_{10}\text{COOH}$	12
16-Mercaptohexadecanoic acid (MHA)	$\text{HS}(\text{CH}_2)_{15}\text{COOH}$	17
PEG4	$\text{HS}(\text{CH}_2\text{CH}_2\text{O})_4\text{CH}_2\text{CH}_2\text{COOH}$	16
PEG7	$\text{HSCH}_2\text{CH}_2(\text{OCH}_2\text{CH}_2)_7\text{OCH}_2\text{CH}_2\text{COOH}$	28

^a Spacer length defined by the number of atoms in the chain including sulfur and carbon of terminal carboxylic acid group.

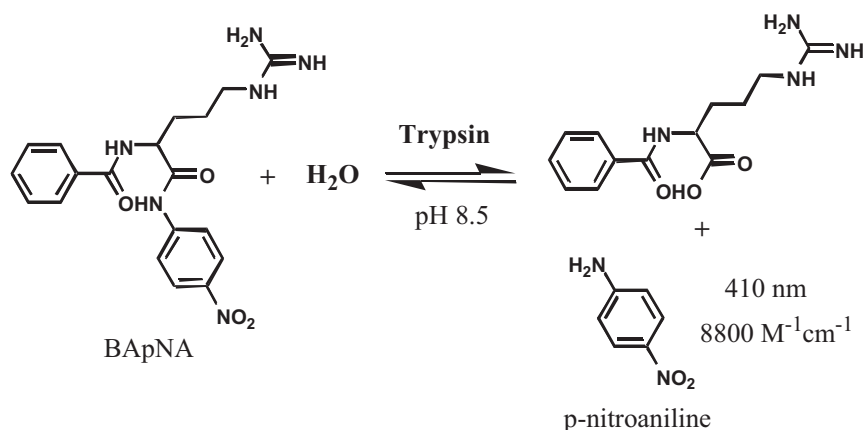


Fig. 2. Cleavage of the substrate BApNA by trypsin. The activity of the enzyme can be measured by the released p-nitroaniline (pNA) with an extinction coefficient of 8800 M⁻¹ cm⁻¹ at an absorbance wavelength of 410 nm.

410 nm. The Michaelis Menten parameter K_m and v_{max} were calculated by 5–7 different concentrations of the substrate BApNA plotted in a Lineweaver–Burk diagram.

2.2.5. Digestion of proteins with trypsin-conjugated GNPs

A mixture of three standard proteins comprising bovine serum albumin (BSA), cytochrome C (CYC) and myoglobin (MYG) (100 μ L, 1 mg mL⁻¹ each) was first denaturated with 10 μ L 80 mM urea and 10 μ L 50 mM TCEP to unfold the proteins and cleave their disulfide bridges by heating up to 60 °C for 30 min. After cooling down to room temperature, the free thiol groups of the proteins were blocked with 10 μ L 150 mM iodoacetamide by reaction in the dark for 30 min.

For protein digestion, trypsin-conjugated GNPs were first concentrated by a factor of 10 by centrifugation of 1 mL of the colloidal solution and resuspension of the centrifuged GNPs in 100 μ L 50 mM ammonium bicarbonate buffer, pH 8.5 (the concentration of GNPs in the solution was calculated in the magnitude of 1–10 nM for a size of 30 nm). Reaction mixtures with trypsin-conjugated GNPs and for comparison also with trypsin in-solution were prepared with different enzyme:protein ratios (1:2 to 1:300) and stopped after various digestion times (5 min to 19 h). These digestions were repeated at several days with the same batches. The digestion was accomplished at 37 °C under slight shaking and finally stopped by adding formic acid (final concentration 1%). Trypsin-conjugated GNPs were removed by centrifugation and the supernatant was filtered by RC Membrane (0.2 μ m 4 mm Syringe Filter) before injection into the LC–ESI–IT–MS.

Finally, with the optimized bioconjugation and digestion protocol the milk protein casein was digested with GNP-PEG7-Trypsin for 1 h to prove applicability of the new bioreactor for other samples.

2.2.6. LC–ESI–MS method

The trypsin digested proteins were separated by HPLC (Agilent 1100 series) hyphenated with ion-trap MS (MSD Trap from Agilent) via electrospray ionization interface using a Phenomenex core-shell particle column (Kinetex 2.6 μ m C18 100 Å, 100 mm \times 3.0 mm) and a KrudKatcher Ultra HPLC in-line filter (0.5 μ m depth filter \times 0.004 in ID) [47]. The mobile phase consisted of Millipore water containing 0.1% formic acid (A) and acetonitrile containing 0.1% formic acid (B). The following gradient was run: 0–5 min: 5% B, 5–60 min: 5–60% B, 60–65 min: 60–95% B, 65–70 min: 95% B, 70–72 min: 95–5% B, 72–90 min: 5% B. The flow rate was 0.4 mL min⁻¹ and the injection of 20 μ L of the sample was performed with needle wash. The scan range in the positive mode

was from 50 to 2200 m/z with a scan resolution of 13,000 m/z s⁻¹ and a maximal accuracy time of 300 ms.

For data analysis, Bruker DataAnalysis Analysis.yep files were converted into the .mgf (Mascot generic file) format using the tool LC/MSD Trap Software 4.2 (DataAnalysis version 2.2). MASCOT MS/MS Ions Search was used for identification of proteins against SwissProt 2011.08 (531,473 sequences; 188,463,640 residues) database. Search parameters were as follows: taxonomy = mammalia, fixed modification = carbamidomethyl cysteine, variable modifications = oxidation (HW and M), proteolytic enzyme = semi-trypsin, maximum number of missed cleavages = 9, peptide tolerance = \pm 1.2 Da, MS/MS tolerance = \pm 0.6 Da.

3. Results and discussion

3.1. Preparation and characterization of GNPs

Size-controlled GNPs were prepared according to Turkevich–Frens method by reduction of HAuCl₄ with trisodium citrate [26,27]. GNPs were characterized by UV/vis spectrometry, DLS, zeta potential and TEM measurement (see (Fig. 3)). Three different specimens of GNPs differing in size were prepared by variation of the molar citrate/HAuCl₄ ratio (2:1, 5:1 and 7:1).

Both, TEM and DLS measurements were in good agreement with the sizes reported in the literature [31]. According to TEM, the average particle diameter changes from 26.7 (\pm 5.2) nm to 15.0 (\pm 1.7) nm to 16.3 (\pm 3.2) nm when the molar ratio of citrate/HAuCl₄ was changed from 2:1, to 5:1 and 7:1, respectively (Fig. 3). The corresponding data for DLS and ZP (NPs were washed before measurement by centrifugation and re-suspending in bidistilled water) range from 29.9 \pm 5.7 nm (DLS = 33.0 \pm 4.2 nm, ZP = -31.6 \pm 2.3 mV) to 15.0 \pm 1.7 nm (22.0 \pm 2.1 nm, -37.6 \pm 3.2 mV) and 16.3 \pm 3.2 nm (18 \pm 0.9 nm, -43.2 \pm 2.8 mV). More details can be found along with the corresponding UV/vis spectra for the distinct particles in the Supplementary Data.

3.2. Immobilization chemistry and its influence on trypsin activity

For further functionalization various reactive bifunctional linkers with terminal thiol and carboxylic acid moieties and distinct lipophilic or hydrophilic spacers varying also in length (see Table 1) were self-assembled via dative thiol-gold bond onto the surface of the GNPs (see Fig. 1).

The effect of the concentration of ligand per mL GNP solution (GNP size of 65 nm in diameter and a calculated concentration of 0.134 nM) with regard to stability of the colloidal solution and

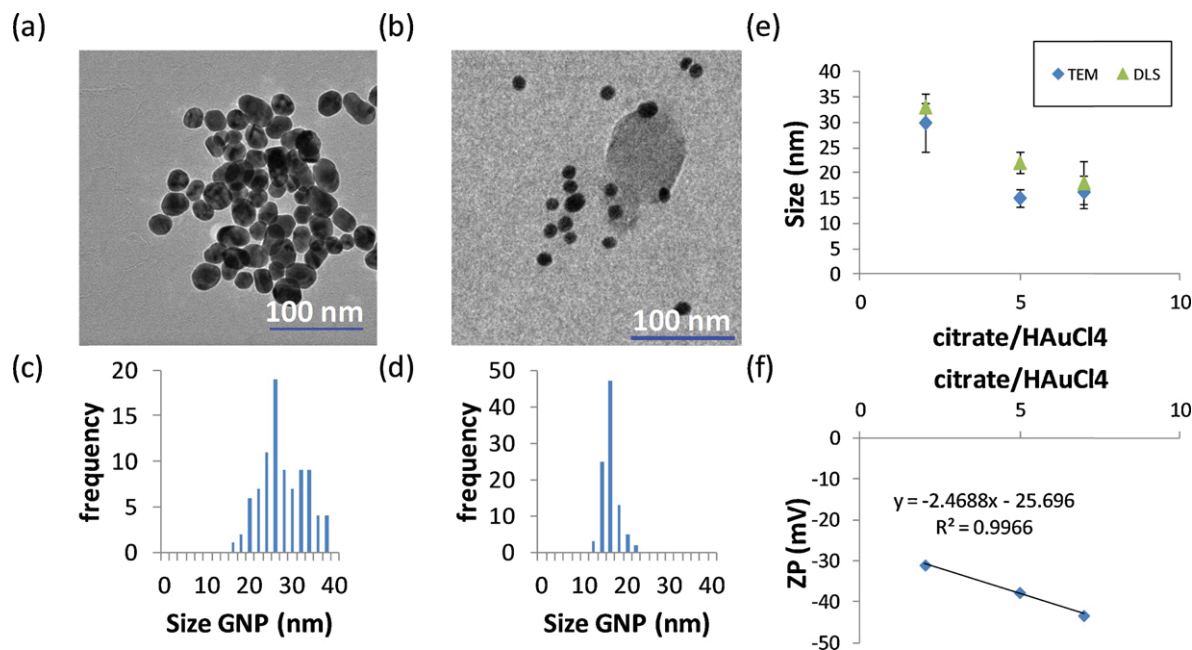


Fig. 3. TEM measurements of size-controlled citrate stabilized GNPs. The size was controlled by different citrate/HAuCl₄ ratios of 2/1 (with an average size of 29.9 ± 5.7 nm) (a), of 5/1 (15.0 ± 1.7 nm) (b) and of 7/1 (16.3 ± 3.2 nm). For the statistical analysis about 100 particles were counted; the corresponding histograms are shown beneath (c and d). A comparison of GNP sizes measured by TEM and Malvern Zetasizer Instruments nano is shown in (e). The zeta potential (ZP) of all three sizes is below -30 mV (f).

maximal coverage was tested by adding different amounts of 16-mercaptohexadecanoic acid followed by measurement of UV/vis spectra and zeta potential. Thereby, a wavelength shift of the surface plasmon absorbance band from 530 nm to 546 nm and concomitantly a decrease of the zeta potential from -25 mV to -39 mV (pH of the GNP solution was between 5 and 6) was observed when the molar ligand concentration was varied between 0 and 0.5 mM. At a ligand concentration of 0.33 mM or higher the colloidal solution became instable and the modified GNPs finally precipitated.

In a next step, trypsin was immobilized via its amino groups on the carboxylic functionalized GNPs by EDC and NHS coupling chemistry (see Fig. 1). The influence of the spacer length on trypsin activity was studied with the standard chromogenic substrate BApNA (Fig. 2). An overview of the spacers is given in (Table 1). The amount of bound trypsin onto GNPs was determined in solution and supernatant, respectively, by mass balance before and after immobilization reaction. Thereby, with increasing spacer length

the amount of trypsin bound onto GNPs could be increased by a factor of about 5.5 from $0.8 \mu\text{mol trypsin mL}^{-1}$ GNP solution when bound directly via ionic and hydrophobic interactions to $4.4 \mu\text{mol mL}^{-1}$ when immobilized via PEG7 spacer. Corresponding data were observed for the enzyme activity measured by the BApNA assay which decreases by a factor of 6 in the supernatant with increase of bound enzymes (Fig. 4a).

3.2.1. Digestion of protein mixture

Next to the activity test with the chromogenic substrate BApNA, trypsin immobilized GNPs with different spacer lengths were also tested for digestion of a mixture of three standard proteins, viz. bovine serum albumin (BSA), cytochrome C (CYC) and myoglobin (MYG). Thereby, the influence of GNP size (33 nm, 22 nm and 18 nm, according to DLS measurement (Fig. 3)) as well as of linker (MHA, spacer length = 17 atoms; PEG7, spacer length = 28 atoms) on the digestion of proteins was studied. With increase of GNP size a

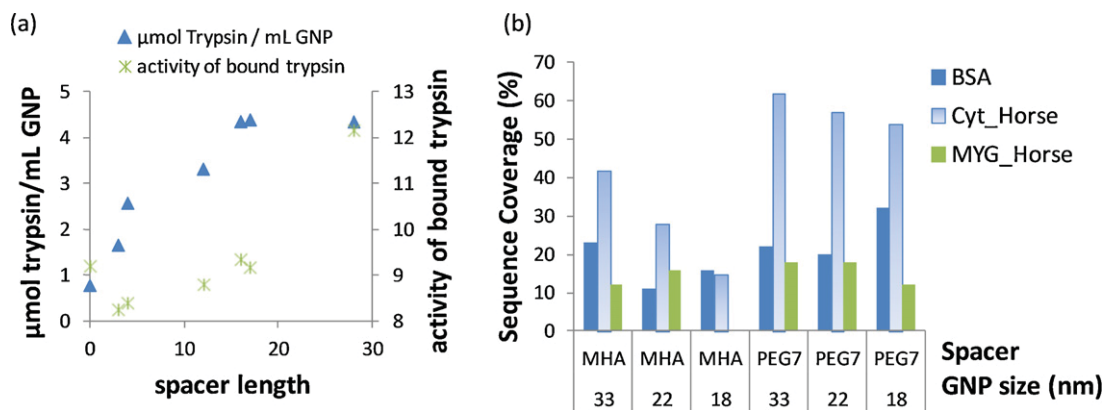


Fig. 4. Influence of spacer length on immobilization chemistry and bioactivity. With increase of immobilized enzymes (blue) an increase of the enzyme activity ($\Delta A_{410\text{nm}} \text{ min}^{-1}$) in the supernatant could be observed as well measured with BApNA assay (green) (a). The right figure shows the sequence coverage (%) of the MAS-COT search result for the digested proteins albumin, cytochrome C and myoglobin as a function of GNP size (33 nm, 22 nm and 18 nm according to DLS measurement) and of spacer length (MHA, mercaptohexadecanoic acid, spacer length: 17 atoms; PEG7, O-(2-carboxyethyl)-O'-(2-mercaptoethyl)heptaethylene glycol, spacer length: 28 atoms) (b).

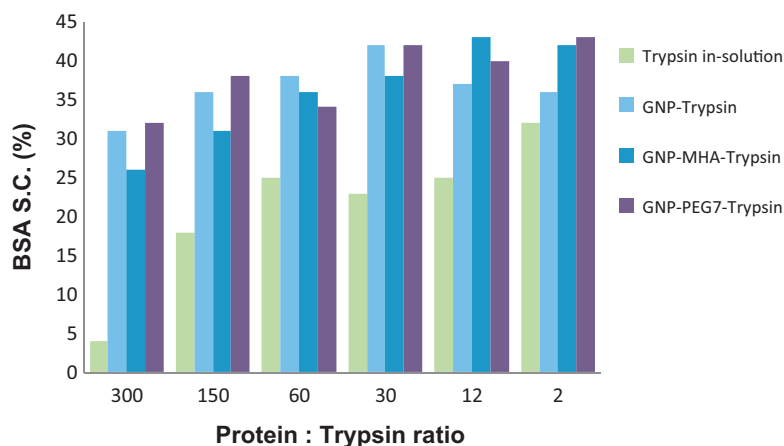


Fig. 5. Influence of trypsin concentration on the sequence coverage (S.C. (%)) of bovine serum albumin. An optimal protein/trypsin ratio of about 30 was found for a digestion time of 19 h.

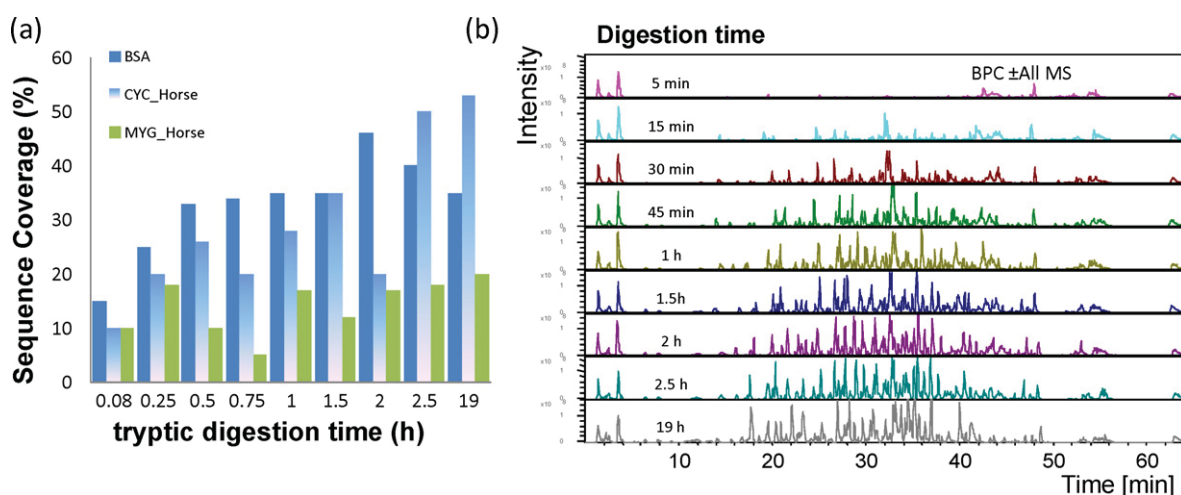


Fig. 6. With a protein/trypsin ratio of about 30 the digestion time could be decreased with GNP-PEG7-Trypsin from 19 h digestion time up to less than 1 h. Shown are the sequence coverage (%) of bovine serum albumin (BSA), cytochrome C (CYC) and myoglobin (MYG) from the GNP-PEG7-trypsin digest stopped with formic acid after different digestion times (a) as well as the corresponding base peak chromatograms (BPC \pm All MS) (b) (experimental and chromatographic conditions are described in experimental parts).

higher sequence coverage was observed. Thus, it makes no sense to use too small particles compared to the size of trypsin (lattice parameter of a non-psychrophilic trypsin from a cold-adapted fish species: $a = 65.91$, $b = 83.11$, $c = 154.79$ Å [48]). However, the greatest influence on the enzyme activity was found switching from the lipophilic spacer MHA (with 17 spacer atoms) to the hydrophilic linker PEG7 with a spacer length of 28 atoms whereby the sequence coverage nearly doubles (Fig. 4b).

The tryptic digest of GNP-PEG7-trypsin was further optimized with regard to protein/enzyme ratio, digestion time and reproducibility. An optimum ratio of protein to trypsin of 30:1 was found for trypsin conjugated GNP and trypsin in-solution digestion, whereby, higher sequence coverage was observed for GNP linked trypsin (Fig. 5).

In a next step, the digestion kinetics was evaluated. It turned out that the tryptic digestion can be enhanced by immobilization onto GNPs and thus, the digestion time could be reduced from 19 h to about 1 h (Fig. 6).

The batch-to-batch reproducibility of bioconjugation of trypsin onto GNPs via PEG7 spacer was tested by three different immobilization batches and intra-day digestion of the same protein mixture. All digestions were repeated in triplicate. Thereby, except for one outlier (cytochrome C, batch 3) a good reproducibility was

found for batch-to-batch as well as for in-batch replications. Higher sequence coverage and digestion efficiency and lower experimental standard deviation was found for GNP immobilized trypsin compared to the digestion of trypsin in-solution (Fig. 7).

For long-time stability one batch of GNP-PEG7-Trypsin and trypsin in-solution, respectively, was used for digestion of the same protein mixture at different days (Fig. 8). All samples were stored

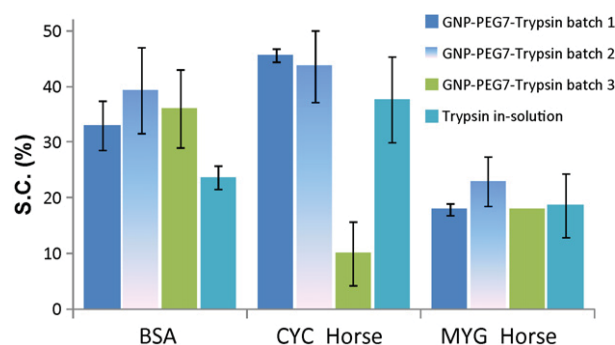


Fig. 7. Intra-day comparison of three different GNP-PEG(7)-trypsin immobilization batches with trypsin in-solution. All digestions were repeated in triplicate.

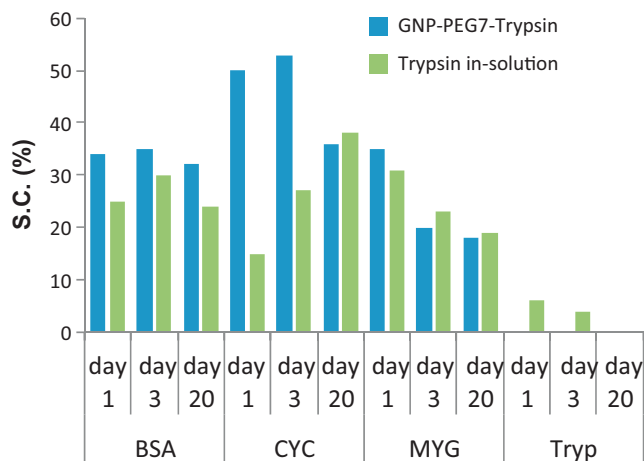


Fig. 8. Inter-day comparison of activity and long-time-stability of trypsin immobilized onto GNPs via PEG(7) spacer (GNP-PEG7-trypsin) vs. trypsin in-solution digestion. Shown are the sequence coverage (S.C. (%)) of the proteins bovine serum albumin (BSA), cytochrome C (CYC.horse) and myoglobin (MYG.horse) digested at different days as well as of the auto-digestion sub-products of trypsin (Tryp) found only with in-solution digestion. All samples were prepared the same day and stored until use at 4 °C.

until use at 4 °C. The sequence coverage of the inter-day digestion batches remains relatively constant over 3 weeks. Thereby, no trypsin or auto-digestion sub-products were found by the Mascot search when trypsin was bound onto GNPs in contrast to trypsin in-solution digestion (mean 7% of trypsin sequence coverage, Fig. 8). This indicates a reduced auto-digestion of the enzyme and trypsin itself can be removed from the solution by simple centrifugation of the bound GNPs.

3.2.2. Digestion of milk protein

The prevalence of allergic reactions to milk proteins, and particularly to casein, among the general population of adults has been reported to be around 0.5–1.0% [49]. Sensitivity to dairy products includes symptoms as flatulence, diarrhea, skin rash and fatigue. Casein is a mixture of several phosphoproteins (α S1, α S2, β , κ) and sum up to about 80% of cow-milk proteins. Their identification is of relevance in food chemistry.

Casein was digested in duplicate with the optimized protocol and trypsin immobilized onto GNPs (GNP-PEG7-trypsin) (see [Supplementary Material](#)). After a digestion time of 1 h, α -casein was found by Mascot search with sequence coverage of 6% and κ -casein with 14% on average. This result proves the applicability of the new nanoparticulate trypsin bioreactor.

4. Conclusions

A systematical study on bioconjugation of trypsin onto gold nanoparticles (GNP) with regard to activity, long-time stability, auto-digestion and reproducibility was accomplished.

In general, our results show that enzyme activity of GNP-trypsin was dependent on GNP size and particularly on the physico-chemical properties of the spacer used for enzyme immobilization. A slight influence on the enzyme activity was observed changing the GNP size from 18 nm to 22 nm and 33 nm, respectively. However, the sequence coverage of digested proteins in the standard mix could be nearly doubled switching from the lipophilic spacer MHA (with 17 spacer atoms) to the hydrophilic spacer PEG7 (with 28 atoms). Especially, the amount of immobilized enzyme and thus its activity could be increased by a factor of around 6 comparing trypsin bound directly onto GNP via ionic and hydrophobic interactions with trypsin linked via PEG7 spacer.

With this new nano-structured biocatalyst, the digestion time could be decreased from 19 h up to less than 1 h. Finally, inter- and intraday measurements demonstrated a good reproducibility of different batches as well as a satisfactory stability and reduced auto-digestion as indicated by measurements over 20 days.

In summary, this new nano-structured biocatalyst shows potential especially for proteomics and biopharmaceuticals analysis. The involved functionalization and spacer chemistry, respectively, may also serve as a successful platform for simple bioconjugation in general and for other enzyme reactors.

Acknowledgments

We thank Thomas Waitz from Physics of Nanostructured Materials, University of Vienna for providing and helping with transmission electron microscopic measurements. Financial support of the “Nano-MALDI” project by the Austrian BMVIT via the “Austrian Nano-Initiative” and “MNT-ERA.NET” is gratefully acknowledged.

Appendix A. Supplementary data

Supplementary data associated with this article can be found, in the online version, at <http://dx.doi.org/10.1016/j.aca.2012.04.036>.

References

- [1] A. Monzo, E. Sperling, A. Guttman, *Trends Anal. Chem.* 28 (2009) 854.
- [2] B.-W. Park, D.-Y. Yoon, D.-S. Kim, *Biosens. Bioelectron.* 26 (2010) 1.
- [3] D. Connolly, B. Twamley, B. Paull, *Chem. Commun.* 46 (2010) 2109.
- [4] J. Krenkova, F. Svec, *J. Sep. Sci.* 32 (2009) 706.
- [5] J. Spross, A. Sinz, *Anal. Bioanal. Chem.* 395 (2009) 1583.
- [6] S. Mouradian, *Curr. Opin. Chem. Biol.* 6 (2002) 51.
- [7] J. Krenkova, K. Kleparnik, F. Foret, *J. Chromatogr. A* 1159 (2007) 110.
- [8] J. Kim, J.W. Grate, P. Wang, *Chem. Eng. Sci.* 61 (2005) 1017.
- [9] Z. Wu, B. Zhang, B. Yan, *Int. J. Mol. Sci.* 10 (2009) 4198.
- [10] B. Xin, G. Xing, *Huazue Jinzhan* 22 (2010) 593.
- [11] A. Popat, S.B. Hartono, F. Stahr, J. Liu, S.Z. Qiao, G.Q. Lu, *Nanoscale* 3 (2011) 2801.
- [12] L.-M. Zhao, L.-E. Shi, Z.-L. Zhang, J.-M. Chen, D.-D. Shi, J. Yang, Z.-X. Tang, *Braz. J. Chem. Eng.* 28 (2011) 353.
- [13] Z. Wang, L. Ma, *Coord. Chem. Rev.* 253 (2009) 1607.
- [14] M. Vidotti, R.F. Carvalhal, R.K. Mendes, D.C.M. Ferreira, L.T. Kubota, *J. Braz. Chem. Soc.* 22 (2011) 3.
- [15] X. Cao, Y. Ye, S. Liu, *Anal. Biochem.* 417 (2011) 1.
- [16] H. Kawasaki, K. Yoshimura, K. Hamaguchi, R. Arakawa, *Anal. Sci.* 27 (2011) 591.
- [17] D. Liu, Z. Wang, X. Jiang, *Nanoscale* 3 (2011) 1421.
- [18] K. Kerman, M. Chikae, S. Yamamura, E. Tamiya, *Anal. Chim. Acta* 588 (2007) 26.
- [19] A. Faccenda, C.A. Bonham, P.O. Vacratsis, X. Zhang, B. Mutus, *J. Am. Chem. Soc.* 132 (2010) 11392.
- [20] M.A. Nash, P. Yager, A.S. Hoffman, P.S. Stayton, *Bioconjugate Chem.* 21 (2010) 2197.
- [21] S. Zhu, Y. Fu, J. Hou, *J. Comput. Theor. Nanosci.* 7 (2010) 1855.
- [22] L.A. Dykman, V.A. Bogatyrev, B.N. Khlebtsov, N.G. Khlebtsov, *Anal. Biochem.* 341 (2005) 16.
- [23] C.-S. Wu, F.-K. Liu, F.-H. Ko, *Anal. Bioanal. Chem.* 399 (2011) 103.
- [24] D. Sykora, V. Kasicka, I. Miksik, P. Rezanka, K. Zaruba, P. Matejka, V. Kral, *J. Sep. Sci.* 33 (2010) 372.
- [25] R. Lucena, B.M. Simonet, S. Cardenas, M. Valcarcel, *J. Chromatogr. A* 1218 (2011) 620.
- [26] J. Turkevich, P.C. Stevenson, J. Hillier, *Discuss. Faraday Soc.* (11) (1951) 55.
- [27] G. Frens, *Nat. Phys. Sci.* 241 (1973) 20.
- [28] I. Ojea-Jimenez, F.M. Romero, N.G. Bastus, V. Puentes, *J. Phys. Chem. C* 114 (2010) 1800.
- [29] J. Polte, M. Herder, R. Erler, S. Rolf, A. Fischer, C. Wuerth, A.F. Thuenemann, R. Kraehnert, F. Emmerling, *Nanoscale* 2 (2010) 2463.
- [30] S. Kumar, K.S. Gandhi, R. Kumar, *Ind. Eng. Chem. Res.* 46 (2007) 3128.
- [31] D. Ghosh, D. Sarkar, A. Girigoswami, N. Chattopadhyay, *J. Nanosci. Nanotechnol.* 11 (2011) 1141.
- [32] N.G. Khlebtsov, *Anal. Chem.* (Washington, DC, United States) 80 (2008) 6620.
- [33] W. Haiss, N.T.K. Thanh, J. Aveyard, D.G. Fernig, *Anal. Chem.* (Washington, DC, United States) 79 (2007) 4215.
- [34] X. Liu, M. Atwater, J. Wang, Q. Huo, *Colloids Surface B: Biointerfaces* 58 (2007) 3.
- [35] B.N. Khlebtsov, N.G. Khlebtsov, *Colloid J.* 73 (2011) 118.
- [36] F.-K. Liu, *Chromatographia* 66 (2007) 791.
- [37] B. Deryagin, L. Landau, *Acta Physicochim. URSS* 14 (1941) 633.
- [38] E.J.W. Verwey, J.T.G. Overbeek, *Theory of the Stability of Lyophobic Colloids*, Elsevier, New York, 1948.

- [39] L. Srisombat, A.C. Jamison, T.R. Lee, *Colloids Surface A: Physicochem. Eng. Aspects* 390 (2011) 1.
- [40] S.-Y. Lin, Y.-T. Tsai, C.-C. Chen, C.-M. Lin, C.-h. Chen, *J. Phys. Chem. B* 108 (2004) 2134.
- [41] B. Kalska-Szostko, M. Rogowska, A. Dubis, K. Szymanski, *Appl. Surf. Sci.* 258 (2012) 2783.
- [42] M. Lv, E. Zhu, Y. Su, Q. Li, W. Li, Y. Zhao, Q. Huang, *Prep. Biochem. Biotechnol.* 39 (2009) 429.
- [43] Y.-F. Huang, C.-C. Huang, H.-T. Chang, *Langmuir* 19 (2003) 7498.
- [44] A. Gole, C.J. Murphy, *Langmuir* 24 (2008) 266.
- [45] Y. Liu, Y. Xue, J. Ji, X. Chen, J. Kong, P. Yang, H.H. Girault, B. Liu, *Mol. Cell. Proteomics* 6 (2007) 1428.
- [46] G. Hermanson, *Bioconjugate Techniques*, Elsevier, Rockford, IL, USA, 2008.
- [47] M. Beneito-Cambra, J.M. Herrero-Martinez, G. Ramis-Ramos, W. Lindner, M. Laemmerhofer, *J. Chromatogr. A* 1218 (2011) 7275.
- [48] H.-K. Schroder, N.P. Willassen, A.O. Smalas, *Acta Crystallogr. D: Biol. Crystallogr.* D54 (1998) 780.
- [49] European Food Safety Authority, *EFSA J.* 9 (2011) 2384.

A-3.1 Supplementary Information

Hinterwirth, H.; Lindner, W.; Laemmerhofer, M.

Analytica Chimica Acta **2012**, 733, 90-97

Supplementary Data

Bioconjugation of trypsin onto gold nanoparticles: effect of surface chemistry on bioactivity

Helmut Hinterwirth ¹, Wolfgang Lindner ¹, Michael Lämmerhofer ^{1,2 *}

¹ *Department of Analytical Chemistry, University of Vienna, Währingerstrasse 38, 1090 Vienna, Austria*

² *New address: Institute of Pharmaceutical Sciences, University of Tübingen, Auf der Morgenstelle 8, 72076 Tübingen, Germany*

* corresponding author:

Prof. Dr. Michael Lämmerhofer

Pharmaceutical Analysis and Bioanalysis

Institute of Pharmaceutical Sciences

University of Tübingen

Auf der Morgenstelle 8

72076 Tübingen, Germany

T +49 7071 29 78793, F +49 7071 29 4565

e-mail: michael.laemmerhofer@uni-tuebingen.de

Gold nanoparticles (GNPs) can be size-controlled prepared by the citrate reduction method of HAuCl_4 as introduced by Frens and Turkevich. Thereby, the characteristic surface plasmon resonance (SPR) of metallic nanoparticles as function of delocalized electrons can be used as size-related property for easy control mechanism. With increase of the nanoparticle size the band gap between the valence band and the conduction band decreases resulting in a shift of the absorbance maximum (Figure 1).

A common method for adequate size determination of nanoparticles is transmission electron microscopy (TEM). However, this method is time consumable. A fast method is dynamic light scattering (DLS) which measures the particle diffusion in a fluid (Brownian motion) and relates it to the size. DLS measures the particles surrounded by fluid as the hydrodynamic diameter depending on the solvent, temperature, salt concentration etc. Corresponding data for TEM, DLS and UV/VIS spectra for GNPs with different sizes are shown in (Figure 2).

However, shifts of SPR maxima and shape changes of SPR curves are not only caused by particle size but also by formation of aggregates and/or adsorption of modifying molecules. GNPs can be surface functionalized by dative binding of bifunctional thiol containing molecules. Increase of the ligand 16-mercaptohexadenoic acid (MHA) to GNP ratio results in a shift of the SPR maxima and in a shape change of the SPR curves. Thereby the wavelength of the absorbance maxima for GNP with a size of 33 nm changes from 535 nm to 546 nm at the concentration of MHA when the nanoparticles aggregate (Figure 3).

With the optimized immobilization and digestion protocol, the milk protein casein was digested for 1h with GNP-PEG7-trypsin. The corresponding base peak chromatograms are shown in (Figure 4).

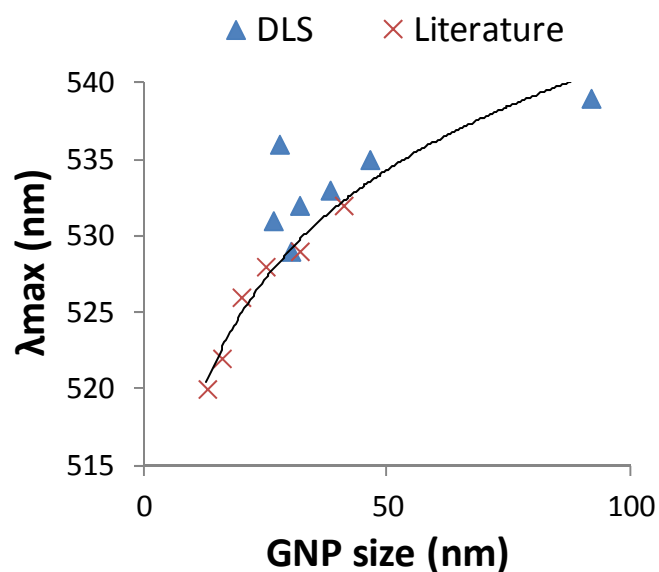


Figure 1: Relationship between GNP size (nm) measured by dynamic light scattering (DLS) and the wavelength of the absorbance maximum from the corresponding UV/VIS spectra (λ_{max} (nm)). Literature data are taken from Ghosh et al., *Journal of Nanoscience and Nanotechnology*, 11 (2011) 1141.

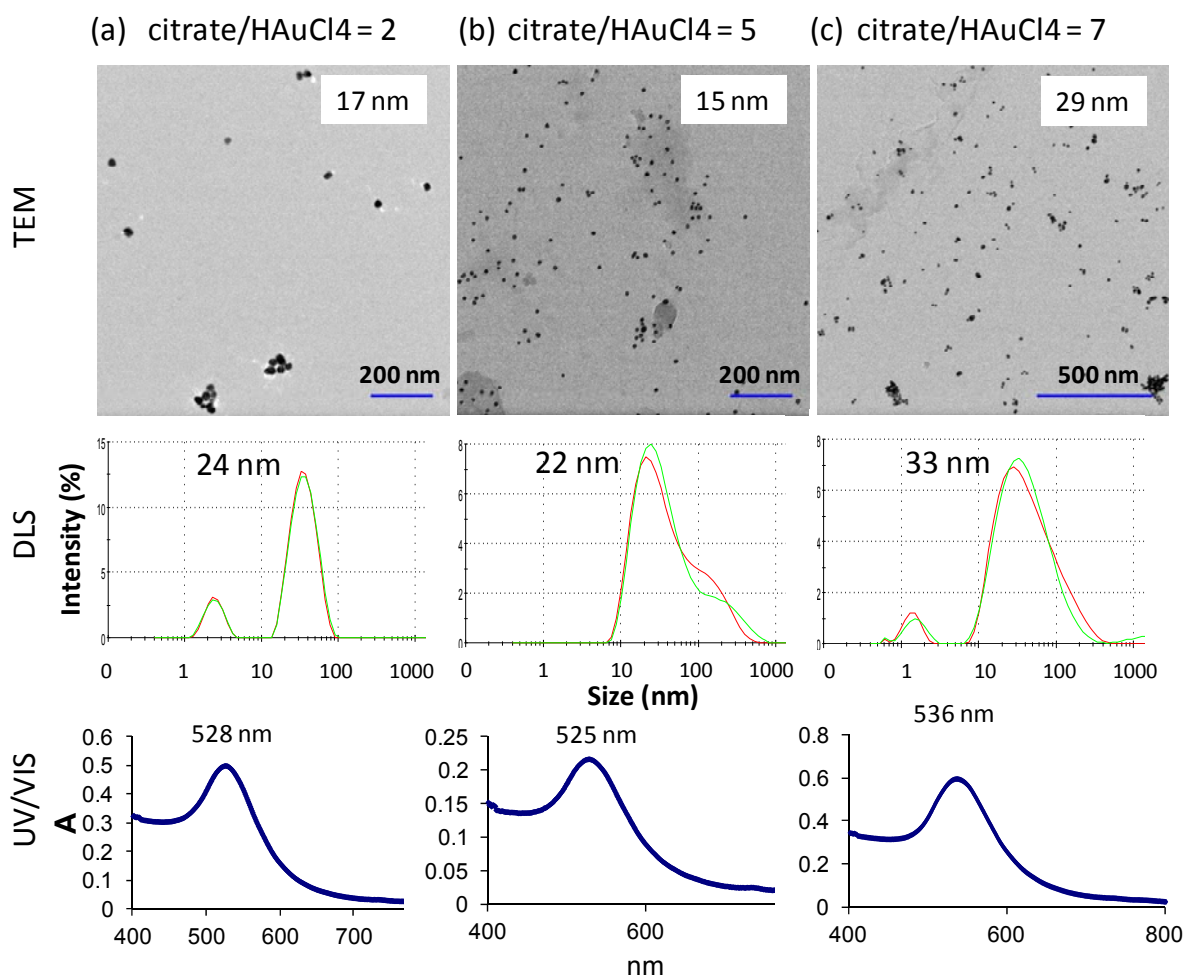


Figure 2: Corresponding data for size controlled GNP synthesis by variation of citrate/HAuCl₄ ratio from 2 to 5 and 7, respectively. Thereby the size change from 17 nm to 15 nm and 29 nm measured by transmission electron microscopy (TEM). The corresponding measurement by dynamic light scattering (DLS) gives the hydrodynamic radius of GNPs slightly higher with 24 nm, 22 nm and 33 nm, respectively. Concurrently, the wavelength of the absorbance maximum from the UV/VIS spectra shifts from 528 nm to 525 nm and 536 nm.

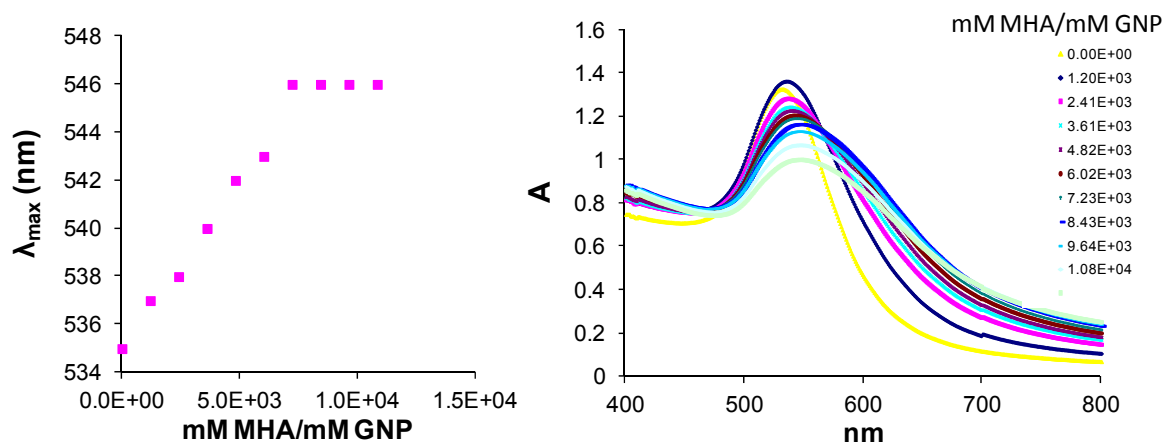


Figure 3: Increase of 16-mercaptohexadecanoic acid (MHA) to GNP ratio results in a shift of the SPR maxima from 535 nm to 546 nm and also in a shape change of the SPR curve.

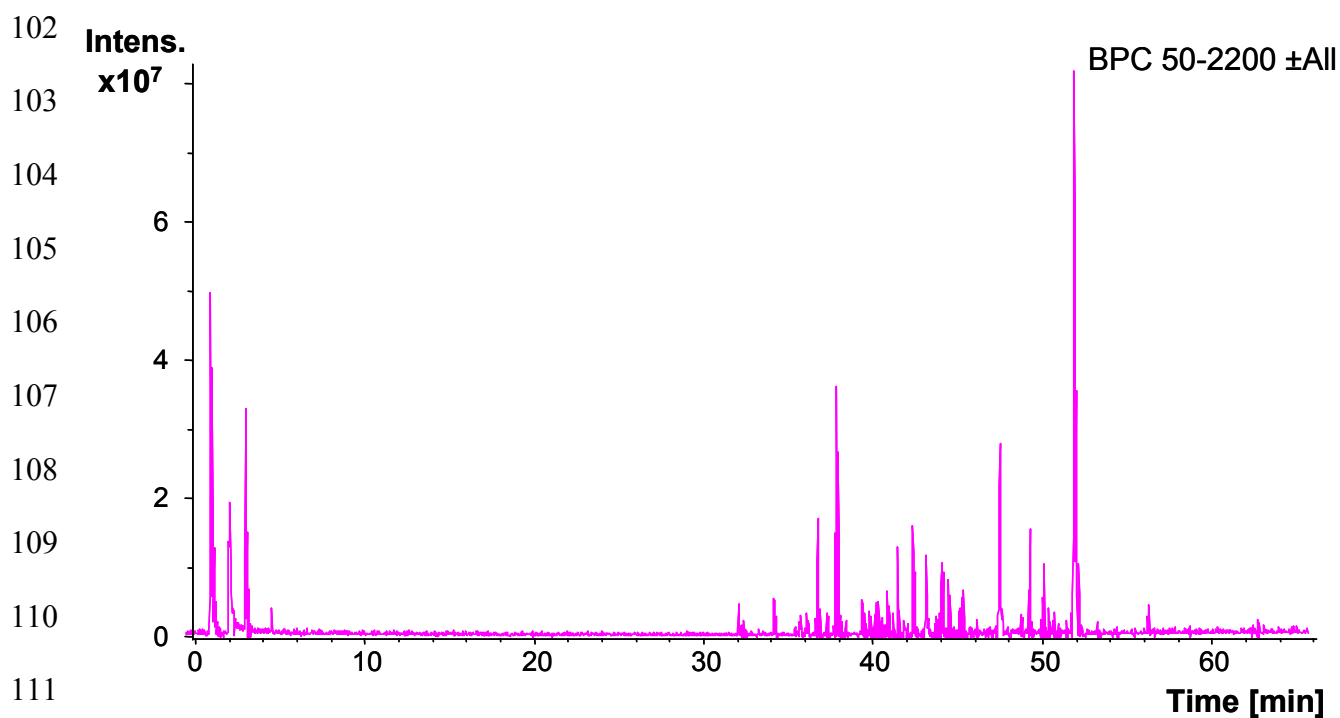


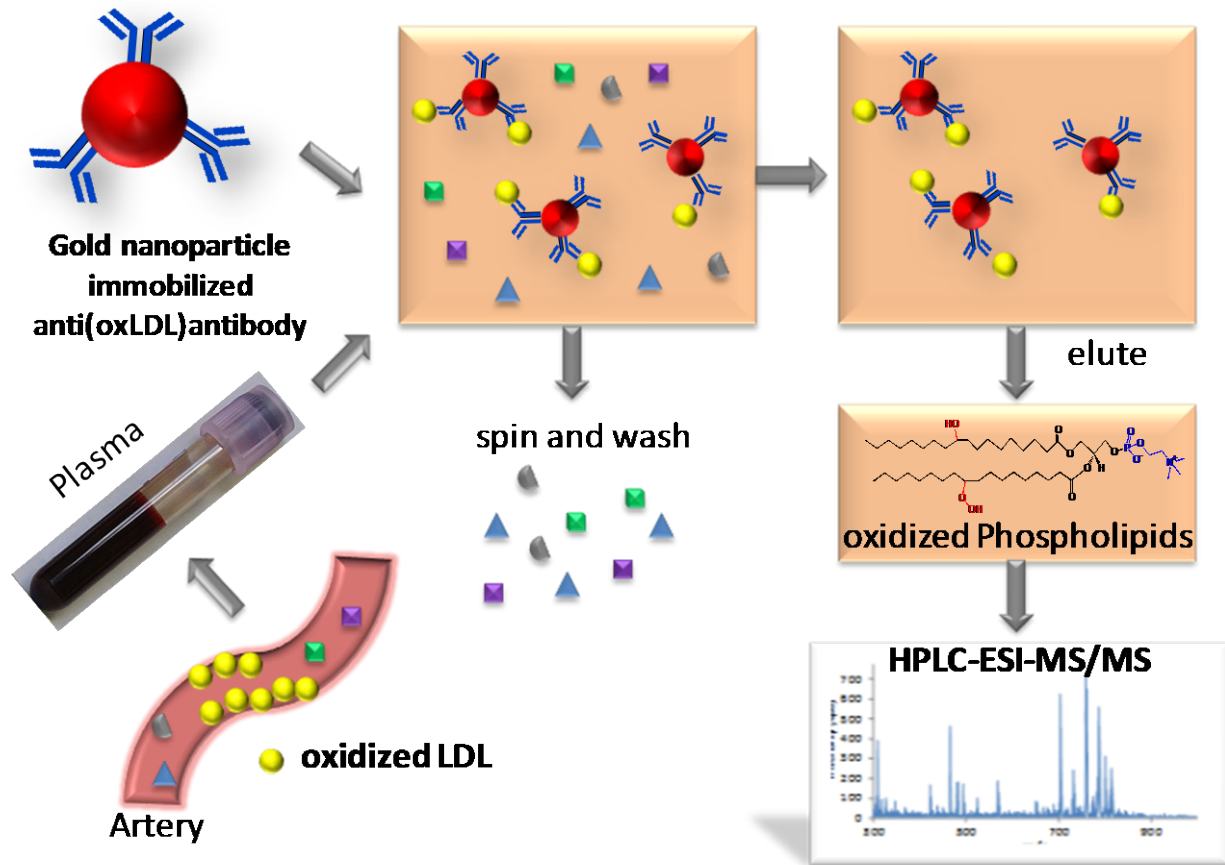
Figure 4: Base peak chromatograms of casein digestion after 1h with GNP-PEG7-trypsin. The digestion was repeated in duplicate (a and b).

A-4. Gold Nanoparticle Conjugated Anti-Oxidized Low-Density Lipoprotein-Antibodies and Liquid Chromatography/Mass Spectrometry as Tools for Targeted Lipidomics.

Hinterwirth H.; Lindner W.; Lämmerhofer M.

unpublished manuscript

1 TOC:



2

3 Gold Nanoparticle Conjugated Anti-Oxidized

4 Low-Density Lipoprotein-Antibodies and Liquid

5 Chromatography/Mass Spectrometry as Tools

6 for Targeted Lipidomics

7 *Helmut Hinterwirth,[†] Wolfgang Lindner,[†] Michael Lämmerhofer^{‡, *}*

8 [†] Department of Analytical Chemistry, University of Vienna, Währingerstrasse 38, 1090

9 Vienna, Austria

10 [‡] Institute of Pharmaceutical Sciences, University of Tübingen, Auf der Morgenstelle 8,

11 72076 Tübingen, Germany

ABSTRACT

Oxidized low-density lipoproteins (oxLDL) and in particular oxidized phosphatidylcholines (oxPCs) are known to cause severe physiological effects such as cardiovascular diseases (CVDs) and are described as potential biomarkers e.g. for atherosclerosis. In our study, we used the specific affinity of anti-oxLDL-antibodies (Ab) conjugated to gold nanoparticles (GNPs) for extraction and enrichment of oxPCs *via* selective trapping of oxLDL from plasma combined with the sensitive detection by liquid chromatography / mass spectrometry (LC-MS/MS). Successful bioconjugation chemistry of Abs *via* bifunctional poly(ethylene glycol) (PEG) spacer and protein G linkage, respectively, was controlled by measuring the surface plasmon resonance (SPR) spectra, size and zeta potentials. Furthermore, the amount of Ab immobilized onto GNP *via* PEG linker (GNP-PEG₇-Ab) was determined. With the optimized immobilization chemistry, the ability and potential of the nanogold-based extraction procedure was shown by determination of an apparent dissociation constant K_d for the sum of (ox)PCs by precursor ion scan at m/z 184.1 in positive ion mode. Moreover, apparent K_d s could also be determined for individual PCs and their oxidation products with compound-specific selected reaction monitoring (SRM) mode, which allows the characterization of the (auto)antibody affinity and thus, of the antigenity of oxPCs. In summary, the application of nanomaterial-based bioanalysis for selective targeting of oxLDL and the fast and sensitive detection by LC-MS/MS offers new possibilities in targeted lipidomics for antibody characterization as well as for fast biomarker screening.

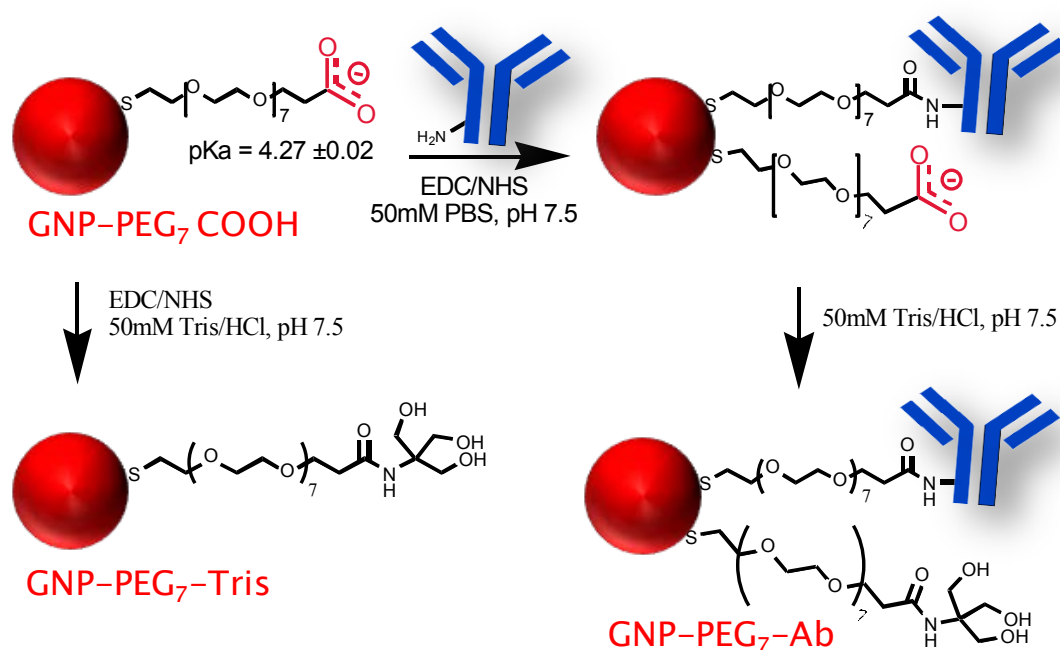
34 Cardiovascular diseases (CVDs) are the number one cause of death globally. Estimated
35 17.3 million people died from CVDs in 2008, representing 30% of all global deaths
36 (WHO, 09/2011). Next to 'traditional' risk factors such as hypercholesterolemia,
37 hypertension, smoking, male gender, and age also both, adaptive and innate immune
38 mechanisms play a role in atherogenesis.^{1, 2} Furthermore, a study with asymptomatic
39 teenagers and young adults showed also a high prevalence of coronary
40 atherosclerosis.³ Thus, the detection of specific biomarkers is essential for early
41 preclinical diagnosis and CVD prevention.

42 Minimally oxidized low-density lipoprotein (minimally modified LDL, mmLDL) and late
43 forms of oxidized LDL (oxLDL) are known to have severe physiological effects in
44 inflammatory diseases like atherosclerosis, whereat oxidized forms of polyunsaturated
45 fatty acids (oxidized PUFAs, oxPUFAs) are described as potential biomarkers that are
46 toxic, pro-inflammatory and ultimately pro-atherogenic.^{1, 2, 4-8} Specific immune receptors
47 (e.g. CD36)⁹ and (auto)antibodies (Ab)¹⁰ have been described as selective agents
48 targeting oxLDL; whereby, Cu²⁺ oxidized LDL (CuLDL) is widely used as model to mimic
49 oxLDL *in vitro*. Phosphatidylcholines (PCs) as a major group of phospholipids (PLs)
50 change their structure if oxidized and expose their head groups, whereby the change of
51 the structural motif of oxidized PCs (oxPCs) is regarded as essential for Ab
52 recognition.^{2, 9, 11} Nevertheless, there is still a necessity for screening of (new)
53 biomarkers which are specific for CVD. In this context, it can be taken advantage of the
54 specificity of autoantibodies for the diagnosis of the antigenicity of oxPLs.

55 Additionally, a significant challenge in targeted lipidomics represents the detection and
56 quantitation of oxPLs out of oxLDL due to their low levels *in vivo* (sub μ M), their

57 structural complexity, and diverse (fragmented and non-fragmented) oxidation products.
58 Moreover, the limited availability of suitable standards further adds to the difficulty of
59 their reliable analysis.^{4, 12, 13} One simple method for extraction of lyso-PLs and PLs from
60 plasma utilizes MeOH as solvent followed by a centrifugation step.¹⁴ 'Soft-ionization'
61 techniques in mass-spectrometry (MS) such as electrospray ionization (ESI-MS) with
62 direct infusion or coupled to liquid chromatography (LC-ESI-MS) are the number one of
63 choice in lipidomics to minimize artefacts caused by decomposition of native PLs.^{13, 15-18}
64 Alongside this, matrix-assisted laser desorption/ionization mass-spectrometry
65 (MALDI-MS) and imaging mass spectrometry are getting more and more popular in
66 lipidomics.¹⁹⁻²¹
67 In our study, we combined both techniques – the advantage of antibody specificity for
68 extraction and enrichment of oxLDL as well as the sensitive detection and quantitation
69 of oxPLs with HPLC-ESI-MS/MS. Along this line, we used the benefits of
70 nanoimmunoprecipitation based on gold nanoparticles (GNP). GNPs are popular carrier
71 for nanotrapping concepts because of their high surface-to-volume ratio and easy and
72 low-cost controlled synthesis with narrow size distribution. The straightforward chemical
73 functionalization of GNPs with thiol containing molecules utilizes the strong dative thiol
74 binding forming a self-assembling monolayer (SAM) with a high surface coverage on
75 the gold surface.²² Furthermore, functionalized GNPs offer a broad range of
76 bioconjugation chemistries for Ab immobilization *via* linker²³⁻²⁸ or direct attachment *via*
77 protein A/G.²⁹
78 The biocompatible coating of GNPs with bifunctional poly(ethylene glycol)
79 (HS-PEG₇-COOH) spacer was used for further immobilization of

anti-(oxLDL)-antibodies (GNP-PEG₇-Ab) and compared to the direct attachment of Ab onto GNPs *via* protein G (GNP-ProtG-Ab). The unspecific binding could be reduced for GNP-PEG₇-Ab by simply changing the immobilization buffer and blocking the residual carboxylic groups with tris(hydroxymethyl)aminomethane (Tris), whereby ionic interactions can be suppressed (Scheme 1).



Scheme 1: Abs were immobilized onto carboxylic acid functionalized GNPs *via* EDC/NHS coupling. Changing the buffer from PBS to the amine-containing Tris/HCl buffer the residual carboxylic groups were blocked finally with Tris. Thus, unspecific binding could be reduced by suppression of ionic interactions.

OxLDL was extracted (as standard as well as from plasma) by the specific recognition of GNP-conjugated Abs and enriched by centrifugation of the GNP-PEG₇-Ab / antigen complex. After removal of the supernatant and washing of the functionalized nanobeads, the precipitate was treated with MeOH and briefly subjected to ultrasonication. Thereby, the antibody-antigen complex dissociates and GNP

immobilized Ab can be readily removed from solution by centrifugation as pellet. The elution with methanol has next to the breaking of the antibody-antigen binding the advantage that proteins (e.g. ApoB from oxLDL) and GNP immobilized Ab precipitate while on the other hand (ox)PLs are dissolved in the supernatant available as sample for HPLC-MS/MS analysis. It is also worth mentioning that the obtained methanolic sample is LC-MS compatible without further time-consuming sample handling steps and also an enrichment step by volume reduction can be incorporated during the entire sample preparation process. Thus, the supernatant containing oxPLs was directly analyzed by HPLC-ESI-MS/MS. Precursor ion scan of the specific product ion at m/z 184.1 allows the fast screening for (new) biomarkers PCs and its oxidation products. On the other hand, compound-specific detection by single reaction monitoring (SRM) mode allows the identification and the quantification of (ox)PCs. Finally, the application for extraction of oxLDL from plasma demonstrates the appropriateness of this bioanalysis with functionalized GNPs.

EXPERIMENTAL SECTION

Materials and Chemicals

Gold(III) chloride trihydrate ($\text{HAuCl}_4 \times 3 \text{ H}_2\text{O}$), trisodium citrate, tris(hydroxymethyl)aminomethane (Tris), *N*-(3-dimethylaminopropyl)-*N*-ethylcarbodiimide (EDC), *N*-hydroxysuccinimide (NHS) and *O*-(2-carboxyethyl)-*O'*-(2-mercaptoethyl)heptaethylene glycol (PEG₇) were all obtained from Sigma-Aldrich (Vienna, Austria). Plasma was received from Technoclone (Vienna, Austria). Protein G was a gift from Rainer Hahn, University of Natural Resources and Life Sciences,

119 Vienna, Austria. Anti-Cu²⁺ oxidized LDL-antibody (anti-CuLDL-Ab; AB3230, rabbit
120 polyclonal antibody) was obtained from Millipore (CA, USA), anti-N^ε-
121 (carboxymethyl)lysine-antibody (anti-CML-Ab; KH024, mouse monoclonal antibody,
122 IgG2a) from TransGenic Inc. (Kobe, Japan), anti-malondialdehyde oxidized LDL-
123 antibody (anti-MDA-Ab; ab17354, mouse monoclonal antibody, IgG2b) from Abcam plc
124 (Cambridge, UK) and EO6 (mouse monoclonal antibody, IgM) from Avanti (Alabaster,
125 USA). Cu²⁺ oxidized human LDL (CuLDL) and native human LDL (natLDL) were
126 obtained from Cell Biolabs, Inc. (San Diego, USA).

127 **Preparation of GNPs and Immobilization of Antibodies**

128 Gold nanoparticles were prepared as described in previous work optimized for
129 immobilization chemistry of proteins.²⁶ In short, 50 mL gold(III) chloride trihydrate
130 solution in bidistilled water (final concentration was 1.14 mM) were heated under stirring
131 until boiling and subsequently reduced with 5 mL trisodium citrate (final concentration
132 was 2.28 mM) to obtain citrate-stabilized GNPs with average diameters of 26.2 ±4.4 nm.
133 Carboxy-pegylation was carried out with 1 μL SH-PEG₇-COOH solution per mL GNP
134 suspension to form self-assembled monolayer (SAM). Excess of unbound ligands was
135 removed by centrifugation and resuspension. Antibodies (1 μL of 1 mg mL⁻¹ solution)
136 were immobilized onto 1 mL GNP-PEG₇-COOH intermediate by EDC/NHS linkage (final
137 concentration of EDC was 1.2 mM and of NHS 6 mM) to obtain GNP-PEG₇-Ab. For
138 blank control the carboxy-pegylated functionalized GNPs were reacted as well with EDC
139 and NHS for 2 h and finally blocked with 50 mM TrisHCl, pH 7.5 followed by several
140 washing steps to give GNP-PEG₇-Tris.

Protein G was immobilized by adsorption onto citrate-stabilized GNPs. Therefore, 100 μ L of protein G solution (1 mg mL⁻¹ in 50 mM PBS, pH 7.5) were added to 1 mL GNP suspension. Unbound protein G was removed by 2x centrifugation and resuspension in buffer. Antibodies (1 μ L of 1 mg mL⁻¹ added to 1 mL GNP-ProtG solution) were bound via their F_c region utilizing the high affinity to protein G. After reacting overnight at 4°C, the unbound antibodies were removed by several centrifugation steps and washed with 50 mM Tris/HCl buffer, pH 7.5.

Extraction and Enrichment of (Oxidized) LDL

10 μ L of GNP-conjugated antibodies were incubated overnight with 10 μ L of LDL suspension or plasma spiked with CuLDL. Unbound LDL was removed by 4 times centrifugation and resuspension in 50 mM Tris/HCl, pH 7.5. The bound CuLDL was finally released by resuspending the pellet in MeOH and short ultrasonication. GNP-conjugated Abs and proteins (e.g. plasma proteins and apolipoprotein from LDL) and buffer salts were removed by centrifugation as pellet. Obtaining MS compatible conditions with pure methanol, the supernatant containing (oxidized) phospholipids was analyzed by HPLC-ESI-MS/MS. CuLDL and CuLDL spiked to plasma, respectively, were directly measured after dilution with methanol.

LC/MS/MS Method

HPLC-ESI-MS/MS experiments were performed on an Agilent 1200 series hyphenated with a 4000 QTrap[®] LC/MS/MS system (Applied Biosystems, Foster City, CA) via electrospray ionization (ESI) interface using a Phenomenex C8-column (Luna (2), 3 μ m C8 150 x 2 mm) and a HPLC in-line filter (0.5 μ m depth filter x 0.004 in ID). The following general settings were optimized by previous work in the group:^{30, 31} ESI

164 voltage was set to 4300 V, the temperature of the ion source was 500°C, and the
165 entrance potential 10 V. Nitrogen was used as nebulizer, heater, and curtain gas with
166 the pressure set to 60, 50, and 10 psi, respectively. The HPLC system was equipped
167 with a binary gradient pump, autosampler, vacuum degasser and a temperature-
168 controlled column compartment (Agilent, Waldbronn, Germany). The mobile phase
169 consisted of methanol / Millipore water (80:20; v/v) containing 10 mM ammonium
170 acetate (A) and methanol containing 10 mM ammonium acetate (B). The following
171 gradient was run: 0 – 10 min: 55 - 100% B, 10 – 20 min: 100% B, 20 – 21 min: 100 –
172 55% B, 21 – 30 min: 55% B. The flow rate was 0.2 mL min⁻¹ and the column
173 temperature was set to 25°C. The injection of 5 µL of the sample was performed with
174 needle wash. The scan range in the positive mode was from 300 – 1000 m/z.
175 Phosphatidylcholines (PCs) were detected by precursor ion scan with m/z 184.1 in the
176 positive ion-mode. Compound specific MS/MS parameters for selected-reaction
177 monitoring (SRM) are shown in Table 1. Data analysis was performed with Analyst 1.5
178 software (Applied Biosystems, Foster City, CA). Overview about the analytes, their
179 compound names and abbreviations, and their structure is given in Table S1 and Figure
180 S1.

181 **Table 1:** Optimized MS/MS conditions for compound-specific detection of PCs and their oxidation products.

Analyte	C:DB	MS/MS conditions				
		parent ion m/z	product ion m/z	DP (V)	CE (V)	CXP (V)
lyso-PCs						
lyso-PC-16	16:0	496.3	184.1	116	35	12
lyso-PC18	26:2	524.4	184.1	101	39	15
Saturated PCs						
DMPC	28:0	678.6	184.1	61	39	15
PMPC	30:0	706.5	184.1	87	43	12
DPPC	32:0	734.7	184.1	96	39	12
DAPC	40:0	846.7	184.1	87	43	12
Unsaturated PCs						
PC (33:1)	33:1	746.6	184.1	87	43	12
PLPC	34:2	758.6	184.1	105	45	10
POPC	34:1	760.6	184.1	87	43	12
PAPC	36:4	782.7	184.1	101	45	14
PC (36:2)	36:2	787.6	184.1	87	43	12
PC (38:4)	38:4	811	184.1	87	43	12
Oxidized PCs						
POVPC	21:0 (Aldo)	594.5	184.1	91	37	10
PONPC	25:0 (Aldo)	650.6	184.1	101	55	14
PAZPC	25:0 (Aldo)	666.6	184.1	81	43	8
PC (33:1)-OH	33:1 (OH)	762.6	184.1	87	43	12
PLPC-OH	34:2 (OH)	774.7	184.1	65	40	15
POPC-OH	34:1 (OH)	776.6	184.1	87	43	12
PC (33:1)-OOH	33:1 (OOH)	778.6	184.1	87	43	12
PLPC-OOH	34:2 (OOH)	790.7	184.1	101	53	14
POPC-OOH	34:1 (OOH)	792.6	184.1	87	43	12
PAPC-OH	36:4 (OH)	798.7	184.1	66	45	12
PC (36:2)-OH	36:2 (OH)	803.6	184.1	87	43	12
PAPC-OOH	36:4 (OOH)	814.8	184.1	51	45	12
PC (36:2)-OOH	36:2 (OOH)	818.6	184.1	87	43	12
PLPC-(OOH) ₂	34:2 (OOH) ₂	822.6	184.1	90	40	12
PEIPC		828.8	184.1	96	45	12
PC (38:4)-OOH	38:4 (OOH)	842.6	184.1	90	40	12
PC (36:2)-(OOH) ₂	36:2 (OOH) ₂	850.6	184.1	90	40	12
PC (38:4)-(OOH) ₂	38:4 (OOH) ₂	874.6	184.1	90	40	12

182

Immunoassay – Determination of K_d

The dissociation constant K_d for anti-CuLDL-Ab was additionally determined with sandwich enzyme linked immunosorbent assay (ELISA). In brief, anti-CuLDL-Ab was dotted onto microtiter plates and incubated overnight with CuLDL. Unbound CuLDL was removed with washing solution (50 mM Tris/HCl, pH 7.5, 0.1% (v/v) Tween20) and the residual microtiter plate was blocked with blocking buffer (50 mM Tris/HCl, pH 7.5, 0.1% (v/v) Tween20, and 2% (w/v) fish gelatine). The bound CuLDL was finally detected with anti-CuLDL-Ab and a secondary horseradish peroxidase (HRP) linked anti-IgG-Ab. The detection was carried out with 3,3',5,5'-tetramethylbenzidine (TMB) as substrate. After stopping the enzyme reaction with sulfuric acid the absorbance was recorded at a wavelength of 450 nm.

Immunoassay – Determination of Ab Bound per GNP

For the determination of the amount of Ab bound per GNP, GNP-PEG₇-Ab suspension was incubated with a HRP anti-IgG-Ab. After several washing steps by centrifugation and resuspension, the bound anti-IgG-Ab linked HRP was detected with TMB. The amount of Ab per GNP was calculated by comparison to the calibration curve obtained by plotting of different anti-CuLDL-Ab concentrations onto a microtiter plate and detection with the same secondary antibody.

Size and Zeta potential measurements

GNPs and the conjugates were characterized at each immobilization step by measuring the size and size distribution by dynamic light scattering (DLS) and their zeta potentials (ZP) by electrophoretic mobility measurements using a Zetasizer instrument (Malvern Zetasizer Instruments Nano series, Prager Instruments).

Calculation of logP values

log P values were calculated using ACD/logP DB (ACD/Labs, 7.00 Release, Product version 7.07).

RESULTS AND DISCUSSION

Characterization of Functionalized GNPs

The nanoparticle-antibody conjugates developed herein must be suitable for selective extraction of oxLDL from plasma samples utilizing the high antibody affinity. Thus, important properties for their efficient functional utility are besides specificity for the target oxLDL over native LDL a reasonable binding capacity and a sufficient colloidal stability of functionalized GNP suspensions. To ensure these properties, various methods of nanoparticle analysis were carried out for quality control and to follow the progress of the immobilization chemistry of Abs onto GNPs thorough characterization of the nanoparticles at each step of functionalization. These include measurements of surface plasmon resonance (SPR) spectra, determination of size and size distributions by dynamic light scattering (DLS) as well as characterization of zeta potentials (ζ -potential, ZP) by electrophoretic mobility measurements (Figure 1).

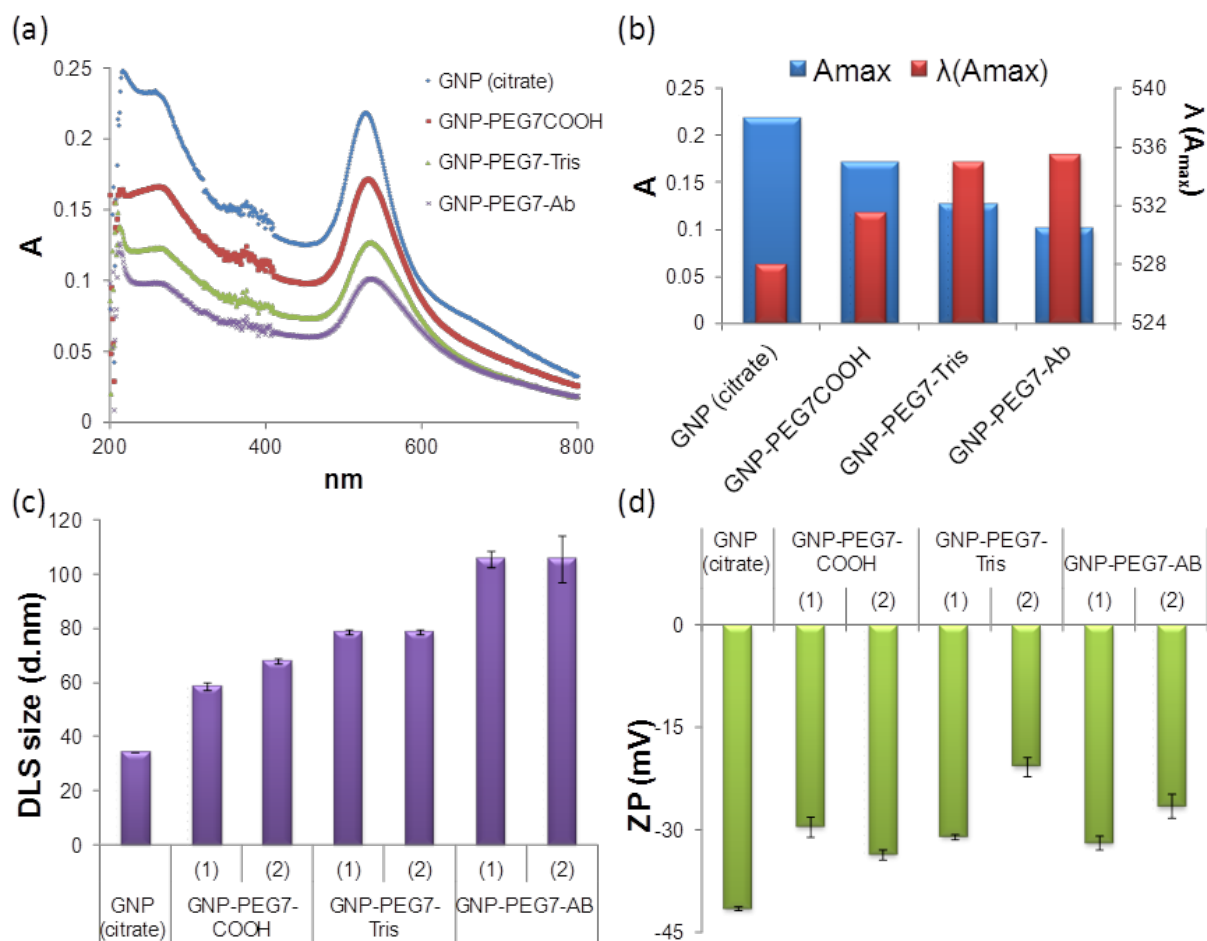


Figure 1: Characterization of functionalized GNPs at distinct stages of surface modification of two different batches by various methods. (a) SPR spectra of citrate-stabilized GNPs (GNP (citrate)), PEG-functionalized GNPs (GNP-PEG₇-COOH and GNP-PEG₇-Tris, respectively), and Ab conjugated GNP (GNP-PEG₇-Ab). (b) SPR spectra show a considerable wavelength shift of the SPR absorption band $\lambda(A_{max})$ and a decrease of its absorbance A with each surface modification step. (c) With each functionalization step, the hydrodynamic diameter of the resultant modified GNPs increases as measured with dynamic light scattering (DLS). (d) All derivatized GNPs showed excellent colloidal stability due to zeta potentials (ZP) of at least -25 mV.

Monitoring wavelength shifts and absorbance variances of the SPR band of GNPs (wavelength maxima around 530 nm) is useful as fast quality control method for the GNP antibody immobilization process and its reproducibility (Figure 1a). With each incremental step of surface chemistry a significant shift of the absorption band to higher wavelength and concomitantly a decrease in the absorbance maximum is observed in

accordance to the Mie theory (Figure 1b). Citrate-capped GNPs reveal the SPR band at 526 nm which is shifted to 532 nm after self-assembly of the bifunctional PEG linker and to 536 nm with the subsequent step of Ab immobilization and Tris-endcapping of carboxylates, respectively, which indicates a slight increase in nanoparticle size. Furthermore, the DLS measurements confirm the increase of size with each successive modification step (Figure 1c, S-1a). The hydrodynamic diameter as determined by DLS shows an increase from 34.3 ± 0.1 nm for citrate-stabilized GNPs over 68 ± 3 nm for carboxy-pegylated GNPs to 106 ± 7 nm for the corresponding GNP-antibody conjugates. The accurate size of supporting citrate-capped GNPs was determined to be 26.2 ± 4.4 nm by transmission electron microscopy and the concentration calculated as $c_{\text{GNP}} = 2.04\text{E-}9$ M.²² Zeta-potentials lower than -25 mV provided all nanoparticle suspensions with satisfactory colloidal stability (Figure 1d, S-1b).

For extraction purposes, the binding capacity of the nano-immunoabsorbent is of prime relevance as well. Thus, the amount of Ab immobilized *via* PEG spacer onto GNPs was quantified in triplicate with enzyme linked anti-IgG-Ab. The quantification was based on a calibration curve obtained by plotting of different anti-CuLDL-Ab concentrations on a microtiter plate. With this approach, the amount of bound Ab per GNP could be determined as 1.7 ± 0.4 Ab / GNP.

Specificity of Distinct GNP-Antibody Conjugates

The effect of immobilization chemistry *via* PEG spacer and direct attachment *via* Protein G binding was studied for different commercially available anti-oxLDL-antibodies by the extraction of Cu^{2+} -oxidized LDL (CuLDL) and native LDL (natLDL), respectively (Figure 2). For this purpose, the sum of the intensities for the precursor ion scan of

m/z 184.1 corresponding to phosphocholines in methanolic extracts of the two proteins as well as of the distinct GNP-Ab conjugates were measured.

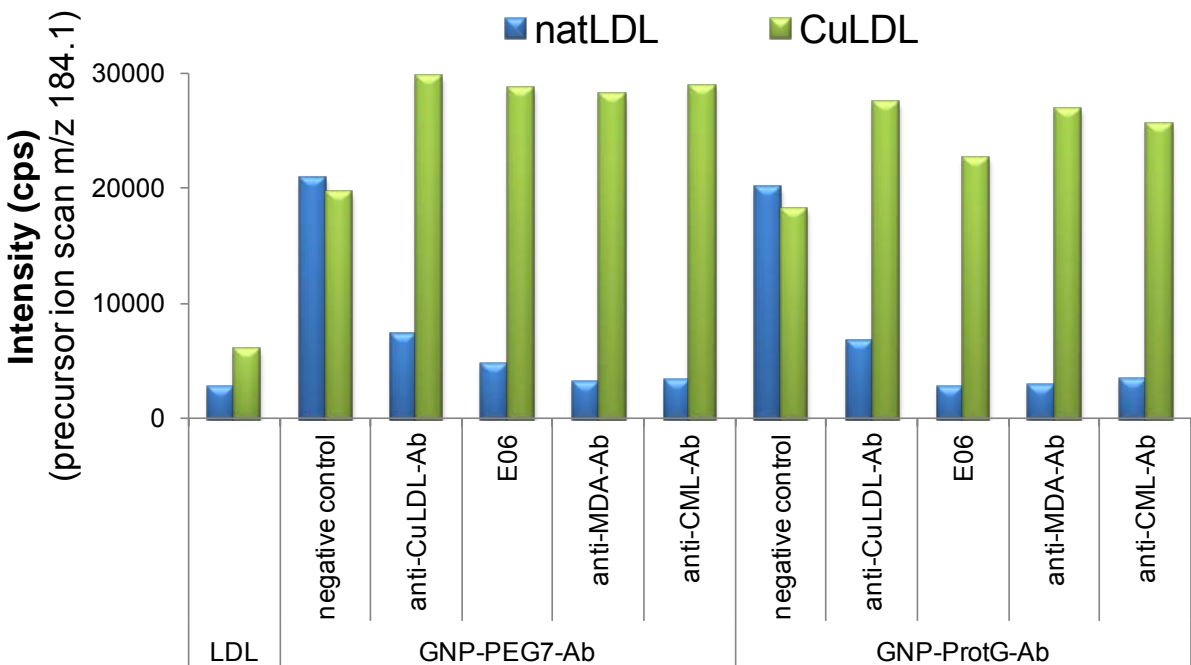


Figure 2: Specificity of distinct Ab-GNP conjugates for oxLDL (CuLDL) vs. native non-oxidized LDL (natLDL) and its dependence on the immobilization chemistry for different antibodies (Ab) via PEG spacer (GNP-PEG₇-Ab) vs. direct attachment via Protein G binding (GNP-ProtG-Ab). Shown are the extraction efficiency for natLDL and CuLDL as sum of extracted (ox)PCs determined with precursor ion scan.

The analysis of natLDL and oxLDL for their content on PCs without enrichment by nanoparticle based trapping reveals nearly the same phosphatidylcholine content for both of them. A significant enrichment of natLDL and oxLDL was furnished when the two lipoprotein solutions were extracted with GNP-PEG₇-COOH as negative control prior to extraction of phospholipids with methanol. These similar signal intensities for both kind of LDL indicate, however, a high unspecific binding. On the contrary, all the GNP-Ab conjugates tested clearly revealed a specific binding and enrichment of the

oxLDL without taking advantage of possible enrichments by volume while natLDL showed solely weak adsorption. Although no significant difference in extraction efficiencies and specificities for (ox)PCs can be derived from these findings in Fig. 2, the covalent immobilization strategy of anti-CuLDL-Ab *via* PEG₇ ligand was preferred for further studies to test this setup for its applicability.

Reduction of Unspecific Binding

Poly(ethylene glycol) ligands are often utilized for creation of biocompatible coatings which repel proteins from the surface.^{32, 33} Furthermore, the hydrophilic HS-PEG₇-COOH spacer ($\log P = -2.07 \pm 0.72$) contributes to the exceptional colloidal stability of the resultant modified GNPs in aqueous solution ($ZP (GNP-PEG_7-COOH) = -31 \pm 2 \text{ mV}$) and is also thought to minimize unspecific bindings of lipophilic phospholipids (*e.g.* $\log P (\text{DMPC}) = 8.75 \pm 0.63$). However, the carboxylic acid groups of the PEG spacer on the outer GNP surface utilized for further conjugation of the Ab to the nanobeads are capable to bind proteins unspecific by ionic interactions. Accordingly, residual carboxylic acid groups were blocked with TRIS after immobilization of Abs onto GNPs to inhibit ionic interactions and hence, to reduce unspecific bindings (Scheme 1, Figure 3).

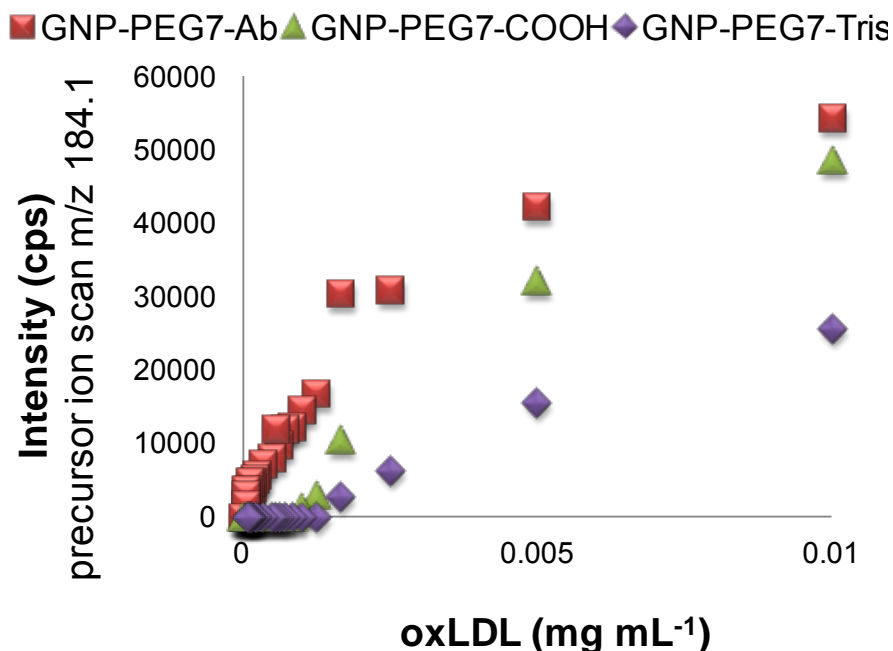


Figure 3: Reduction of unspecific binding by blocking of residual carboxylic groups of GNP-PEG₇-COOH with Tris (GNP-PEG₇-Tris) as measured by a decrease of the summed signal intensities of the precursor ion scan for extracted phosphocholines. In contrast to GNP-PEG₇-Ab, no significant CuLDL binding was observed for GNP-PEG₇-Tris in the low concentration range.

The unspecific binding was tested for HS-PEG₇-COOH modified GNPs without immobilized Abs as negative control in comparison to the corresponding Tris-blocked GNPs. Figure 3 shows the difference of signal intensities of precursor ion scans for phosphocholines summed up in each case after and before blocking with Tris. A significant reduction of unspecific binding was obtained when the residual carboxylic groups were blocked as well as compared to the extraction with GNP-PEG₇-Ab. It is evident that the GNP-Ab conjugate has higher binding capacity especially in the lower concentration range as compared to the negative control (GNP-PEG₇-Tris). Generally, the total unspecific binding on GNP-PEG₇-Ab is thought to be much lower than shown for GNP-PEG₇-Tris due to the additional steric hindrance of immobilized Abs on the GNP.

Determination of GNP-PEG₇-Ab Affinity and Binding Capacity

In order to characterize the specific binding properties of the optimized GNP-Ab conjugate, a binding assay with oxidized LDL (CuLDL) was performed. Thus, a dilution series of Cu²⁺-oxidized LDL was, after incubation, extracted with GNP-PEG₇-Ab and the supernatants discarded. After several washing steps the bound lipids were extracted from the nanoparticle precipitate with methanol of the same volume as the original sample (*i.e.* no volume enrichment factor was incorporated). All extracted samples as well as the standard solutions before extraction were measured by HPLC-ESI-MS/MS with precursor ion scan monitoring phosphocholines. The sum of the signal intensities were then plotted against the initial CuLDL concentration of the feed solution. Thereby, a saturation curve was obtained for sum of (ox)PCs (Figure 4a, red curve).

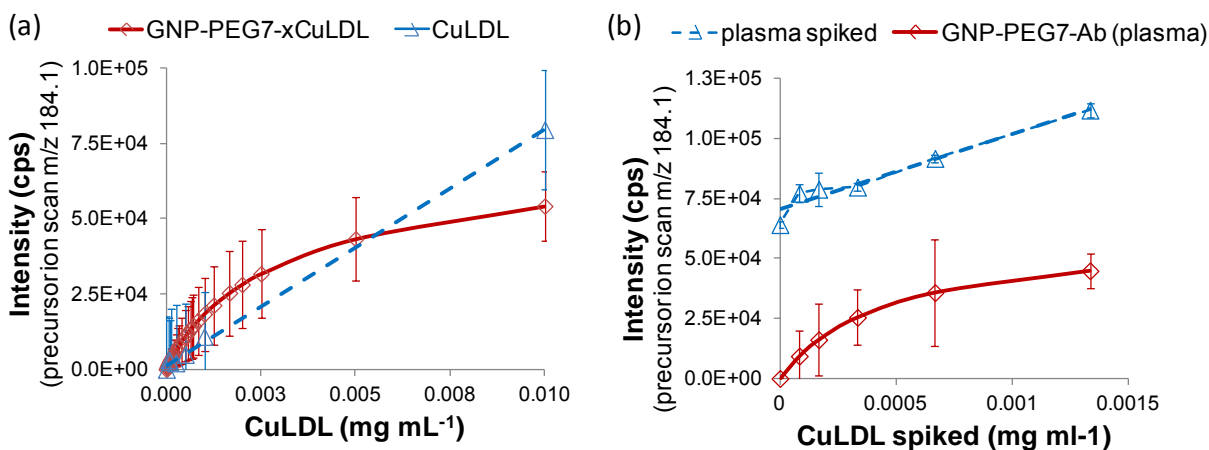


Figure 4: (a) Langmuir adsorption isotherms of steady-state measurements feature saturation curves for CuLDL (red curve) and (b) plasma spiked CuLDL extracted with GNP-PEG₇-Ab (red curve), whereas initial CuLDL and standard addition of plasma gives a linear relationship (blue dashed lines). Both, extraction of standard CuLDL and CuLDL spiked to plasma show a comparable maximum of the binding capacity with an intensity of 5.6E4 and 6.0E4, respectively.

It can be seen that the slope of the saturation curve is nearly the same as for the initial CuLDL without extraction (Figure 4a, blue dashed line) which indicates that oxLDL can

be efficiently extracted with close to quantitative yields in the lower concentration range. At higher concentrations, however, the GNP-Ab conjugate reaches saturation and hence the recovered concentration after extraction by the GNP-Ab conjugate gets lower.

The same experiment was repeated with human plasma as matrix (Figure 4b). OxLDL was spiked at the same concentration levels, and analyzed by HPLC-ESI-MS/MS once without nanoparticle-based extraction (just workup by addition of methanol and analysis from the supernatant, blue dashed line)) and once after nanoparticle-based extraction and elution of (ox)PLs with methanol (red curve). The standard addition method allows further the estimation of (ox)LDL concentration in plasma and it can be seen from Figure 4b that the signal intensities of the initial solutions without nanoparticle-based extraction are significantly higher. Yet, it shows a saturation behavior as expected. Compared to the saturation curve obtained with the standard solution the one resulting from plasma extraction reaches saturation at lower spiked CuLDL which can be explained by the presence of oxLDL in plasma. This may be regarded as indication that the GNP-Ab conjugate is functional and that the GNP-Ab based extraction procedure works. In principle, the binding capacity of the GNP-conjugate can be adjusted with this setup for quantitative yield either by increase of the GNP-Ab conjugate concentration or by utilizing a volume enrichment step after releasing with methanol.

In quantitative terms, the above nanoparticle-based Ab/antigen reaction can be described by the Langmuir adsorption isotherm (equation 1):

$$(1) [RL] = \frac{[RL]_{\max} \cdot [L]}{K_{d(RL)} + [L]}$$

wherein $[RL]$ is the Ab-Ag complex, $[L]$ the equilibrium concentration of free antigen Ag
 (here for sake of simplicity the initial CuLDL), $[RL]_{\max}$ the maximal binding capacity
 (saturation capacity), and $K_{d(RL)}$ the dissociation constant. Fitting eq. 1 to the isotherm
 data (of Fig. 4a using CuLDL standard solutions) for binding of CuLDL to GNP-Ab
 conjugate, provides an apparent dissociation constant K_d of $1.13 \pm 0.73 \text{E-9 M}$. Although
 this K_d -value has to be regarded as a rough estimate of the binding affinity due to
 simplifying assumptions (initial instead of equilibrium CuLDL concentrations, sum of
 precursor ion scan intensity instead of complex concentrations) it is striking that it is in
 the same order of magnitude as determined with immunoassay ($K_d = 1.55 \pm 0.26 \text{E-9 M}$;
 a molecular weight of CuLDL of MW $\sim 3,500$ kDa was used for calculation). It documents
 once more that the GNP-Ab conjugate is functional. Using the CuLDL reference curve
 (blue line in Fig. 4a) as calibration function the maximal binding capacity was
 determined to be $RL_{\max} = 9.53 \pm 1.32 \mu\text{g mL}^{-1}$ ($2.72 \pm 0.38 \text{E-9 M}$). With a nanoparticle
 concentration of approximately $c_{\text{GNP}} = 2.04 \text{E-9 M}$ the bound amount of antigen can be
 calculated as 1.33 ± 0.18 molecules of CuLDL per GNP-PEG₇-Ab conjugate.
 Up to now, the antigenity of (ox)PLs was determined by competitive immunoassays
 using anti-(oxLDL)-Abs. Thereby, the change of the structural motif of oxPCs is
 described as essential for recognition.^{9, 11, 34} Furthermore, Friedman *et al.* declare a
 relationship between the decrease of fatty acid chain length and thus, a decrease of
 hydrophobicity and an increase of the antibody EO6 recognition.¹¹
 With our new approach, an apparent binding constant K_d as measure of antibody affinity
 and thus, of the antigenity of oxPLS, can be determined simultaneously for individual

(oxidized) phospholipids which allows the fast screening, identification and quantitation of a plenty of (new) biomarkers.

To do so, saturation curves were constructed for individual PCs and oxPCs by monitoring MS intensities of compound-specific SRM transitions in positive ion mode (Figure S-3, S-4). Figure 5 shows the estimates of K_d for several known PCs and their oxidation products as obtained by extraction with GNP-PEG₇-Ab and compound-specific SRM detection (Figure 4b).

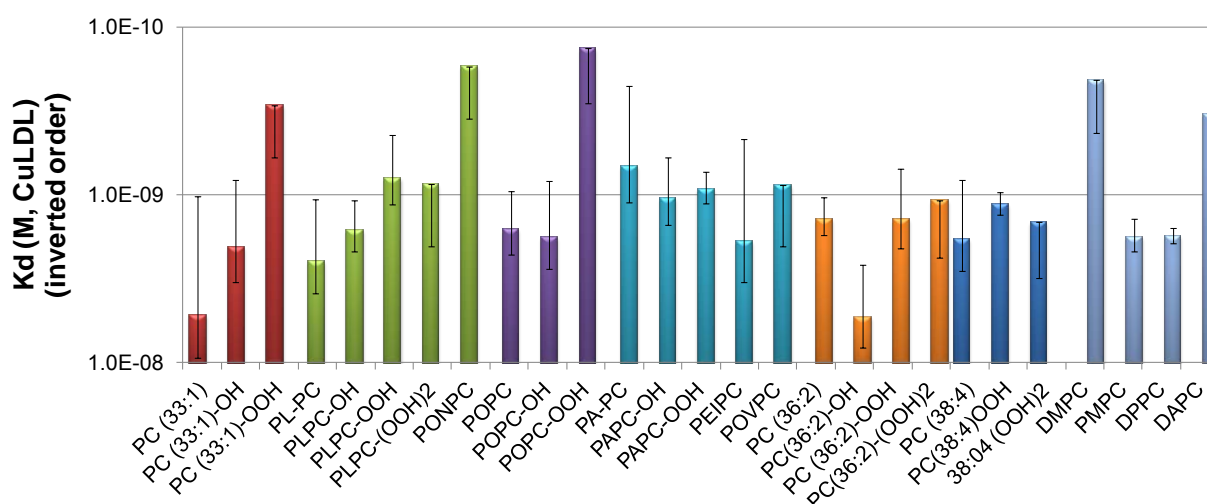


Figure 5: Apparent dissociation constants K_d for several PCs and their oxidation products.

Thereby, with increase of hydroxylation and peroxydation rate a decrease of K_d and thus, an increase of antibody affinity is observed for the oxidation products of PC(33:1), PLPC, and POPC, respectively. This fact signifies the importance of PC oxidation for recognition of oxLDL by the antibody. In contrast, no increase of antibody affinity was found for the PCs with longer chain length such as PAPC (C:DB, 36:4) and PC(36:2) or for saturated PCs such as DMPC, PMPC, PPPC, and DAPC, respectively. This finding

is in accordance to the postulation of Friedman *et al.* who described a decrease of antibody recognition with increase of fatty acid chain lengths.¹¹

CONCLUSIONS

In this paper, we could show the ability and potential of GNP-conjugated anti-(oxLDL)-antibodies for specific recognition, extraction, and enrichment of oxPCs. Combined with LC-ESI-MS/MS analysis sensitive detection, identification, and quantitation of oxidation products of PLs can be performed as a fast screening for biomarkers. Optimization of bioconjugation chemistry to reduce unspecific binding yielded functional nanoparticles with binding capacity for oxLDL. The implementation of these nanoparticles in clinical analysis of plasma samples allows the extraction and enrichment of low-abundant phospholipids while proteins and buffer salts are depleted when methanol is used for release of bound oxLDL from GNP-PEG₇-Ab conjugate. Methanolic supernatants are LC-MS compatible and can be directly injected without further workup. Characterization methods for bioconjugation chemistry such as SPR spectra, size, and zeta potential measurements offer fast control mechanisms. Furthermore, the amount of Ab bound per GNP could be determined by indirect approach with secondary anti-IgG-Ab with 1.7 ± 0.4 Ab / GNP.

Within this systematical study, we could demonstrate the efficiency of the developed GNP-Ab conjugate by determining the dissociation constant K_d for CuLDL with $1.13 \pm 0.73 \text{E-}9$ M which was approved by immunoassay ($K_d = 1.55 \pm 0.26 \text{E-}9$ M). With a maximal binding capacity of $9.5 \pm 1.3 \mu\text{g mL}^{-1}$ ($2.7 \pm 0.4 \text{E-}9$ M) the extraction efficiency can be calculated with 1.33 ± 0.18 CuLDL per GNP-PEG₇-Ab. Additionally, the determination of apparent K_d s for individual PCs and oxPCs offers new possibilities in

targeted lipidomics for fast screening of the antigenity of (oxidized) phospholipids by the autoantibody. In accordance to literature, the oxidation of PCs is found to be essential for antibody recognition, whereas for longer fatty acid chain lengths no antigenity could be observed.

ASSOCIATED CONTENT

Supporting Information

Plots of size (DLS) and zeta-potential measurements, overview about (ox)PCs structures, and further Langmuir plots.

AUTHOR INFORMATION

*** Corresponding Author**

Prof. Dr. Michael Lämmerhofer
Pharmaceutical Analysis and Bioanalysis
Institute of Pharmaceutical Sciences
University of Tübingen
Auf der Morgenstelle 8
72076 Tübingen, Germany
T +49 7071 29 78793, F +49 7071 29 4565
E-mail: michael.laemmerhofer@uni-tuebingen.de

Author Contributions

The manuscript was written through contributions of all authors. All authors have given approval to the final version of the manuscript.

Notes

The authors declare no competing financial interest.

ACKNOWLEDGMENT

Financial support of the “Nano-MALDI” project by the Austrian BMVIT via the “Austrian Nano-Initiative” and “MNT-ERA.NET” is gratefully acknowledged. Gerald Stübiger from the Medical University of Vienna is acknowledged for providing anti-(oxLDL)-antibodies.

REFERENCES

1. Binder, C. J.; Chang, M.-K.; Shaw, P. X.; Miller, Y. I.; Hartvigsen, K.; Dewan, A.; Witztum, J. L., Innate and Acquired Immunity in Atherogenesis. *Nat. Med.* **2002**, *8*, 1218-1226.
2. Weismann, D.; Binder, C. J., The Innate Immune Response to Products of Phospholipid Peroxidation. *Biochim. Biophys. Acta, Biomembr.* **2012**, *1818*, 2465-2475.
3. Tuzcu, E. M.; Kapadia, S. R.; Tutar, E.; Ziada, K. M.; Hobbs, R. E.; McCarthy, P. M.; Young, J. B.; Nissen, S. E., High Prevalence of Coronary Atherosclerosis in Asymptomatic Teenagers and Young Adults: Evidence from Intravascular Ultrasound. *Circulation* **2001**, *103*, 2705-10.
4. Bochkov, V. N.; Oskolkova, O. V.; Birukov, K. G.; Levonen, A.-L.; Binder, C. J.; Stoeckl, J., Generation and Biological Activities of Oxidized Phospholipids. *Antioxid. Redox Signaling* **2010**, *12*, 1009-1059.
5. Greig, F. H.; Kennedy, S.; Spickett, C. M., Physiological Effects of Oxidized Phospholipids and Their Cellular Signaling Mechanisms in Inflammation. *Free Radical Biol. Med.* **2012**, *52*, 266-280.
6. Postle, A. D., Phospholipid Lipidomics in Health and Disease. *Eur. J. Lipid Sci. Technol.* **2009**, *111*, 2-13.
7. Itabe, H., Oxidized Low-Density Lipoprotein as a Biomarker of in Vivo Oxidative Stress: From Atherosclerosis to Periodontitis. *J. Clin. Biochem. Nutr.* **2012**, *51*, 1-8.
8. Berliner, J. A.; Leitinger, N.; Tsimikas, S., The Role of Oxidized Phospholipids in Atherosclerosis. *J Lipid Res* **2009**, *50 Suppl*, S207-12.
9. Boullier, A.; Friedman, P.; Harkewicz, R.; Hartvigsen, K.; Green, S. R.; Almazan, F.; Dennis, E. A.; Steinberg, D.; Witztum, J. L.; Quehenberger, O., Phosphocholine as a Pattern Recognition Ligand for Cd36. *J. Lipid Res.* **2005**, *46*, 969-976.
10. Hulthe, J., Antibodies to Oxidized Ldl in Atherosclerosis Development-Clinical and Animal Studies. *Clin. Chim. Acta* **2004**, *348*, 1-8.
11. Friedman, P.; Horkko, S.; Steinberg, D.; Witztum, J. L.; Dennis, E. A., Correlation of Antiphospholipid Antibody Recognition with the Structure of Synthetic Oxidized Phospholipids.

- Importance of Schiff Base Formation and Aldol Condensation. *J. Biol. Chem.* **2002**, 277, 7010-7020.
12. Yang, K.; Han, X., Accurate Quantification of Lipid Species by Electrospray Ionization Mass Spectrometry - Meets a Key Challenge in Lipidomics. *Metabolites* **2011**, 1, 21-40.
 13. Brouwers, J. F., Liquid Chromatographic-Mass Spectrometric Analysis of Phospholipids. Chromatography, Ionization and Quantification. *Biochim. Biophys. Acta, Mol. Cell Biol. Lipids* **2011**, 1811, 763-775.
 14. Zhao, Z.; Xu, Y., An Extremely Simple Method for Extraction of Lysophospholipids and Phospholipids from Blood Samples. *J. Lipid Res.* **2010**, 51, 652-659.
 15. Li, M.; Zhou, Z.; Nie, H.; Bai, Y.; Liu, H., Recent Advances of Chromatography and Mass Spectrometry in Lipidomics. *Anal Bioanal Chem* **2011**, 399, 243-9.
 16. Spickett, C. M.; Dever, G., Studies of Phospholipid Oxidation by Electrospray Mass Spectrometry: From Analysis in Cells to Biological Effects. *BioFactors* **2005**, 24, 17-31.
 17. Postle, A. D.; Wilton, D. C.; Hunt, A. N.; Attard, G. S., Probing Phospholipid Dynamics by Electrospray Ionisation Mass Spectrometry. *Prog. Lipid Res.* **2007**, 46, 200-224.
 18. O'Donnell, V. B., Mass Spectrometry Analysis of Oxidized Phosphatidylcholine and Phosphatidylethanolamine. *Biochim. Biophys. Acta, Mol. Cell Biol. Lipids* **2011**, 1811, 818-826.
 19. Sparvero, L. J.; Amoscato, A. A.; Dixon, C. E.; Long, J. B.; Kochanek, P. M.; Pitt, B. R.; Bayir, H.; Kagan, V. E., Mapping of Phospholipids by Maldi Imaging (Maldi-Msi): Realities and Expectations. *Chem Phys Lipids* **2012**, 165, 545-62.
 20. Eberlin, L. S.; Ferreira, C. R.; Dill, A. L.; Ifa, D. R.; Cooks, R. G., Desorption Electrospray Ionization Mass Spectrometry for Lipid Characterization and Biological Tissue Imaging. *Biochim. Biophys. Acta, Mol. Cell Biol. Lipids* **2011**, 1811, 946-960.
 21. Fuchs, B.; Schiller, J., Application of Maldi-Tof Mass Spectrometry in Lipidomics. *Eur. J. Lipid Sci. Technol.* **2009**, 111, 83-98.
 22. Hinterwirth, H.; Kappel, S.; Waitz, T.; Prohaska, T.; Lindner, W.; Lammerhofer, M., Quantifying Thiol Ligand Density of Self-Assembled Monolayers on Gold Nanoparticles by Inductively Coupled Plasma-Mass Spectrometry. *ACS Nano* **2013**, 7, 1129-1136.
 23. McKenzie, F.; Steven, V.; Ingram, A.; Graham, D., Quantitation of Biomolecules Conjugated to Nanoparticles by Enzyme Hydrolysis. *Chem. Commun.* **2009**, 2872-2874.
 24. Wen, S.; Liu, D.-F.; Liu, Z.; Harris, S.; Yao, Y.-Y.; Ding, Q.; Nie, F.; Lu, T.; Chen, H.-J.; An, Y.-L.; Zang, F.-C.; Teng, G.-J., Oxldl-Targeted Iron Oxide Nanoparticles for in Vivo Mri Detection of Perivascular Carotid Collar Induced Atherosclerotic Lesions in Apoe-Deficient Mice. *J. Lipid Res.* **2012**, 53, 829-838.
 25. Oliveira, M. D. L.; Abdalla, D. S. P.; Guilherme, D. F.; Faulin, T. E. S.; Andrade, C. A. S., Impedimetric Immunosensor for Electronegative Low Density Lipoprotein (Ldl-) Based on Monoclonal Antibody Adsorbed on (Polyvinyl Formal)-Gold Nanoparticles Matrix. *Sens. Actuators, B* **2011**, B155, 775-781.
 26. Hinterwirth, H.; Lindner, W.; Laemmerhofer, M., Bioconjugation of Trypsin onto Gold Nanoparticles: Effect of Surface Chemistry on Bioactivity. *Anal. Chim. Acta* **2012**, 733, 90-97.
 27. Di Pasqua, A. J.; Mishler, R. E.; Ship, Y.-L.; Dabrowiak, J. C.; Asefa, T., Preparation of Antibody-Conjugated Gold Nanoparticles. *Mater. Lett.* **2009**, 63, 1876-1879.
 28. Masson, J.-F.; Battaglia, T. M.; Cramer, J.; Beaudoin, S.; Sierks, M.; Booksh, K. S., Reduction of Nonspecific Protein Binding on Surface Plasmon Resonance Biosensors. *Anal. Bioanal. Chem.* **2006**, 386, 1951-1959.

29. James, A. E.; Driskell, J. D., Monitoring Gold Nanoparticle Conjugation and Analysis of Biomolecular Binding with Nanoparticle Tracking Analysis (Nta) and Dynamic Light Scattering (Dls). *Analyst* **2013**, *138*, 1212-1218.
30. Oskolkova, O. V.; Afonyushkin, T.; Preinerstorfer, B.; Bicker, W.; von, S. E.; Hainzl, E.; Demyanets, S.; Schabbauer, G.; Lindner, W.; Tselepis, A. D.; Wojta, J.; Binder, B. R.; Bochkov, V. N., Oxidized Phospholipids Are More Potent Antagonists of Lipopolysaccharide Than Inducers of Inflammation. *J. Immunol.* **2010**, *185*, 7706-7712.
31. Gonzalez, A.; Preinerstorfer, B.; Lindner, W., Selective Enrichment of Phosphatidylcholines from Food and Biological Matrices Using Metal Oxides as Solid-Phase Extraction Materials Prior to Analysis by Hplc-Esi-Ms/Ms. *Anal. Bioanal. Chem.* **2010**, *396*, 2965-2975.
32. Chen, H.; Yuan, L.; Song, W.; Wu, Z.; Li, D., Biocompatible Polymer Materials: Role of Protein-Surface Interactions. *Prog. Polym. Sci.* **2008**, *33*, 1059-1087.
33. Knop, K.; Hoogenboom, R.; Fischer, D.; Schubert, U. S., Poly(Ethylene Glycol) in Drug Delivery: Pros and Cons as Well as Potential Alternatives. *Angew. Chem., Int. Ed.* **2010**, *49*, 6288-6308.
34. Itabe, H.; Yamamoto, H.; Imanaka, T.; Shimamura, K.; Uchiyama, H.; Kimura, J.; Sanaka, T.; Hata, Y.; Takano, T., Sensitive Detection of Oxidatively Modified Low Density Lipoprotein Using a Monoclonal Antibody. *J. Lipid Res.* **1996**, *37*, 45-53.

A-4.1 Supplementary Information

Hinterwirth H.; Lindner W.; Lämmerhofer M.

unpublished manuscript

Gold Nanoparticle Conjugated Anti-Oxidized Low-Density Lipoprotein-Antibodies and Liquid Chromatography/Mass Spectrometry as Tool for Targeted Lipidomics

*Helmut Hinterwirth,[†] Wolfgang Lindner,[†] Michael Lämmerhofer^{‡, *}*

[†] Department of Analytical Chemistry, University of Vienna, Währingerstrasse 38,
1090 Vienna, Austria

[‡] Institute of Pharmaceutical Sciences, University of Tübingen, Auf der
Morgenstelle 8, 72076 Tübingen, Germany

*** Corresponding Author**

Prof. Dr. Michael Lämmerhofer

Pharmaceutical Analysis and Bioanalysis

Institute of Pharmaceutical Sciences

University of Tübingen

Auf der Morgenstelle 8

72076 Tübingen, Germany

T +49 7071 29 78793, F +49 7071 29 4565

E-mail: michael.laemmerhofer@uni-tuebingen.de

24 **ABSTRACT**

25 The supporting information shows distribution curves of size and zeta potential
26 measurements. Furthermore, saturation curves of phosphatidylcholines (PCs) and
27 their oxidation products (oxPCs) used for the apparent dissociation constant
28 calculation (see main manuscript) are depicted.

29 **Size and Zeta Potential Measurements**

30 Fast analysis methods are required as control mechanism for characterization of
31 immobilization chemistry. Next to the measurement of the surface plasmon
32 resonance (SPR) spectra, the increase of size with each immobilization layer is a
33 useful tool to monitor the success of GNP modification. Although size and size
34 distributions are always overestimated by dynamic light scattering (DLS)¹ in
35 comparison to transmission electron microscopy, because it measures the
36 hydrodynamic diameter, it offers a simple control tool for the success of the
37 immobilization chemistry (Figure S1a). Furthermore, the zeta potential (ZP) is a
38 measure for the stability of the colloidal suspension (Figure S-1b).² DLS and ZP were
39 measured with Malvern Zetasizer Instruments Nano series, Prager Instruments.

40

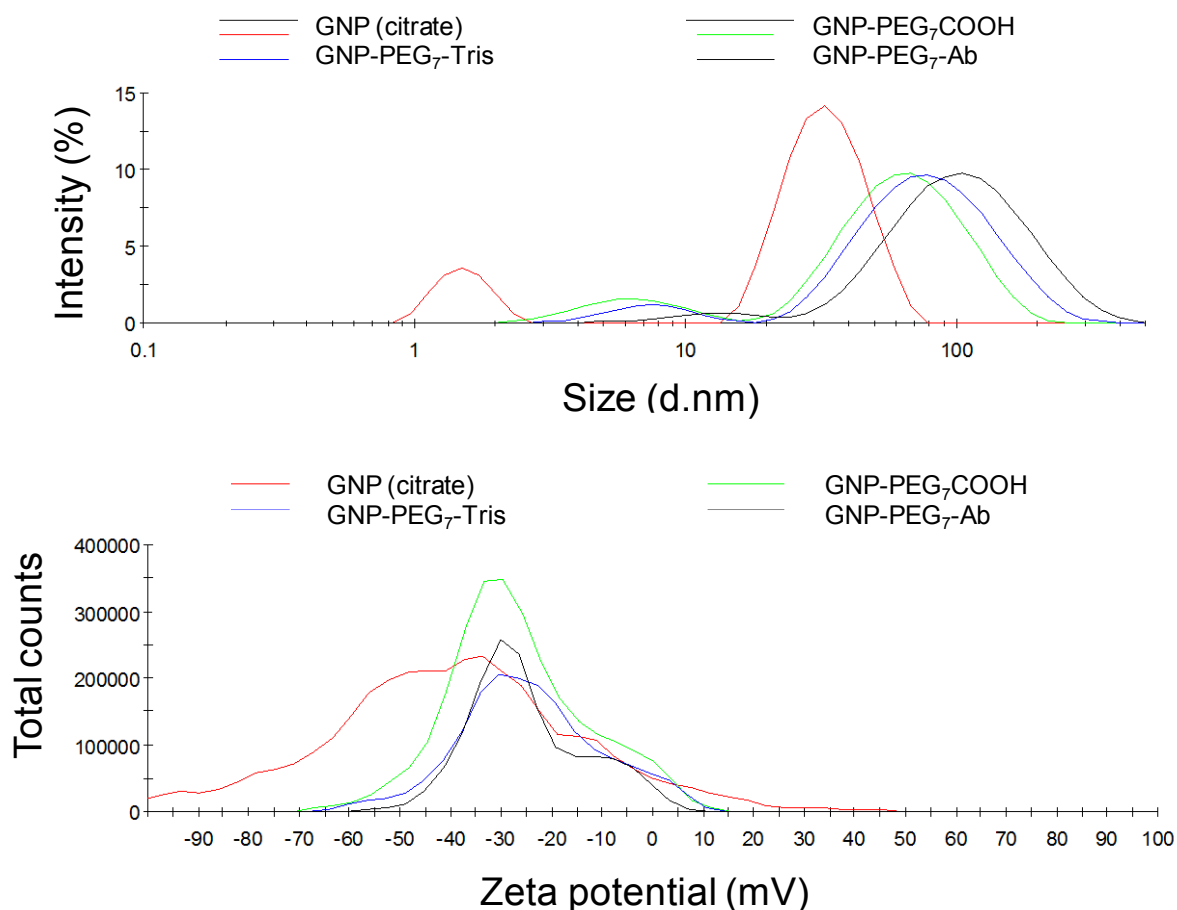


Figure S1: (a) Plots of nanoparticle size distributions as measured by dynamic light scattering (DLS) show an increase of the hydrodynamic diameter with each immobilization step from citrate stabilized GNPs (GNP (citrate)) to SAM formation of PEG (GNP-PEG₇-COOH and GNP-PEG₇-Tris, respectively) and immobilization of antibody (GNP-PEG₇-Ab). (b) All GNPs were quite stable with a zeta potential lower than -25mV.

Phosphatidylcholines

Table S1 gives an overview about the compound names, their abbreviations, and structure composition of (ox)PCs used in the main document.

Table S1: Overview about PCs and oxPCs

Abbreviation	Compound name	Formula	sn-1	sn-2
lyso-PC16	1-Palmitoyl-2-hydroxy- <i>sn</i> -glycero-3-phosphocholine	C ₂₄ H ₅₀ NO ₇ P	16:0	0:0
lyso-PC18	1-Stearoyl-2-hydroxy- <i>sn</i> -glycero-3-phosphocholine	C ₂₆ H ₅₄ NO ₇ P	18:0	0:0
POVPC	1-Palmitoyl-2-(5-oxo-valeroyl)- <i>sn</i> -glycero-3-phosphocholine	C ₂₉ H ₅₆ NO ₉ P	16:0	5:0 (Aldo)
PONPC	1-Palmitoyl-2-(9'-oxo-nonanoyl)- <i>sn</i> -glycero-3-phosphocholine	C ₃₃ H ₆₄ NO ₉ P	16:0	9:0 (Aldo)
PAZPC	1-Palmitoyl-2-azelaoyl- <i>sn</i> -glycero-3-phosphocholine	C ₃₃ H ₆₄ NO ₁₀ P	16:0	9:0 (COOH)
DMPC	1,2-Dimyristoyl- <i>sn</i> -glycero-3-phosphocholine	C ₃₆ H ₇₂ NO ₈ P	14:0	14:0
PMPC	1-Palmitoyl-2-myristoyl- <i>sn</i> -glycero-3-phosphocholine	C ₃₈ H ₇₆ NO ₈ P	16:0	14:0
DPPC	1,2-Dipalmitoyl- <i>sn</i> -glycero-3-phosphocholine	C ₄₀ H ₈₀ NO ₈ P	16:0	16:0
PC (33:1)	1-Vaccenoyl-2-pentadecanoyl- <i>sn</i> -glycero-3-phosphocholine	C ₄₁ H ₈₀ NO ₈ P	18:1 (11Z)	15:0
PLPC	1-Palmitoyl-2-linoleoyl- <i>sn</i> -glycero-3-phosphocholine	C ₄₂ H ₈₀ O ₈ NP	16:0	18:2 (9Z, 12Z)
POPC	1-Palmitoyl-2-oleoyl- <i>sn</i> -glycero-3-phosphocholine	C ₄₂ H ₈₂ NO ₈ P	16:0	18:1 (9Z)
PAPC	1-Palmitoyl-2-arachidonoyl- <i>sn</i> -glycero-3-phosphocholine	C ₄₄ H ₈₀ NO ₈ P	16:0	20:4 (5Z, 8Z, 11Z, 14Z)
PC (36:2)	1-octadecanoyl-2-(9Z, 12Z-octadecadienoyl)- <i>sn</i> -glycero-3-phosphocholine	C ₄₄ H ₈₄ NO ₈ P	18:0	18:2 (9Z, 12Z)
PC (38:4)	1-stearoyl-2-arachidonoyl- <i>sn</i> -glycero-3-phosphocholine	C ₄₆ H ₈₄ NO ₈ P	18:0	20:4 (5Z, 8Z, 11Z, 14Z)
DAPC	1,2-Diarachidoyl- <i>sn</i> -glycero-3-phosphocholine	C ₄₈ H ₉₆ NO ₈ P	20:0	20:0
PEIPC	1-Palmitoyl-2-(5,6)-epoxyisoprostane E2- <i>sn</i> -glycero-3-phosphocholine			

Figure S2 shows the structure of saturated, unsaturated, and oxidized PCs as well as of lyso-PCs as they are used for SRM detection.

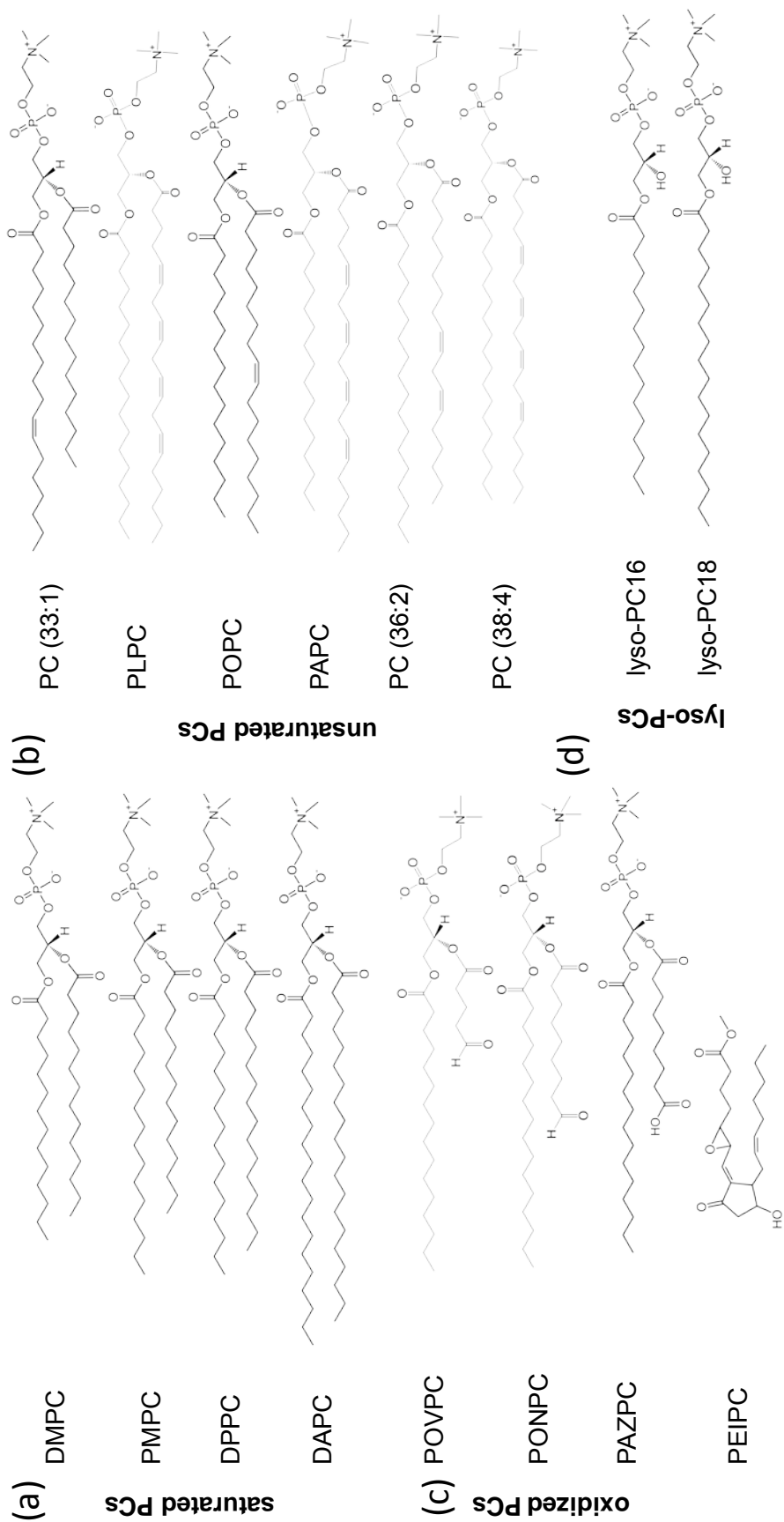


Figure S2: Overview about the structures of (a) saturated PCs, (b) unsaturated PCs, (c) oxidized PCs, and (d) lyso-PCs used for SRM detection.

Determination of Antibody Affinity and GNP-PEG₇-Ab binding capacity

Figure S3 shows Langmuir isotherm plots of different PCs and their oxidation products compared to the direct measurements of CuLDL. The isotherms were determined by steady-state measurements of different CuLDL concentrations extracted with GNP-PEG₇-Ab conjugate and release of the (ox)PCs from the GNP-Ab conjugate with methanol.

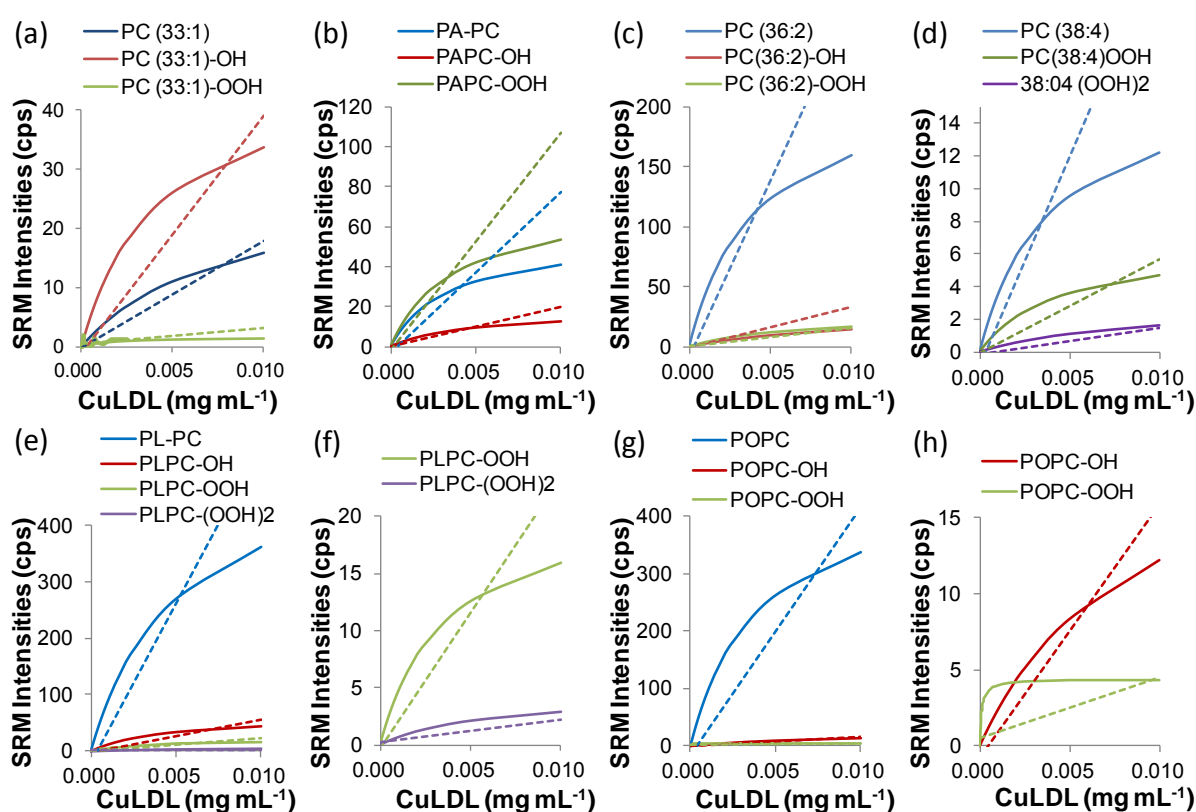


Figure S3: Extraction of CuLDL with GNP-PEG₇-Ab. Shown are the saturation curves after extraction (solid line) compared to direct measurements of CuLDL (dotted line) for several PCs and their oxidation products: (a) PC(33:1), (b) PAPC, (c) PC(36:2), (d) PC(38:4), (e) PLPC, (f) zoom in of PLPC oxidation products, (g) POPC (h) zoom in of POPC oxidation products.

The efficiency of GNP-PEG₇-Ab conjugate for CuLDL extraction was proved by using plasma spiked CuLDL as matrix. The saturation curves of for CuLDL and plasma spiked CuLDL along with corresponding direct measurement without extraction are shown for several PCs and their oxidation products (Figure S-4, a-f).

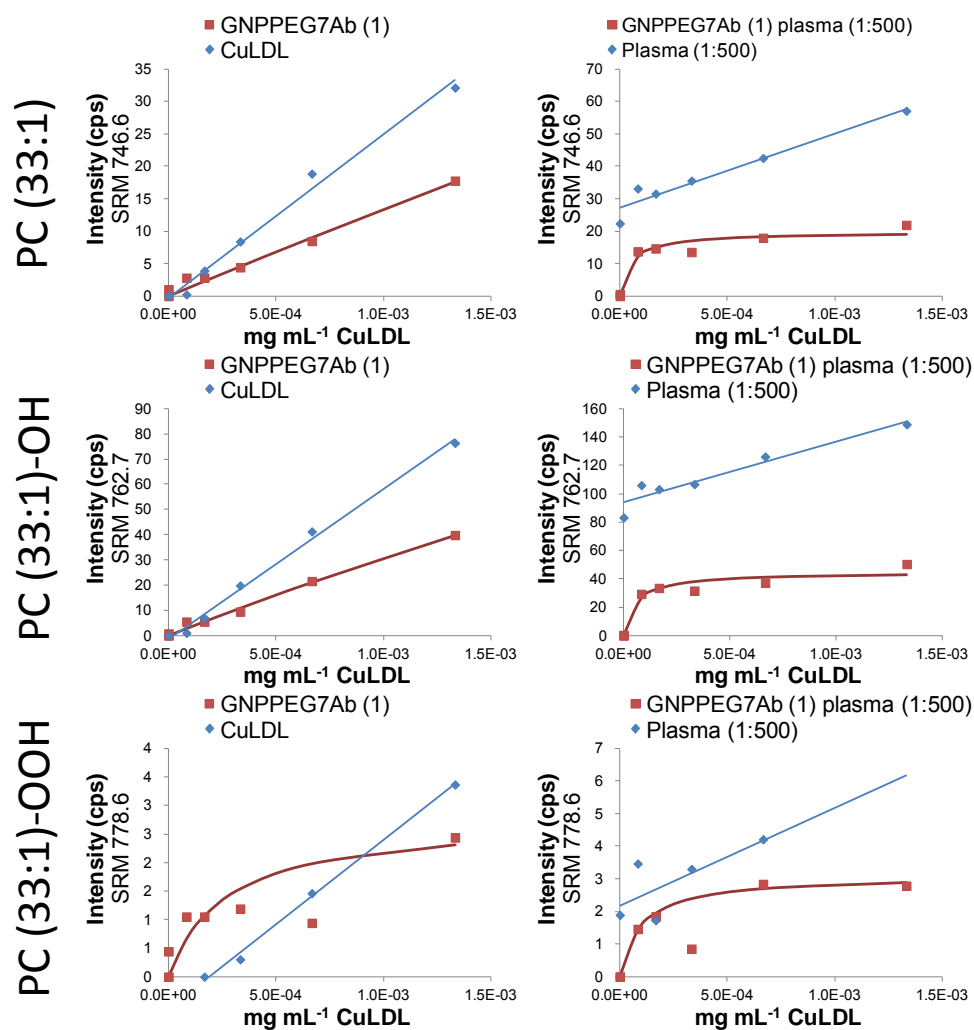


Figure S4a: Extraction of CuLDL (left, red line) and plasma spiked CuLDL (right, red line) with GNP-PEG₇-Ab is shown for PC(33:1) and its oxidation products. Comparison to direct measurement of CuLDL and plasma standard addition, respectively (blue lines).

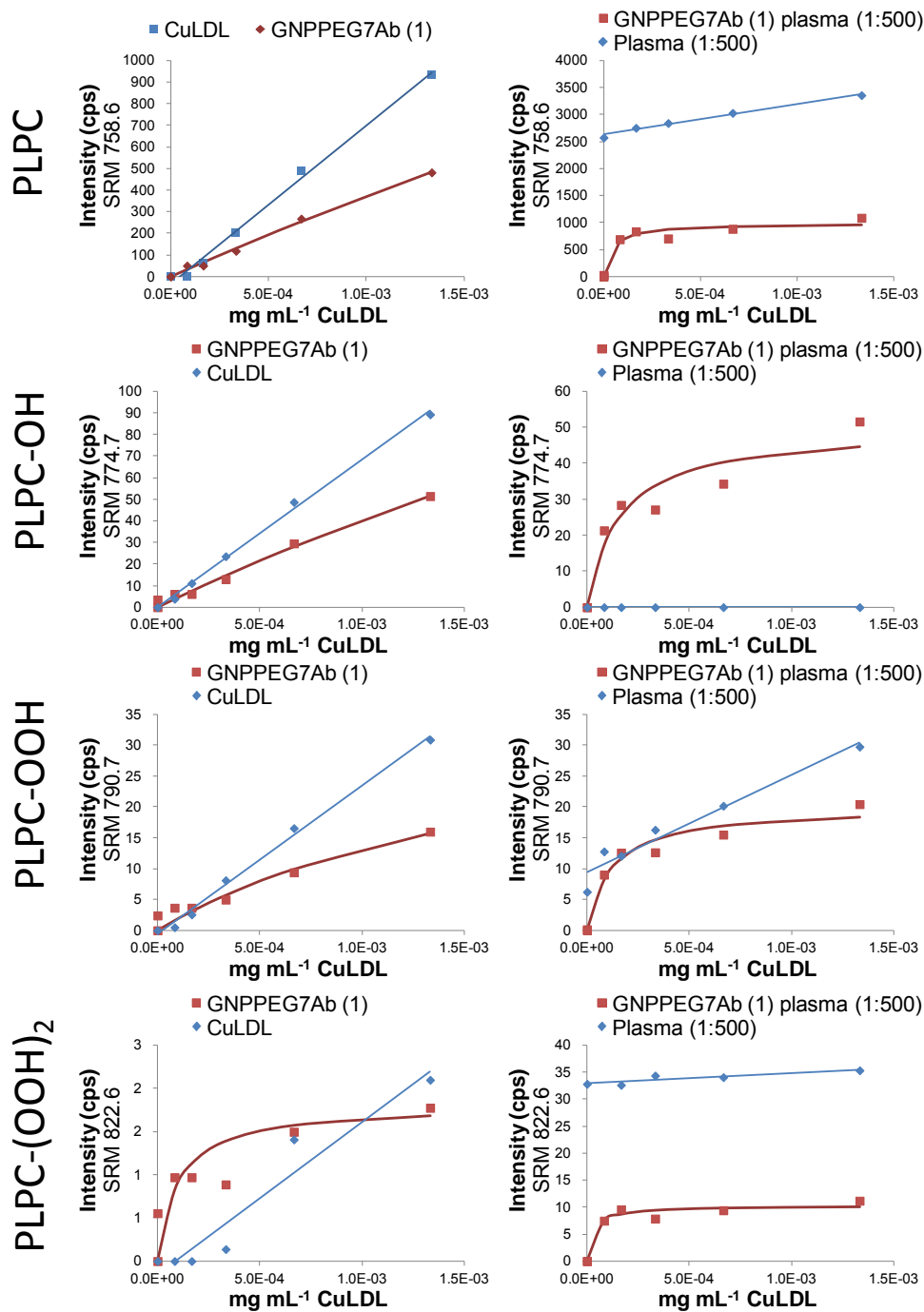


Figure S4b: Extraction of CuLDL (left, blue line) and plasma spiked CuLDL (right, blue line) with GNP-PEG₇-Ab is shown for PLPC and its oxidation products. Comparison to direct measurement of CuLDL and plasma standard addition, respectively (red lines).

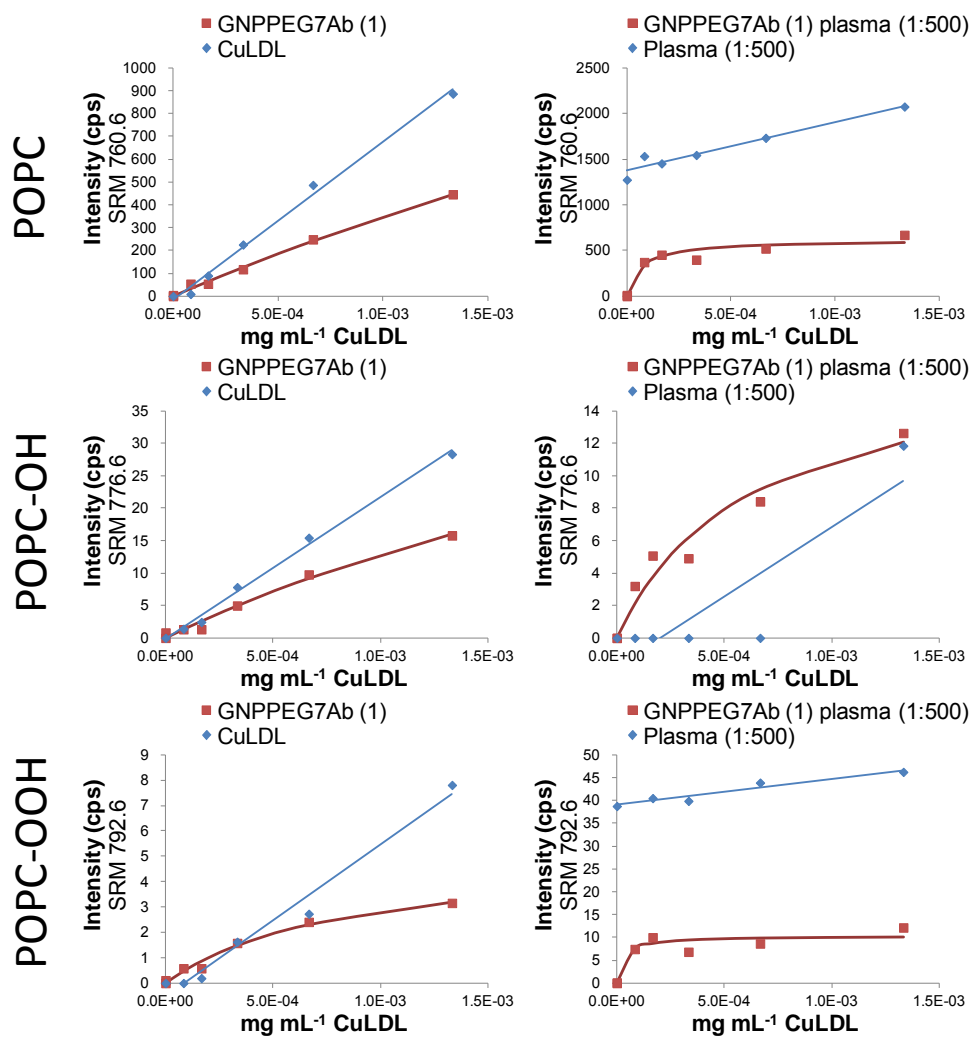


Figure S4c: Extraction of CuLDL (left, blue line) and plasma spiked CuLDL (right, blue line) with GNP-PEG₇-Ab is shown for POPC and its oxidation products. Comparison to direct measurement of CuLDL and plasma standard addition, respectively (red lines).

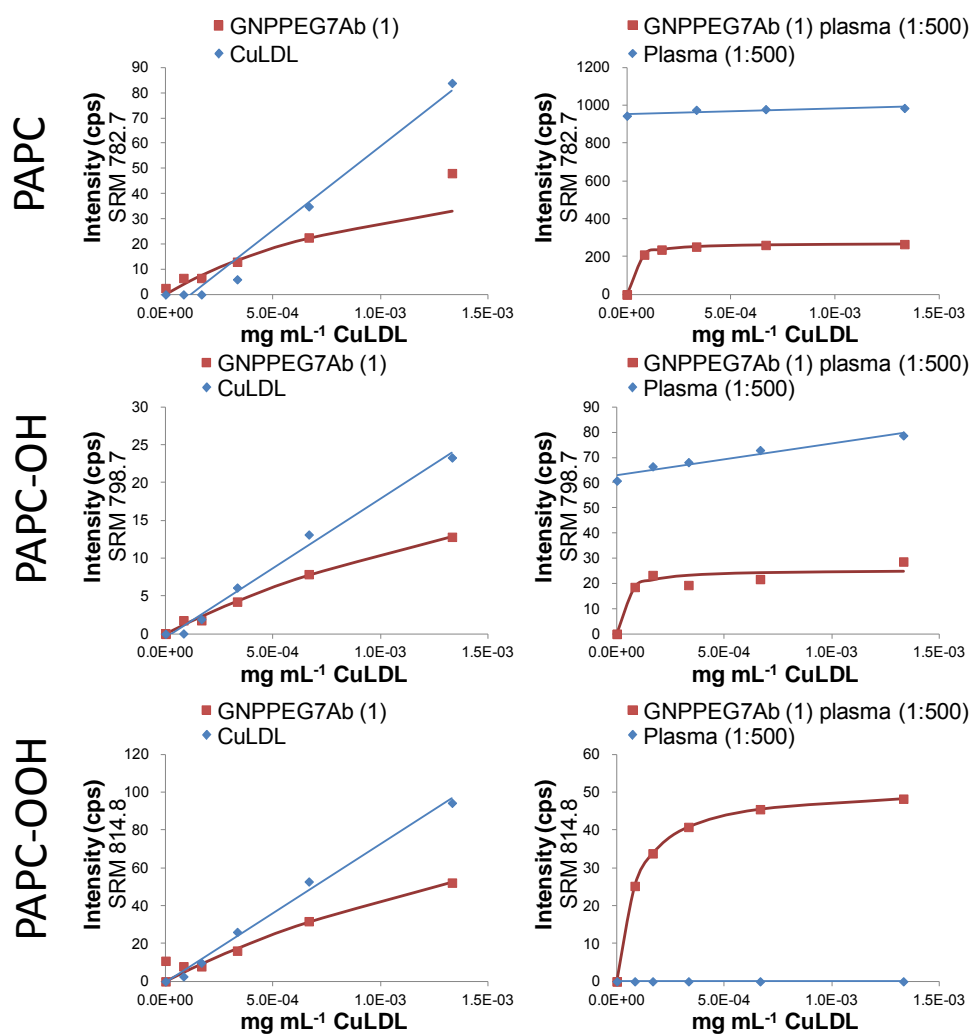


Figure S4d: Extraction of CuLDL (left, blue line) and plasma spiked CuLDL (right, blue line) with GNP-PEG₇-Ab is shown for PAPC and its oxidation products. Comparison to direct measurement of CuLDL and plasma standard addition, respectively (red lines).

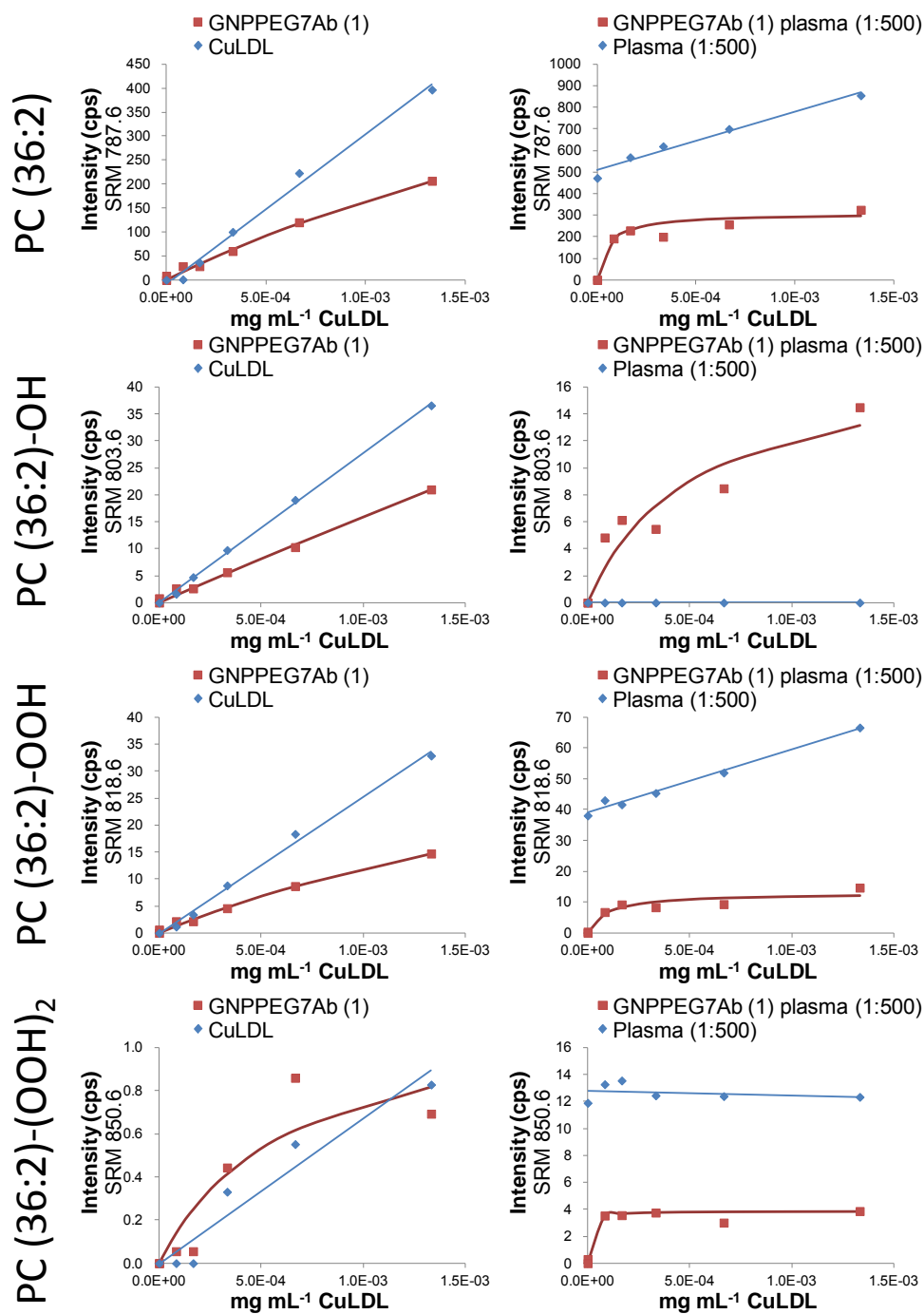


Figure S4e: Extraction of CuLDL (left, blue line) and plasma spiked CuLDL (right, blue line) with GNP-PEG₇-Ab is shown for PC (36:2) and its oxidation products. Comparison to direct measurement of CuLDL and plasma standard addition, respectively (red lines).

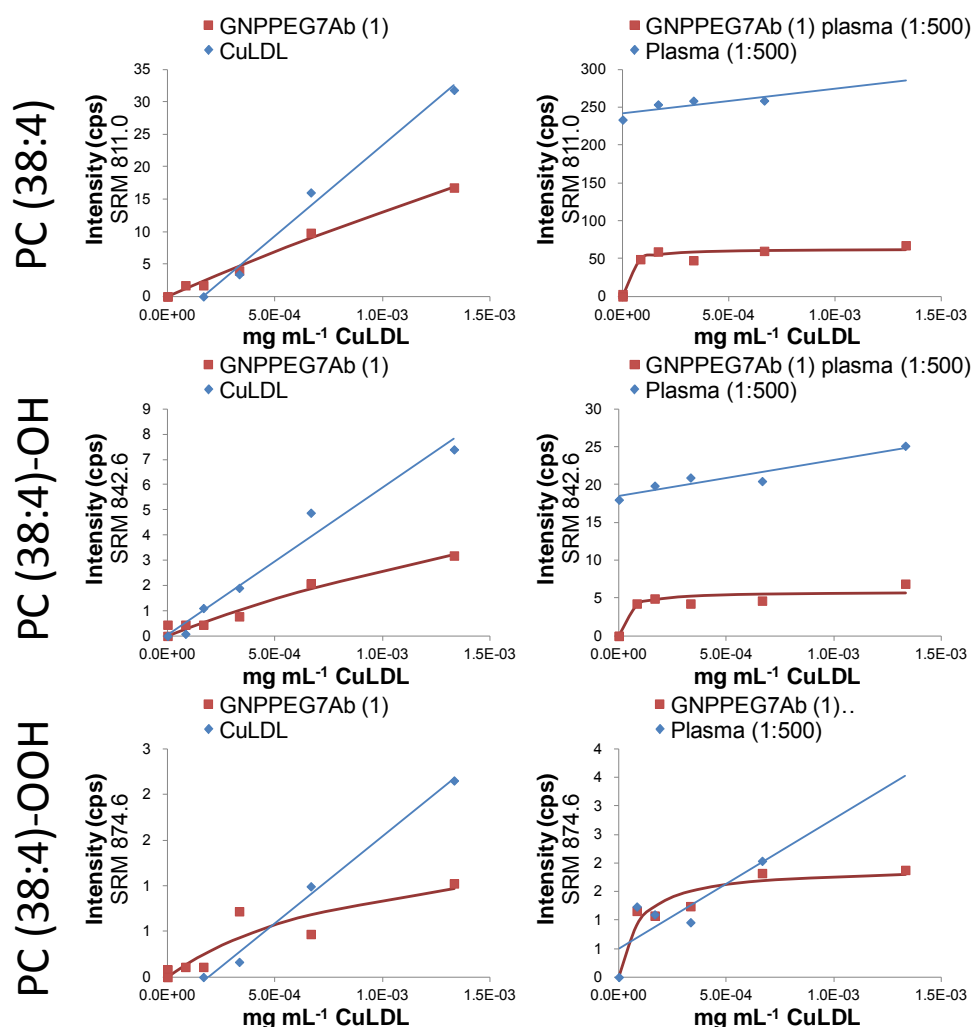


Figure S4f: Extraction of CuLDL (left, blue line) and plasma spiked CuLDL (right, blue line) with GNP-PEG₇-Ab is shown for PC (38:4) and its oxidation products. Comparison to direct measurement of CuLDL and plasma standard addition, respectively (red lines).

REFERENCES

1. Khlebtsov, B. N.; Khlebtsov, N. G., On the measurement of gold nanoparticle sizes by the dynamic light scattering method. *Colloid J.* **2011**, 73 (1), 118-127.
2. Doane, T. L.; Chuang, C.-H.; Hill, R. J.; Burda, C., Nanoparticle ζ -Potentials. *Acc. Chem. Res.* **2012**, 45, 317-326.

B-1. Selectivity Issues in Targeted Metabolomics: Separation of Phosphorylated Carbohydrate Isomers by Mixed-Mode Hydrophilic Interaction/Weak Anion Exchange Chromatography

Hinterwirth, H.; Laemmerhofer, M.; Preinerstorfer, B.; Gargano, A.; Reischl, R.; Bicker, W.; Trapp, O.; Brecker, L.; Lindner, W.

Journal of Separation Science **2010**, 33, 3273-3282.

Helmut Hinterwirth¹
 Michael Lämmerhofer¹
 Beatrix Preinerstorfer¹
 Andrea Gargano¹
 Roland Reischl¹
 Wolfgang Bicker¹
 Oliver Trapp²
 Lothar Brecker³
 Wolfgang Lindner¹

¹Department of Analytical Chemistry, University of Vienna, Vienna, Austria

²Organisch-Chemisches Institut, Ruprecht-Karls-Universität Heidelberg, Heidelberg, Germany

³Department of Organic Chemistry, University of Vienna, Vienna, Austria

Received June 10, 2010

Revised July 20, 2010

Accepted August 15, 2010

Research Article

Selectivity issues in targeted metabolomics: Separation of phosphorylated carbohydrate isomers by mixed-mode hydrophilic interaction/weak anion exchange chromatography

Phosphorylated carbohydrates are important intracellular metabolites and thus of prime interest in metabolomics research. Complications in their analysis arise from the existence of structural isomers that do have similar fragmentation patterns in MS/MS and are hard to resolve chromatographically. Herein, we present selective methods for the liquid chromatographic separation of sugar phosphates, such as hexose and pentose phosphates, 2- and 3-phosphoglycerate, dihydroxyacetone phosphate and glyceraldehyde 3-phosphate, as well as glucosamine 1- and 6-phosphate utilizing mixed-mode chromatography with reversed-phase/weak anion-exchangers and a charged aerosol detector. The best results were obtained when the reversed-phase/weak anion-exchanger column was operated under hydrophilic interaction liquid chromatography elution conditions. The effects of various chromatographic parameters were examined and are discussed on the basis of a simple stoichiometric displacement model for explaining ion-exchange processes. Employed acidic conditions have led to the complete separation of α - and β -anomers of glucose 6-phosphate at low temperature. The anomers coeluted in a single peak at elevated temperatures ($>40^{\circ}\text{C}$) (peak coalescence), while at intermediate temperatures on-column interconversion with a plateau in-between resolved anomer peaks was observed with apparent reaction rate constants between 0.1 and $27.8 \times 10^{-4} \text{ s}^{-1}$. Dynamic HPLC under specified conditions enabled to investigate mutarotation of phosphorylated carbohydrates, their interconversion kinetics, and energy barriers for interconversion. A complex mixture of six hexose phosphate structural isomers could be resolved almost completely.

Keywords: Charged aerosol detection / Hydrophilic interaction liquid chromatography (HILIC) / Mixed-mode stationary phase / Reversed-phase/weak anion-exchange material / Sugar phosphate isomers
 DOI 10.1002/jssc.201000412



1 Introduction

Phosphorylated carbohydrates are key metabolites in various central metabolic pathways including glycolysis and glycogenolysis pathways as well as the pentosephosphate cycle. Therefore, their reliable analytical determination is of prime

importance in metabolomics research [1–3], in particular for the monitoring of intracellular metabolites in quantitative metabolic profiling studies [4–8].

However, the quantitative determination of phosphorylated carbohydrates is far from being a trivial task. Difficulties arise from their hydrophilicity (making them inadequate for common RPLC analysis), their propensity to adhere to glass and stainless steel surfaces [9] associated with analyte losses and low sensitivity, lack of specific fragmentations in MS/MS revealing typically non-specific water and phosphate cleavage, and in particular the existence of various structural isomers with similar fragmentation patterns in MS/MS.

Owing to missing chromatographic and mass spectrometric differentiation in the course of analysis of isomeric phosphorylated carbohydrates, many analytical assays determined hexose and pentose phosphates as well as other sugar phosphates as a sum of their individual

Correspondence: Dr. Michael Lämmerhofer, University of Vienna, Faculty of Chemistry, Department of Analytical Chemistry, Waehringer Strasse 38, A-1090 Vienna, Austria
E-mail: michael.laemmerhofer@univie.ac.at
Fax: +43-1-4277-9523

Abbreviations: **G1P**, D-glucose 1-phosphate; **G6P**, D-glucose 6-phosphate; **F6P**, D-fructose 6-phosphate; **Gal1P**, D-galactose 1-phosphate; **M1P**, D-mannose 1-phosphate; **M6P**, D-mannose 6-phosphate; **Rib5P**, D-ribose 5-phosphate; **Rul5P**, D-ribulose 5-phosphate; **Xyl5P**, D-xylulose 5-phosphate

isomeric forms [6, 7, 10–12]. Yet, various partially selective chromatographic assays were proposed as well which allowed separation of some isomeric forms while others coeluted, including for instance a HILIC method with ZIC-HILIC column [13], stereoselective HPLC with β -cyclodextrin-bonded stationary phases [14, 15], HPLC with porous graphitic carbon [15, 16], anion-exchange chromatography [17, 18], anion-exchange chromatography combined with pulsed amperometric detection [19], mixed-mode chromatography employing Primesep SB, a mixed-mode column packed with reversed-phase material carrying strong embedded basic ion-pairing groups [20], and last but not least RPLC with volatile ion-pair reagents such as tributylammonium acetate [21–23].

Lack of chromatographic selectivity was sometimes attempted to be overcome by the selection of product ions with unique ion intensities [14, 16]. Similarly, a deconvolution approach of coeluting isomeric sugar phosphates in reversed-phase ultra-HPLC/electrospray-MS/MS was proposed by Ross *et al.* [24]. The coeluted isomers were quantified as their sum and their relative ratios were deconvoluted by calibration functions based on unique product ion ratios. A selective analysis of some isomeric sugar phosphates was also reported by a capillary electrophoresis-TOF-MS method [25].

Recently, we proposed an HPLC-ESI-MS/MS-based platform for quantitative metabolic profiling consisting of two HILIC and two RPLC methods [7, 26, 27].

Sugar phosphates were mainly determined by HILIC at pH 7.5 with ZIC-HILIC as stationary phase. However, structural isomers could not be analyzed individually due to lack of chromatographic and mass spectrometric selectivities as selective reaction monitoring (SRM) transitions are group-selective rather than compound-specific [7] for these compounds. They were therefore determined as the sum over all isomers.

Herein, we propose a methodology that provides satisfactory chromatographic selectivity for the structural isomers of various phosphorylated carbohydrates. It is based on the use of mixed-mode anion-exchangers (Fig. 1) that have proven to be valuable and flexible stationary phases for the analysis of hydrophilic compounds including peptides, polar drugs, metabolites and mycotoxins [28–34].

2 Materials and methods

2.1 Materials

A list of the phosphorylated carbohydrates examined in this study is given in Table 1 along with some of their characteristic properties. The test compounds D-glucose 1-phosphate (G1P), D-glucose 6-phosphate (G6P), D-fructose 6-phosphate (F6P), D-galactose 1-phosphate (Gal1P), D-mannose 1-phosphate (M1P), D-mannose 6-phosphate (M6P), D-ribose 5-phosphate (Rib5P), D-ribulose 5-phosphate (Ru5P), D-xylulose 5-phosphate (Xyl5P), 2- and 3-phosphoglycerate, dihydroxyacetone phosphate (DHAP), glyceraldehyde 3-phosphate (GAP), D-glucosamine 1-phosphate (GlcN1P) and D-glucosamine 6-phosphate (GlcN6P) were all obtained from Sigma-Aldrich (Vienna, Austria). D-Inositol 3-phosphate, D-inositol 4,5-bisphosphate, D-inositol 1,2,4-trisphosphate and D-inositol 1,2,4,5-tetrakisphosphate were a kind gift by S. Adelt from the University of Wuppertal, Germany. Their pK_a -values were calculated with ACD Software (ACD/Labs 7.00, Advanced Chemistry Development, Toronto, Canada) (see Table 1).

The employed stationary phases were weak anion-exchangers. The quinine carbamate stationary phase tBuCQN-WAX (120 Å pore size, 5 μ m) (Fig. 1A) (150 \times 4 mm id) was a prototype now commercially available as Chiralpak QN-AX from Chiral Technologies (Illkirch, France). The mixed-mode columns 3-aminoquinuclidine-derived reversed-phase/weak anion-exchanger (AQ-RP/WAX) (Fig. 1B) and 3- α -aminotropane-derived RP/WAX (AT-RP/WAX) (Fig. 1C) were both based on Daisogel 120 Å, 5 μ m with column dimension of 150 \times 4 mm id each and are described in more detail elsewhere [33].

ACN and methanol (MeOH) of HPLC grade (VWR, Vienna, Austria), trifluoroacetic acid (TFA; Fluka, for HPLC, $\geq 98.0\%$) as well as distilled water filtered through a Milli-Pore (Milli-Q) water purification system to 18.2 M Ω quality were used for the preparation of the mobile phases.

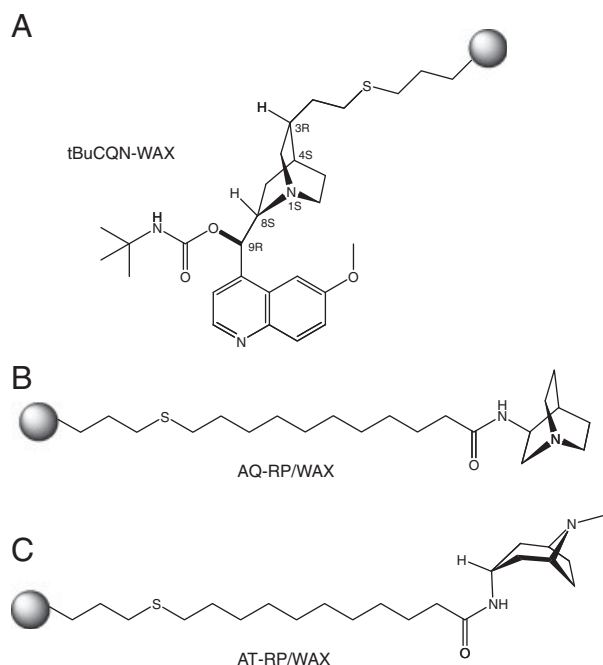


Figure 1. Structures of investigated WAX-type stationary phases: (A) tBuCQN-WAX (Chiralpak QN-AX; quinine derived) ($pK_{a,1} = 4.33$; $pK_{a,2} = 9.22$), (B) AQ-RP/WAX ($pK_a = 9.89$), (C) AT-RP/WAX ($pK_a = 10.74$) (all pK_a values calculated with ACD software).

Table 1. Analytes and characteristics

Compound	Abbreviation	M_r	pK_a (ACD)
Dihydroxyacetone phosphate	DHAP	170.1	1.65, 6.11
Glyceraldehyde 3-phosphate	GAP	170.1	1.80, 6.29
2-Phosphoglycerate	2PG	186.1	1.65, 2.34, 6.46
3-Phosphoglycerate	3PG	186.1	2.24, 3.69, 8.03
Xylulose 5-phosphate	Xyl5P	230.1	1.66, 6.13
Ribose 5-phosphate	Rib5P	230.1	1.83, 6.33
Ribulose 5-phosphate	Ru5P	230.1	1.90, 6.40
Glucosamine 1-phosphate	GlcN1P	259.2	1.73, 6.21, 8.25
Glucosamine 6-phosphate	GlcN6P	259.2	1.86, 6.36, 8.42
Fructose 6-phosphate	F6P	260.1	1.86, 6.36
Glucose 1-phosphate	G1P	260.1	1.73, 6.21
Glucose 6-phosphate	G6P	260.1	1.86, 6.36
Mannose 1-phosphate	M1P	260.1	1.73, 6.21
Mannose 6-phosphate	M6P	260.1	1.86, 6.36
Galactose 1-phosphate	Gal1P	260.2	1.73, 6.21
D-Inositol 3-phosphate	D-Ins(3)P1	260.1	1.91, 6.41
D-Inositol-4,5-bisphosphate	D-Ins(4,5)P2	340.1	1.61, 2.03, 6.29, 6.71
D-Inositol-1,2,4-trisphosphate	D-Ins(1,2,4)P3	420.1	1.54, 1.91, 2.21, 5.70, 6.11, 6.41
D-Inositol-1,2,4,5-tetrakisphosphate	D-Ins(1,2,4,5)P4	500.1	1.30, 1.66, 1.91, 2.11, 6.21, 6.41, 6.66, 7.02

2.2 Instrumentation

HPLC experiments were carried out using an 1100 series LC system from Agilent Technologies (Waldbronn, Germany) equipped with a binary gradient pump, autosampler, autosampler thermostat (temperature set to 5°C), vacuum degasser, temperature-controlled column compartment (Agilent) and a Corona CADTM charged aerosol detector (ESA Analytical, Aylesbury, England). The nitrogen inlet pressure and flow rate for the CAD were set to 35 psi and 1.53 L/min. The data were processed with the Agilent ChemStation software (Rev. A. 10.01). For the temperature studies the eluent was pre-thermostated by flowing through the heat exchanger of the temperature-controlled column compartment before entering into the column and the column was submerged in a cryostatic bath.

The composition of the mobile phase is specified in Section 3. The mobile phase flow rate was 1.0 mL/min and the column temperature was set to 25°C, if not stated otherwise. The injection volume was 10 µL.

3 Results and discussion

3.1 Mechanistic aspects

3.1.1 Stoichiometric displacement model

The stationary phases tested in this study for their capability to separate isomers of phosphorylated carbohydrates are all weak anion-exchangers (Fig. 1). Since balance of retention of phosphorylated carbohydrates under volatile mobile

phase conditions on anion-exchangers is a complicated matter with narrow windows for elution conditions, we herein and in the next subchapters briefly discuss ways to adjust retention on the basis of simple ion-exchange theory. The stoichiometric displacement model [35, 36, 37] has been frequently invoked as a simple framework to rationalize retention of oppositely charged compounds on ion-exchangers. This model treats ion-exchange as a stoichiometric process in which one solute ion is displaced from the ion-exchange site by one counterion C, and vice versa. It follows that plots of $\log k$ versus $\log [C]$ are linear according to Eq. (1)

$$\log k = \log K_Z - Z \cdot \log [C] \quad (1)$$

wherein k is the retention factor, $[C]$ the molar concentration of the counterion in the eluent, Z is the slope of the linear regression line, and $\log K_Z$ the intercept.

In Eq. (1) K_Z represents a system-specific constant that is related to the ion-exchange equilibrium constant K (in L/mol), the surface area S (in m²/g stationary phase), the charge density on the surface *i.e.* the number of ion-exchange sites q_x available for adsorption (in mol/m²) and the mobile phase volume V_0 (in L) in the column as described by Eq. (2)

$$K_Z = \frac{K \cdot S \cdot (q_x)^Z}{V_0} \quad (2)$$

The slope Z is indicative for the charges being involved in the ion-exchange process. Z depends directly proportionally on the ratio of the effective charge numbers of solute ($z_{\text{eff},S}$) and counterion ($z_{\text{eff},C}$). This explains the rapid increase in retention for multiply charged species such as phosphorylated carbohydrates on anion-exchangers. The effective

charge of weak electrolytes is obtained as the linear combination of the ionic charges z_i of each ionic species in the fast equilibrating ensemble averaged over their respective molar fractions f_i (Eq. 3) [38].

$$z_{\text{eff},i} = f_i^0 \cdot z_i^0 + f_i^1 \cdot z_i^1 + f_i^2 \cdot z_i^2 + f_i^3 \cdot z_i^3 + \dots + f_i^n \cdot z_i^n \quad (3)$$

In this equation the superscript represents the charge number. As can be derived from Eq. (1), counterion concentration and type are primary experimental variables to adjust retention. The other most important experimental variable that governs retention in ion-exchange processes, in particular for weak electrolytes and ion-exchangers, is the pH value through its influence on ionization of the solutes, of the ion-exchange site, and of the counterion as well. Assuming absence of other retention contributions the retention factor k is roughly proportional to

$$k \propto \frac{\alpha_S^* \cdot \alpha_{\text{IEX}}^*}{\alpha_C^*} \quad (4)$$

wherein α_S^* , α_{IEX}^* , α_C^* are the degree of dissociation of solute, ion-exchange site, and counterion, respectively.

3.1.2 Analyte charge

One particular problem for efficient analysis of phosphorylated carbohydrates on anion-exchangers under MS-compatible conditions is the strong electrostatic interaction between the bivalent phosphate group and the ion-exchange site. It can be properly balanced by increase in the counterion concentration (Eq. 1), albeit this is usually accompanied by loss of detection sensitivity for both CAD and ESI-MS. In order to attenuate this strong ionic interaction at low ionic strength conditions, it may be attempted to reduce either the ionization of the anion-exchanger or of the solute (Eq. 4). Suppression of the dissociation of the phosphate moiety requires strongly acidic conditions, e.g. addition of TFA to the eluent (compromising MS detection compatibility due to negative impact on MS signal intensities). Reasonably fast separations could be achieved with such eluents on the WAX-type phases for mono-phosphorylated carbohydrates. However, with higher degree of phosphorylation retention rapidly increased as illustrated for a series of inositol phosphates for which a linear dependency between $\log k$ and the effective charge number (z_{eff}) was observed in accordance with Eqs. (1) and (3) (Fig. 2). Compounds with more than two phosphate groups may be hard to elute without discharging the WAX site.

3.1.3 Eluent pH

The other option for accelerating separations is thus to discharge the anion-exchanger. Figure 3A depicts the variation of the retention factor of G1P as a model compound with the mobile phase pH ($^{\text{pH}}$). It can be seen that the maximum retention is observed at pH 7. At this pH, the WAX site is fully ionized and G1P is essentially

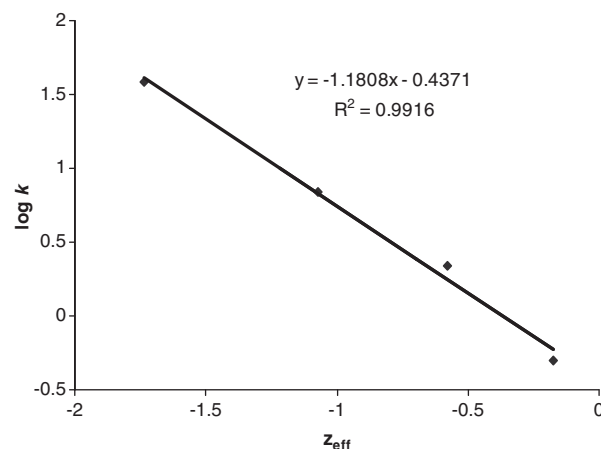


Figure 2. Dependence of retention factors on effective charge numbers in phosphorylated carbohydrate (inositol phosphate) separations. Experimental conditions: column, tBuCQN-WAX; mobile phase, 0.5% (v/v) TFA in ACN/water (10:90; v/v) (pH measured in the hydroorganic mixture with glass electrode was 1.24 i.e. represents $^{\text{pH}}$); flow rate, 1 mL/min; T, 25 °C; sample: inositol mono-, di-, tri-, and tetra-phosphate.

doubly negatively charged leading to strong retention. When the pH is reduced the effective charge of the solute is decreased. At higher pH, the decrease in retention is mostly driven by discharge of the weak anion-exchange site. Actually, due to residual silanols silica-based WAX phases show zwitterionic behavior and for the quinine carbamate-based stationary phase the pI of the surface was shown to be around pH 8 [39]. In order to afford reasonably fast separations, pH values around 8 or even higher are required on this side of the pH regime with the current mixed-mode RP/WAX phases and chiral anion-exchanger, respectively. Since so far no successful separation for a complex mixture of targeted phosphorylated carbohydrate isomers could be achieved at high pH, we opted for strongly acidic conditions for further experiments on isomer separations (*vide infra*).

3.1.4 Organic modifier content

Ion-exchangers are known to be potentially useful for HILIC separations if run with higher amounts of organic solvents, in particular ACN. To investigate whether a HILIC mechanism is superimposed upon the primary ion-exchange process, the effect of the organic modifier percentage on retention factors was examined (Fig. 3B). It can be derived from Fig. 3B that in the solvent range above 50% modifier a mixed-mode HILIC/WAX mechanism may exist while in the low organic solvent range (< 50%) a mere anion-exchange process should be dominating. The effect of these two distinct regimens on the sugar phosphate isomer separation will be addressed below.

3.1.5 Counterion concentration

Figure 3C depicts the dependency of the retention factors on the counterion concentration, which is here TFA. In

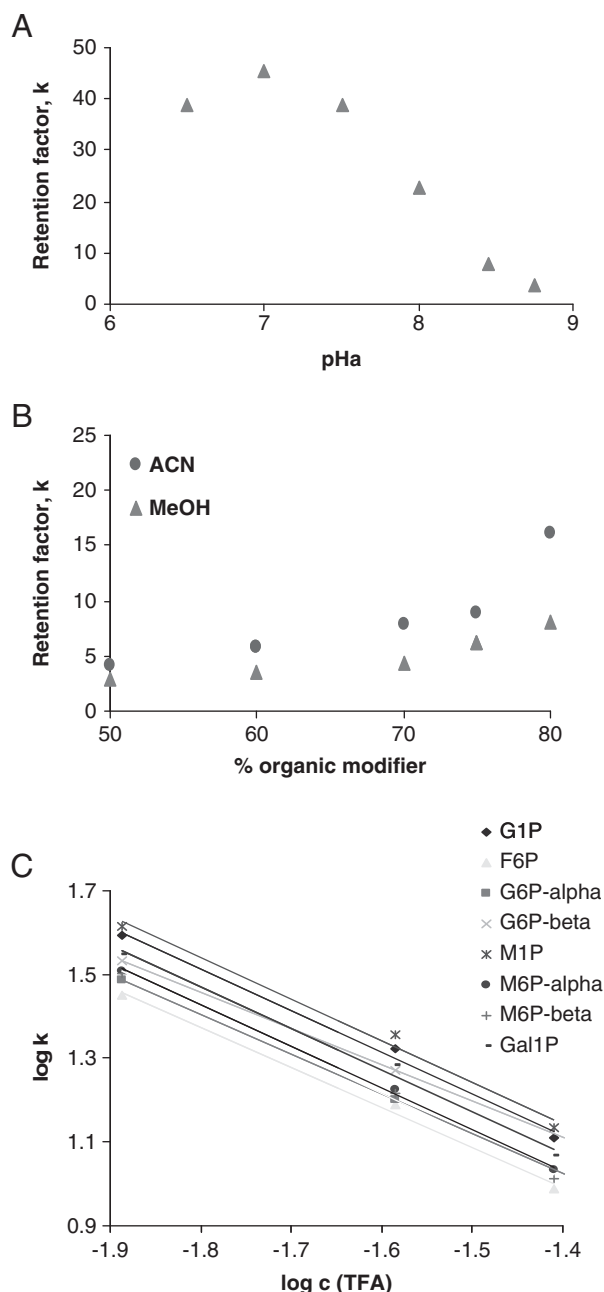


Figure 3. Effect of eluent pH (pH_s) (A), of organic modifier percentage (B), and of counterion concentration (TFA) (C) on the retention factor k of G1P (A, B) and various sugar phosphates (C) on AT-RP/WAX (A and B) and AQ-RP/WAX (C). Experimental conditions: (A) 50 mM acetic acid in MeOH/water (70:30; v/v), pH adjusted in the mixture with 12% ammonia (pH_s); (B) 50 mM acetic acid in a mixture of organic modifier/water, pH adjusted in the mixture with 12% ammonia to 8.5; (C) TFA in ACN/water (80:20; v/v); column temperature, 25°C.

accordance with the stoichiometric displacement model and Eq. (1), respectively, plots between $\log k$ and $\log [TFA]$ are linear. It is seen that all the trend lines for the different sugar phosphates drop parallel to each other, which implies that this experimental variable is suitable to adjust retention,

but is not an effective means to optimize selectivity between the individual sugar phosphate peaks.

3.2 Mutarotation

Carbohydrates with aldehyde group (aldohexoses, aldopentoses), such as the monosaccharide glucose, exist in solution in cyclic form yielding a mixture of α - and β -anomers [40, 41]. For example, when solid α -D-glucose is dissolved in water it mainly exists as the α -D-glucopyranose form which dynamically equilibrates by inversion of the configuration at the stereogenic center of C1 via the non-cyclic open form to yield a mixture of α - and β -glucopyranose (36 and 64%, resp. at equilibrium at 25°C in water) ([40] and references therein). This effect is known as mutarotation and refers in sugar chemistry to the epimerization at the hemiacetal carbon of carbohydrates. It has also been reported for G6P [42, 43]. For analytical purposes such as in quantitative metabolic profiling it may be convenient to avoid the separation of the anomers and the splitting of the targeted sugar compound into two peaks. Thus, sugar analysis is commonly performed under basic conditions where inter-conversion between the two anomers is rapid relative to the chromatographic time scale and thus a single peak representing the time-averaged migration of the two species is observed.

For the separation of the isomeric sugar phosphates on the current mixed-mode phases, basic conditions did not provide adequate selectivity for constitutional isomers and hence acidic conditions were employed. Under the given acidic mobile phase conditions, mutarotation was found for G6P but not for G1P (see Fig. 4A). Substitution in 1-position obviously precludes epimerization. In order to determine the elution order of the anomers a fresh sample of β -G6P (see also Supporting Information) was dissolved in water and immediately injected. Repeated injection after certain time intervals allowed the monitoring of the epimerization kinetics under given conditions and the determination of the ratio between α - and β -anomer under equilibrium. As can be seen from Fig. 4B the equilibrium is established after about one hour and an equilibrium mixture of about 40% α -anomer and 60% β -anomer is obtained at 25°C for G6P. It is worth noting that the α/β -anomer ratio is the same as specified in a recent paper [43] and largely in agreement with that of D-glucose for which an α/β -anomer ratio of 36 to 64% under equilibrium has been reported [40] (see also Supporting Information).

As mentioned, for application of the method in metabolic profiling mutarotation should be greatly accelerated to get a single peak. Since increase in pH is not possible due to loss of selectivity for separation of constitutional isomers, temperature has been investigated as a variable to reach this goal. The result is shown in Fig. 5A. As can be seen α - and β -anomers merge into a single peak at temperature above 45°C while baseline separation between G6P and G1P is still maintained. In contrast, at low temperatures anomers are

resolved but the resolution between β -G6P and G1P vanishes so that these constitutional isomers are completely overlapping at a column temperature of 5°C. It is remarkable that there is only a weak temperature effect on retention under these mobile phase conditions. A possible explanation could be a superimposed temperature effect on dissociation of the hexose phosphates. At higher temperature, the hexose phosphates are supposed to be dissociated to a larger degree leading to stronger retention which counteracts the expected decrease in retention with increase in temperature (as expected for enthalpically dominated adsorption processes). This is, however, only valid for elution conditions being composed of low ACN percentages (Fig. 5A). In sharp contrast, a mixed-mode HILIC/WAX-type separation mode is obtained when using 80% ACN and this imparts much better selectivities for the separation of both anomers and constitutional isomers at the expense of longer run times (Fig. 5B). Interesting to note is that at temperatures above 45°C anomers again coelute, indicating that the interconversion kinetics is accelerated and much faster than the kinetics of chromatographic partitioning *i.e.* it is fast as compared to the time scale of the separation. On the other hand, at low temperature *e.g.* at 5°C the interconversion kinetics appears to be extremely slow, slower than the timescale of the chromatographic separation and hence two completely separated anomer peaks without plateau in-between are detected. At such conditions the area ratio of the anomer peaks corresponds to the anomer ratio in the sample. In the intermediate temperature range the interconversion kinetics is in about the same timescale as the chromatographic separation and hence two separated peaks with a plateau in-between are observed (on-column interconversion [44, 45]). The situation is similar for mannose 6-phosphate (Supporting Information).

Apparent reaction rate constants of interconversion (apparent because they have been obtained in presence of the stationary phase; see Fig. 5C) were determined using the unified equation [46]. All calculations were performed with the software DCXplorer, which is available from O. T. upon request as an executable program running under the operating system Microsoft Windows XP, Vista, and 7. The results are given in Table 2.

For the evaluation of activation parameters of the mutarotation process of G6P in the presence of the stationary phase, experiments between 5 and 35°C were considered. At higher temperatures peak coalescence occurred and therefore rate constants could not be determined with sufficient precision. The Gibbs free activation energy $\Delta G^\ddagger(T)$ was calculated according to the Eyring equation (Eq. 5) with k_B as the Boltzmann constant ($k_B = 1.380662 \times 10^{-23} \text{ J} \cdot \text{K}^{-1}$), T as the epimerization temperature (in K), h as Planck's constant ($h = 6.62617 \times 10^{-34} \text{ J} \cdot \text{s}$), R as the gas constant ($R = 8.31441 \text{ J} \cdot \text{K}^{-1} \cdot \text{mol}^{-1}$). The statistical factor κ was set to 1.

$$G^\ddagger(T) = -RT \ln \frac{k_1 \cdot h}{\kappa \cdot k_B \cdot T} \quad (5)$$

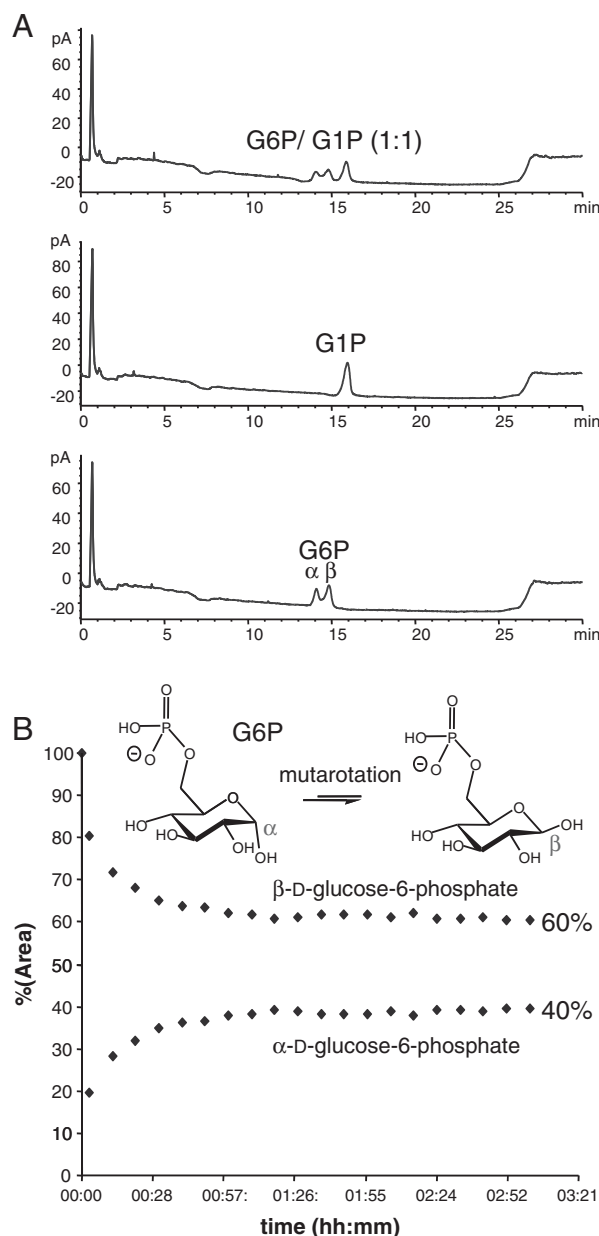


Figure 4. Chromatograms showing the separation of G6P and G1P (A) as well as the mutarotation of G6P (B). Experimental conditions: (A) Stationary phase, AT-RP/WAX; gradient elution: channel A, water with 0.1% (v/v) TFA; channel B, ACN with 0.1% (v/v) TFA; gradient profile, 5% B to 50% B in 20 min. (B) Stationary phase, AQ-RP/WAX; isocratic elution: mobile phase, 0.1% (v/v) TFA in ACN/water (35:65; v/v); column temperature, 20°C; sample, β -G6P dissolved in water at 1 mg/mL and stored in autosampler tray at 5°C; injection of 5 μ L after specified time intervals.

The activation enthalpy ΔH^\ddagger of the epimerization process was obtained from the slope and the activation entropy ΔS^\ddagger from the intercept of the Eyring plot ($\ln(k_1/T)$ vs. T^{-1}) (Fig. 6). The results are summarized in Table 3. For comparison, also the data for M6P obtained under identical conditions are shown (see also Supporting Information).

Overall, it is evident that column temperatures above 45°C must be utilized under acidic mobile phase conditions with the employed RP/WAX column, if the anomer separation should be avoided in analytical applications.

3.3 Isomer separations

As mentioned in Section 1 formerly published methods for separation of isomers of carbohydrates have shown some limitations. While some of the sugar phosphate isomers have been reported to be resolved, selectivity for a larger group of carbohydrate isomers was usually lacking. The currently investigated mixed-mode phases make use of specific interactions combining presumably hydrogen-bond mediated anion-exchange with directional hydrogen-bonding at the adjacent amide group. Such simultaneous multivalent interactions can provide these stationary phases with molecular recognition capabilities for satisfactory resolution of all of the investigated isomers of interest.

Of particular interest are isomeric structures of the glycolysis pathway. For example, DHAP and GAP, which

are constitutional isomers resulting from cleavage of fructose 1,6-diphosphate and are enzymatically interconverted by triose phosphate isomerase, can be well resolved chromatographically on the mixed-mode RP/WAX column (Figs. 7A and B). In subsequent steps of the glycolysis pathway 3-phosphoglycerate is formed from GAP via 1,3-diphosphoglycerate which is further converted to 2-phosphoglycerate. These constitutional isomers show significantly different elution times on the mixed-mode phases enabling reliable quantitation by AQ-RP/WAX (Fig. 7C). Glucosamine 6-phosphate and glucosamine 1-phosphate are central metabolites in the amino sugar pathway. Glucosamine 6-phosphate splits into α - and β -anomer peaks, which are both well separated from the constitutional isomer glucosamine 1-phosphate (Fig. 7D).

A particular challenge constitutes the specific analysis of the individual isomeric hexose phosphates (G1P, G6P, M1P, M6P, Gal1P, F6P) when they are all present simultaneously in a sample. They all eluted within less than a minute in our previous HILIC assay (pH 7.5 with ZIC-HILIC) [7] and enabled only a sum determination due to identical precursor and product ions without compound specific MS/MS char-

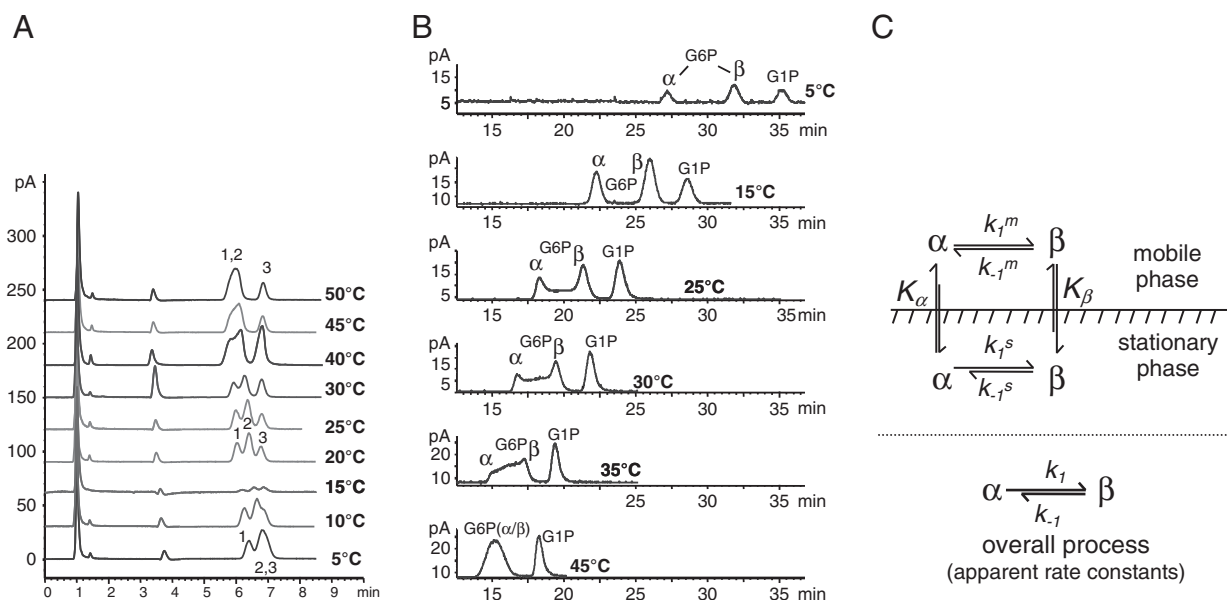


Figure 5. Temperature dependence of on-column mutarotation of G6P in two distinct elution modes: WAX (A) and HILIC/WAX (B). Experimental conditions: stationary phase, AQ-RP/WAX; mobile phase, (A) 0.1% (v/v) TFA in ACN/water (35:65; v/v); (B) 0.1% (v/v) TFA in ACN/water (80:20; v/v). Peak notation in (A): 1, G6P(α); 2, G6P(β); 3, G1P.

Table 2. Summary of the apparent reaction rate constants of the α/β mutarotation of G6P obtained by temperature-dependent measurements (experimental conditions see Fig. 5B)

T (°C)	$k_{\alpha\text{-G6P} \rightarrow \beta\text{-G6P}}$ (10^{-4} s^{-1})	$t_{1/2, \alpha\text{-G6P} \rightarrow \beta\text{-G6P}}$ (min)	$k_{\beta\text{-G6P} \rightarrow \alpha\text{-G6P}}$ (10^{-4} s^{-1})	$t_{1/2, \beta\text{-G6P} \rightarrow \alpha\text{-G6P}}$ (min)
5	0.2	577.6	0.1	1155.2
15	0.7	165.0	0.5	231.0
25	9.3	12.4	6.2	18.6
30	14.7	7.9	9.8	11.8
35	27.8	4.2	18.5	6.2

acteristics aside from minor peculiarities in terms of fragment ion intensities [16, 24] (see also Supporting Information). A similar situation applies for the isomeric pentose phosphates (Rib5P, Rul5P, Xyl5P). Both hexose phosphates and pentose phosphates were injected along with D-glucosamine 6-phosphate and D-glucosamine 1-phosphate as a complex mixture onto the AQ-RP/WAX column. As the chromatogram in Fig. 8 illustrates this stationary phase reveals remarkable selectivities for this challenging sample. All hexose phosphates are separated at least partially. The three hexose 1-phosphates (Gal1P, G1P, and M1P) are more or less baseline separated and the β -anomer of G6P as well. F6P on the other hand is resolved from G6P but partially overlaps with M6P. The problem of

partially overlapping bands of F6P and M6P is supposed to be solvable by MS/MS detection by selective SRM transitions for these two isomers (see Supporting Information). Thus, it is expected that the resolution would be good enough for reliable quantitative analysis by HPLC-MS/MS. Some improvements in resolution, on the other hand, are needed for the pentose phosphate pair, Rib5P and Rul5P. Bonding of the same chromatographic ligand onto 3 μm and sub-2 μm particles, respectively, might provide a simple means to achieve this goal due to gain in efficiency. Overall, only in this study and a very recent paper about ion-pair RP-UHPLC-MS/MS [23] reasonable resolution of a complex mixture of isomeric hexose phosphates could be achieved.

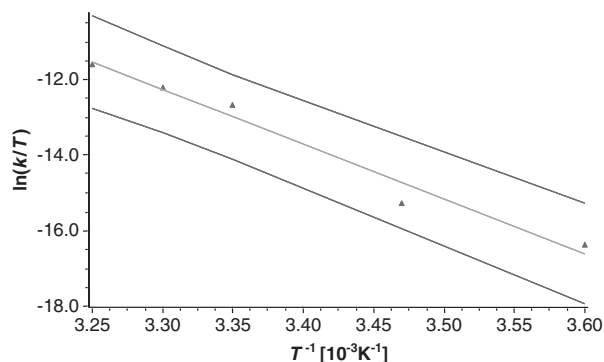


Figure 6. The Eyring plot for the interconversion reaction of G6P obtained with conditions specified in Fig. 5B).

Table 3. Summary of the activation parameters obtained by temperature-dependent measurements of G6P and M6P (experimental conditions see Fig. 5B)

	α -G6P \rightarrow β -G6P	β -G6P \rightarrow α -G6P	α -M6P \rightarrow β -M6P	β -M6P \rightarrow α -M6P
ΔH^\ddagger (kJ/mol)	119.9	119.9	102.9	102.9
ΔS^\ddagger (J (K mol) $^{-1}$)	96	93	46	49
ΔG^\ddagger (298.15 K) (kJ/mol)	91.3	92.3	89.2	88.2

4 Concluding remarks

The reliable analysis of individual isomeric forms of phosphorylated carbohydrates is of significant relevance in metabolomic studies such as the quantitative metabolic profiling of intracellular metabolites. Their isobaric character along with similar fragmentation patterns does not allow their distinction by MS/MS detection. Chromatographic separation, though, is still a major challenge. HILIC, anion-exchange chromatography, ion-pair RPLC, LC with porous graphitic carbon column, and stereo-selective cyclodextrin-bonded stationary phases have been previously employed for this purpose but do usually not provide sufficient selectivity for all isomeric forms. Deconvolution of coeluting isomers by use of mass ratio-dependent transitions has been proposed but may not always be reliable enough. Herein, we presented the chromatographic separation of isomeric sugar phosphates by mixed-mode chromatography. Employing HILIC-type elution conditions a 3-aminoquinuclidine-derived reversed-phase/weak anion-exchanger furnished remarkable selectivities for various isomeric sugar phosphates. For example, a complex mixture of several structural isomers of hexose phosphates could be almost completely resolved. Structural isomers of important metabolites from the glycolysis

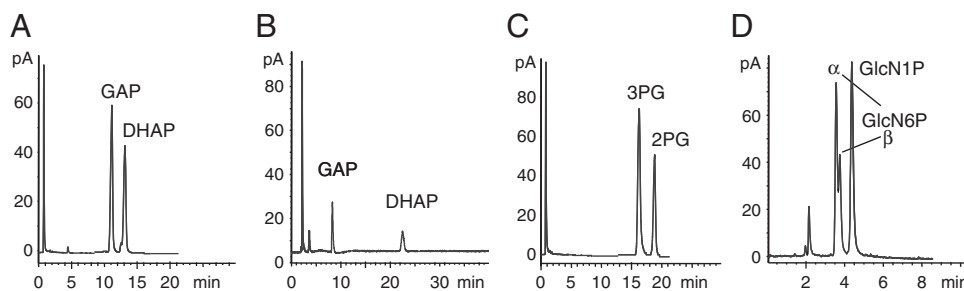


Figure 7. Isomer separations of various phosphorylated carbohydrates: DHAP and GAP (A) and (B), 2- and 3-phosphoglycerate (C), and glucosamine 6-phosphate and glucosamine 1-phosphate (D). Experimental conditions: (A, C) stationary phase, AQ-RP/WAX; gradient elution: channel A, water with 0.1% (v/v) TFA; channel B, ACN with 0.1% (v/v) TFA; gradient profile, 80% B to 20% B in 20 min; (B, D) stationary phase, tandem column obtained by coupling of AQ-RP/WAX with AT-RP/WAX; 0.1% (v/v) TFA in ACN/water (35:65; v/v); flow rate, 0.8 mL/min (A, C) and 0.6 mL/min (B, D), respectively.

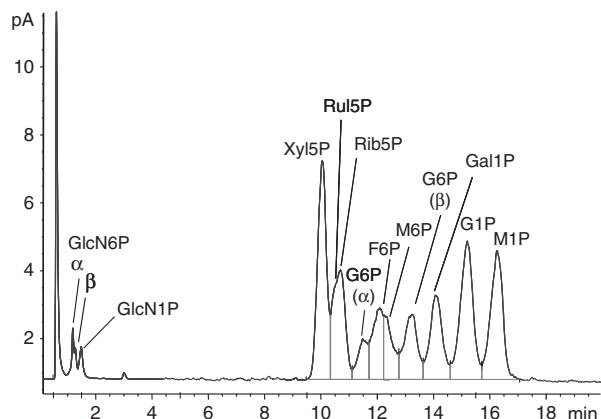


Figure 8. Chromatogram of complex mixture of phosphorylated carbohydrates including hexose phosphates and pentose phosphates as well as glucosamine phosphates. Experimental conditions: stationary phase, AQ-RP/WAX; mobile phase, 0.1% (v/v) TFA in ACN/H₂O (70:30); column temperature, 25°C; flow rate, 1 mL/min.

pathway could also be distinguished. For analysis of biological extracts in metabolomic studies MS/MS will be used for detection (instead of the CAD employed in this preliminary study to develop a selective separation). Yet, TFA as additive is unfavorable for ESI-MS detection sensitivity of phosphorylated carbohydrates. Investigations are underway to solve this issue so that the method can be implemented into our established HPLC-MS/MS platform for metabolic profiling.

The financial support of the Christian-Doppler Research Society and the industry partners Sandoz (Kundl, Austria), Merck KGaA (Darmstadt, Germany) and AstraZeneca (Mölnådal, Sweden) is gratefully acknowledged. Partial support of this work by the University of Vienna via the graduate training program entitled “Functional Molecules” (grant no. IK 1041-N) is acknowledged as well. Furthermore, we are also grateful to Stephan Adelt (University of Wuppertal, Germany) for providing inositol phosphate standards.

The authors have declared no conflict of interest.

5 References

- Oldiges, M., Luetz, S., Pflug, S., Schroer, K., Stein, N., Wiendahl, C., *Appl. Microbiol. Biotechnol.* 2007, **76**, 495–511.
- Dettmer, K., Aronov, P. A., Hammock, B. D., *Mass Spectrom. Rev.* 2007, **26**, 51–78.
- Theodoridis, G., Gika, H. G., Wilson, I. D., *Trends Anal. Chem.* 2008, **27**, 251–260.
- Werf, M. J. v. d., Overkamp, K. M., Muilwijk, B., Coulier, L., Hankemeier, T., *Anal. Biochem.* 2007, **370**, 17–25.
- van der Werf, M. J., Jellema, R. H., Hankemeier, T., *J. Ind. Microbiol. Biotechnol.* 2005, **32**, 234–252.
- Bajad, S. U., Lu, W., Kimball, E. H., Yuan, J., Peterson, C., Rabinowitz, J. D., *J. Chromatogr. A* 2006, **1125**, 76–88.
- Preinerstorfer, B., Schiesel, S., Lämmerhofer, M., Lindner, W., *J. Chromatogr. A* 2010, **1217**, 312–328.
- Büscher, J. M., Czernik, D., Ewald, J. C., Sauer, U., Zamboni, N., *Anal. Chem.* 2009, **81**, 2135–2143.
- Tuytten, R., Lemièrre, F., Witters, E., Van Dongen, W., Slegers, H., Newton, R. P., Van Onckelen, H., Esmans, E. L., *J. Chromatogr. A* 2006, **1104**, 209–221.
- Wamelink, M. M. C., Struys, E. A., Huck, J. H. J., Roos, B., van der Knaap, M. S., Jakobs, C., Verhoeven, N. M., *J. Chromatogr. B* 2005, **823**, 18–25.
- Vizan, P., Alcarraz-Vizan, G., Diaz-Moralli, S., Rodriguez-Prados, J. C., Zanuy, M., Centelles, J. J., Jauregui, O., Marta Cascante, *Anal. Chem.* 2007, **79**, 5000–5005.
- Kiefer, P., Portais, J.-C., Vorholt, J. A., *Anal. Biochem.* 2008, **382**, 94–100.
- Antonio, C., Larson, T., Gilday, A., Graham, I., Bergström, E., Thomas-Oates, J., *Rapid Commun. Mass Spectrom.* 2008, **22**, 1399–1407.
- Feurle, J., Jomaa, H., Wilhelm, M., Gutsche, B., Herderich, M., *J. Chromatogr. A* 1998, **803**, 111–119.
- Buchholz, A., Takors, R., Wandrey, C., *Anal. Biochem.* 2001, **295**, 129–137.
- Antonio, C., Larson, T., Gilday, A., Graham, I., Bergström, E., Thomas-Oates, J., *J. Chromatogr. A* 2007, **1172**, 170–178.
- Swezey, R. R., *J. Chromatogr. B* 1995, **669**, 171–176.
- Sawada, S., Ono, R., Sato, T., Suzuki, S., Arakawa, O., Kasai, M., *Anal. Biochem.* 2003, **314**, 63–69.
- Jeong, J.-S., Kwon, H.-J., Lee, Y.-M., Yoon, H.-R., Honga, S.-P., *J. Chromatogr. A* 2007, **1164**, 167–173.
- Cruz, J. A., Emery, C., Wüst, M., Kramer, D. M., Lange, B. M., *Plant J.* 2008, **55**, 1047–1060.
- Luo, B., Groenke, K., Takors, R., Wandrey, C., Oldiges, M., *J. Chromatogr. A* 2007, **1147**, 153–164.
- Lu, W., Clasquin, M. F., Melamud, E., Amador-Noguez, D., Caudy, A. A., Rabinowitz, J. D., *Anal. Chem.* 2010, **82**, 3212–3221.
- Buescher, J. M., Moco, S., Sauer, U., Zamboni, N., *Anal. Chem.* 2010, **82**, 4403–4412.
- Ross, K. L., Dalluge, J. J., *Anal. Chem.* 2009, **81**, 4021–4026.
- Timischl, B., Dettmer, K., Kaspar, H., Thieme, M., Oefner, P. J., *Electrophoresis* 2008, **29**, 2203–2214.
- Schiesel, S., Lämmerhofer, M., Lindner, W., *Anal. Bioanal. Chem.* 2010, **396**, 1655–1679.
- Schiesel, S., Lämmerhofer, M., Lindner, W., *Anal. Bioanal. Chem.* 2010, **397**, 147–160.
- Nogueira, R., Lämmerhofer, M., Lindner, W., *J. Chromatogr. A* 2005, **1089**, 158–169.
- Bicker, W., Lämmerhofer, M., Lindner, W., *J. Chromatogr. B* 2005, **822**, 160–169.

- [30] Nogueira, R., Lubda, D., Leitner, A., Bicker, W., Maier, N. M., Laemmerhofer, M., Linder, W., *J. Sep. Sci.* 2006, 29, 966–978.
- [31] Bicker, W., Lämmerhofer, M., Keller, T., Schuhmacher, R., Krska, R., Lindner, W., *Anal. Chem.* 2006, 78, 5884–5892.
- [32] Apfelthaler, E., Bicker, W., Lämmerhofer, M., Sulyok, M., Krska, R., Lindner, W., Schuhmacher, R., *J. Chromatogr. A* 2008, 1191, 171–181.
- [33] Lämmerhofer, M., Richter, M., Wu, J., Nogueira, R., Bicker, W., Lindner, W., *J. Sep. Sci.* 2008, 31, 2572–2588.
- [34] Bicker, W., Laemmerhofer, M., Lindner, W., *Anal. Bioanal. Chem.* 2008, 390, 263–266.
- [35] Kopaciewicz, W., Rounds, M. A., Fausnaugh, F., Regnier, F. E., *J. Chromatogr.* 1983, 266, 3–21.
- [36] Millot, M.-C., Debranche, T., Pantazaki, A., Gherghi, I., Seville, B., Vidla-Madjar, C., *Chromatographia* 2003, 58, 365–373.
- [37] Stahlberg, J., *J. Chromatogr. A* 1999, 855, 3–55.
- [38] Williams, B. A., Vigh, G., *J. Chromatogr. A* 1997, 777, 295–309.
- [39] Muñoz, O. L. S., Hernández, E. P., Lämmerhofer, M., Lindner, W., Kenndler, E., *Electrophoresis* 2003, 24, 390–398.
- [40] Pazourek, J., *J. Sep. Sci.* 2010, 33, 974–981.
- [41] Moni, L., Ciogli, A., D'Acquarica, I., Dondoni, A., Gasparrini, F., Marra, A., *Chem. Eur. J.* 2010, 16, 5712–5722.
- [42] Salas, M., Vinuela, E., Sols, A., *J. Biol. Chem.* 1965, 240, 561–568.
- [43] Rodríguez-Pérez, T., Lavandera, I., Fernández, S., Sanghvi, Y. S., Ferrero, M., Gotor, V., *Eur. J. Org. Chem.* 2007, 2769–2778.
- [44] Schurig, V., *Chirality* 1998, 10, 140–146.
- [45] Trapp, O., Schoetz, G., Schurig, V., *Chirality* 2001, 13, 403–414.
- [46] Trapp, O., *J. Chromatogr. B* 2008, 875, 42–47.

B-1.1 Supplementary Information

Hinterwirth, H.; Laemmerhofer, M.; Preinerstorfer, B.; Gargano, A.; Reischl, R.; Bicker, W.; Trapp, O.; Brecker, L.; Lindner, W.

Journal of Separation Science **2010**, 33, 3273-3282.

Supplementary Material for the Manuscript

Selectivity issues in targeted metabolomics: Separation of phosphorylated carbohydrate isomers by mixed-mode hydrophilic interaction / weak anion exchange chromatography

Helmut Hinterwirth¹, Michael Lämmerhofer^{1*}, Beatrix Preinerstorfer¹, Andrea Gargano¹,
Roland Reischl¹, Wolfgang Bicker¹, Oliver Trapp², Lothar Brecker³, Wolfgang Lindner¹

¹ Department of Analytical Chemistry, University of Vienna, Waehringer Strasse 38, 1090 Vienna, Austria

² Organisch-Chemisches Institut, Ruprecht-Karls-Universität Heidelberg, Im Neuenheimer Feld 270, 69120 Heidelberg, Germany

³ Department of Organic Chemistry, University of Vienna, Waehringer Strasse 38, 1090 Vienna, Austria

Correspondence:
Michael Lämmerhofer
University of Vienna, Faculty of Chemistry
Department of Analytical Chemistry
Waehringer Strasse 38
A-1090 Vienna, Austria
T +43-1-4277-523 23
F +43-1-4277-9523
michael.laemmerhofer@univie.ac.at

1 Determination of configurations of the samples (anomer assignment) and investigations of mutarotation by ¹H-NMR in D₂O solution

Since information on the stereochemistry at C1-position of the employed products was ambiguous we performed ¹H-NMR studies in order to unequivocally assign the hydroxyl group at C1 to either α- or β-configuration. The samples that were used in this study are summarized in Table S1.

Table S1: Specifications of samples employed in the present study for investigations of mutarotation

Sample ¹	Salt ¹	MW	CAS	$[\alpha]_D^{20}$ ¹	supplier	product no.	Educt anomer
D-Glucose 6-phosphate	Sodium	282.12	[54010-71-8]	+34±1	Fluka	16301	β
D-Mannose 6-phosphate	Sodium	282.12	[870442-25-0]		Sigma	M3655	β
D-(+)-Glucose monohydrate		198.17	[50-99-7]	+52.5-53.5	Sigma	16301	α
D-Glucosamine 6-phosphate		259.2	[3616-42-0]		Sigma	G5509	α

¹ as specified by supplier

Experimental conditions: ¹H NMR spectra were acquired at 25°C on a Bruker DRX 400MHz spectrometer. The chemical shifts (δ) are given in parts per million (ppm) and the coupling constants (*J*) in Hertz (Hz). 10 mg of each sample was dissolved in 1 mL D₂O and immediately measured. The measurement was repeated in regular time intervals to monitor the mutarotation reaction. Exemplary spectra of each sample after the equilibrium between α- and β-anomers has been reached are given in Figure S1.

Figure S1: ¹H NMR spectra acquired after equilibration in D₂O solution at 25°C.

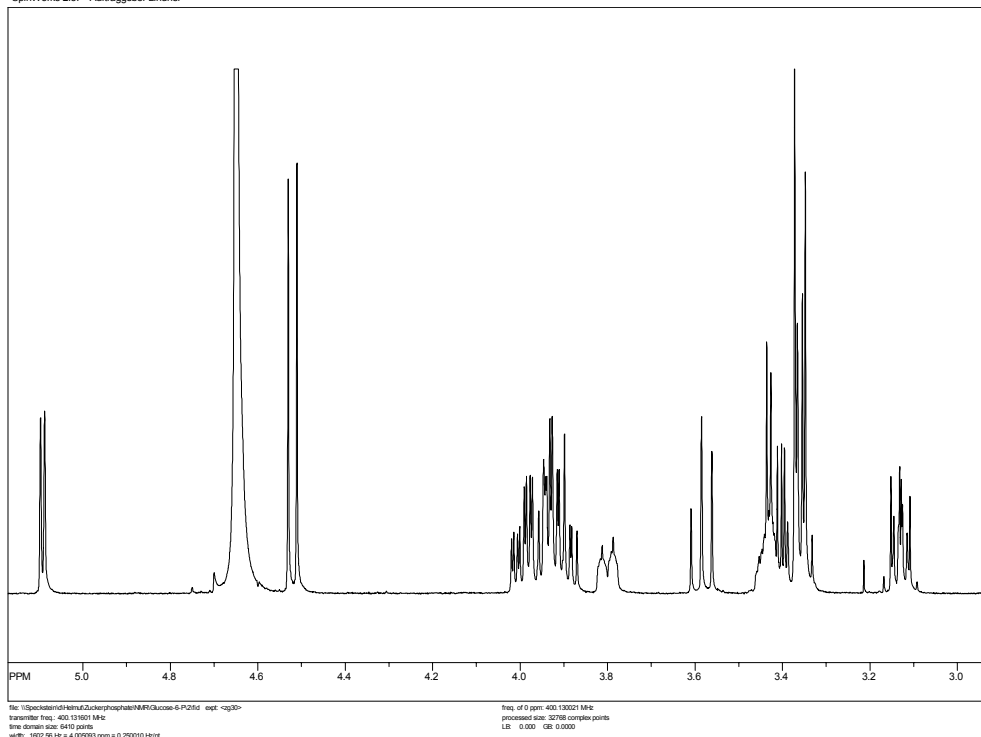


Figure S1, (a): D-Glucose 6-phosphate: ^1H NMR (D_2O , 400 MHz): $\delta = 5.09$ (d, $^3J_{\text{HH}} = 3.7$ Hz, 1 H, 1-H α -anomer), 4.52 (d, $^3J_{\text{HH}} = 8.3$ Hz, 1 H, 1-H β -anomer), 4.03-3.08 (m, 6 H α -anomer & 6 H β -anomer) ppm. (ref. HDO = 4.70 ppm) (ratio $\alpha/\beta = 39/61$; T = 25°C) (after 21 h and 10 min)

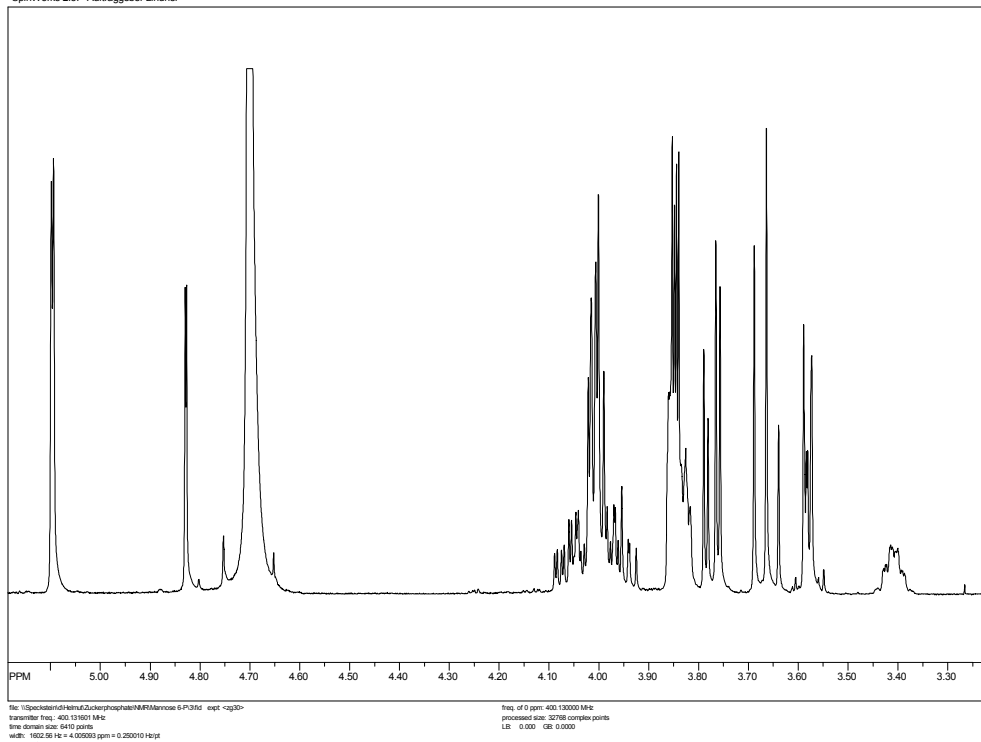


Figure S1, (b): D-Mannose 6-phosphate: ^1H NMR (D_2O , 400 MHz): $\delta = 5.10$ (d, $^3J_{\text{HH}} = 1.7$ Hz, 1 H, 1-H α -anomer), 4.83 (d, $^3J_{\text{HH}} = 1.1$ Hz, 1 H, 1-H β -anomer), 4.11-3.35 (m, 6 H α -anomer & 6 H β -anomer) ppm. (ref. HDO = 4.70 ppm) (ratio $\alpha/\beta = 68/32$; T = 25°C) (after 19 h and 27 min)

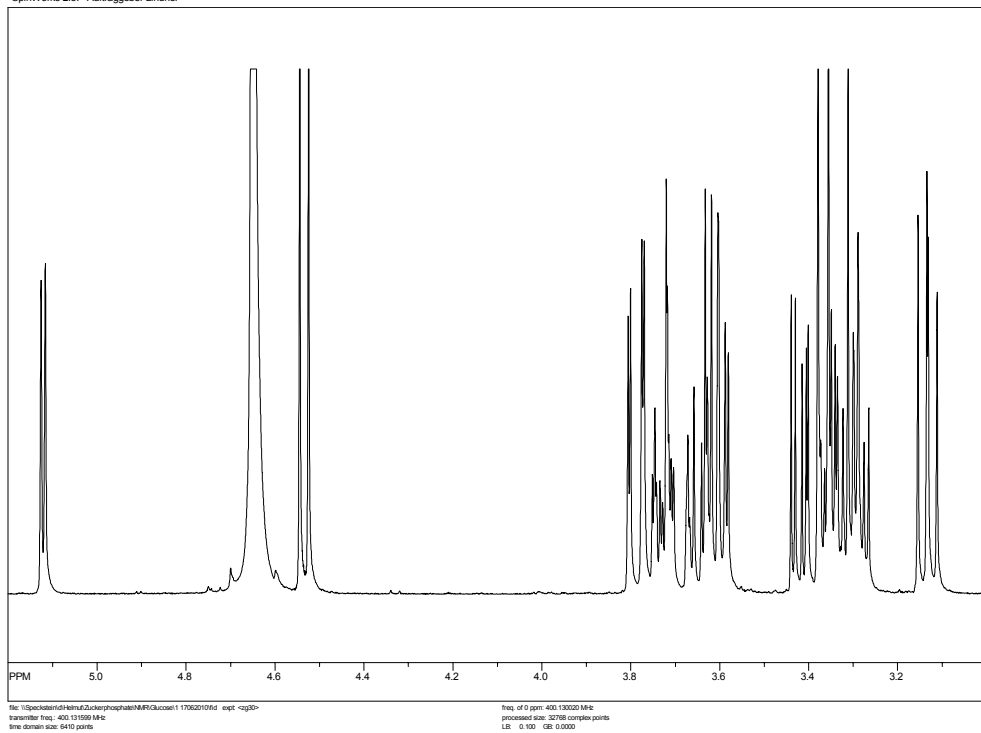


Figure S1, (c): D-Glucose: ^1H NMR (D_2O , 400 MHz): $\delta = 5.12$ (d, $^3J_{\text{HH}} = 3.7$ Hz, 1 H, 1-H α -anomer), 4.53 (d, $^3J_{\text{HH}} = 7.9$ Hz, 1 H, 1-H β -anomer), 3.82-3.26 (m, 6 H α -anomer & 5 H β -anomer), 3.13 (dd, $^3J_{\text{HH}} = 8.1$ Hz, 1 H, 2-H β -anomer), ppm. (ref. HDO = 4.70 ppm) (ratio $\alpha/\beta = 36/64$; $T = 25^\circ\text{C}$) (after 22 h and 19 min)

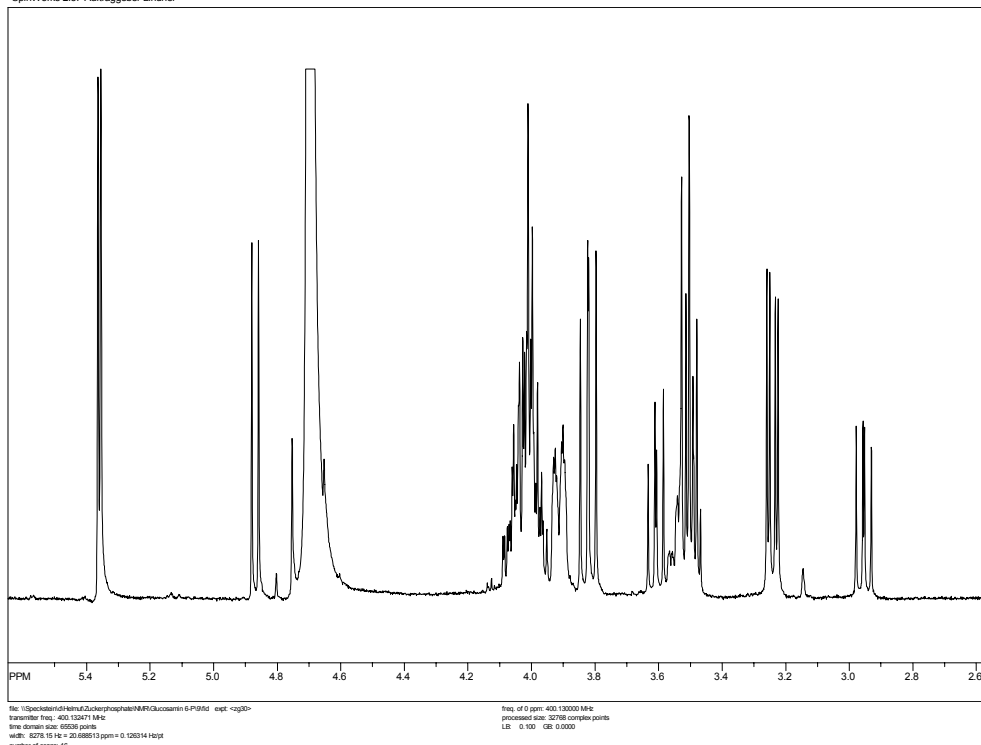
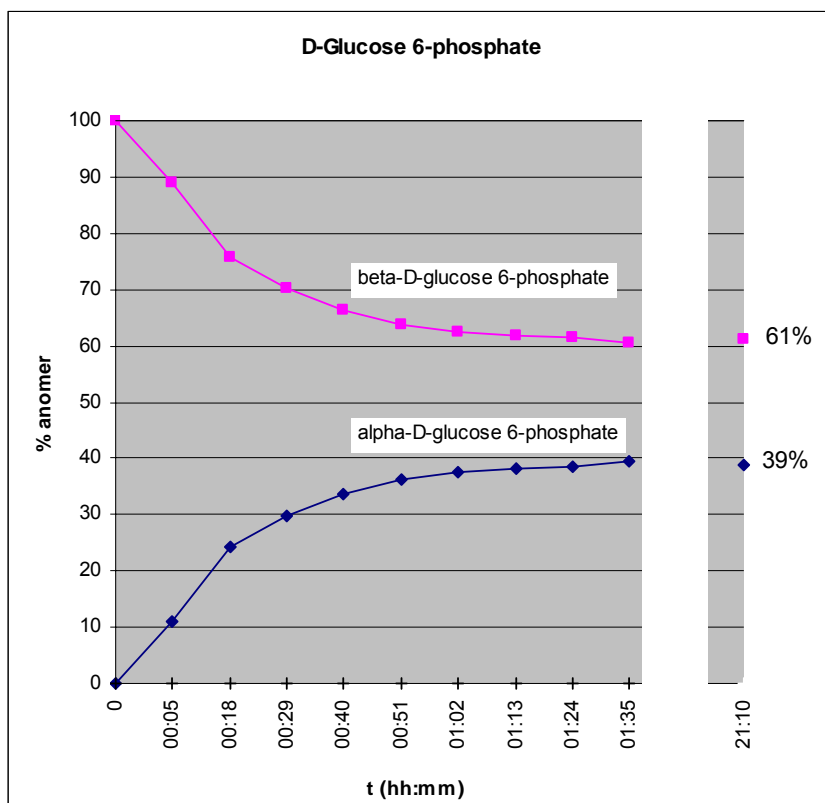


Figure S1, (d): D-Glucosamin 6-phosphate: ^1H NMR (D_2O , 400 MHz): $\delta = 5.36$ (d, $^3J_{\text{HH}} = 3.6$ Hz, 1 H, 1-H α -anomer), 4.87 (d, $^3J_{\text{HH}} = 8.6$ Hz, 1 H, 1-H β -anomer), 4.10-2.95 (m, 6 H α -anomer & 6 H β -anomer) ppm. (ref. HDO = 4.70 ppm) (ratio $\alpha/\beta = 68/32$; $T = 25^\circ\text{C}$) (after 4 h and 17 min).

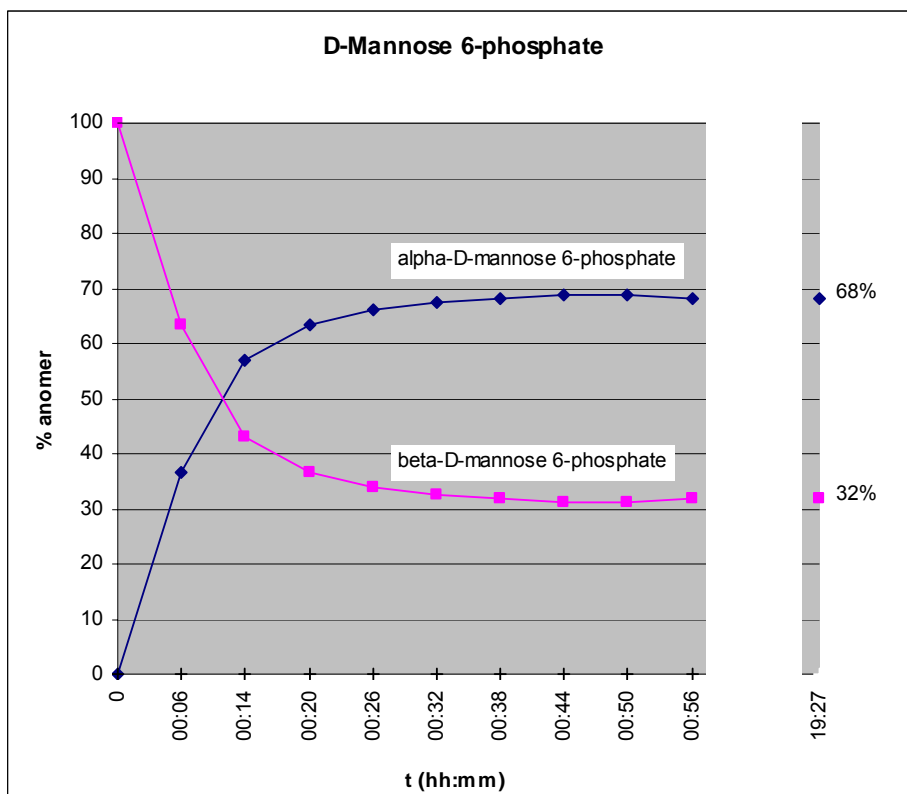
From the initial measurements (i.e. spectra taken at $t = 0$ min) the stereochemistry of the employed samples could be derived. Table S1 contains information on the anomer assignment of the various compounds used in this study as derived from these initial ^1H -NMR spectra.

Figure S2 shows the time-dependence of mutarotation for D-glucose 6-phosphate (a), D-mannose 6-phosphate (b), D-glucose (c), and D-glucosamine 6-phosphate. A summary of the anomer ratios of the equilibrium mixtures after equilibration at 25°C is given in Table S2.

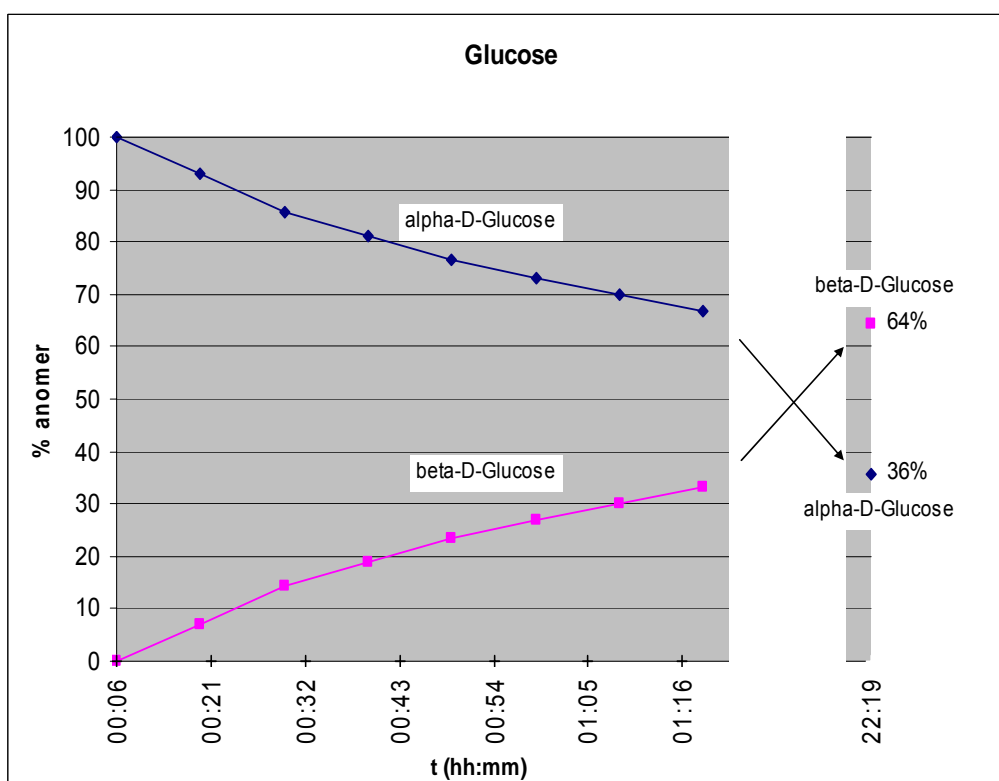
(a)



(b)



(c)



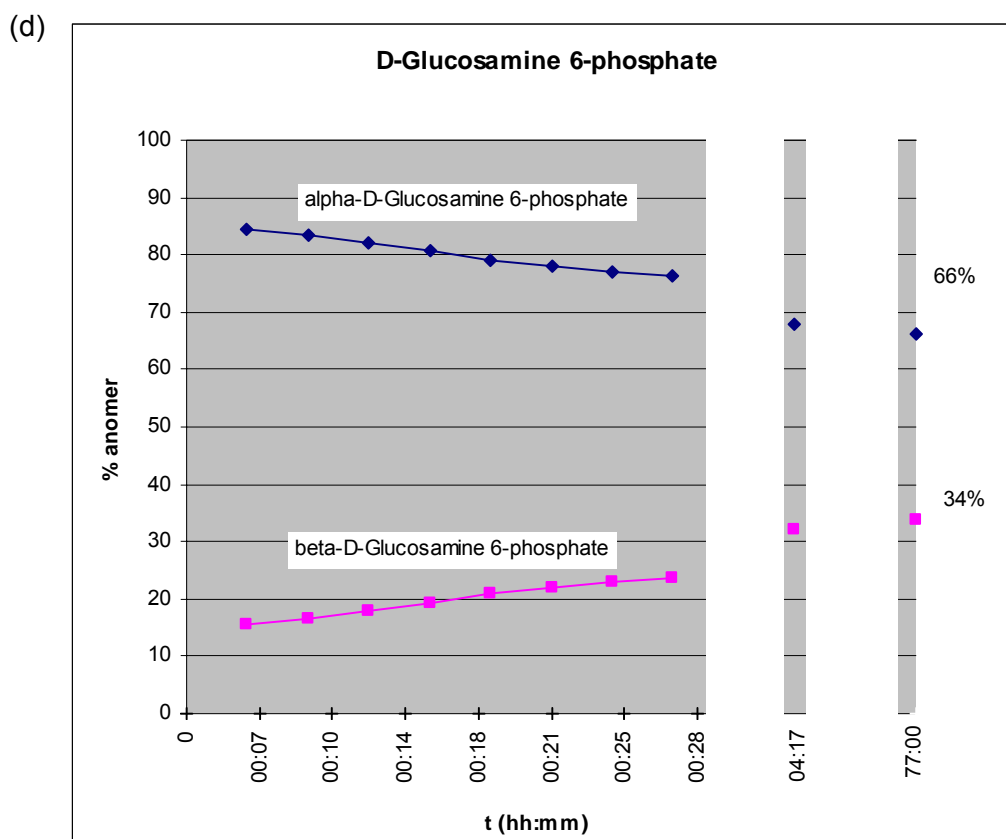


Figure S2: Monitoring of mutarotation of (a) D-glucose 6-phosphate, (b) D-mannose 6-phosphate, (c) D-glucose and (d) D-glucosamine 6-phosphate. The series of spectra was obtained by repeated ^1H -NMR measurements of a freshly prepared sample (about 10 mg in 1 mL D_2O) after specified time.

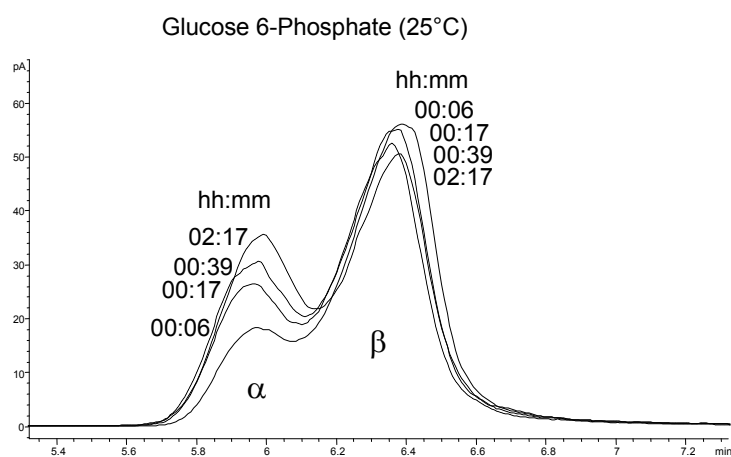
Table S2: Summary of anomer ratios under equilibrium (in D_2O at 25°C after ca. 20 h except for D-glucosamine for which the equilibrium mixture was measured after 77 h)

	Educt	Anomer ratio after equilibration (D_2O)	
		% α	% β
Sample¹	anomer		
D-Glucose 6-phosphate	β	39	61
D-Mannose 6-phosphate	β	68	32
D-(+)-Glucose monohydrate	α	36	64
D-Glucosamine 6-phosphate	α	66	34

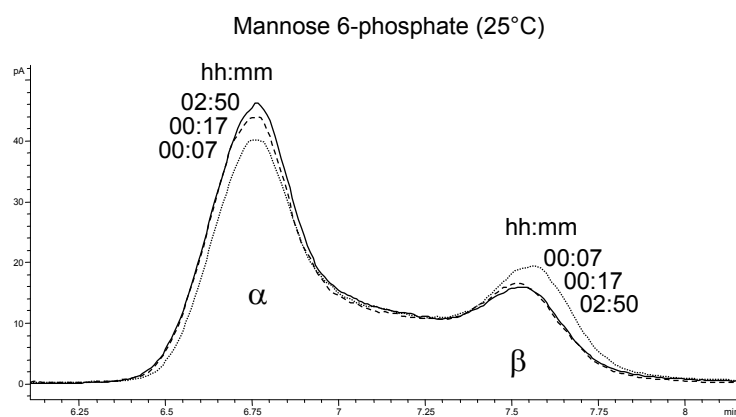
¹ as specified by supplier

2 Monitoring of mutarotation by HPLC with mixed-mode RP/WAX column

(a)



(b)



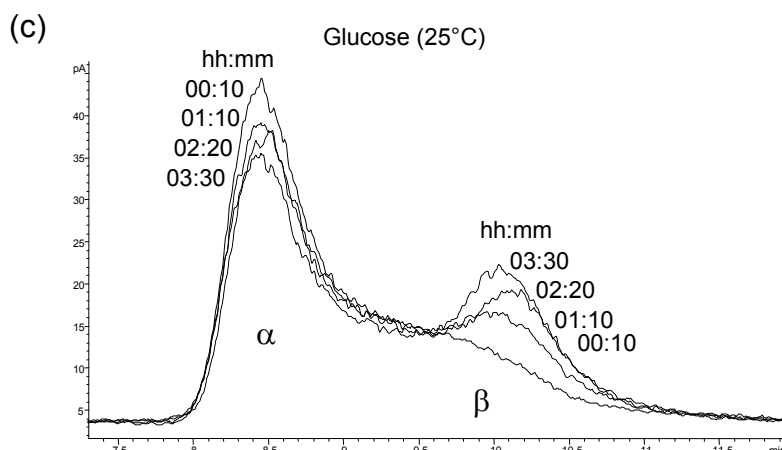
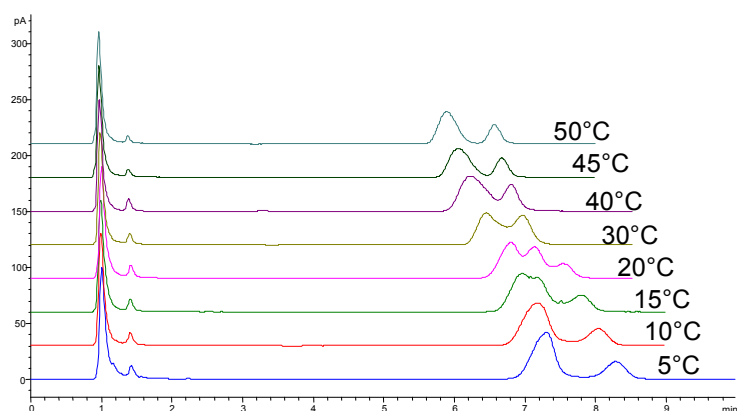


Figure S3: Monitoring of mutarotation of (a) β -D-glucose 6-phosphate, (b) β -D-mannose 6-phosphate, and (c) α -D-glucose. The series of chromatograms were obtained by repeated injection of a freshly prepared sample in water. Experimental conditions: stationary phase, AQ-RP/WAX; injection of 5 μ l G6P (a), M6P (b) and glucose (c) (each 1 mg/mL) at specific time intervals with the sample vial being thermostated at 5°C in the autosampler tray; (a, b) 0.1% (v/v) TFA in ACN / water (35 / 65; v/v); (c) 0.1% (v/v) TFA in ACN / water (98 / 02; v/v), column temperature, 25°C.

The data from the NMR studies and the current HPLC mutarotation studies by injection of freshly prepared samples in regular time intervals allowed to pinpoint unequivocally the elution orders of the respective anomers. In all cases, the α -anomer was eluted first and the β -anomer was eluted as the second isomer.

3 Temperature dependency of on-column mutarotation of D-mannose 6-phosphate as investigated by HPLC with mixed-mode RP/WAX column

(a)



(b)

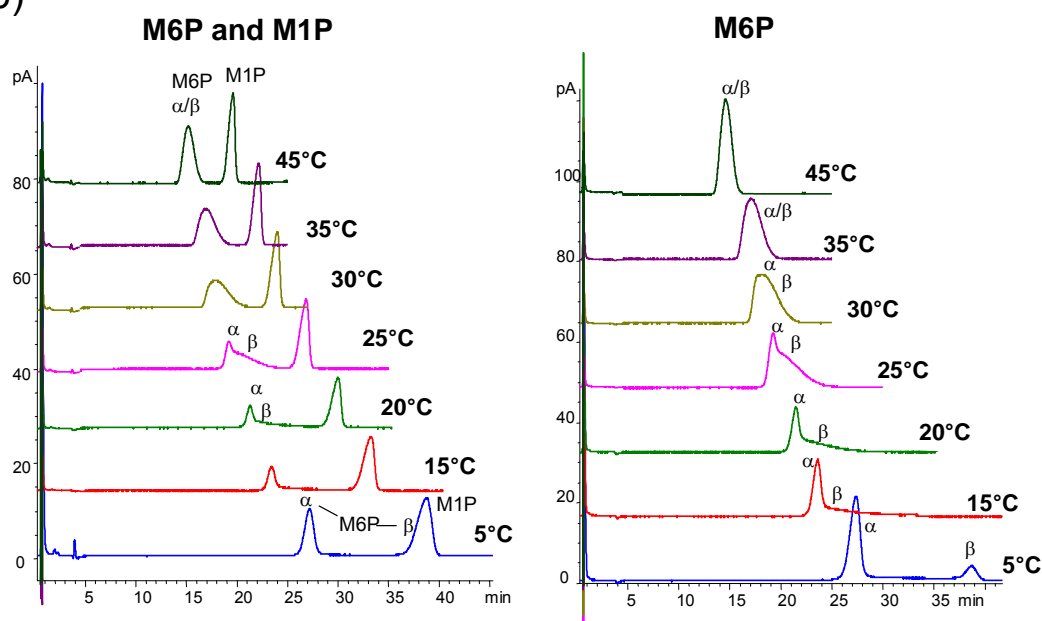


Figure S4: Temperature dependence of on-column mutarotation of mannose 6-phosphate and its separation from mannose 1-phosphate in dual modes, WAX (a) and HILIC/WAX (b). Experimental conditions: stationary phase, AQ-RP/WAX; mobile phase, (a) 0.1% (v/v) TFA in ACN / water (35 / 65; v/v); (b) 0.1% (v/v) TFA in ACN / water (80 / 20; v/v); flow rate, 1 mL/min. Last eluted peak in (a) is mannose 1-phosphate, at 5°C co-eluted with β -M6P.

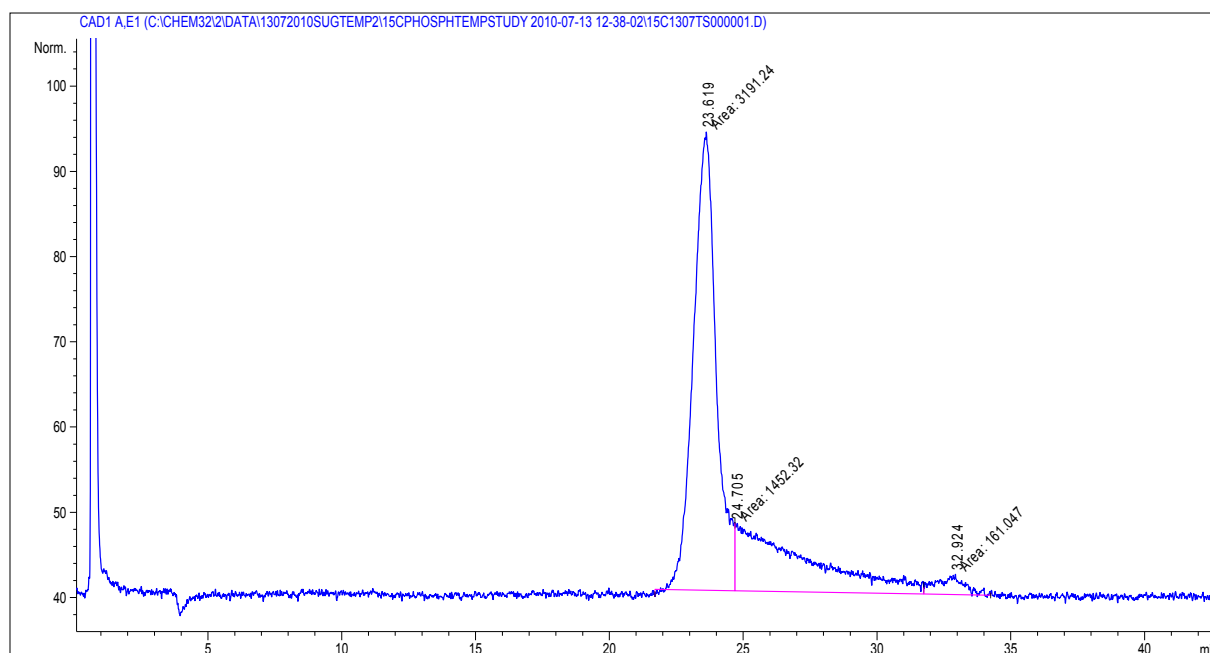


Figure S5: On-column mutarotation of mannose 6-phosphate: Zoomed-in chromatogram obtained at 15°C. Experimental conditions: stationary phase, AQ-RP/WAX; mobile phase, 0.1% (v/v) TFA in ACN / water (80 / 20; v/v).

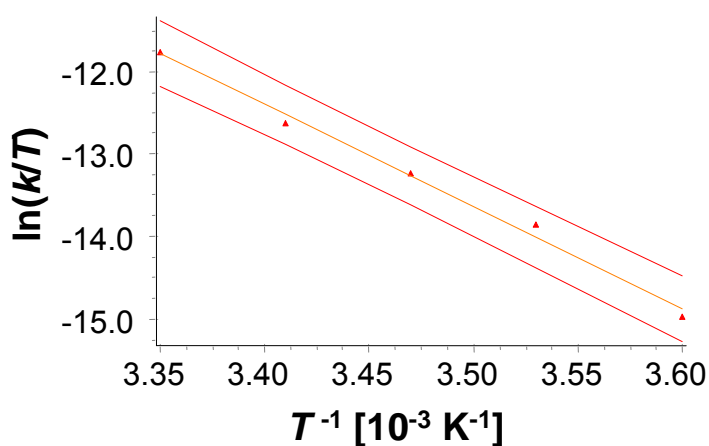


Figure S6: Eyring plot for the interconversion reaction of mannose 6-phosphate obtained with conditions specified in Fig. S4b.

Table S3: Summary of the activation parameters for the interconversion of the anomers of mannose 6-phosphate obtained by temperature dependent measurements (experimental conditions see Fig. S4b).

	α -M6P \rightarrow β -M6P	β -M6P \rightarrow α -M6P
ΔH^\ddagger [kJ·mol ⁻¹]	102.9	102.9
ΔS^\ddagger [J (K·mol) ⁻¹]	46	49
$\Delta G^\ddagger(298.15\text{ K})$ [kJ·mol ⁻¹]	89.2	88.2

4 Response of charged aerosol detector and sensitivity

It is known that the response function of the CAD (like for ELSD) does not linearly depend on the injected mass if a wide concentration range is investigated. Actually the response of the Corona CAD (used here) results typically in non-linear power function curves. This would restrict its application for the study of the kinetic rate constants by dynamic HPLC (DHPLC) because the peak area ratio would not exactly correlate with the isomer amounts in the peaks i.e. the results would be distorted especially at extreme peak area ratios (Wipf et al., Chirality, 2007, 19, 5-9). This is actually the case for the ELSD and kinetic constants derived by DHPLC with ELSD detection are supposed to be subjected to a significant systematic error. Transformation functions would be required to provide rate constants with physicochemical meaning (Wipf et al., Chirality, 2007, 19, 5-9; J. Pazourek, J. Sep. Sci., 2010, 33, 974).

However, in sharp contrast to the ELSD, the CAD gives usually a linear response in the low concentration range (e.g. for quaternary ammonium ions and amino acids between 10 and 200 ng injected to the column) (A. Stojanovic et al. J. Chromatogr. A, 2008, 1209, 179). In fact, also for the current sugar phosphate the detector response is linear in the low concentration range (see Fig. S7 and S8). Since current studies have been always performed in the specified linear concentration range also the rate constants derived by DHPLC are supposed to be devoid of systematic errors from distortions due to non-linear power function curves. It can also be seen from Fig. S7 that α - and β -glucose 6-phosphate give the same detector response as indicated by identical slopes of the calibration curves. Reasonable linearity is also observed for the other sugar phosphates investigated (see e.g. Fig. S8) and moreover also their detector response is very similar (cf. slopes in Fig. S7 and S8).

Overall, it is, however, striking that the sensitivity of the CAD for the currently investigated sugar phosphates is very low. LOQs are around 150 ng (injected on column) which is by a factor of about 10 higher than for other analytes e.g. quaternary ammonium compounds (A. Stojanovic et al. J. Chromatogr. A, 2008, 1209, 179) and amino acids. We suppose that at low concentrations the analytes are lost due to adsorption to metal or glass surfaces.

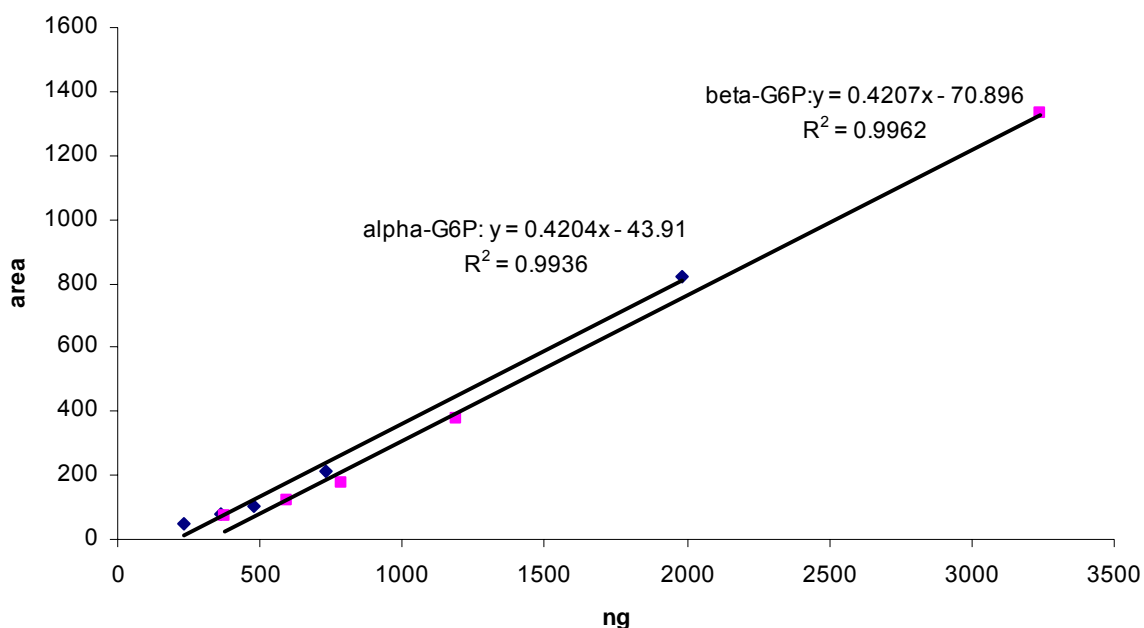


Figure S7: Calibration curves for α -G6P and β -G6P showing identical detector response and reasonable linearity of the signal within the measurement range employed in this study. The lowest data points (around 100 ng of isomers injected) were already below the LOQ and difficult to integrate correctly. They have been omitted. The LOQ was estimated to be at about 150 ng.

Experimental conditions: stationary phase, AQ-RP/WAX; mobile phase, 0.1% (v/v) TFA in ACN / water (80 / 20; v/v), temperature, 5°C; flow rate, 1.5 mL/min.

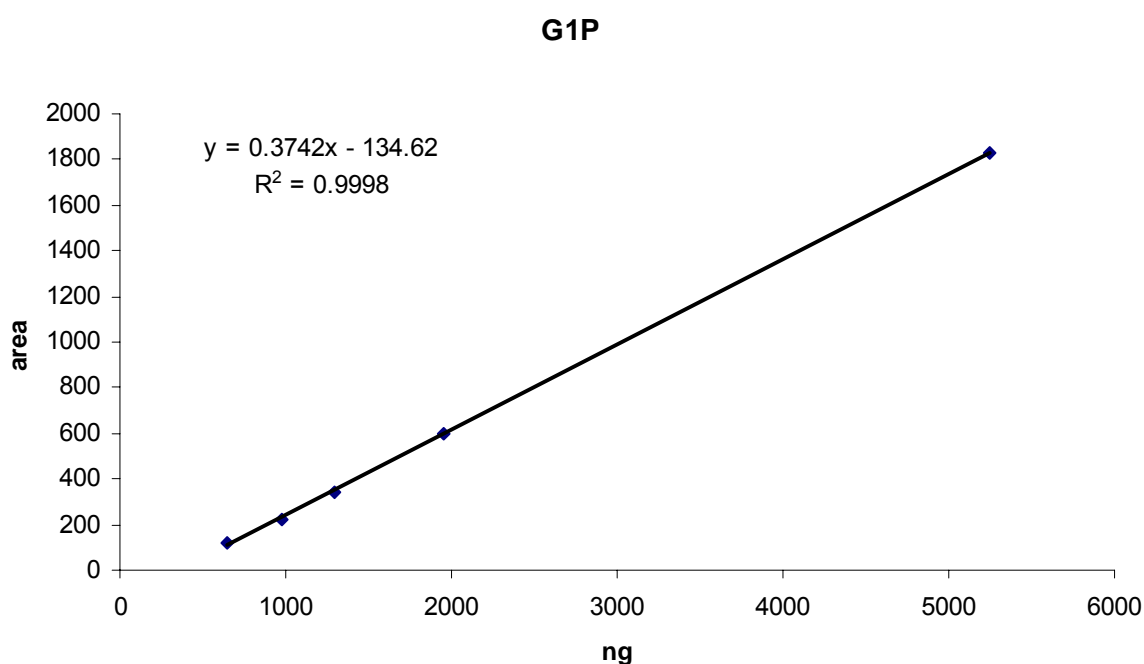


Figure S8: Calibration curve for G1P showing very similar detector response (cf. slopes of G6P) and reasonable linearity of the signal within the measurement range employed in this study. Experimental conditions: as in Fig. S7.

5 Preliminary investigations on the relative ESI-MS sensitivities of the hexose phosphate isomers

The currently employed mobile phase is not ideal in terms of ESI-MS ionization efficiency. Future work will address this issue and attempts are currently made to overcome this limitation for MS coupling of the current selective liquid chromatography method.

In order to elucidate to what extent certain SRM transitions are to some degree unique in their intensities and thus may be exploited to introduce MS/MS detection selectivity supporting the chromatographic separation, we have undertaken infusion experiments to test the relative sensitivities of various fragment ions of the hexose phosphates. The results are given in Figure S9. It is seen that the fragment ions with m/z 79 and 97 are the most intensive ones for all of the hexose phosphates. Interestingly, glucose 1-phosphate and galactose 1-phosphate exhibit higher intensity for the fragment ion m/z 79 compared to m/z 97, while for the other hexose phosphates the situation is reversed. Other fragment ions show some unique intensities such as m/z 223 which was observed for fructose 6-phosphate only, however, have relatively lower intensity.

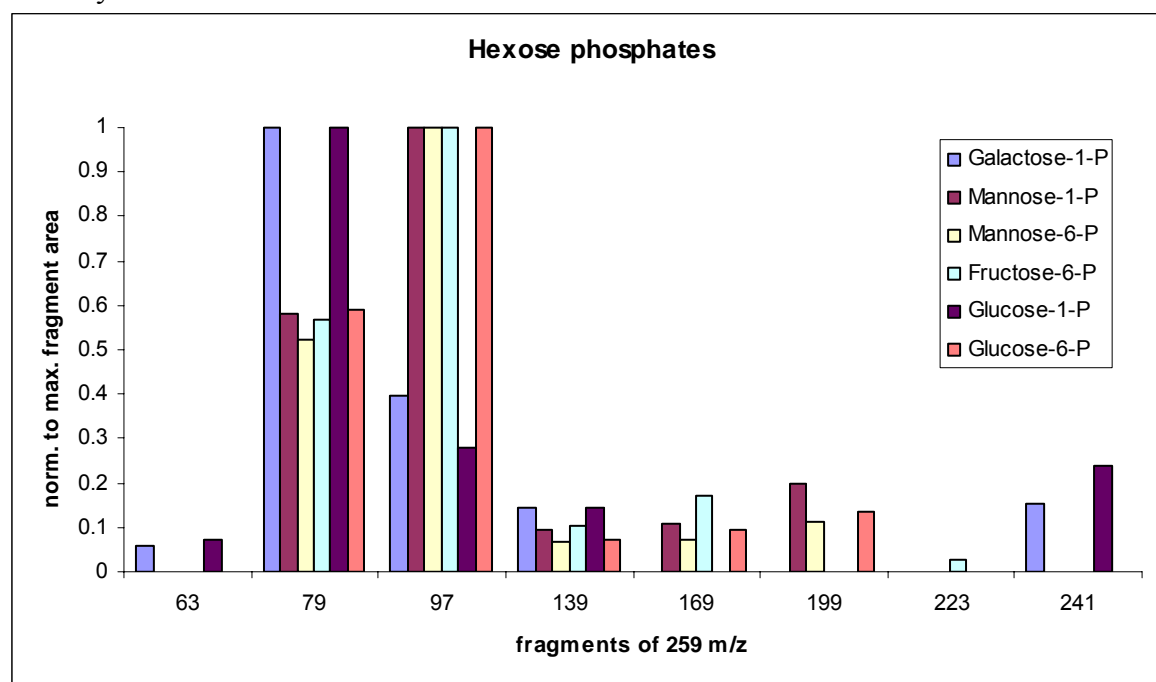


Figure S9: Relative MS sensitivities of various fragment ions of hexose phosphates as measured by infusion experiments. AB Sciex 4000QTrap with TurboIon Spray and analyst 1.5 software. Experimental conditions: ESI voltage, -4500 V; dry gas temperature, 650°C; declustering potential, -45 V; electron multiplier voltage, -2300 V; sample dissolved in acetonitrile/water (80:20; v/v) containing 0.05% (v/v) TFA (ca. 1 mg/mL).

CURRICULUM VITAE

Mag. Helmut HINTERWIRTH

University of Vienna
Department of Analytical Chemistry
Währingerstraße 38, 1090 Vienna, Austria
E-mail: helmut.hinterwirth@univie.ac.at
Phone: +43/1/4277-52323
Fax: +43/1/4277-9523



PERSONAL DATA

Date of birth: 1981/11/20
Place of birth: 4400 Steyr, Austria
Nationality: Austria
Languages: German (native), English (fluent)

EDUCATIONAL BACKGROUND

2012/05 – 06 Research period in Olomouc, Czech Republic

Since 2009/09 PhD thesis *Functionalized Gold-Nanoparticles for Bioanalysis* at the University of Vienna, Institute of Analytical Chemistry, Vienna, Austria, Research Group for Molecular Recognition Materials, Separation Science & Mass Spectrometry, Prof. Dr. Michael Lämmerhofer (now at University of Tübingen, Germany); Teaching Assistant

2009/06/26 Magister rerum naturalium

2008/09 – 2009/06 Master thesis: *Contributions to the Development of Novel Biocompatible Coatings of Medically Relevant Materials with Regard to "Drug-Targeting"-Efficiency*; Tutorial for internships

2002/10 – 2009/06 Studies of Chemistry, University of Vienna, Vienna, Austria

FURTHER EDUCATIONS

2011/11 Patent research workshop

2009/07 – 2010/01 University course: *Quality Assurance in chemical laboratory*; Montanuniversität Leoben (Basics and applications of QA, quality management, industrial management point of view)